LOW TEMPERATURE PRECURSORS FOR

METAL OXIDE CATALYSTS

By

ABDULAZIZ AHMED BAGABAS

Bachelor of Science

King Saud University

Riyadh, Saudi Arabia

1997

Submitted to the Faculty of the
Graduate College of the
Oklahoma State University
in partial fulfillment of
the requirements for
the Degree of
DOCTOR OF PHILOSOPHY
July, 2005

COPYRIGHT

By

Abdulaziz Ahmed Bagabas

July, 2005

LOW TEMPERATURE PRECURSORS FOR

METAL OXIDE CATALYSTS

Dissertation Approved:

Dr. Allen Apblett

_____

Dissertation Adviser

Dr. K. D. Berlin

_____

Dr. LeGrande M. Slaughter

_____

Dr. Gary Foutch

_____

Dr. A. Gordon Emslie

_____

Dean of the Graduate College

ACKNOWLEDGMENTS

In the Name of Allah, Most Gracious, Most Merciful

First of all and formost, I direct all my thanks and praises to Almighty Allah, The Cherisher and Sustainer of the Worlds, for His guidance and assistance that facilitate every stage in my postgraduate studies and in my whole life. Really, my success in everything can only come from Allah. In Him I trust, and unto Him I turn.

I would like to express my sincere appreciation and gratitude to my mentor and academic advisor, Dr. Allen W. Apblett, for his invaluable guidance and great support over the years of my graduate studies and during my dissertation research work at Oklahoma State University.

I am very grateful and indebted to my advisory committee member and friend Dr. Kenneth Darrell Berlin, Regents Professor of Organic Chemistry, for his precious advice, comments, suggestions, and eternal encouragement throughout my academic program and this investigation. Dr. Berlin was a great reference, a teaching model, a man of honesty and principle, and a brilliant chemist. I will always carry with me his wisdom and exuberance.

I also extend my cordial thanks to the rest of my advisory committee members, Dr. LeGrande M. Slaughter, Dr. Gary Foutch, and the late Professor Dr. Elizabeth M. Holt, for their kind cooperation and friendship.

I would like also to express my sincere gratitudes to Dr. Margaret Eastman, the manager of Oklahoma statewide NMR facility and solid-state NMR, for recording the ^{13}C

solid-state NMR spectra for my solid specimens. She was very cooperative and helpful in the work. My appreciation and thanks also go to the late Professor Dr. Elizabeth M. Holt and Dr. Masood A. Khan, the staff crystallographer in the Department of Chemistry at the University of Oklahoma, for single-crystal X-ray diffraction structural determinations. They were ready to lend a hand. Dr. Nicholas F. Materer also deserves my gratefulness for the X-ray photoelectron spectroscopy analysis and his nice friendship. I also express my gratitude to Phoebe Doss, EM Lab manager, for her assistance with the transmission electron microscope (TEM) and scanning electron microscope (SEM) images.

I would also like to take this opportunity to thank all the faculty members of the Department of Chemistry at Oklahoma State University from whom I learned a lot during the time of my graduate studies. In addition, I thank the staff and secretaries of the Department of Chemistry for their kindness and cooperation.

I kindly thank my beloved parents for their supplications, patience, and support. I ask Allah to bestow on you thy mercy even as you cherished me in childhood. I wish also to express my gratitude to my darling grandmother, Mariam Bukhari, for her prayers, love, and concern. My deepest thanks also go to my brothers and sister and all uncles and aunts for their encouragement and support.

I thank my wife, Serene AL-Momen, for her assistance and encouragement. My deepest thanks also go to my beloved kids, who are my great love and the jewels of my life, Zeid Bagabas, Norah AL-Othman, and Abdullah AL-Othman for their cheerfulness. I ask Allah to bless and take care of them.

I am extremely grateful to my chummy, loyal brother Zeid AL-Othman for his constant encouragement, support, assistance, friendship, and advice. He was always available in person to help me at almost all the times. I also express my sincere thanks to his parents, brothers, and relatives for their continual concern and inquiry about me and my studies.

I would like also to acknowledge the help of my brothers, Mohammad Al-Ahmadi and Marzook Ashamary, in teaching me how to use the needed computer programs more efficiently.

I would like also to thank my lab-mate Dr. B. P. Kiran for his help in GC/MS analysis and for his nice companionship. I also appreciate the friendship and support of all other lab-mates in Dr. Apblett's group.

I extend my thanks and gratitude to my close friends Dr. Othman AL-Nashwan, Dr. Mohammed AL-Saleh, Mohomodou Boncan, Mohammad Elyyan, Muhammad Shahrim AbKarim, Dr. Mumtaz Hussain, Saleh Ashaghathra, Sayeed Mohammad and Majed Nassar for their encouragement, support, and friendship.

I appreciate also the great supervision and help of my academic advisors, Dr. Eman Ahmad, Ali Badi, and Dr. Musaed AL-Assaf, at the Royal Embassy of Saudi Arabia Cultrual Mission Attache in Washington, D.C., USA.

Last but not the least, I would like to express my thanks to my boss, Dr. Solaiman AL-Khowaiter, my colleagues, and staff at the Petroleum and Petrochemicals Research Institute (PAPRI) for their aid and encouragement. I would also like to acknowledge the financial support of my sponsor King Abdulaziz City for Science and Technology (KACST), Riyadh, Kingdom of Saudi Arabia.

I conclude these acknowledgements with the supplication of Prophet Solomon (Peace and Blessing upon him) as narrated by the Almighty Allah in The Holy Qur-ān in Sūrat An-Naml (Ants), verse 19, “O my Lord! So order me that I may be grateful for thy favors, which thou has bestowed on me and on my parents, and that I may work the righteousness that will please thee and admit me, by thy grace, to the ranks of thy righteous servants”.

TABLE OF CONTENTS

Chapter Page

COPYRIGHT ii

ACKNOWLEDGMENTS iv

TABLE OF CONTENTS viii

LIST OF TABLES xiii

LIST OF FIGURES xv

1. INTRODUCTION 1

1.1. SYNTHESIS OF SOLIDS 1
1.2. CERAMIC METHOD 1
1.3 CERAMICS: DEFINITION AND CLASSIFICATION 3
1.4. CERAMICS: PROPERTIES AND IMPORTANCE 3
1.5. SCOPE OF THIS STUDY 4
REFERENCES 7

2. SYNTHESIS OF PYRUVIC ACID OXIME (PAO) METAL COMPLEXES 9

2.1. BACKGROUND 9
HPAO and its Complexes 14
2.2. EXPERIMENTAL 20
Materials 20
Physical and Analytical Measurements 21
Synthesis 22
Precursors for Metal Oxides 22
Pyruvic Acid Oxime (HPAO) 22
PAO^- Salts of Main Group Elements 23
$Mg(PAO)_2(H_2O)_3 \cdot 2H_2O$ 23
$HOAl(PAO)_2 \cdot 2H_2O$ 24
$Pb(PAO)_2 \cdot 2H_2O$ 25
PAO^- Salts of Group 12 Metals 25
$Zn(PAO)_2 \cdot 2H_2O$ 25
$Hg(PAO)_2$ 27
PAO^- Salts of Divalent 3d Transition Metals 27

Chapter Page

$Mn_4(PAO)_8 \cdot 2H_2O$ ... 27
$Fe(PAO)_2 \cdot 2H_2O$ ... 28
$Co(PAO)_2 \cdot 2H_2O$ ... 28
$Ni(PAO)_2 \cdot 2H_2O$ ... 29
$Cu(PAO)_2 \cdot 2H_2O$ ... 29
PAO^- Salts of Some Lanthanides ... 30
$Ce(PAO)_3$ ... 30
$Pr(PAO)_3$ ... 30
PAO^{2-} Salts ... 31
$[(H_3C)_4N]^+[Cu(PAO^-)(PAO^{2-})(H_2O)]^- \cdot H_2O$ ... 31
$[H_3C(H_2C)_{15}NH_3]^+[Fe(PAO^-)(PAO^{2-})]^-$ ... 31
$[H_3C(H_2C)_{15}NH_3]^+[Zn(PAO^-)(PAO^{2-})(H_2O)]^-$ ... 32
$[H_3C(H_2C)_{15}NH_3]^+[Ce(PAO^-)_2(PAO^{2-})(H_2O)]^-$ ... 32
X-ray Data Collection and Structure Determinations ... 33
X-ray Structure Determination of $Mg(PAO)_2(H_2O)_3 \cdot 2H_2O$ ... 34
X-ray Structure Determination of $Zn(PAO)_2 \cdot 2H_2O$ ... 35
X-ray Structure Determination of $Cu(PAO)_2 \cdot 2H_2O$ ... 37
X-ray Structure Determination of $Pr(PAO)_3(H_2O)_2$ ... 38
X-ray Structure Determination of $[(H_3C)_4N][Cu(PAO^-)(PAO^{2-})(H_2O)] \cdot H_2O$ ... 39
Pyrolysis ... 40
Pyrolysis of PAO^- Salts of Main Group Elements ... 40
Drying $Mg(PAO)_2(H2O)_3 \cdot 2H_2O$ under Vacuum ... 40
Dehydration of $Mg(PAO)_2(H_2O)_3 \cdot 2H_2O$ at 80 ^oC ... 40
Pyrolysis of $Mg(PAO)_2(H_2O)_3 \cdot 2H_2O$ at 175^oC ... 41
Pyrolysis of $Mg(PAO)_2(H_2O)_3 \cdot 2H_2O$ at 220^oC ... 41
Pyrolysis of $Mg(PAO)_2(H_2O)_3 \cdot 2H_2O$ at 250^oC ... 41
Pyrolysis of $Mg(PAO)_2(H_2O)_3 \cdot 2H_2O$ at 450^oC ... 41
Pyrolysis of $Mg(PAO)_2(H_2O)_3 \cdot 2H_2O$ at 500^oC ... 42
Pyrolysis of $Mg(PAO)_2(H_2O)_3 \cdot 2H_2O$ at 600^oC ... 42
Pyrolysis of $Mg(PAO)_2(H2O)_3 \cdot 2H_2O$ at 900^oC ... 42
Pyrolysis of $HOAl(PAO)_2 \cdot 2H_2O$ at 100^oC ... 42
Pyrolysis of $HOAl(PAO)_2 \cdot 2H_2O$ at 125^oC ... 43
Pyrolysis of $HOAl(PAO)_2 \cdot 2H_2O$ at 150^oC ... 43
Pyrolysis of $HOAl(PAO)_2 \cdot 2H_2O$ at 200^oC ... 43
Pyrolysis of $HOAl(PAO)_2 \cdot 2H_2O$ at 250^oC ... 43
Pyrolysis of $HOAl(PAO)_2 \cdot 2H_2O$ at 300^oC ... 44
Pyrolysis of $HOAl(PAO)_2 \cdot 2H_2O$ at 450^oC ... 44
Pyrolysis of $HOAl(PAO)_2 \cdot 2H_2O$ at 600^oC ... 44

Chapter Page

Pyrolysis of PAO^- Salts of Group 12 Metals 44
Pyrolysis of $Zn(PAO)_2 \cdot 2H_2O$ at 150°C 44
Pyrolysis of $Zn(PAO)_2 \cdot 2H_2O$ at 200°C 45
Pyrolysis of $Zn(PAO)_2 \cdot 2H_2O$ at 290°C 45
Pyrolysis of $Zn(PAO)_2 \cdot 2H_2O$ at 389°C 45
Pyrolysis of $Cd(PAO)_2$ at 200°C 46
Pyrolysis of $Cd(PAO)_2$ at 300°C 46
Pyrolysis of $Cd(PAO)_2$ at 400°C 46
Pyrolysis of $Hg(PAO)_2$ at 90°C 46
Pyrolysis of PAO^- Salts of Divalent 3d Transition Metals 47
Pyrolysis of $Mn_4(PAO)_8.2H_2O$ at 200°C Under N_2 47
Pyrolysis of $Mn_4(PAO)_8.2H_2O$ at 533°C 47
Pyrolysis of $Fe(PAO)_2.2H_2O$ at 285°C 47
Pyrolysis of $Fe(PAO)_2 \cdot 2H_2O$ at 463°C 48
Pyrolysis of $Co(PAO)_2 \cdot 2H_2O$ at 276°C 48
Pyrolysis of $Ni(PAO)_2 \cdot 2H_2O$ at 349°C 48
Hydrolysis of $Cu(PAO)_2 \cdot 2H_2O$ 48
Pyrolysis of $Cu(PAO)_2 \cdot 2H_2O$ at 421°C 49
Pyrolysis of PAO^{2-} Salts 49
Pyrolysis of $[(H_3C)_4N]^+[Cu(PAO^-)(PAO^{2-})(H_2O)]^- \cdot H_2O$ 49
Pyrolysis of $[H_3C(H_2C)_{15}NH_3]^+[Fe(PAO^-)(PAO^{2-})]^-$ at 574°C 49
Pyrolysis of $[H_3C(H_2C)_{15}NH_3]^+[Zn(PAO^-)(PAO^{2-})(H_2O)]^-$ at 101°C .. 50
Sintering of $[H_3C(H_2C)_{15}NH_3]^+[Zn(PAO^-)(PAO^{2-})(H_2O)]^-$ at 140°C .. 50
Sintering of $[H_3C(H_2C)_{15}NH_3]^+[Zn(PAO^-)(PAO^{2-})(H_2O)]^-$ at 208°C .. 50
Sintering of $[H_3C(H_2C)_{15}NH_3]^+[Zn(PAO^-)(PAO^{2-})(H_2O)]^-$ at 411°C .. 50
Pyrolysis of $[H_3C(H_2C)_{15}NH_3]^+[Ce(PAO^-)_2(PAO^{2-})(H_2O)]^-$ at 289°C. 51
Acidity and Basicity Measurements 51
2.3. RESULTS AND DISCUSSION 52
PAO^- Salts of Main Group Elements 52
Spectroscopic Characterization of PAO^- Salts of Main Group Elements 59
Thermal Behavior of PAO^- Salts of Main Group Elements 66
Textural and Surface Acid-Base Properties of Main Group Element Oxides 72
PAO^- Salts of Group 12 Metals 75
Spectroscopic Characterization of PAO^- Salts of Group 12 Metals 83
Thermal Behavior of PAO^- Salts of Group 12 Metals 88
Textural and Surface Acid-Base Properties of Group 12 Metal Oxides 98
PAO^- Salts of Divalent 3d Transition Metals 100
Spectroscopic Characterization of PAO^- Salts of Divalent 3d Transition Metals 106
Thermal Behavior of PAO^- Salts of Divalent 3d Transition Metals 108
PAO^- Salts of Some Trivalent Lanthanides 125
Spectroscopic Characterization of PAO^- Salts of Some Trivalent Lanthanides

Chapter Page

.... 136
Thermal Behavior of PAO^- Salts of Some Trivalent Lanthanides 137
PAO^{2-} Salts 138
Spectroscopic Characterization of PAO^{2-} Salts 150
Thermal Behavior of PAO^{2-} Salts 152
2.4. CONCLUSION 155
REFERENCES 155

3. PYRUVIC ACID OXIME COMPLEXES PYROLYSIS MECHANISM 165

3.1. INTRODUCTION 165
3.2. EXPERIMENTAL 171
3.3. RESULTS AND DISCUSSION 172
3.4. CONCLUSION 174
REFERENCES 175

4. CATALYTIC CLAISEN-SCHMIDT CONDENSATION USING NANOPARTICULATE $Zn(PAO)_2 \cdot 2H_2O$-DERIVED ZINC OXIDE 178

4.1. INTRODUCTION 178
4.2. EXPERIMENTAL 183
Acidity and Basicity Measurements 184
4.3. RESULTS AND DISCUSSION 185
4.4. CONCLUSION 194
REFERENCES 195

5. SELECTIVE N-METHYLATION OF ANILINE USING DIMETHYL CARBONATE AND NANOPARTICULATE PAO^--DERIVED FERRITE 204

5.1. INTRODUCTION 204
5.2. EXPERIMENTAL 206
Preparation of NZFPAO Catalyst 209
Preparation of NZFOH Catalyst 209
Catalyst Characterization 210
Acidity and Basicity Measurements 211
XPS Measurements 213
5.3. RESULTS AND DISCUSSION 213
Mechanism of the Reaction 226
REFERENCES 234

6. FRIEDEL-CRAFTS ALLYLATION OF BENZENE PROMOTED BY NANOPARTICULATE $Co(PAO)_2 \cdot 2H_2O$-DERIVED TRICOBALT TETRAOXIDE 241

6.1. INTRODUCTION 241

Chapter Page

6.2. EXPERIMENTAL 248
Acidity and Basicity Measurements 250
6.3. RESULTS AND DISCUSSION 251
6.4. CONCLUSION 263
REFERENCES 263

7. ARSENIC REMIDIATION IN AQUEOUS MEDIUM USING NANOPARTICULATE TRANSITION METAL OXIDES 265

7.1. INTRODUCTION 265
7.2. EXPERIMENTAL 273
Acidity and Basicity Measurements 274
7.3. RESULTS AND DISCUSSION 275
7.4. CONCLUSION 280
REFERENCES 280

APPENDICES 283

APPENDIX A 284
CRYSTALLOGRAPHIC DATA 284

LIST OF TABLES

Table Page

Table 2.1. ^{13}C $\{^{1}H\}$ NMR Chemical Shifts (ppm) of PA and HPAO 15

Table 2.2. Crystallographic Data for $Mg(PAO)_2(H_2O)_3 \cdot 2H_2O$ 35

Table 2.3. Crystallographic Data for $Zn(PAO)_2 \cdot 2H_2O$ 36

Table 2.4. Crystallographic Data for $Cu(O_2CC(=NOH)CH_3)_2 \cdot 2H_2O$ 37

Table 2.5. Crystallographic Data for $Pr(PAO)_3(H_2O)_2$ 38

Table 2.6. Crystallographic Data for $[(H_3C)_4N][Cu(PAO^-)(PAO^{2-})(H_2O)] \cdot H_2O$ 39

Table 2.7. Bond Distances (Å) for $Mg(PAO)_2(H_2O)_3 \cdot 2H_2O$ 54

Table 2.8. Interbond Angles (^{o}) for $Mg(PAO)_2(H_2O)_3 \cdot 2H_2O$ 57

Table 2.9. Distinctive IR Vibrational Frequencies (cm^{-1}) of the Salts of Main Group Elements of PAO^- 60

Table 2.10. Solid-State ^{13}C NMR CPMAS Chemical Shifts (ppm) of the Salts of Main Group Elements of PAO^- 64

Table 2.11 . Chemical and Textural Properties of MgO 74

Table 2.12. Bond Distances (Å) for $Zn(PAO)_2.2H_2O$ 78

Table 2.13. Interbond Angles (^{o}) for $Zn(PAO)_2 \cdot 2H_2O$ 81

Table 2.14. Hydrogen Bonds for $Zn(PAO)_2 \cdot 2H_2O$ [Å and ^{o}] 82

Table 2.15. Distinctive IR Vibrational Frequencies (cm^{-1}) of the Salts of Group 12 Elements of PAO^- 83

Table 2.16. Solid-State ^{13}C NMR CPMAS Chemical Shifts (ppm) of the Salts of Group 12 Elements of PAO^- 86

Table 2.17. Chemical and Textural Properties of ZnO 99

Table 2.18. Bond Distances (Å) for $Cu(PAO)_2 \cdot 2H_2O$ 103

Table 2.19. Interbond Angles (^{o}) for $Cu(PAO)_2 \cdot 2H_2O$ 104

Table 2.20. Distinctive IR Vibrational Frequencies (cm^{-1}) of the PAO^- Salts of Divalent 3d Transition Metals 106

Table 2.21. Bond Distances (Å) for $Pr(PAO)_3(H_2O)_2$ 127

Table Page

Table 2.22. Interbond Angles (^{o}) for $Pr(PAO)_3(H_2O)_2$ 132

Table 2.23. Hydrogen Bonds for $Pr(PAO)_3(H_2O)_2$ (Å and ^{o}) 135

Table 2.24. Distinctive IR Vibrational Frequencies (cm^{-1}) of the PAO^- Salts of Some Trivalent Lanthanides 136

Table 2.25. Bond Distances (Å) for $[(H_3C)_4N][Cu(PAO^-)(PAO^{2-})(H_2O)]\cdot H_2O$ 141

Table 2.26. Hydrogen Bonds for $[(H_3C)_4N][Cu(PAO^-)(PAO^{2-})(H_2O)]\cdot H_2O$ [Å and ^{o}]. 142

Table 2.27. Interbond Angles (^{o}) for $[(H_3C)_4N][Cu(PAO^-)(PAO^{2-})(H_2O)]\cdot H_2O$ 145

Table 2.28. Distinctive IR Vibrational Frequencies (cm^{-1}) of the Salts of PAO^{2-} 151

Table 5.1. Characters of the Prepared Catalysts Characters of the Prepared Catalysts 210

Table 5.2. Surface Metal Composition Ratios of the Catalysts as Determined by XPS 213

Table 6.1. Specific Surface Area of each Catalyst Used to Promote the Allylation of Benzene 254

Table A 1. Atomic coordinatates ($x\ 10^4$) and equivalent isotopic displacement 285

Table A 2. Anisotropic displacement coefficients ($Å^2\ x\ 10^3$) for $Mg(PAO)_2(H_2O)_3\cdot 2H_2O$ 286

Table A 3. H-Atoms coordination ($x\ 10^4$) and isotropic displacement coefficients 287

Table A 4. Atomic coordinates ($x\ 10^4$) and equivalent isotropic displaceme 288

Table A 5. Anisotropic displacement parameters ($Å^2\ x\ 10^3$) for $Zn(PAO)_2\cdot 2H_2O$ 288

Table A 6. Hydrogen coordinates ($x\ 10^4$) and isotropic displacement parameters 288

Table A 7. Torsion angles [°] for $Zn(PAO)_2\cdot 2H_2O$ 289

Table A 8. Atomic coordinates ($x\ 10^4$) and equivalent isotropic displacement 290

Table A 9. Anisotropic displacement parameters ($Å^2\ x\ 10^3$) for $Pr(PAO)_3(H_2O)_2$ 291

Table A 10. Hydrogen coordinates ($x\ 10^4$) and isotropic displacement parameters 292

Table A 11. Torsion angles [°] for $Pr(PAO)_3(H_2O)_2$ 293

Table A 12. Atomic coordinates ($x\ 10^4$) and equivalent isotropic displacement 295

Table A 13. Anisotropic displacement parameters ($Å^2\ x\ 10^3$) for $[(H_3C)_4N][Cu(PAO^-)$ 296

Table A 14 Hydrogen coordinates ($x\ 10^4$) and isotropic displacement parameters 297

Table A 15. Torsion angles [°] for $[(H_3C)_4N][Cu(PAO^-)(PAO^{2-})(H_2O)]\cdot H_2O$ 298

LIST OF FIGURES

Figure Page

Figure 2.1 Oxime-amine-carboxylic acid chain (adapted from reference 18) 10

Figure 2.2. π-Resonance structures resulted from the carboxyl-oxime conjugation in the α-oximinocarboxylic acids 11

Figure 2.3. The two diastereomers of an α-oximinocarboxylic acid 12

Figure 2.4. The molecular structure of HPAO 16

Figure 2.5. The N, O-chelate of PAO^- ligand to a metal center 17

Figure 2.6. Crystal structure of $Mg(PAO)_2(H_2O)_3{\cdot}2H_2O$ 54

Figure 2.7. A view of the unit cell contents of $[Mg(PAO)_2(H_2O)_3]$ complex molecules joined by hydrogen bonds, denoted by the dashed lines 58

Figure 2.8. Hydrogen-bonded $[Mg(PAO)_2(H_2O)_3{\cdot}2H_2O]$ units within the unit cell and adjacent unit cells. The dashed lines represent the hydrogen-bonds 59

Figure 2.9. A suggested structure of $HOAl(PAO)_2{\cdot}2H_2O$ 63

Figure 2.10. The TGA trace for $Mg(PAO)_2(H_2O)_3{\cdot}2H_2O$, contaminated with NaCl, in dry air with a heating rate of 1 ^oC/min 66

Figure 2.11. The TGA trace for pure $Mg(PAO)_2(H_2O)_3{\cdot}2H_2O$ in dry air with a heating rate of 1 ^oC/min 69

Figure 2.12. The TGA trace for $HOAl(PAO)_2{\cdot}2H_2O$ in dry air with a heating rate of 1 ^oC/min 70

Figure 2.13. SEM electromicrographs of $HOAl(PAO)_2{\cdot}2H_2O$ heated to 300 ^oC 71

Figure 2.14. The XRD pattern of $HOAl(PAO)_2{\cdot}2H_2O$ calcined at 900 ^oC 71

Figure 2.15. Change of S_{BET} with temperature for calcined $HOAl(PAO)_2{\cdot}2H_2O$ 75

Figure 2.16. The XRD patterns of (A) $Zn(PAO)_2{\cdot}2H_2O$, (B) $Cd(PAO)_2$, and (C) $Hg(PAO)_2$ 76

Figure 2.17. Crystal structure of $Zn(PAO)_2{\cdot}2H_2O$ drawn at 50% level 77

Figure 2.18. A perspective view of the zinc complex sheet along the yz-plane 83

Figure 2.19. The TGA and DTA traces for $Zn(PAO)_2{\cdot}2H_2O$ in dry air with a heating rate

of 1 ^{o}C/min 88

Figure 2.20. Solid-state ^{13}C CPMAS NMR spectra of $Zn(PAO)_2 \cdot 2H_2O$ heated to (A) 25^{o}C, (B) 150^{o}C, (C) 200^{o}C, and (D) 290^{o}C. (E) is the spectrum of synthesized $ZnCO_3$ 90

Figure 2.21. XRD patterns of $Zn(PAO)_2 \cdot 2H_2O$ heated to 150, 200, 290, and 389^{o}C 91

Figure 2.22. Crystallite size measurements by XRD of ZnO obtained at 290 ^{o}C (left) and at 389 ^{o}C (right) 92

Figure 2.23. TEM images of ZnO particles obtained at 290^{o}C (top) and at 389^{o}C (bottom) 93

Figure 2.24. SEM electromicrographs of $Zn(PAO)_2 \cdot 2H_2O$ and its pyrolysis products ... 94

Figure 2.25. Variation of specific surface area (S_{BET}) with temperature for $Zn(PAO)_2 \cdot 2H_2O$ 95

Figure 2.26. Decomposition temperature in ^{o}C of the divalent group 12 metal 2-hydroxyiminpropanoates as a function of the metal ion radius 96

Figure 2.27. Decomposition temperatures versus the ionic radius of PAO^{-} complexes of metals of periods (A) 4, (B) 5, and (C) 6 97

Figure 2.28. XRD patterns of (A) $Mn_4(PAO)_8 \cdot 2H_2O$, (B) $Fe(PAO)_2 \cdot 2H_2O$, (C) $Co(PAO)_2 \cdot 2H_2O$, (D) $Ni(PAO)_2 \cdot 2H_2O$, (E) $Cu(PAO)_2 \cdot 2H_2O$, (F) $Zn(PAO)_2 \cdot 2H_2O$ 101

Figure 2.29. Crystal structure of $Cu(PAO)_2 \cdot 2H_2O$ 102

Figure 2.30. Perspective view of (A) the stacked chains of the copper complexes along the a-axis and (B) the extensive network of hydrogen bonds tying the copper complexes 105

Figure 2.31. Suggested structure of iron, cobalt, and nickel PAO^{-} complexes based on their IR and XRD spectra 108

Figure 2.32. The TGA trace for $Mn_4(PAO)_8.2H_2O$ in dry air with a heating rate of 1 ^{o}C per minute 109

Figure 2.33. The TGA and DTA traces for $Fe(PAO)_2 \cdot 2H_2O$ in dry air with a heating rate of 1 ^{o}C/min 112

Figure 2.34. The XRD spectra for $Fe(PAO)_2 \cdot 2H_2O$ heated under air stream to (A) 285 ^{o}C and (B) 463 ^{o}C 114

Figure 2.35. The TGA trace for $Co(PAO)_2 \cdot 2H_2O$ in dry air with a heating rate of 1 ^{o}C/min 115

Figure 2.36. The XRD spectrum for $Co(PAO)_2 \cdot 2H_2O$ heated under air stream to 276 ^{o}C 116

Figure 2.37. Crystallite size of Co_3O_4 obtained under air stream at 276 ^{o}C 116

Figure Page

Figure 2.38. The SEM electromicrographs of Co_3O_4 obtained at 276 ^oC 117

Figure 2.39. The TGA and DTA traces for $Ni(PAO)_2 \cdot 2H_2O$ in dry air with a heating rate of 1 ^oC/min 118

Figure 2.40. The XRD spectra for $Ni(PAO)_2 \cdot 2H_2O$ heated to (A) 340 ^oC and (B) 538 ^oC 120

Figure 2.41. The TGA and DTA traces for $Cu(PAO)_2 \cdot 2H_2O$ in dry air with a heating rate of 1 ^oC/min 122

Figure 2.42. Radical pyrolysis pathway of $Cu(PAO)_2$ 122

Figure 2.43. The XRD spectrum for $Cu(PAO)_2 \cdot 2H_2O$ heated under air stream to 220 ^oC 123

Figure 2.44. Crystallite size of CuO obtained under air stream at 220 ^oC 124

Figure 2.45. SEM electronmicrograph of CuO obtained under air at 220 ^oC 125

Figure 2.46. Crystal structure of $Pr(PAO)_3(H_2O)_2$ drawn at 50% level 126

Figure 2.47. Perspective view of the 3-D network of $Pr(PAO)_3(H_2O)_2$ along the a-axis 135

Figure 2.48. The TGA trace of $Pr(PAO)_3(H_2O)_2$ complex 138

Figure 2.49. Crystal structure of $[(H_3C)_4N][Cu(PAO^-)(PAO^{2-})(H_2O)] \cdot H_2O$ drawn at 50% level 140

Figure 2.50. A view along the b-axis of the network showing some of the hydrogen bonds connecting the cuprate anions and the crystallization water molecules in $[(H_3C)_4N][Cu(PAO^-)(PAO^{2-})(H_2O)] \cdot H_2O$ 149

Figure 2.51.A perspective view of the cuprate anion ribbon $[Cu(PAO^-)(PAO^2(H_2O)]$.. 149

Figure 3.1. Synchronous production of acetonitrile, carbon dioxide, and water during the thermal decomposition of $Ce(PAO)_3$. Adapted from the literature[1] 167

Figure 4.1. Langmuir adsorption isotherm of (A) acidity and (B) basicity of ZnO 186

Figure 4.2. Mole fraction (X) of reactants and product versus time at 150^oC 188

Figure 4.3. Second-order plot for the Claisen-Schmidt condensation between acetophenone and benzaldehyde catalyzed by 5 wt% reactants ZnO at 150^oC 189

Figure 4.4. Pseudo first-order reaction in (A) acetophenone and (B) benzaldehyde..... 190

Figure 4.5. Second-order plot for the Claisen-Schmidt condensation between acetophenone and benzaldehyde catalyzed by 5 wt% reactants ZnO at 130^oC 191

Figure 4.6. Change of the mole fraction (X) of reactants and products with time at 130^oC 191

Figure 4.7. Variation of mole fraction (X) of reactant and product at 110^oC with time 192

Figure 4.8. Second-order for the aldol condensation between acetophenone and

benzaldehyde at 110°C promoted by 5 wt% reactants ZnO 193

Figure 4.9. The Arrhenius plot for the Claisen-Schmidt Condensation between acetophenone and benzaldehyde catalyzed by 5 wt% reactants ZnO 193

Figure 5.1. Langmuir adsorption basicity isotherms for (A) NZFOH and (B) NZFPAO 212

Figure 5.2. The multistep, sequential reaction between aniline and DMC 214

Figure 5.3. First-order plot for the methylation of aniline with DMC at 150 °C over NZFPAO catalyst 215

Figure 5.4. Change of mole fraction of aniline, NMA, and NNDMA with reaction time in methylation process with DMC over NZFPAO catalyst at 150°C 216

Figure 5.5. Conversion % of aniline and selectivity % towards NMA and NNDMA in the methylation reaction of aniline with DMC over NZFPAO catalyst at 150°C 217

Figure 5.6. First-order plot for the methylation of aniline with DMC at 150 °C over NZFOH catalyst 218

Figure 5.7. Change of mole fraction of aniline, NMA, and NNDMA with reaction time in methylation process with DMC over NZFOH catalyst at 150°C 219

Figure 5.8. Conversion % of aniline and selectivity % towards NMA and NNDMA in the methylation reaction of aniline with DMC over NZFOH catalyst at 150°C 220

Figure 5.9. First-order plot for the methylation of aniline with methanol at 150°C over NZFOH catalyst 221

Figure 5.10. Change of mole fraction of aniline, NMA, and NNDMA with reaction time in methylation process with methanol over NZFOH catalyst at 150°C 222

Figure 5.11. Conversion % of aniline and selectivity % towards NMA and NNDMA in the methylation reaction of aniline with methanol over NZFOH catalyst at 150°C 223

Figure 5.12. First-order plot for the methylation of aniline with DMC at 150 °C without catalyst 224

Figure 5.13. Change of mole fraction of aniline, NMA, and NNDMA with reaction time in methylation process with DMC without catalyst at 150°C 225

Figure 5.14. Conversion % of aniline and selectivity % towards NMA and NNDMA in the methylation reaction of aniline with DMC without catalyst at 150°C 226

Figure 5.15. Proposed mechanism of N-methylation of aniline with DMC over ferrite catalyst 228

Figure 5.16. Proposed mechanism of N-methylation of aniline with methanol over ferrite catalyst 229

Figure 5.17. Proposed mechanism of N-methylation of aniline with DMC without catalyst 231

Figure Page

Figure 6.1. Langmuir adsorption isotherm of (A) acidity and (B) basicity of $Co_2(PAO)_2 \cdot 2H_2O$-derived Co_3O_4 251

Figure 6.2. First-order plot of changing the concentration of allyl bromide with time .. 254

Figure 6.3. Conversion % of allyl bromide in the Friedel-Crafts allylation of benzene at 150^oC 256

Figure 6.4. SEM micrographs of the $Co_2(PAO)_2 \cdot 2H_2O$-derived Co_3O_4 (A) x 1,000 and (B) x 10,000 256

Figure 6.5. SEM micrographs of the $CoBr_2$-derived Co_3O_4 taken at voltage of 20 kV and magnifications of (A) 1000, (B) 4000, and (C) 7000 257

Figure 6.6. EDXS (A), primary electron back-scattered image (B), and secondary electron back-scattered image (C) of the $CoBr_2$-derived Co_3O_4 taken at a voltage of 20 kV and magnification of 2700 258

Figure 6.7. SEM micrographs of anhydrous $CoBr_2$ taken at a voltage of 25 kV and magnification of (A) 1000 and (B) 1400 259

Figure 6.8. SEM micrographs of the supported catalyst at magnification of (A) 1400, (B) 3500, (C) 4500, and (D) 7000. Primary electron back-scattered image (E) and secondary electron back-scattered image (F) at magnification of 2300 260

Figure 6.9. EDXS images and spectrum of the supported catalyst at magnification of 2300 261

Figure 6.10. SEM micrographs of the supported catalyst after removing the silica support at magnification of (A) 1500, (B) 5000, and (C) 2700. (D), (E), and (F) are the mapping images obtained from EDXS at magnification of 2700 262

Figure 7.1. Langmuir adsorption isotherm of (A) acidity and (B) basicity of Fe_2O_3 obtained upon pyrolysis of $Fe(PAO)_2 \cdot 2H_2O$ at 463^oC 275

Figure 7.2. Langmuir sorption isotherm for arsenate by iron oxide obtained at 285^oC 276

Figure 7.3. Langmuir sorption isotherm for arsenate by iron oxide obtained at 463^oC 277

Figure 7.4. Langmuir sorption isotherm for arsenate by zinc oxide obtained at 389^oC 278

Figure 7.5. Langmuir sorption isotherm for arsenate by Co3O4 obtained at 276^oC 279

Figure 7.6. The chemisorption of arsenate on the surface of transition metal oxide nanoparticulate 279

CHAPTER 1

1. INTRODUCTION

1.1. SYNTHESIS OF SOLIDS

There are five general preparative techniques employed for the synthesis of solid materials. First, the high-temperature processes, which include the ceramic method and the vapor phase transport (VPT) method. Second, the low-temperature processes, which include the precursor method, a modification of existing structure method (either by intercalation or by ion-exchange), and the sol-gel synthesis method. The third class includes the dry, high-pressure method and the hydrothermal method, which both fall under high-pressure processes. The fourth technique is a crystal growth method that can be used either for mono- or multi-component systems. The last set of preparative techniques encompasses the chemical and physical preparations of thin films.[1,2] The second, third, and fifth techniques are incorporated into what is called *soft chemistry* "*chimie douce*" routes, which are useful for synthesis of metastable phases that are hard to prepare by the conventional ceramic procedure. These techniques provide better control over structure, chemical and textural homogeneity, and stoichiometry and yield solid materials in various forms such as fibers, monoliths, and coatings with improved or superior properties in comparison to those obtained by the traditional ceramic method.[1-3]

1.2. CERAMIC METHOD

Solid materials are classically prepared by the ceramic method, also known as "*shake and bake*" or "*heat and beat*", in which metal oxides, carbonates, carboxylates,

or other compounds of the desired metals are mixed and ground together into powders to eventually be calcined at high temperatures. In short, the ceramic method is usually a direct solid-state reaction of solid raw materials at high temperatures.[1,2] Pulverization of reactant powders together is imperative to obtain high surface area grains and to maximize contact between the reactants in order to accelerate the reaction in the solid-state.[1,3] Another important factor for the success of the ceramic method is the pelletization of the ground reactant powders for minimization of void spaces and increasing contact between grains.[3] The ceramic method has many shortcomings that make the soft chemistry routes more preferable for preparation of solid materials. A solid-state reaction usually occurs in the ceramic method, which makes the reaction slow because the product formation totally depends upon the diffusion of reactant components over long distances. Thus, a mixture of reactants and products is often obtained, complicating the separation of the desired products. Moreover, the ceramic method occasionally does not lead to the formation of a homogeneously constituent product, even if the reaction is essentially complete. Utilizing chemical methods, such as freeze-drying, spray-drying, co-precipitation, sol-gel, and other techniques, can minimize drawbacks of the ceramic method by reducing the lengths of the diffusion path, increasing the surface area, and increasing the homogeneity by making the particle size of reactants smaller and therefore allow more effective mixing of reactants. Nevertheless, the ceramic method has been employed extensively for synthesis of solid materials because the reagents used in the alternative soft chemistry methods are often expensive and difficult to handle on a large scale.[1-3]

1.3 CERAMICS: DEFINITION AND CLASSIFICATION

Ceramic is a translation of the Greek word *keramos*, which means pottery or "burnt-stuff".[4,5] Moreover, it has an ancient Sanskrit origin designating a substance developed with the aid of fire.[5] Accordingly, ceramics were traditionally defined as those materials made of silicate, such as clay products, cement, and silicate glasses.[4,6] However, this definition is too restrictive to include the modern advancements in procedures of synthesis and the exploitation of unprecedented properties of such materials for specific applications. Hence, ceramics are better specified as the art and science of making and using solids made up of inorganic, nonmetallic materials, which are high-temperature treated during their fabrication or manufacture.[5,7] This broader definition covers both the old classic ceramics and advanced ceramics, also known as engineering ceramics. The former category includes materials like pottery, porcelain, enamels, structural clay products, cements, glass, abrasives, and refractories. All of these materials are fabricated from metallic silicates, oxides, aluminides, beryllides, borides, carbides, nitrides, silicides, or sulfides. The latter category comprises materials such as high-temperature oxide superconductors, electroceramics, ferroelectric ceramics, non-silicate glasses, structural components, and single crystals.[4-7]

1.4. CERAMICS: PROPERTIES AND IMPORTANCE

Ceramics have attracted increasing attention because they combine several desirable attributes. They possess remarkable chemical- and weathering-resistance, excellent electrical-resistance, high stability at high temperatures, good tensile strength, and great compressive strength.[5] Therefore, they have found many mechanical, architectural, electrical, and magnetic applications.[4] Besides their useful characteristic

properties, ceramics are one of the large-scale industries that provide a foundation for other industries. For instance, abrasives are crucial for the machine-tool and car industries. Electrical and magnetic ceramics, as another example, play a key role for the development of computers and other electrical devices.[6,7]

1.5. SCOPE OF THIS STUDY

The investigation of ceramics is based upon two major types of research. One of them is concerned with the creation of novel ceramic materials, while the other focuses on the advancement of the synthesis methods of known materials in order to promote their features and reduce their manufacturing expenses.[8,9] The research reported herein addresses the latter concern and utilizes the precursor method and the co-precipitation approach for preparation of unary-, binary-, and ternary-metal oxides at lower temperatures, with high surface areas and better control over the metallic constituents in case of mixtures of metal ceramics. The precursor has the advantages of increasing the degree of homogeneity, dramatically reducing or eliminating the diffusion path of the cations and yielding of small particle sizes including nanoparticulate material.[1-3] Co-precipitation produces a solid-state solution of metal cations blended on an atomic or molecular scale. Both methods provide lower temperature of ceramic synthesis and faster reaction times in comparison to the traditional ceramic method.[1,2] The success of the precursor method is controlled by the relative solubilities of precipitates in the solvent, the rate of their sedimentation, and prevention of the formation of supersaturated solutions.[1] Furthermore, co-precipitation is much more favorable when the precipitates of the metal cations are isostructural, i.e. possess the same structure. In this investigation, pyruvic acid oxime ligand (PAO^-) was used to prepare pre-ceramic materials by

precipitation of single cations or cation mixtures from their aqueous solution. Coordination complexes of this ligand decompose readily at low temperatures to yield the corresponding metal hydroxide, carbonate, or oxide, and volatile organics, including acetonitrile and carbon dioxide.

In chapter 2, the preparation procedure for the PAO complexes of a variety of representative, transition, and inner transition metals is described. These complexes were spectroscopically characterized by infrared (IR), solid-state ^{13}C nuclear magnetic resonance (NMR), and X-ray diffraction (XRD). The crystal structure of some of these compounds had been determined by single crystal X-ray technique. Furthermore, the thermal behavior of these synthesized compounds was investigated by thermal gravimetric analysis (TGA) and differential thermal analysis (DTA). The morphology of their solid pyrolysis products was studied by scanning and transmission electron microscopes (SEM and TEM). The crystallite size of the solid pyrolysis products was measured by XRD. The surface area, acidity, and basicity of the solid pyrolysis products were established by nitrogen adsorption at the temperature of liquid nitrogen and adsorption of a proper probing molecule at room temperature, respectively.

Chapter 3 provides the reader with a plausible mechanism for the thermal decomposition of the prepared PAO complexes. This mechanism was established on the basis of the analyses of the gaseous pyrolysis products by tandem gas chromatography/mass spectroscopy (GC/MS), and by analyses of the solid pyrolysis products by IR and XRD spectroscopy techniques.

Chapters 4, 5, 6, and 7 deal with applications of some of the prepared metal oxides, as environmentally benign, inexpensive, heterogeneous catalysts and adsorbents.

These oxides are examples of potential catalysts that may save pharmaceutical and petrochemical industries billions of dollars annually.

In Chapter 4, the synthesis of a significant pharmaceutical compound is described. Zinc oxide in the nanometric crystallite size, obtained from the thermal decomposition of $Zn(PAO)_2 \cdot 2H_2O$, was used to catalyze the formation of *trans*-chalcone from benzaldehyde and acetophenone at low temperature. A very good yield of this product was obtained employing a very small quantity of the catalyst.

Nanocrystalline nickel zinc ferrite, produced from the PAO precursor, successfully promoted the selective *N*-methylation of aniline by dimethyl carbonate (DMC) at low temperature, using a very small amount of the catalyst, as described in Chapter 5. The catalyst was also prepared by co-precipitation of metals hydroxide and then used as for the same reaction under the same conditions employing either DMC or MeOH as a methylating agent. This helped to realize the effect of the synthetic procedure of the catalyst on its catalytic behavior. In addition, the reaction was investigated without catalyst under the same circumstances. This latter process helped to understand the reaction behavior and pathway in the absence of the influence of the promoter.

Cobaltic oxide with nanocryatalline phase, prepared from the pyrolysis of $Co(PAO)_2 \cdot 2H_2O$, was the first oxide used as a catalyst for the allylation of benzene and displayed a remarkable activity and selectivity, as described in Chapter 6. The effect of changing the source of the oxide and supporting it on silica was also studied.

The removal of highly toxic arsenic from aqueous medium is the subject of Chapter 7. This process took advantage of the high surface area of the iron oxide formed

from the thermal decomposition of $Fe(PAO)_2 \cdot 2H_2O$. The motivation for this investigation was previous reports that pointed out the high capacity of nanoparticulate iron oxide for the remediation of arsenic.[10,-12] In addition, zinc and cobaltic oxides, obtained from their corresponding PAO complexes, were also utilized as adsorbents for arsenic and their adsorption capacities were compared with that of iron oxide. To the best of our knowledge, cobaltic oxide was used for the first time in such an application.

REFERENCES

1. A. R. West "Solid State Chemistry and Its Applications" John Wiley and Sons: New York, 1984; pp. 4-46.

2. A. R. West "Basic Solid State Chemistry" John Wiley and Sons: New York, 2001; pp. 407-439.

3. C. N. R. Rao and B. Raveau "Transition Metal Oxides: Structure, Properties, and Synthetic of Ceramic Oxides" John Wiley and Sons: New York, 1998; pp. 325-363.

4. D. Segal "Chemical Synthesis of Advanced Ceramic Materials" in *Chemistry of Solid State Materials,* A. R. West and H. Baxter eds., Cambridge University Press: Cambridge, Great Britain, 1989; p. 1-16.

5. P. W. Lee "Ceramics" Reinhold Publishing Corporation: New York, 1961; p. 1-6.

6. W. D. Kingery "Introduction to Ceramics" John Wiley and Sons: New York, 1960; p. 3-10.

7. H. Yanagida, K. Koumoto, and M. Miyayama "The Chemistry of Ceramics" John Wiley and Sons: New York, 1996; p. 1-10.

8. G. D. Georgieva "Metal Carboxylate Precursors for Ceramic Materials and Waste Forms for Radionuclides" Ph.D. Dissertation, Tulane University, New Orleans, 1995.

9. A. C. Vecoven "Innovative Processes for Metal Oxide Ceramic Synthesis" M.S. Thesis, Oklahoma State University, Stillwater, 2001.

10. A. W. Apblett, S. I. Kuriyavar, and B. P. Kiran, "Preparation of Micron-Sized Spherical Porous Iron Oxide Particles", *J. Mater. Chem.*, **2003,** *13* (5), 983-985.

11. S. Khaodhiar, M. F. Azizian, K. Osathaphan, and P. O. Nelson, "Copper, Chromium, and Arsenic Adsorption and Equilibrium Modeling in an Iron-Oxide-Coated Sand, Background Electrolyte System", *Water, Air, Soil Pollut.,* **2000,** *119* (1-4), 105-120.

12. T. H. Hsia, S. L. Lo, and C. F. Lin, "Arsenic(V) Adsorption on Amorphous Iron Oxide: Triple Layer Modeling" *Chemosphere,* **1992,** *25* (12), 1825-1837.

CHAPTER 2

2. SYNTHESIS OF PYRUVIC ACID OXIME (PAO) METAL COMPLEXES

2.1. BACKGROUND

Thermally unstable pre-ceramic compounds can furnish low temperature routes to high surface area, porous, nanocrystalline metals and metal oxides. Additionally, these pre-ceramic materials can be beneficial for the fabrication of metastable phases and coating of heat-sensitive substrates.[1-4] Among these useful precursor materials are the metal complexes of α-oximinocarboxylates, which have two functionalities, the carboxylate and oximino moieties that are capable of coordinating to a metal ion center. Accordingly, such ligands may bond to a metal center by adopting several binding modes such as monodentate carboxylate,[5] bidentate carboxylate (O,O-chelate) forming four-membered metallacycles,[6] N,O-chelation forming five-membered metallacycles,[6-24] and N,O,O-chelate-bridging where the second carboxylate oxygen atom serves as a bridge to an adjacent metal ion center.[1,6,11,14,15,19,21] These various ligating abilities of α-oximinocarboxylates to metal ions may lead to the formation of 3-dimensionally extended frameworks and/or polymeric materials.[1,6-11,14-22] The complexes formed by these ligands are also significant from the point of view of preparative inorganic[1-24] and bioinorganic[8-10,12,13,17-20,23-25] chemistry for several reasons. They are structurally comparable with the α-amino acids and related to them as shown explicitly in the following equation (adapted from reference 18):

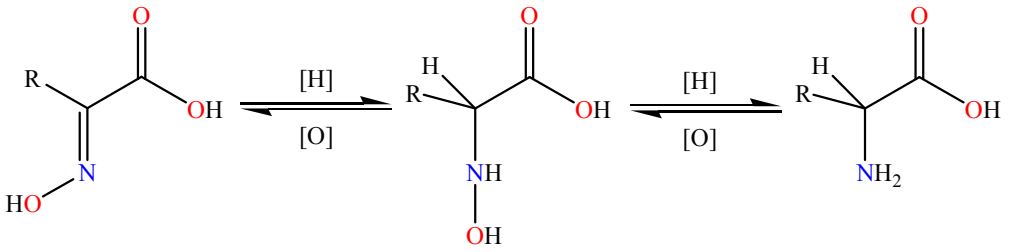

(Eq. 2.1)

These compounds, furthermore, may be theoretically advantageous for understanding the concerted effect of the donating groups, the modification in the coordinating attributes of α-amino acids upon the replacement of the amino group with an oxime, and the establishment of a probable stereoselective reaction based on the contribution of coordinated ligands.[18] All of these expected benefits of α-oximinocarboxylate complexes can be realized when recognizing that their parent acids, α-oximinocarboxylic acids, are important constituents in a chain relating them to their pertinent amines and carboxylic acids,[18] as displayed in Figure 2.1:

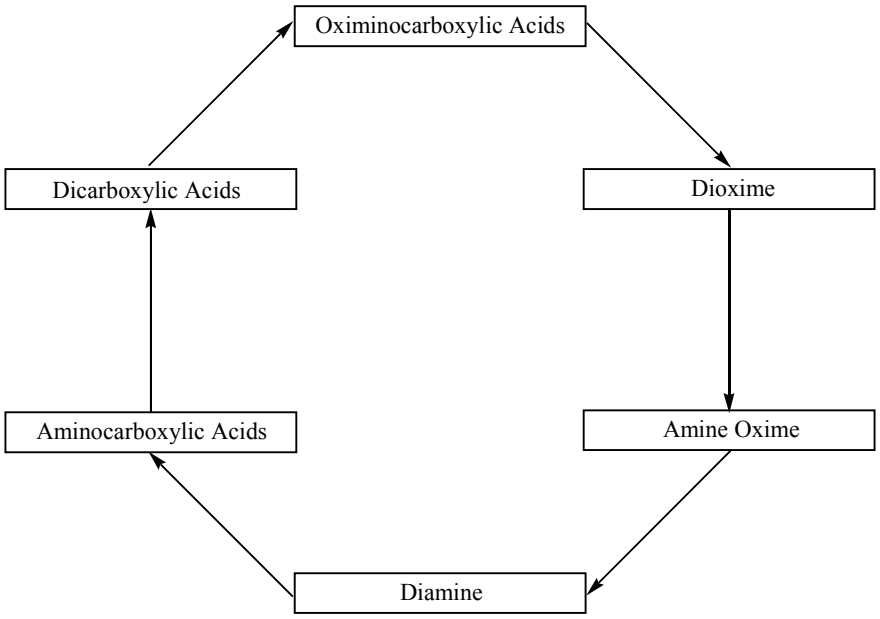

Figure 2.1 Oxime-amine-carboxylic acid chain (adapted from reference 18)

The α-oximinocarboxylic acids are regarded as diprotic acids because both the carboxyl and the oxime hydroxyl groups can be deprotonated by the action of a strong base. The latter group would be deprotonated much easier after the coordination of α-oximinocarboxylic acid to a metal center, a result of exercising the metal center the role of an electron-withdrawing group.[7,8,12,11,18,20-22] The acidity of the oxime hydroxyl group can be perceived through the π-resonance resulting from conjugation between the carboxyl and oxime groups as illustrated in Figure 2.2.

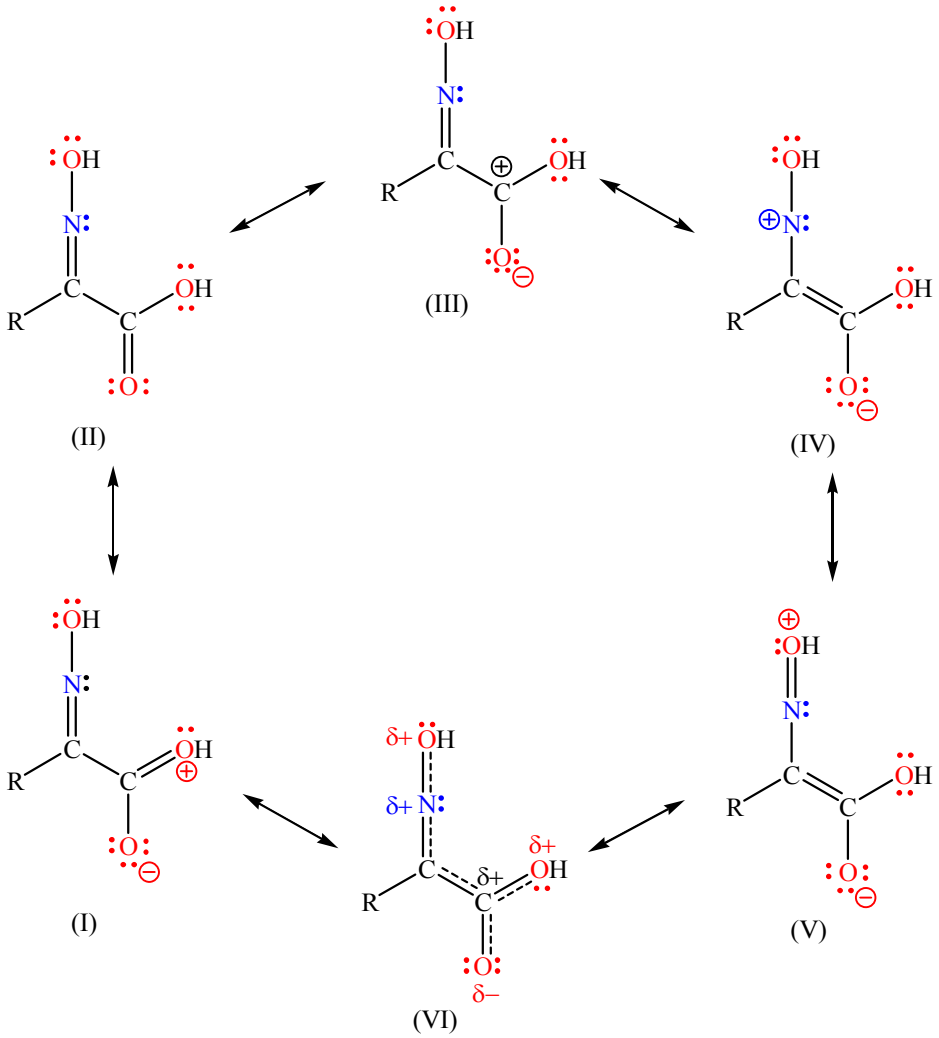

Figure 2.2. π-Resonance structures resulted from the carboxyl-oxime conjugation in the α-oximinocarboxylic acids

The side chain, R, of an α-oximinocarboxylic acid has a considerable influence on the molecular conformation, and hence on the crystal packing pattern, the solubility, and both the thermal stability and behavior of this acid and its salts.[9, 11, 14, 26] The adopted conformation is also restricted by the rotation hindrance caused by the π-bonding nature of the oxime imino group, resulting in the possibility for two different configurations, syn (*Z*) and anti (*E*), as seen in Figure 2.3. Depending on the R substituent, some of α-oximinocarboxylic acids are found only in one configuration while some of them can exist in both forms.

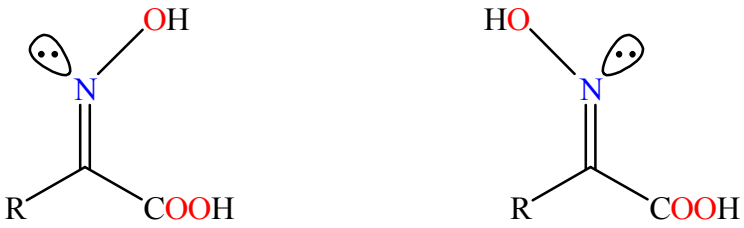

Syn (*Z*) isomer Anti (*E*) isomer

Figure 2.3. The two diastereomers of an α-oximinocarboxylic acid

α-Oximinocarboxylic acids are subjected to a concerted decarboxylation and dehydration to give lower nitriles upon refluxing in aqueous medium, under nitrogen,[26] as represented in the following dissociation equation:

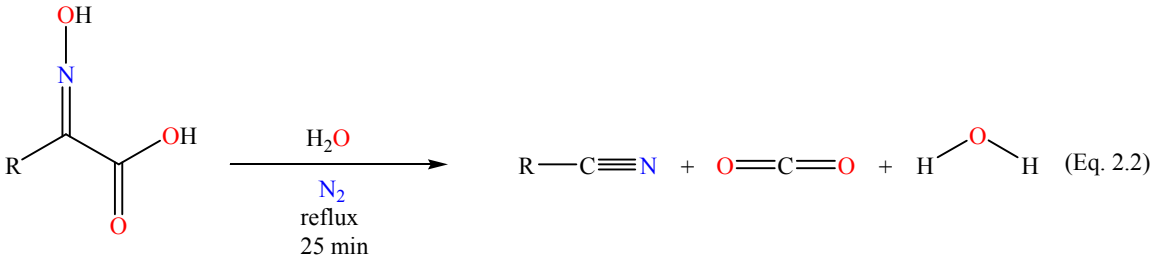

(Eq. 2.2)

A similar result was obtained when hydrolyzing α-oximinocarboxylic acids in 0.1 M aqueous HCl. The α-oximinocarboxylic acids pyrolyze at their melting points with the evolution of CO_2 gas to give nitriles.[26] Ahmad[27] also established a simple method for the synthesis of nitriles at room temperature from α-oximinocarboxylic acids by treating the latter with PhN═C═O or PhN═C═S in dry C_6H_6 under N_2. The conversion of α-oximinocarboxylic acids to nitriles by this procedure is almost complete with concomitant precipitation of diphenylurea or diphenylthiourea and the evolution of CO_2 and/or COS. Recent investigations of the thermolysis of α-oximinocarboxylic acids also confirmed their decomposition to nitriles in two steps. The first is a loss of CO from the α-oximinocarboxylic acid to produce a hydroxamic acid which dehydrates to produce nitrile.[21] In short, hydrolysis and thermal decomposition of α-oximinocarboxylic acids pave the way for the synthesis of functionalized nitriles.[26-28]

α-Oximinocarboxylic acids are also promising selective precipitating agents for gravimetric analysis determination of metal analytes.[29-33] In addition, α-oximinocarboxylic acids can be slowly generated in the solution of the latter to afford homogeneous precipitates, a process called precipitation from homogeneous solution (PFHS).[31] Copper(II) ions, for instance, were gravimetrically determined by the action of phenylpyruvic acid oxime (PPAO), $C_6H_5CH_2C(═NOH)COOH$, as a precipitant and a complexing reagent in a pH range of 1.0-5.5, where acidity was adjusted by HCl or NH_3. It was found that copper could be either estimated in a weighing form of $Cu[O_2CC(═NOH)CH_2C_6H_5]_2$, after drying the complex at 110-115^oC, or as CuO, after firing the precipitate.[29-31] Generation of PPAO *in situ* led to the formation of a homogeneous, light blue precipitate and allowed for the gravimetrically quantitative

determination of Cu(II) too.[31] PPAO also selectively precipitated Cu(II) as a blue complex from an H_2SO_4 medium containing both of Cu(II) and Cd(II) ions in the pH range of 1-2.[32] In addition, both of copper and zinc in brass were determined gravimetrically upon utilizing *p*-methoxyphenylpyruvic acid oxime as a precipitant and by controlling the pH parameter of the solution.[33]

The coordination chemistry of α-oximinocarboxylic acids and the thermal decomposition of their metal complexes have not been studied extensively. Only recently have they attracted the attention of inorganic chemists to explore their complexation ability and properties and to develop promising pre-ceramics for high surface area, porous, nanocrystalline metal oxides.[1-4,6,7,9-11,13-16,18-21,23,24] In this research project, several main group and transition metals complexes based on pyruvic acid oxime (HPAO), α-oximinopropionic acid, were prepared, characterized, and pyrolyzed to metal oxides for catalysis and environmental applications.

HPAO and its Complexes

HPAO is a white, crystalline, water-soluble solid that exists only in the *E* configuration, as determined by the single-crystal X-ray diffraction analyses of its structure[34,35] and the structures of several of its salts such as $Ce(PAO)_3$,[1,3] $Ca(PAO)_2{\cdot}H_2O$,[6] $K[Cu(HA)A]{\cdot}H_2O$,[8] $[Cu(phen)A(H_2O)]$,[10] $Na(PAO){\cdot}H_2O$,[14] $Y(PAO)_3(DMSO)(H_2O){\cdot}2H_2O$,[15] $Ni(PAO)_2(MeOH)_2{\cdot}2MeOH$,[16] trans-$[Co(HA)A(Im)_2]$,[18] trans-$[Co(HA)A(Py)_2]$,[18] $Mn_4(PAO)_8{\cdot}2H_2O$,[19] $Cu(HA)A(Py)$,[20] $Ni_2(HA)A(Im)_5.EtOH$,[21] [cinchonidinium][PAO],[36] [ephedrinium][PAO],[36] and [HPy][PAO].HPAO,[37] where HA is the monoanionic form of HPAO, A is the dianionic form of HPAO obtained by deprotonation of both hydroxyl carboxyl and hydroxyl oximino groups, and phen, Im,

and Py refers to 1,10-phenanthroline, imidazole and pyridine ligands, respectively. Crystal structure investigations of other complexes of PAO performed in the course of this research are in agreement with the results of the preceding structural studies. Moreover, the ^{1}H and ^{13}C NMR spectra of HPAO show only one set of signals rather than two sets, indicating the existence of one isomer only.[14-15] The ^{13}C NMR spectroscopy studies of isonitrosoketone,[38] aldoximes, and ketoximes[39-43] revealed that C_{α} atoms that are syn (cis) with respect to the hydroxyl oximino group are significantly shielded when compared with their corresponding shifts in parent α-diketones, aldehydes, and ketones. The ^{13}C chemical shift of the methyl group in HPAO is much more upfield than that of the methyl group in pyruvic acid (PA)[44] as shown in Table 2.1 (*vide infra*). Consequently, an assignment of anti configuration about the C=N for HPAO can be deduced. Another supportive evidence for the fact that HPAO has only the *E* configuration is that all attempts to prepare the *Z* isomer failed.[45]

Table 2.1. 13C {1H} NMR Chemical Shifts (ppm) of PA and HPAO

Compound	CH_3	C=O	C=N	COO
PA[a]	25.45	193.67	---	161.37
HPAO[b, c]	10.9 (10.2)	---	148.9 (150.16)	166.0 (167.22)

[a]From reference 44.
[b]From reference 14.
[c]Values in parenthesis are from reference 36.

The crystal structure of HPAO showed that the hydroxyl of the carboxylate group and the C=N of the oximino group adopt a *cisoid* conformation.[34] *Ab initio* quantum-chemical calculations proved that this observed conformation of HPAO is more stable by

-7.8712 kJ/mol than the conformation in which the mentioned groups are trans to each other.[35] Therefore, the structural formula of HPAO is represented schematically as follows:

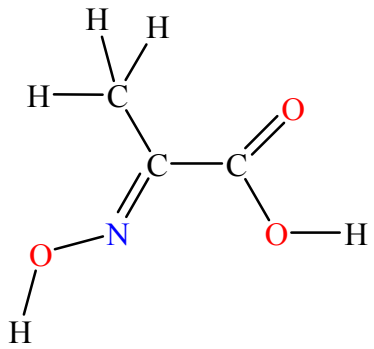

Figure 2.4. The molecular structure of HPAO

The structure adopted by HPAO suggests a chelating mode of the PAO^- ligand to a metal center through the nitrogen atom of the oximino group and the oxygen atom of the carboxylate to form a five-membered metallacycles. The structure can also be important in explaining the thermal behavior and the mechanism of the decomposition of PAO^- metal salts.

HPAO is a moderately strong acid with a pK_a of 3.325,[26] (an average of four reported pK_a values in the literature), making it more acidic than formic acid (pK_a = 3.745).[46] This is a result of the inductive effect of the α-oximino group. However, HPAO is a weaker acid than its corresponding α-oxocarboxylic acid, pyruvic acid (pKa = 2.495),[46] suggesting that the α-oxo group is stronger electron-withdrawing group than the α-oximino group.

The PAO^- ligand complexes of divalent first-row transition metals (Mn-Zn) were first synthesized because of interest in their anticipated bioactivities.[19,20,22-25] Their

structures were determined and the ligating properties of the PAO^- ligand were examined on the basis of UV-Visible and infrared spectra, magnetic susceptibility measurements, and thermal gravimetric analyses. The results suggested a bidentate chelation of the PAO^- via the oxime nitrogen atom and the oxygen atom of the deprotonated carboxyl hydroxyl group to create a five-membered metallacycles[23] as illustratively shown in Figure 2.5. This conclusion about the metal complex structure is consistent with the fact that the stable structure of HPAO has the oximino moiety and the carboxyl hydroxyl group cis to each other as mentioned earlier.[34,35] Complexes of PAO^- of Co(III),[18] Cu(II),[20] and

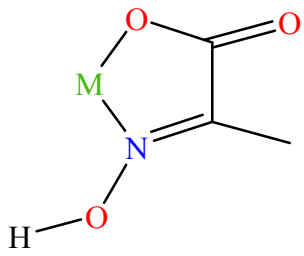

Figure 2.5. The N,O-chelate of PAO^- ligand to a metal center

Ni (II)[21] with nitrogen based ligands such as imidazole and pyridine had their crystal structures determined by single-crystal X-ray diffraction, confirming the formation of such five-membered metallacycle. The structure of these compounds consisted of two equatorial, coplanar metallacycles where the oximino moieties around the metal were cis to each other owing to the formation of a hydrogen bond between the deprotonated oxime hydroxyl of PAO^{2-} and the protonated oxime hydroxyl of PAO^-.[13,15-16] Such a configuration is also known for dimethylglyoxime complexes.[47-59] Although metal oxides were the ultimate products of the thermal dissociation of all the transition metal PAO^- complexes, the foregoing studies were not aimed at fabrication of low temperature metal oxide precursors. Apbett *et al.*[1-4] recently exploited the low temperature pyrolysis

properties of PAO^- compounds to design effective metal oxide preceramics. For instance, they synthesized a suitable precursor for zirconia that decomposed at 251°C and gave ZrO_2 at 520°C. Zirconia, however, was produced directly at 186 °C from $Zr(PAO^{2-})_2$ in which the PAO ligand was double deprotonated.[4] Moreover, they were successful in preparing anatase titania phase with a nanocrystallite size of 12 nm from the decomposition of titania preceramic based on the monoanion of PAO. On the other hand, when a titania ceramic precursor was based on the dianion of PAO, decomposition took place at 170°C.[2] They additionally found that the PAO^- ligand, along with fumarate dianion, were very useful for incorporating radioactive waste into Synroc, a crystalline titanate based upon $BaAl_2Ti_6O_{16}$, $CaTiO_3$, and $CaZrTi_2O_7$.[3] Furthermore, PAO complexes have been demonstrated to be potential precursors for ceramic metal oxide catalysts. Ceria, CeO_2, for example, a combustion catalyst, was prepared with a relatively high surface area of 44 m^2/g and a crystallite size smaller than 2 nm upon firing $Ce(PAO)_3$ at 170 °C.[1] An oxide-ion conductor containing both cerium and samarium, $Ce_{0.8}Sm_{0.2}O_{1.9}$, was obtained as a dense, amorphous material from the pyrolysis at 163°C of $Ce_4Sm(PAO)_{15}$ and as crystalline material upon calcination at 700°C.[1] Nickel ferrite, $NiFe_2O_4$, was formed as a fibrous, amorphous material when pyrolyzing $NiFe(PAO)_6 \cdot 6H_2O$ at 200°C and as a crystalline material at 300°C.[1] The success in the preparations of these two binary metal oxides is attributed to the formation of a homogeneous solid solution upon the co-precipitation of metal ions by PAO^-. This is a result of structural isomorphism between $Ce(PAO)_3$ and $Sm(PAO)_3$ in the former case and between $Ni(PAO)_2 \cdot 2H_2O$ and $Fe(PAO)_2 \cdot 2H_2O$ in the latter example.[1] Notably, PAO^- complexes were established as significant low temperature precursors to both of uni- and

bimetallic oxides. The PAO^- salts of alkali and alkaline earth metals were also investigated by Apblett et al.,[6,14] who concluded that all such salts decompose to their corresponding carbonates as demonstrated by the mass change in the thermal gravimetric traces and X-ray diffraction patterns. In addition, they were able to determine the structure of $Ca(PAO)_2 \cdot H_2O$,[6] $Na(PAO) \cdot H_2O$,[14] $Y(PAO)_3(DMSO)(OH_2) \cdot 2H_2O$,[15] and $Ce(PAO)_3$[1] by the aid of single-crystal X-ray diffraction. Again, the PAO^- ligand chelates the metal ion center through the nitrogen atom of the oximino moiety and the deprotonated hydroxyl oxygen atom of the carboxyl moiety to form a five-membered metallacycle, while the other oxygen atom of the carboxyl group is attached to a neighboring metal ion center to form a bridge that leads to an extended network in the three dimensions. The ease of decomposition of these complexes and their decomposition temperatures is essentially controlled by three factors, their crystalline structure, the binding mode of the PAO^- ligand, and the formation of strained five-membered metallacycles.[6,14,15]

The complexes of PAO^- pyrolyze to metal oxides or carbonates, depending upon the metal, with evolution of small, volatile, organic byproducts of water, carbon dioxide, and acetonitrile. The gases are produced simultaneously as determined by off-gas analysis by TGA/MS.[4,7,14,15] The violent outgassing and low decomposition temperatures that inhibit sintering, are likely to be the main factors responsible for generation of nano-crystalline, high surface-area, amorphous ceramic materials.

2.2. EXPERIMENTAL

Materials

Sodium pyruvate [$H_3CC(O)CO_2Na$ (TCI)], hydroxylamine hydrochloride [$HONH_2{\cdot}HCl$ (Fisher Scientific)], sodium carbonate [$Na_2CO_3{\cdot}H_2O$ (EM Science)], lead nitrate crystals [$Pb(NO_3)_2$ (EM Science)], basic aluminum acetate [$(H_3CCO_2)_2AlOH$ (Aldrich)], Celite 545 (Fisher Scientific), magnesium chloride hexahydrate [$MgCl_2{\cdot}6H_2O$, ACS reagent (Spectrum Quality Products, Inc.)], zinc sulfate, 7-hydrate [$ZnSO_4{\cdot}7H_2O$ (J. T. Baker Chemical Co.)], cadmium nitrate tetrahydrate [$Cd(NO_3)_2{\cdot}4H_2O$ (Strem Chemicals)], mercuric chloride [$HgCl_2$, crystal (Fisher Scientific)], manganese (II) sulfate monohydrate [$MnSO_4{\cdot}H_2O$ (Aldrich)], ferrous sulfate [$FeSO_4{\cdot}7H_2O$ (Mallinckrodt Chemical)], cobaltous acetate [$Co(O_2CCH_3)_2{\cdot}4H_2O$ (Fisher Scientific)], nickelous sulfate [$NiSO_4{\cdot}6H_2O$ (Merck & Co. Inc.)], curpric nitrate [$Cu(NO_3)_2{\cdot}2.5H_2O$ (Fisher Scientific)], cupric sulfate [$CuSO_4{\cdot}5H_2O$ (EM Science)], potassium bicarbonate [$KHCO_3$, ACS reagent grade (ICN Biomedical Inc.)], tetramethylammonium hydroxide {[$(H_3C)_4N$]OH, 25% in aqueous solution (Alfa AESAR)}, tetrachloro-1,4-benzoquinone [(*p*-chloranil) (Aldrich)], phenol [C_6H_5OH (EM Science)], cyclohexylamine [$C_6H_{11}NH_2$ (Aldrich)], 1-hexadecylamine [$H_3C(CH_2)_{15}NH_2$ 98%(Aldrich)], cyclohexane [C_6H_{12}, reagent grade(Fisher Scientific)], anhydrous ethanol [USP grade (Pharmco)], and dimethylglyoxime [$H_3CC(=NOH)C(=NOH)CH_3$, ACS reagent (Aldrich)], were commercial reagents and used without further purification. Lead acetate [$Pb(O_2CCH_3)_2{\cdot}3H_2O$ (J. T. Baker Chemical Co.)] was refined by recrystallization from water containing several drops of glacial acetic acid. All $FeSO_4{\cdot}7H_2O$ solutions were

filtered off before use in order to eliminate basic iron (III) sulfate impurities that result from the gradual oxidation of iron (II) sulfate.[60] The sodium salt of pyruvic acid oxime, [Na(PAO)·H_2O][14] and zinc carbonate [$ZnCO_3$][61] were prepared by literature methods.

Physical and Analytical Measurements

Diffuse reflectance infrared fourier transform (DRIFT) spectra of a ground powders diluted with KBr were recorded on a Nicolet Magna 750 FTIR. Solid-state carbon-13 nuclear magnetic resonance (NMR) spectra were recorded on a Chemagnetics CMX-II solid-state NMR spectrometer operating at 75.694 MHz with a Chemagnetics 5 mm double resonance magic-angle spinning probe and were referenced to tetramethylsilane (TMS). The ^{13}C cross-polarization/magnetic-angle spinning (CP/MAS) was executed with a quasi-adiabatic sequence[62] employing two pulse phase modulation (TPPM) proton decoupling.[63] The ^{13}C CP contact pulse of either 5 or 12 millisecond length was divided into 11 steps of equal length with ascending radio frequency field strength, while the ^{1}H contact pulse had constant radio frequency field strength. From 1024 to 10,800 scans were acquired with a delay of 1.0 s, 5.0 s, or 20.0 s between scans. The MAS sample spinning frequency was 5.0 kHz, 6.0 kHz, or 10.0 kHz and was maintained to within a range of ± 5 Hz or less with a Chemagnetics speed controller. The X-ray powder diffraction (XRD) patterns were acquired on a Bruker AXS D8 Advance diffractometer using copper K_α radiation. The molecular structure of some complexes prepared in this study were established by single-crystal X-ray crystallography using either a Siemens P4 automated four-circle diffractometer outfitted with a PC-486DX computer (performed by the late Professor Elizabeth M. Holt) or a Bruker Apex diffractometer (performed by Dr. Masood Khan). The UV-visible spectra of adsorbed

titrants dissolved in either acetonitrile or cyclohexane were obtained on a Hewlett-Packard 8453 diode array spectrophotometer. Thermogravimetric analyses (TGA) and thermal differential analyses (DTA) were performed on a Seiko EXSTAR 6000 TG/DTA 6200 instrument using between 2 mg and 30 mg sample under a flow of air of 100 ml/min. The temperature was ramped from 25 ^{o}C to 625 ^{o}C at a rate of 1^{o}C/min. Bulk pyrolyses at different temperatures were executed in ambient air in a temperature-programmable muffle furnace employing a temperature ramp of 1^{o}C/min. A JEOL JXM 6400 Scanning Electron Microscope and a JEOL JEM 100 CX II Transmission Electron Microscope were used to study the morphology, shape, and size of the particles of precursors and their decomposition products. The BET six-point surface area measurements were performed on a Quantachrome Nova 1200 instrument by nitrogen adsorption at the temperature of liquid nitrogen. All compounds prepared were vacuum-dried at room temperature at ~ 30 mm Hg.

Synthesis

Precursors for Metal Oxides

Generally, aqueous solutions of metal sulfates, nitrates, acetates, or chlorides and the sodium salt of pyruvic acid oxime were combined in the suitable stoichiometric ratio. Complexes of paramagnetic metal ions, such as Mn^{+2}, Fe^{+2}, Co^{+2}, Ni^{+2}, and Cu^{+2} could not be analyzed by solid-state ^{13}C CPMAS NMR analysis due to the failure of NMR to be useful for paramagnetic materials.

Pyruvic Acid Oxime (HPAO)

Pyruvic acid oxime was prepared according to the published procedure[18] used to prepare Na(PAO).H_2O, but without adding sodium carbonate to the solution of sodium pyruvate and hydroxylamine hydrochloride. A sample of $NaO_2CC(O)CH_3$ (11.004 g, 100

mmol) was dissolved in 30 ml of distilled water. Then $HONH_2 \cdot HCl$ (6.949 g, 100 mmol) was dissolved in 30 ml of distilled H_2O in a separate beaker and was immediately added to the solution of sodium pyruvate. This mixture was stirred for around 3 minutes and was then placed in refrigerator at 5°C for 2 days. The HPAO was collected in portions of colorless crystals. The yield of HPAO was 9.84 g (95.53%). The XRD pattern of HPAO showed the presence of sodium chloride. Thus, HPAO was purified by dissolving it in 2-propanol to produce pure, colorless crystals of HPAO, free of NaCl, as indicated by XRD. Solid-state ^{13}C CPMAS NMR: δ (ppm) 11.4 (CH_3), 149.0 (C═N), 167.6 (C═O). IR (cm^{-1}) (KBr): 3222(s, br), 3070(s), 2894(s), 2841(m), 2700(w), 2568(m), 2467(w), 2116(vw), 1986(vw), 1941(vw), 1770(w), 1695(vs), 1654(m), 1465(s), 1420(m), 1376(w), 1363(w), 1303(m), 1230(vw), 1178(vs), 1043(vs), 989(m), 912(s), 816(s), 762(m), 705(vs), 530(w), 462(m).

PAO^- Salts of Main Group Elements

$Mg(PAO)_2(H_2O)_3 \cdot 2H_2O$

A sample of $MgCl_2 \cdot 6H_2O$ (10.17 g, 50 mmol) was dissolved in 50 ml of H_2O and was mixed with a 50-ml, aqueous solution of $Na(PAO).H_2O$ (14.3 g, 100 mmol). The reaction mixture was kept at 5°C for 2 days and deposited colorless crystals of $Mg(PAO)_2(H_2O)_3 \cdot 2H_2O$, which were filtered off and dried under vacuum to yield 13.81 g (87.1%) of product. Mg Calcd.: 7.55%. Found: 7.37%. Solid-state ^{13}C CPMAS NMR: δ (ppm) 9.5, and 11.5 (CH_3), 154.2 (C═N), 170.1 (C═O), 173.2 (C═O). IR (cm^{-1}) (KBr): 3477(m, br), 3266(m, br), 3071(m), 2947(w), 2874(m), 2421(vw), 2349(vw), 2275(vw), 1757(w), 1672(vs), 1623(vs), 1412(s), 1370(s), 1222(s), 1063(s), 1011(w), 958(vw), 904(vw), 858(m), 778(m), 742(s), 691(w), 570(w), 547(vw), 513(w), 442(vw),

429(vw). Analysis of the pyrolysis product of $Mg(PAO)_2(H_2O)_3 \cdot 2H_2O$ obtained at 600 ^oC by XRD revealed a contamination of the MgO with the halite phase of sodium chloride. The existence of the latter side product had a pronounced impact on the thermal behavior of $Mg(PAO)_2(H_2O)_3 \cdot 2H_2O$, as reflected in its TGA trace. Therefore, the magnesium salt of PAO^- was prepared using magnesium hydrodxide (0.598 g, 10.0 mmol) and HPAO (2.04 g, 20 mmol) to avoid the formation of the byproduct of sodium chloride. The powder of magnesium hydroxide was gradually added to 20-ml, aqueous solution of HPAO. The resultant mixture was magnetically stirred until the magnesium hydroxide dissolved and a clear, light yellow solution was obtained. The latter solution was filtered off and allowed to evaporate slowly at room temperature to yield nice, hexagonal crystals of the desired product, which were separated and dried under vacuum to give a yield of 3.035 (95.29%). The TGA of these crystals is thoroughly different from that of contaminated with NaCl. XRD patterns of the pyrolysis products of these crystals at different temperatures have not shown any peaks referred to sodium chloride.

$HOAl(PAO)_2 \cdot 2H_2O$

A sample of $HOAl(O_2CCH_3)_2$ (8.104 g, 50 mmol) was slowly added to a 35-ml, aqueous solution of HPAO (10.3 g, 100 mmol). The reaction mixture was stirred for 13 days and was then filtered using Celite to give a clear pale yellow solution. The latter stood in a hood until all the water had evaporated to leave a yellow solid. The solid was stirred with acetone (100 ml), producing a white gelatinous precipitate which was filtered off using a membrane filter and dried under vacuum to provide a yield of 10.36 g (72.9%) of product. Solid-state ^{13}C CPMAS NMR: δ (ppm) 8.4 (CH_3), 152.0 (C═N), 168.9 (C═O). IR (cm^{-1}) (KBr): 3382(w, br), 3065(w), 2951(w), 2887(w), 2834(w), 2363(vw),

2339(vw), 1684(m), 1653(m), 1602(m), 1541(w), 1456(w), 1368(m), 1225(m), 1184(w), 1091(w), 1031(w), 884(w), 801(w), 769(w), 730(w), 685(w), 610(w), 487(vw), 460(vw), 445(vw), 432(vw).

$Pb(PAO)_2 \cdot 2H_2O$

The lead salt of pyruvic acid oxime was obtained as a white precipitate upon mixing a 50-ml, aqueous solution of recrystallized $Pb(H_3CCO_2)_2 \cdot 3H_2O$ (3.79 g, 10 mmol) with $Na(PAO) \cdot H_2O$ (2.86 g, 20 mmol) in 50 ml of distilled water. After stirring the mixture overnight, the solid was filtered and dried under vacuum yielding 3.39 g (75.8%) of product. Alternatively, lead nitrate was used as a source of lead instead of lead acetate. A quantity of 0.70 g (78.3%) of $Pb(PAO)_2 \cdot 2H_2O$ was obtained from the reaction of $Pb(NO_3)_2$ (0.662 g, 2 mmol) in 10 ml of distilled water with a 10-ml, aqueous solution of $Na(PAO) \cdot H_2O$ (0.57 g, 4 mmol). The ^{13}C and IR spectra of $Pb(PAO)_2 \cdot 2H_2O$ obtained by both routes were identical. The following data are those of the one obtained from acetate route. Solid-state ^{13}C CPMAS NMR: δ (ppm) 11.4, 12.2, and 13.9 (CH_3), 155.4,159.7 (C═N), 170.1 (COO). IR (cm^{-1}) (KBr): 3140(s, br), 3055(s), 2923(m), 2813(s)1660(s), 1619(vs), 1581(vs), 1524(s), 1453(s), 1394(s), 1369(s), 1348(s), 1195(s), 1035(vs), 991(vw), 859(w),846(m), 792(w), 766(s), 732(vs), 541(m), 485(m), 458(w).

PAO^- Salts of Group 12 Metals

$Zn(PAO)_2 \cdot 2H_2O$

A 100-ml, aqueous solution of $ZnSO_4 \cdot 7H_2O$ (14.375 g, 50 mmol) was combined with a 100-ml, aqueous solution of $Na(PAO) \cdot H_2O$ (14.30 g, 100 mmol). A white precipitate of $Zn(PAO)_2 \cdot 2H_2O$ resulted upon mixing of the reactants. The precipitate was filtered off and then dried under vacuum overnight to give 15.02 g (98.37%) of product.

Zn Calc.: 21.41%. Found: 21.69%. Solid-state ^{13}C CPMAS NMR: δ (ppm) 11.0 (CH_3), 157.6 (C═N), 166.5 (C═O). IR (cm^{-1}) (KBr): 3214(s, br), 3107(s, br), 2946(s), 2266(w), 2094(vw), 2041(vw), 1963(vw), 1771(w), 1675(vs), 1653(vs), 1533(m), 1486(s), 1429(m), 1391(s), 1367(vs), 1219(s), 1054(s), 1026(w, sh), 886(s), 859(s), 768(s), 707(m), 560(w), 501(s). Crystals of $Zn(PAO)_2 \cdot 2H_2O$ were successfully obtained upon gradual addition of a 20-ml, aqueous of $Na(PAO) \cdot H_2O$ (0.143 g, 1.0 mmol) to a 20-ml, aqueous solution of zinc sulfate, heptahydrate (2.875 g, 10.0 mmol). The high mole ratio of Zn^{2+} to PAO^- liagand (10:1) does not provide the enough stoichiometric of the ligand, and hence prevents the precipitation of the zinc complex and permit the slow nucleation for the formation of crystals. Such conditions would lead to the slow formation (kinetic control) of mono-PAO intermediate complex $[Zn(PAO)(H_2O)_4]^+$, which in turn exist in very low concentration in the solution (Eq. 2.3a). The latter intermediate complex either exchanges the water ligand with a PAO^- ligand (Eq. 2.3b) or two complexes of it inter-exchange ligands with each other to produce the desired crystalline bis-PAO complex (Eq. 2.3c):

$$[Zn(OH_2)_6]^{2+}(aq) + PAO^-(aq) \rightleftharpoons [Zn(PAO)(OH_2)_4]^+(aq) + 2H_2O(l) \quad \text{Eq. 2.3a}$$

$$[Zn(PAO)(OH_2)_4]^+(aq) + PAO^-(aq) \rightleftharpoons [Zn(PAO)_2(OH_2)_2](aq) + 2H_2O(l) \quad \text{Eq. 2.3b}$$

$$2[Zn(PAO)(OH_2)_4]^+(aq) \rightleftharpoons [Zn(PAO)_2(OH_2)_2](aq) + [Zn(OH_2)_6]^{2+}(aq) \quad \text{Eq. 2.3c}$$

$Cd(PAO)_2$

A solution of $Cd(NO_3)_2 \cdot 4H_2O$ (6.17 g, 20 mmol) in 20 ml of water was added to a solution of $Na(PAO) \cdot H_2O$ (5.72 g. 40 mmol) in 30 ml of water. This reaction mixture

precipitated a white solid of $Cd(PAO)_2$ which, after stirring the mixture overnight, was filtered off and dried under vacuum to give 5.86 g (83.10%) of product. Cd Calc. 35.52%. Found: 35.80%. Solid-state ^{13}C CPMAS NMR: δ (ppm) 11.4 (CH_3), 154.9 (C═N), 167.5 (C═O). IR (cm^{-1}) (KBr): 3590(vw), 3336(w), 3209(w), 3058(w), 2771(m), 2717(m), 2411(w), 2228(w), 2114(vw), 2050(vw), 1952(vw), 1761(w), 1678(m), 1634(s), 1532(vw), 1495(w), 1417(w), 1371(m), 1362(m), 1220(s), 1204(s), 1065(vs), 851(s), 766(m), 739(s), 556(m), 513(s), 490(m).

$Hg(PAO)_2$

A white precipitate of $Hg(PAO)_2$ in a yield of 2.419 g (27.45 %) was obtained upon combining $HgCl_2$ (5.43 g, 20 mmol) in 100 ml of H_2O with a 36-ml, aqueous solution of $Na(PAO)\cdot H_2O$ (5.72 g, 40 mmol). Solid-state ^{13}C CPMAS NMR: δ (ppm) 12.6 (CH_3), 158.2 (C═N), 164.0, and 166.4 (C═O). IR (cm^{-1}) (KBr): 3582(vw), 3213(s), 2928(m), 1732(vw), 1656(m), 1610(vs), 1472(m), 1379(s), 1280(vw), 1252(vw), 1206(s), 1073(w), 1011(s), 961(s), 838(s), 782(s), 732(s), 562(vw), 535(w), 512(vw), 469(vw), 444(m).

PAO^- Salts of Divalent 3d Transition Metals

$Mn_4(PAO)_8\cdot 2H_2O$

A sample of $Mn_4(PAO)_8\cdot 2H_2O$ was obtained as a white precipitate from the reaction of $MnSO_4\cdot H_2O$ (6.227 g, 25 mmol) in 70 ml of H_2O with a 50-ml, aqueous solution of $Na(PAO)\cdot H_2O$ (7.150 g, 50 mmol). The resultant mixture was stirred overnight, and the precipitate was then filtered off and dried in vacuum to yield 3.02 g (51.18%) of product. Mn Calc. 20.50%. Found: 20.32%. IR (cm^{-1}) (KBr): 3373(vs), 3167(vs), 3035(vs), 2843(vs, br), 2406(w), 2231(w), 2114(vw), 2055(vw), 1919(vw),

1772(vw), 1667(s), 1633(s), 1423(m), 1370(m), 1219(s), 1069(s), 859(m), 818(m), 770(m), 746(m), 552(m), 513(m), 428(vw).

$Fe(PAO)_2 \cdot 2H_2O$

A yellow green precipitate of $Fe(PAO)_2 \cdot 2H_2O$ in a yield of 5.310 g (95.99%) was obtained upon combining $FeSO_4 \cdot 7H_2O$ (13.9005 g, 50 mmol) in 100 ml of H_2O with a 70-ml, aqueous solution of $Na(PAO) \cdot H_2O$ (14.3 g, 100 mmol). Fe Calc. 18.88%. Found: 18.67%. IR (cm^{-1}) (KBr): 3232(s, br), 3106(s, br), 2947(s), 2875(s), 2830(s), 2389(m), 2305(m), 2075(vw), 2026(vw),1830(w), 1768(w), 1668(vs), 1650(vs), 1534(m), 1480(s), 1434(m), 1389(s), 1367(vs), 1217(vs), 1045(s), 889(m), 858(s), 781(s), 768(s, sh), 694(m), 558(w), 497(m).

$Co(PAO)_2 \cdot 2H_2O$

A sample of $Co(PAO)_2 \cdot 2H_2O$ was obtained as a light orange precipitate from the reaction of $Co(O_2CCH_3)_2 \cdot 4H_2O$ (6.227 g, 25 mmol) in 100 ml of H_2O with a 40 ml aqueous solution of $Na(PAO) \cdot H_2O$ (7.150 g, 50 mmol). The resultant mixture was stirred overnight, and the precipitate was then filtered off and dried in vacuum to provide 6.432 g (86.07%) of product. Co Calc. 19.71%. Found: 19.21%. IR (cm^{-1}) (KBr): 3226(s, br), 3077 (s, br), 2945 (s), 2868(s), 2829(s), 2387(w), 2276(w), 2084(vw), 2031(vw), 1828(w), 1771(w), 1669(vs), 1651(vs), 1535(m), 1479(s), 1434(m), 1390(s), 1367(vs), 1269(vw), 1218(vs), 1050(vs), 895(m), 860(s), 778(s), 770(s, sh), 697(m), 565(w), 502(m).

$Ni(PAO)_2 \cdot 2H_2O$

A solution of $NiSO_4 \cdot 6H_2O$ (7.8807 g, 30 mmol) in 40 ml of water was added to a solution of $Na(PAO) \cdot H_2O$ (8.580 g, 60 mmol) in 50 ml of water. From this reaction mixture, a blue solid $Ni(PAO)_2 \cdot 2H_2O$ precipitated, which, after stirring the mixture overnight, was filtered off and dried under vacuum to give 8.49 g (94.75%) of product. Ni Calcd. 19.65%. Found: 19.04%. IR (cm^{-1}) (KBr): 3210(s, br), 3072(s, br), 2950(s), 2833(s), 2389(w), 2278(w), 2098(vw), 2039(vw), 1831(w), 1780(w), 1672(vs), 1655(vs), 1533(m), 1474(s), 1395(s), 1368(vs), 1222(s), 1058(m), 1025(w, sh), 909(m), 863(m), 782(m), 767(m, sh), 692(w), 568(w), 500(m).

$Cu(PAO)_2 \cdot 2H_2O$

A 100-ml, aqueous solution of $CuSO_4 \cdot 5H_2O$ (12.48 g, 50 mmol) was combined with a 100-ml, aqueous solution of $Na(PAO) \cdot H_2O$ (14.30 g, 100 mmol). A blue precipitate of $Cu(PAO)_2 \cdot 2H_2O$ resulted upon stirring the mixture of reactants. The precipitate was filtered off and then dried under vacuum overnight to give a yield of 14.38 g (94.79%) of product. Suitable crystals of $Cu(PAO)_2 \cdot 2H_2O$ for X-ray structure determination were obtained by adding solid $Cu(PAO)_2 \cdot 2H_2O$ (0.201g, 0.662 mmol) to a 10 ml, 2.0 *M* solution of $Na(PAO) \cdot H_2O$. This mixture was filtered off after 1 day to calculate the amount of undissolved $Cu(PAO)_2 \cdot 2H_2O$, and hence the amount of dissolved complex (0.182 g, 0.6 mmol). Slow evaporation of the filtrate left behind rectangular, pale blue crystals of $Cu(PAO)_2 \cdot 2H_2O$. Cu Calc. 20.93%. Found: 21.02%. IR (cm^{-1}) (KBr): 3160(s, br), 2884(m), 2812(m), 1776(vw), 1674(vs), 1632(vs), 1523(vw),

1442(m), 1388(m), 1365(s), 1220(s), 1097(s), 1085(s), 1026(vw), 998(w), 865(w), 761(m), 634(vw), 573(vw), 512(m), 451(vw).

PAO^- Salts of Some Lanthanides

$Ce(PAO)_3$

A 7-ml, aqueous solution of $CeCl_3 \cdot 7H_2O$ (11.18 g, 30 mmol) was combined with a 100-ml, aqueous solution of $Na(PAO) \cdot H_2O$ (12.87 g, 90 mmol). A white precipitate of $Ce(PAO)_3$ resulted upon stirring the mixture of reactants. The precipitate was filtered off and then dried under vacuum overnight to give 13.35 g (99.75%) of product. IR (cm^{-1}) (KBr): 3286(s, br), 2383(vw), 2264(vw), 2090(vw), 2033(vw), 1909(vw), 1763(vw), 1686(m),, 1666(m), 1633(m), 1469(w),1414(w), 1371(w), 1216(m), 1058(m), 987(w), 854(w), 779(w), 735(w), 550(vw), 472(w), 427(vw), 411(vw).

$Pr(PAO)_3$

A 20-ml, aqueous solution of $Pr(NO_3)_3 \cdot 6H_2O$ (8.709 g, 20 mmol) was combined with a 60-ml, aqueous solution of $Na(PAO) \cdot H_2O$ (8.58 g, 60 mmol). A light green, crystalline precipitate of $Pr(PAO)_3$ resulted after 10 minutes of combining the solutions of reactants. The precipitate was filtered off and then dried under vacuum overnight to give 8.84 g (98.88%) of product. Very pretty, light green crystals of the praseodymium(III) complex were obtained by the slow evaporation of the filtrate over a period of two months. These crystals were collected to get the crystal structure. The yield of the desired Pr(III) complex becomes 100% upon the summation of the precipitate and crystals weights. Therefore, complexation with an equivalent amount of PAO^- ligand in aqueous medium furnished a simple, gravimetric determination procedure for Pr(III). IR (cm^{-1}) (KBr): 3439(vs, br), 3348(vs, br), 3197(vs, br), 2892(s), 2608(vw),

2363(vw), 2342(vw), 2268(vw), 2092(vw), 2036(vw), 1908(vw), 1852(vw), 1764(w), 1688(s), 1666(s), 1640(s), 1468(m), 1412(m), 1372(m), 1216(m), 1060(m), 988(w), 855(w), 779(w), 734(w), 557(w), 478(w), 426(vw), 408(vw).

PAO^{2-} Salts

$[(H_3C)_4N]^+[Cu(PAO^-)(PAO^{2-})(H_2O)]^-\cdot H_2O$

A sample of $Cu(PAO)_2\cdot 2H_2O$ (6.071 g, 20 mmol) was gradually added to an aqueous solution of 25% wt/wt $[(H_3C)_4N]OH$ (1.82 g, 20 mmol), diluted by 100 ml of H_2O. This mixture was stirred until the $Cu(PAO)_2\cdot 2H_2O$ completely dissolved, resulting in a dark, deep blue solution, which gave dark blue, star-like crystals of the desired product upon the slow evaporation of the solution at room temperature over a period of 10 days. These crystals were filtered off and air dried to provide a yield of 7.408 g of product (the extra mass is a result of hydration of the product). The structure of this product was resolved by single-crystal, X-ray crystallography. IR (cm^{-1}) (KBr): 3549(w), 3281(w), 3036(m), 2964(w), 2923(w), 2671(vw), 2596(vw), 2527(vw), 2498(vw), 2365(vw), 2339(vw), 1788(vw), 1722(vw), 1658(m), 1649(m), 1642(m), 1632(m), 1614(m), 1597(m), 1546(w), 1517(vw), 1490(m), 1389(m), 1376(m), 1342(s), 1290(w), 1208(s), 1129(m), 1078(w), 1028(vw), 990(w), 952(m), 920(w), 863(w), 851(w), 765(m), 745(w), 668(vw), 569(vw), 501(w), 454(w), 416(w), 411(w).

$[H_3C(H_2C)_{15}NH_3]^+[Fe(PAO^-)(PAO^{2-})]^-$

A sample of technical grade (90%) of 1-hexadecylamine (1.16 g, 4.328 mmol) was dissolved in 50 ml of methanol. This solution was then filtered through a membrane filter. To this latter filtrate, a sample of solid $Fe(PAO)_2\cdot 2H_2O$ (1.28 g, 4.328 mmol) was gradually added over 5 minutes to give a brown suspension that turned to a clear brown

solution after twenty minutes. The resultant solution was left to stir overnight, and then the methanol was evaporated using a rotary evaporator to deposit a crystalline, brown substance (1.94 g, 89.40%). IR (cm^{-1}) (KBr): 2920(vs), 2851(vs), 2058(vw), 1765(vw), 1657(s), 1641(s), 1631(s), 1612(s), 1549(m), 1502(w), 1467(m), 1355(m), 1214(m), 1116(m), 1023(vw), 955(vw), 865(m), 769(m), 721(w), 587(w), 558(w).

$[H_3C(H_2C)_{15}NH_3]^+[Zn(PAO^-)(PAO^{2-})(H_2O)]^-$

A sample of technical grade (90%) of 1-hexadecylamine (2.68 g, 10 mmol) was dissolved in 100 ml of methanol. This solution was then filtered through a membrane filter to eliminate the insoluble impurities. To this latter solution, a sample of solid $Zn(PAO)_2{\cdot}2H_2O$ (3.0539 g, 10 mmol) was gradually added over 5 minutes. This gave a white suspension that turned to a clear solution after stirring for few minutes. The resultant solution was filtered, and then the methanol was evaporated using a rotary evaporator to deposit a crystalline, white substance (4.02 g, 78.69%). IR (cm^{-1}) (KBr): 3297(m), 3269(m), 2922(s), 2852(s), 2063(vw), 1761(vw), 1632(m), 1617(m), 1582(m), 1469(m), 1362(m), 1214(m), 1118(m), 1078(m), 1024(m), 979(vw), 905(w), 855(m), 773(m), 746(m), 726(m), 666(vw), 550(w), 494(w), 438(vw).

$[H_3C(H_2C)_{15}NH_3]^+[Ce(PAO^-)_2(PAO^{2-})(H_2O)]^-$

A sample of 1-hexadecylamine (2.46 g, 10 mmol) was dissolved in 100 ml of methanol. This solution was then filtered through filter paper. Solid $Ce(PAO)_3$ (4.46 g, 10 mmol) was gradually added to this methanolic solution to give a yellowish suspension that turned to a clear yellow solution after twenty minutes. The resultant solution was left to stir for 3 hours, and then the methanol was evaporated using a rotary evaporator to deposit a crystalline, yellow substance (6.72 g, 97.04%). IR (cm^{-1}) (KBr): 3177(m, br),

3053(s), 2924(vs), 2853(vs), 2072(vw), 1745(w), 1605(vs, br), 1466(m), 1363(s), 1209(s), 1046(s), 981(w), 851(m), 776(w), 736(m), 664(vw), 597(vw), 543(w), 474(w).

X-ray Data Collection and Structure Determinations

Method 1: This method describes the technique used by Dr. Elizabeth M. Holt. Generally, crystals of suitable dimensions were selected to execute structural determinations on the basis of diffraction of monochromatic X-ray beams emitted from a molybdenum anode at a wavelength of 0.71073 Å (a weighted average of $K_{\alpha 1}$ and $K_{\alpha 2}$). A good quality single crystal was mounted on a glass fiber carried on a brass support, which was placed in a goniometer head and mounted on a Siemens P4 automated four-circle diffractometer equipped with a PC-486DX computer. Unit cell dimensions were determined using the centered angles from 25-50 independent strong reflections which were refined by least-squares method using automated procedure in **XSCANS**.[64] Intensity data were collected at 28°C using a variable scan rate, a θ-2θ scan mode and a scan range of 0.60 below $k_{\alpha 1}$ and 0.60 above $k_{\alpha 2}$ to a maximum 2θ value (normally 60.00°). Backgrounds were measured at the ends of the scan range for a combined time equal to the total scan time. The intensities of three standard reflections were remeasured after every 97 reflections to monitor crystal decomposition.[65] The raw intensity data collected were corrected for Lorentz, polarization, absorption, decomposition, centering and background effects (semi-empirical based on ψ scans),[66] after which redundant and space group forbidden data were removed. The profile fitting technique for data reduction was employed. Observed reflections [$\boldsymbol{F} > 4.0\ \boldsymbol{F}(\mathrm{l})$] were used to arrive at the non-hydrogen atoms positions by direct methods.[67-69] Refinement of the scale factor, positional and anisotropic thermal parameters for all atoms was carried out using either

XLS (refinement on F)[70] or **SHELXL**[71] (refinement on F^2) to convergence. Scattering factors were taken from the International Tables for Crystallography.[72] Hydrogen atoms positions were calculated using idealized geometry. A weighting scheme {$w = [\sigma^2(F) + abs(g)(F^2)]^{-1}$} and extinction correction were applied at the last stages of refinement. Final refinement led to the agreement factor, R [$R = \sum(|F_o| - |F_c|)/\sum[|F_o|)$].

Method 2: This method describes the technique used by Dr. Masood Khan. The data were collected at a range of 120-173 K on a Bruker Apex diffractometer[73] using MoK_α (λ = 0.71703 Å) radiation. Intensity data which approximately covered the full sphere of the reciprocal space were measured as a series of ω oscillation frames each 0.3° for 4-15 sec/frame. The detector was operated in 512 x 512 mode and was positioned 6.12 cm. from the crystal. Coverage of unique data was 97.3-99.3% complete to 52.0°-55.04° (*2θ).* Cell parameters were determined from a non-linear least square fit of 2345-6723 reflections in the range of $3.2^o < \theta < 26.9^o$. A total of 3375-17502 reflections were measured.

The structure was solved by the direct method using **SHELXTL** system,[74] and refined by full-matrix least square on F^2 using all reflections. All the non-hydrogen atoms were refined anisotropically and were included with idealized parameters.

Final R_1 = 0.013-0.042 was based on 3374-3610 "observed reflections" [$I>2\sigma(I)$] and wR^2 = 0.034-0.111 was based on all reflections (3375-3617 reflections). Thermal ellipsoids were drawn at 50% level.

X-ray Structure Determination of $Mg(PAO)_2(H_2O)_3 \cdot 2H_2O$

Crystals of the titled compound were obtained upon cooling the reaction solution to 5°C for a couple of days. A single crystal having the dimensions of 0.2 x 0.2 x 0.2 mm

was mounted on the above mentioned diffractometer, and the crystallographic data and structure refinement were performed as described previously (*vide supra*). The crystallographic data and data collection parameters are summarized in Table 2.2.

Table 2.2. Crystallographic Data for Mg(PAO)2(H2O)3·2H2O

Empirical formula	$C_6H_{18}Mg\ N_2O_{11}$
Color; Habit	Colorless rhombic
Formula weight	318.5
Crystal size	0.2 x 0.2 x 0.2 mm
Crystal system	Triclinic
Space group	$P\bar{1}$
Unit cell dimensions	a = 7.696(9) Å α = 108.88(6)° b = 9.545(10) Å β = 99.16(6)° c = 10.629(14) Å γ = 99.72(5)°
Volume	707.4(14) $Å^3$
Z, Calculated density	2, 1.495 Mg/m^3
Absorption coefficient (μ_o)	0.181 mm^{-1}
F(000)	336
2θ Range	3.5-60.0°
Scan speed	Variable; 10.00 to 30.00°/min in ω
Scan range (ω)	1.20° plus K_α-separation
Index ranges	$-10 \le h \le 1$, $-12 \le k \le 12$, $-14 \le l \le 14$
Reflections	
Collected	4869
Independent	4031 ($\boldsymbol{R}_{int}$ = 0.0826)
observed	3170 [$\boldsymbol{F} > 6.0\sigma(\boldsymbol{F})$]
Number of parameters refined	182
Final ***R*** indices (observed data)	$\boldsymbol{R}$ = 0.0511, w$\boldsymbol{R}$ = 0.0709
R indices (all data)	$\boldsymbol{R}$ = 0.0615, w$\boldsymbol{R}$ = 0.0791
Goodness-of-fit (GOF)	1.79
Extinction coefficient (χ)	0.0058(13)
Largest difference peak and hole ($\Delta\rho_{max, min}$)	0.77 and -0.40 $eÅ^{-3}$

X-ray Structure Determination of $Zn(PAO)_2 \cdot 2H_2O$

A sample of $ZnSO_4 \cdot 7H_2O$ (2.875 g, 10.0 mmol) was dissolved in 20 ml of distilled water. A 20-ml, aqueous solution of $Na(PAO) \cdot H_2O$ (0.143 g, 1.0 mmol) was

added gradually to the solution of zinc through the beaker's wall. Small crystals were obtained after one week upon slow evaporation of the solution. These crystals were separated and re-dissolved in 100 ml of distilled water. Slow evaporation of this mother liquor led to the formation of large, twin crystals. The IR spectrum of these crystals was similar to that of the zinc PAO complex precipitate obtained on large scale of $1Zn^{2+}$:$2PAO^{-}$ mole ratio. A crystal having the dimensions of 0.28 x 0.20 x 0.18 mm was mounted on the above mentioned diffractometer, and the crystallographic data and structure refinement were performed as described previously. The crystal data are given in Table 2.3.

Table 2.3. Crystallographic Data for Zn(PAO)2·2H2O

Empirical formula	$C_6H_{12}N_2O_8Zn$
Color; Habit	Colorless block
Formula weight	305.55
Crystal size	0.28 x 0.20 x 0.18 mm
Crystal system	Triclinic
Space group	P-1
Unit cell dimensions	a = 4.6920(11) Å α = 85.643(4)° b = 6.4211(16) Å β = 89.169(4)° c = 8.9746(16) Å γ = 74.847(4)°
Volume	260.23(10) $Å^3$
Z, Calculated density	1, 1.950 Mg/m^3
Absorption coefficient (μ_o)	2.396 mm^{-1}
$\boldsymbol{F}$(000)	156
2θ Range	3.30-27.49°
Index ranges	$-6 \le h \le 6$, $-8 \le k \le 8$, $-11 \le l \le 11$
Reflections Collected	3371
Independent	3375 ($\boldsymbol{R}_{int}$ = 0.0000)
Number of parameters refined	83
Final $\boldsymbol{R}$ indices [I > 2σ(I)]	$\boldsymbol{R}_1$ =0.0420, w$\boldsymbol{R}_2$ = 0.1114
$\boldsymbol{R}$ indices (all data)	$\boldsymbol{R}_1$ =0.0420, w$\boldsymbol{R}_2$ = 0.1114
Goodness-of-fit (GOF) on $\boldsymbol{F}^2$	1.054
Largest difference peak and hole ($\Delta\rho_{max, min}$)	0.394 and -0.534 $eÅ^{-3}$

X-ray Structure Determination of $Cu(PAO)_2 \cdot 2H_2O$

Saturation of 10 ml, 2 M $Na(PAO) \cdot H_2O$ solution with $Cu(PAO)_2 \cdot 2H_2O$, followed by slow evaporation of the mother liquor, led to the formation of the crystals of $Cu(PAO)_2 \cdot 2H_2O$. A single crystal of appropriate dimensions (0.1 x 0.3 x 0.3 mm) was mounted on the diffractometer and its crystallographic data and structure refinement were determined as elucidated formerly. Table 2.4 displays the crystal data structure refinement of the titled compound.

Table 2.4. Crystallographic Data for Cu(O2CC(=NOH)CH3)2·2H2O

Empirical formula	$C_6H_{12}Cu\ N_2O_8$
Color; Habit	Blue plate
Formula weight	303.7
Crystal size	0.1 x 0.3 x 0.3 mm
Crystal system	Triclinic
Space group	$P\bar{1}$
Unit cell dimensions	a = 4.907(7) Å $\alpha = 87.71(1)^o$ b = 6.680(11) Å $\beta = 87.83(1)^o$ c = 8.770(13) Å $\gamma = 76.11(1)^o$
Volume	278.7(9) $Å^3$
Z, Calculated density	1, 1.810 Mg/m^3
Absorption coefficient (μ_o)	1.993 mm^{-1}
Reflections	
Collected	2076
Independent	1572
observed	1260 [$\boldsymbol{F} > 5.0\sigma(\boldsymbol{F})$]
Number of parameters refined	80
$\boldsymbol{R}$	0.0590
$\boldsymbol{R}_w$	0.0864
Goodness-of-fit (GOF)	1. 09
Largest difference peak and hole ($\Delta\rho_{max, min}$)	1.00 and -1.42 $eÅ^{-3}$

X-ray Structure Determination of $Pr(PAO)_3(H_2O)_2$

The filtrate of the reaction solution after the removal of the PAO complex of Pr^{3+} precipitate was kept due to its very light green color, indicating the existence of some Pr^{3+} ions. Slow evaporation of the filtrate over 2 months at room temperature led to the formation of very beautiful light green crystals of the titled complex. The crystallographic data of this complex are provided in Table 2.5.

Table 2.5. Crystallographic Data for Pr(PAO)3(H2O)2

Empirical formula	$C_9H_{16}N_3O_{11}Pr$
Color	Light green
Formula weight	483.16
Crystal size	0.46 x 0.42 x 0.38 mm
Crystal system	Orthorhombic
Space group	Pna2(1)
Unit cell dimensions	a = 7.6679(4) Å $\alpha = 90^o$ b = 18.3180(9) Å $\beta = 90^o$ c = 11.3777(6) Å $\gamma = 90^o$
Volume	1598.12(14) $Å^3$
Z, Calculated density	4, 2.008 Mg/m^3
Absorption coefficient (μ_o)	3.111 mm^{-1}
$F(000)$	952
2θ Range	$2.22\text{-}27.52^o$
Index ranges	$-9 \le h \le 9, -23 \le k \le 23, -14 \le l \le 14$
Reflections	
Collected	17502
Independent	3617 (R_{int} = 0.0204)
Number of parameters refined	236
Final R indices [$I > 2\sigma(I)$]	R_1 =0.0128, wR_2 = 0.0341
R indices (all data)	R_1 =0.0129, wR_2 = 0.0341
Goodness-of-fit (GOF) on F^2	1.076
Extinction coefficient (χ)	0.00796(16)
Largest difference peak and hole ($\Delta\rho_{max, min}$)	0.322 and -0.458 $eÅ^{-3}$

X-ray Structure Determination of $[(H_3C)_4N][Cu(PAO^-)(PAO^{2-})(H_2O)]\cdot H_2O$

Crystals of the title compound were obtained upon slow evaporation of the reaction solution at room temperature over a period of 10 days. The crystal data, data collection, and structure refinement were summarized in Table 2.6.

Table 2.6. Crystallographic Data for [(H3C)4N][Cu(PAO-)(PAO2-)(H2O)]·H2O

Empirical formula	$C_{10}H_{23}Cu\ N_3O_8$
Formula weight	376.85
Crystal size	0.40 x 0.15 x 0.06 mm
Crystal system	Monoclinic
Space group	P2(1)
Unit cell dimensions	a = 11.0905(7) Å $\alpha = 90^o$ b = 6.6715(4) Å $\beta = 113.1010(10)^o$ c = 11.5372(7) Å $\gamma = 90^o$
Volume	785.19(8) $Å^3$
Z, Calculated density	2, 1.594 Mg/m^3
Absorption coefficient (μ_o)	1.434 mm^{-1}
$F(000)$	394
2θ Range	$1.92\text{-}28.31^o$
Index ranges	$-14 \le h \le 14, -8 \le k \le 8, -15 \le l \le 15$
Reflections	
Collected	7894
Independent	3616 (R_{int} = 0.0169)
Number of parameters refined	220
Final R indices [$I > 2\sigma(I)$]	R_1 = 0.0203, wR_2 = 0.0542
R indices (all data)	R_1 = 0.0205, wR_2 = 0.0543
Goodness-of-fit (GOF) on F^2	1.078
Largest difference peak and hole ($\Delta\rho_{max, min}$)	0.353 and -0.248 $eÅ^{-3}$

Pyrolysis

The metal PAO salts were pyrolyzed in a temperature programmable, muffle furnace under ambient air at temperatures that corresponded to completion of decomposition steps observed by TGA experiments. The solid product obtained at every thermal decomposition step was characterized by IR and XRD analyses.

Pyrolysis of PAO^- Salts of Main Group Elements

Drying $Mg(PAO)_2(H2O)_3 \cdot 2H_2O$ under Vacuum

A specimen of 0.9212 g of $Mg(PAO)_2 \cdot 5H_2O$ was placed in a preweighed 20-ml, vial with cover. The vial was then placed in a desiccator under vacuum at room temperature for 3 nights to yield 0.7065 g (76.69%) of a white product. The change in weight corresponded to the loss of 4 moles of water. Therefore, the product obtained had a molecular formula of $Mg(PAO)_2 \cdot H_2O$. IR (cm^{-1}) (KBr): 3363(m), 3205(m), 3075(m), 2256(vw), 2116(vw), 1932(vw), 1628(vs), 1413(s), 1370(s), 1221(s), 1063(s), 858(m), 779(m), 743(m), 649(w), 565(w), 517(w), 449(vw).

Dehydration of $Mg(PAO)_2(H_2O)_3 \cdot 2H_2O$ at 80 ^oC

A sample of 0.9780 g of $Mg(PAO)_2 \cdot 5H_2O$ was placed in a 250-ml, Erlenmeyer flask. The magnesium salt was then heated in the muffle furnace at 80 ^oC overnight to give a yield of 0.7669 g (78.42%) of a white product. IR (cm^{-1}) (KBr): 3943(vw), 3550(m, sharp), 3182(s), 3053(s), 2416(vw), 2299(vw), 2245(vw), 2134(vw), 2058(vw), 1942(vw), 1788(w), 1672(s), 1645(vs), 1603(vs), 1552(s),1505(s), 1475(s), 1435(vs), 1413(vs), 1368(s), 1225(s), 1073(s), 1039(s), 998(vw), 856(s), 833(s),814(s), 777(m), 744(s), 685(w), 525(m), 495(w), 440(vw), 432(vw), 420(vw).

Pyrolysis of $Mg(PAO)_2(H_2O)_3 \cdot 2H_2O$ at 175°C

A sample of 0.8443 g of $Mg(PAO)_2 \cdot 5H_2O$ was placed in a 250-ml, Erlenmeyer flask. The magnesium salt was then heated in the muffle furnace at 175°C overnight to yield 0.5534 g (65.55%) of a white product. IR (cm^{-1}) (KBr): 3180(s), 3052(s), 2946(s), 2868(s), 2844(s), 2416(vw), 2363(vw), 2299(vw), 2222(vw), 2176(vw), 2138(vw), 2069(vw), 2057(vw), 1965(vw), 1941(vw), 1787(w), 1674(s), 1648(vs), 1603(vs), 1471(m), 1435(s), 1412(s), 1367(s), 1227(s), 1079(s), 1034(w), 998(vw), 858(m), 809(m), 748(m), 555(vw), 523(w), 459(vw), 448(vw), 438(vw), 432(vw), 424(vw), 406(vw).

Pyrolysis of $Mg(PAO)_2(H_2O)_3 \cdot 2H_2O$ at 220°C

A sample of 1.0670 g of $Mg(PAO)_2 \cdot 5H_2O$ was placed in a 250 ml Erlenmeyer flask and heated to 220 °C in a muffle furnace overnight to yield 0.3022 g (28.32%) of a white product. IR (cm^{-1}) (KBr): 3456(m, br), 2427(vw), 2275(vw), 1967(vw), 1769(vw), 1507(s), 1439(s), 1385(s), 1220(w), 1103(w), 859(m), 780(w), 759(w), 692(w).

Pyrolysis of $Mg(PAO)_2(H_2O)_3 \cdot 2H_2O$ at 250°C

A sample of 0.8883 g of $Mg(PAO)_2 \cdot 5H_2O$ was placed in a 250-ml, Erlenmeyer flask. The magnesium salt was then heated in the muffle furnace at 250°C overnight to yield 0.2343 g (26.38%) of a white product. IR (cm^{-1}) (KBr): 3554(m, br), 2617(vw), 2427(vw), 2206(vw), 1961(vw), 1794(vw), 1520(s), 1445(s), 1223(vw), 1104(w), 1026(vw), 858(w), 781(w), 760(w), 620(w).

Pyrolysis of $Mg(PAO)_2(H_2O)_3 \cdot 2H_2O$ at 450°C

A sample of 1.0769 g of $Mg(PAO)_2 \cdot 5H_2O$ was placed in a 100-ml, volumetric flask. The magnesium salt was then heated in the muffle furnace at 450°C overnight to

yield 0.1402 g (13.02%) of a white product. IR (cm^{-1}) (KBr): 3613(w, br), 3472(w), 3600(vw), 2926(vw), 2848(vw), 2207(vw), 1636(vw), 1497(w), 1436(w), 1393(w), 1070(vw), 1043(vw), 940(vw), 864(vw), 602(m, br).

Pyrolysis of $Mg(PAO)_2(H_2O)_3 \cdot 2H_2O$ at 500°C

A sample of 0.9510 g of $Mg(PAO)_2 \cdot 5H_2O$ was placed in a 250-ml, Erlenmeyer flask. The magnesium salt was then heated in a muffle furnace at 500 °C overnight to yield 0.1367 g (14.37%) of a white product. IR (cm^{-1}) (KBr):3768(vw, sh), 3719(vw, sh), 3609(w, br), 3471(w), 3088(vw), 2343(vw), 2210(vw), 1773(vw), 1506(m), 1430(m), 1380(w), 1252(vw), 1147(vw), 1067(vw), 983(vw), 864(w), 652(s, br).

Pyrolysis of $Mg(PAO)_2(H_2O)_3 \cdot 2H_2O$ at 600°C

A porcelain crucible containing 0.8367 g of $Mg(PAO)_2 \cdot 5H_2O$ was placed in a muffle furnace and heated to 600 °C overnight to yield 0.1233 g (14.74%) of a white product. IR (cm^{-1}) (KBr): 3567(w), 3465(w), 1636(w), 1496(m), 1220(vw), 1148(vw), 1080(vw), 979(vw), 861(vw), 652(m, br).

Pyrolysis of $Mg(PAO)_2(H2O)_3 \cdot 2H_2O$ at 900°C

A yield of 0.1323 g (13.04%) of a white product was obtained when 1.0147 g of $Mg(PAO)_2 \cdot 5H_2O$ was heated overnight at 900 °C in a muffle furnace. IR (cm^{-1}) (KBr): 3478(vw, br), 3048(vw), 1758(vw), 1685(vw), 1636(vw), 1506(vw), 1437(vw), 1391(vw), 1372(vw), 1207(vw), 1069(vw), 938(vw), 848(vw), 589(s, br).

Pyrolysis of $HOAl(PAO)_2 \cdot 2H_2O$ at 100°C

A sample of 0.2794 g of $HOAl(PAO)_2 \cdot 2H_2O$ was taken in a 250-ml Erlenmeyer flask and placed in a muffle furnace and heated to 100 °C overnight to yield 0.2350 g (84.12%) of a white product. IR (cm^{-1}) (KBr): 3365(s, br), 2477(w), 1942(vw), 1669(vs),

1439(m), 1363(s), 1228(s), 1145(s), 1086(m), 1029(w), 885(w), 801(w), 772(w), 610(w, br), 427(vw), 419(vw), 407(vw), 401(vw).

Pyrolysis of $HOAl(PAO)_2 \cdot 2H_2O$ at 125°C

A sample of 0.2685 g of $HOAl(PAO)_2 \cdot 2H_2O$ was placed in a 250-ml, Erlenmeyer flask. The aluminum salt was then heated in a muffle furnace at 125 °C overnight to give 0.1974 g (73.25%) of a white product. IR (cm^{-1}) (KBr): 3400(s, br), 2926(m), 2854(m), 2450(vw), 2256(vw), 2089(vw), 1940(vw), 1672(s), 1440(m), 1363(s), 1229(m), 1147(m), 1026(w), 1005(w), 884(w), 800(w), 772(w), 752(w), 635(w, br), 442(vw), 430(vw), 422(vw), 407(vw).

Pyrolysis of $HOAl(PAO)_2 \cdot 2H_2O$ at 150°C

A yield of 0.6433 g (59.78%) of a white product was obtained when 1.0762 g of $HOAl(PAO)_2 \cdot 2H_2O$ was heated overnight at 150 °C in a muffle furnace. IR (cm^{-1}) (KBr): 3461(m, br), 2845(w), 2363(vw), 2337(vw), 2259(vw), 1622(s), 1654(s), 1506(vw), 1437(w), 1364(m), 1229(m), 1147(m), 1022(vw), 999(vw), 885(w), 801(w), 774(vw).

Pyrolysis of $HOAl(PAO)_2 \cdot 2H_2O$ at 200°C

A sample of 0.2908 g of $HOAl(PAO)_2 \cdot 2H_2O$ was placed in a 250-ml, Erlenmeyer flask and heated to 100 °C in a muffle furnace overnight to yield 0.1133 g (38.96%) of a white product. IR (cm^{-1}) (KBr): 3508(m, br), 2447(vw, br), 2223(vw), 1883(vw), 1763(vw), 1653(m), 1603(m), 1449(w), 1394(w), 1229(vw), 1143(vw), 886(m), 866(m), 726(m), 458(vw), 442(vw), 437(vw), 417(vw).

Pyrolysis of $HOAl(PAO)_2 \cdot 2H_2O$ at 250°C

A sample of 0.3372 g of $HOAl(PAO)_2 \cdot 2H_2O$ was placed in a 250-ml, Erlenmeyer flask. The aluminum salt was then heated in a muffle furnace at 250°C overnight to give

0.1151 g (34.13%) of a white product. IR (cm^{-1}) (KBr): 3518(m, br), 2503(vw), 2245(vw), 2035(vw), 1817(vw), 1594(m), 1465(w), 1420(w), 1299(vw), 1141(vw), 1052(w), 887(m), 868(m), 446(vw), 442(vw), 435(vw), 428(vw), 419(vw), 411(vw), 403(vw).

Pyrolysis of $HOAl(PAO)_2 \cdot 2H_2O$ at 300°C

A sample of 1.3759 g of $HOAl(PAO)_2 \cdot 2H_2O$ was put in a porcelain crucible and calcined at 300 °C in a muffle furnace overnight to yield 1.3991 g (29.00%) of a white product. IR (cm^{-1}) (KBr): 3479(w, br), 2932(vw), 2851(vw), 2418(vw), 1595(w), 1465(w), 1381(vw), 1300(vw), 1238(vw), 1173(vw), 1053(vw), 838(w, br).

Pyrolysis of $HOAl(PAO)_2 \cdot 2H_2O$ at 450°C

A sample of 4.4799 g of $HOAl(PAO)_2 \cdot 2H_2O$ was placed in a 250-ml, Erlenmeyer flask. The aluminum salt was then heated in a muffle furnace at 450 °C overnight to give 1.5838 g (35.35%) of a white product. IR (cm^{-1}) (KBr): 3511(m, br), 2349(vw), 2284(vw), 1652(vw), 1540(vw), 1061(w), 869(w, br), 664(w), 408(vw).

Pyrolysis of $HOAl(PAO)_2 \cdot 2H_2O$ at 600°C

A yield of 2.4028 g (82.77%) of a white product was obtained when 2.9031 g of $HOAl(PAO)_2 \cdot 2H_2O$, previously pyrolyzed at 450°C, was heated overnight at 600°C in a muffle furnace. IR (cm^{-1}) (KBr): 3514(m, br), 2351(w), 2363(vw), 2093(vw), 1645(w), 1540(w), 1291(vw), 1069(w), 890(w), 773(w).

Pyrolysis of PAO^- Salts of Group 12 Metals

Pyrolysis of $Zn(PAO)_2 \cdot 2H_2O$ at 150°C

A sample of 0.9963 g of $Zn(PAO)_2 \cdot 2H_2O$ was placed in a 250-ml, Erlenmeyer

flask. The zinc salt was then heated in a muffle furnace at 150°C overnight to give 0.5886 g (59.08%) of light pink product. Solid-state ^{13}C CPMAS NMR: δ (ppm) 9.1 and 20.8 (CH_3), 153.4 (C═N), 169.3 (COO). IR (cm^{-1}) (KBr): 3208(s, br), 3058(s, br), 2836(s, br), 1792(w), 1618(vs), 1415(m), 1367(s), 1223(s), 1121(m), 1075(s), 994(vw), 947(vw), 866(m), 772(m), 670(vw), 579(vw), 510(vw), 424(w).

Pyrolysis of $Zn(PAO)_2 \cdot 2H_2O$ at 200°C

A sample of 1.4192 g of $Zn(PAO)_2 \cdot 2H_2O$ was placed in a 250-ml, Erlenmeyer flask and heated to 200 °C in a muffle furnace overnight to yield 0.6325 g (44.57%) of a white product. Solid-state ^{13}C CPMAS NMR: δ (ppm) 10.3 and 22.3 (CH_3), 152.2 and 158.0 (C═N), 171.2 (COO), and 181.7 (C═O). IR (cm^{-1}) (KBr): 3359(s, br), 1608(vs), 1437(s), 1365(s), 1224(m), 1127(m), 868(w), 772(w), 675(vw), 550(vw).

Pyrolysis of $Zn(PAO)_2 \cdot 2H_2O$ at 290°C

A sample of 2.0098 g of $Zn(PAO)_2 \cdot 2H_2O$ was put in a 250-ml, Erlenmeyer flask and calcined at 290°C in a muffle furnace overnight to give 0.5378 g (26.76%) of a white product. Solid-state ^{13}C CPMAS NMR: δ (ppm) 166.9 (COO). IR (cm^{-1}) (KBr): 3479(m, br), 2359(vw), 2079(vw), 1912(vw), 1813(vw), 1521(vs), 1362(s), 1250(vw), 1129(vw), 1065(vw), 890(w), 569(m).

Pyrolysis of $Zn(PAO)_2 \cdot 2H_2O$ at 389°C

A yield of 0.2282 g (26.52%) of an off white product was obtained when 0.8605 g of $Zn(PAO)_2 \cdot 2H_2O$ was heated overnight at 389°C in a muffle furnace. IR (cm^{-1}) (KBr): 3519(w, br), 1522(w, br), 1348(w), 884(w, br), 527(vs).

Pyrolysis of $Cd(PAO)_2$ at 200°C

A 100-ml, volumetric flask containing 1.0247 g of $Cd(PAO)_2$ was placed in a muffle furnace and heated to 200°C overnight to yield 0.6481 g (63.25%) of a pink product. Solid-state ^{13}C CPMAS NMR: δ (ppm) 13.6 (CH_3), 160.5 (C═N), 173.7 (COO). IR (cm^{-1}) (KBr): 3346(m,br), 2968(w), 2796(w), 2575(vw), 2453(vw), 2241(vw), 2073(vw), 1607(s), 1588(m), 1552(m), 1387(m), 1368(m), 1209(m), 1066(s), 863(s), 776(s), 755(s), 678(vw), 619(vw), 533(w), 505(vw), 440(vw), 403(vw).

Pyrolysis of $Cd(PAO)_2$ at 300°C

A sample of 1.1007 g of $Cd(PAO)_2$ was placed in a 100-ml, volumetric flask. The cadmium salt was then heated in a muffle furnace at 300°C overnight to give 0.3851 g (34.99%) of red-brown product. IR (cm^{-1}) (KBr): 3007(m, vbr), 493(vw).

Pyrolysis of $Cd(PAO)_2$ at 400°C

A sample of 1.9127 g of $Cd(PAO)_2$ was placed in a 100-ml, volumetric flask and heated to 400 °C in a muffle furnace overnight to yield 0.6731 g (35.19%) of red-brown product. IR (cm^{-1}) (KBr): 3511(vw), 2479(vw, br), 1483(vw), 1356(vw), 1186(vw), 1078(vw), 949(vw), 859(vw), 514(vw), 448(vw), 429(vw), 420(vw), 409(vw).

Pyrolysis of $Hg(PAO)_2$ at 90°C

A sample of 1.0534 g of $Hg(PAO)_2$ was put in a 150-ml, Erlenmeyer flask and pyrolyzed at 90°C in the muffle furnace overnight to yield 0.9641 g (91.52%) of a white product. Solid-state ^{13}C CPMAS NMR: δ (ppm) 24.8 (CH_3), 178.8 (COO). IR (cm^{-1}) (KBr): 3331(s,), 3211(m), 2991(w), 2927(w), 2465(vw), 2291(vw), 1943(vw), 1668(s), 1598(s), 1534(s), 1450(m), 1422(m), 1390(m), 1226(w), 1164(vw), 1013(w), 938(vw), 881(vw), 805(vw), 716(w), 673(vw), 565(w), 455(vw), 414(vw).

Pyrolysis of PAO^- Salts of Divalent 3d Transition Metals

Pyrolysis of $Mn_4(PAO)_8.2H_2O$ at 200°C Under N_2

A sample of 2.00 g of $Mn(PAO)_2 \cdot 2H_2O$ was placed in a pressure tube, which was then evacuated and filled with ultra high purity N_2 gas for 4 hours. The tube was then placed in a cylindrical oven at 200 °C (overnight). A brown solid resulted from the pyrolysis. This product, along with the tube, was washed with H_2CCl_2 and then was placed in the sonicator for 1 hour. The H_2CCl_2 extract (1 x 30 ml) was then analyzed by GC/MS, which identified the presence of acetamide. The brown solid obtained was washed with MeOH and then with water. After drying, the IR and XRD analyses of this solid matched the spectrum of $MnCO_3$. IR (cm^{-1}) (KBr): 3373(vw), 2885(vw), 2834(vw), 2490(vw), 1796(vw), 1635(vw), 1477(m), 1211(vw), 1075(vw), 968(vw), 864(w), 725(vw), 614(vw), 513(vw).

Pyrolysis of $Mn_4(PAO)_8.2H_2O$ at 533°C

A sample of 0.8219 g of $Mn_4(PAO)_8 \cdot 2H_2O$ was placed in a 250-ml, Erlenmeyer flask. This PAO salt was then heated in a muffle furnace at 533°C overnight to give 0.2399 g (29.19%) of a black product. IR (cm^{-1}) (KBr): 3360(vw), 3036(vw), 2837(vw), 2338(vw), 1759(vw), 1570(vw), 1325(vw), 975(vw), 674(w), 606(w), 401(vw).

Pyrolysis of $Fe(PAO)_2.2H_2O$ at 285°C

A sample of 1.3461 g of $Fe(PAO)_2 \cdot 2H_2O$ was placed in a 100-ml, volumetric flask. This PAO salt was then heated in a muffle furnace at 522°C overnight to give 0.3707 g (27.54%) of a brown product. IR (cm^{-1}) (KBr): 3670(m, sharp), 3629(m, sharp), 3431(s, br), 2338(m), 2200(vw), 1734(vw), 1653(m), 1559(m), 1506(m), 1339(m), 754(vs), 617(m), 494(m).

Pyrolysis of $Fe(PAO)_2 \cdot 2H_2O$ at 463°C

A sample of 1.1040 g of $Fe_2(PAO)_2 \cdot 2H_2O$ was placed in a 250-ml, Erlenmeyer flask and was heated to 463°C in a muffle furnace overnight to yield 0.2947 g (26.93%) of a brown product. IR (cm^{-1}) (KBr): 3736(vw), 3508(vw, br), 3008(vw, br), 2892(vw), 2342(vw), 1772(vw), 546(s), 474(s).

Pyrolysis of $Co(PAO)_2 \cdot 2H_2O$ at 276°C

A sample of 0.8395 g of $Co(PAO)_2 \cdot 2H_2O$ was placed in a 250-ml, Erlenmeyer flask. The cobalt salt was then heated in a muffle furnace at 276°C overnight to give 0.2196 g (26.16%) of a black product. IR (cm^{-1}) (KBr): 3711(vw, br), 3363(vw), 3021(vw), 2953(vw), 2886(vw), 2341(vw), 1384(vw), 665(s), 576(s).

Pyrolysis of $Ni(PAO)_2 \cdot 2H_2O$ at 349°C

A yield of 0.1313 g (25.45%) of a black product was obtained when 0.5160 g of $Ni(PAO)_2 \cdot 2H_2O$ was heated overnight at 471°C in a muffle furnace. IR (cm^{-1}) (KBr): 3558(w), 2924(vw), 2852(vw), 2426(vw), 1940(vw), 1769(vw), 1769(vw), 1718(vw), 1641(vw), 1506(vw), 1384(m), 1119(vw), 1041(vw), 839(vw), 578(m), 425(vw), 404(vw).

Hydrolysis of $Cu(PAO)_2 \cdot 2H_2O$

A sample of $Cu(PAO)_2 \cdot 2H_2O$ (10 g, 32.94 mmol) was mixed with 250 ml of distilled water in a 500-ml, round-bottomed flask. This mixture was refluxed for a month to give 2.26 g of light brown, highly crystalline Cu_2O, as indicated by the very sharp peaks in the X-ray diffraction spectrum. This result corresponded to 95.89% reduction of Cu^{2+} to Cu^{1+}. The filtrate was turquoise in color due to the presence of the unreduced Cu^{2+}, which made this filtrate slightly acidic (pH = 5.034) and caused a broad absorption

peak in the visible region that had a maximum at 694 nm and absorption of 0.236. This filtrate, after 2 days, precipitated 0.09 g of a well-crystallized, light blue material that was identified by XRD to be copper oxalate.

Pyrolysis of $Cu(PAO)_2 \cdot 2H_2O$ at 421°C

A sample of 0.4153 g of $Cu(PAO)_2 \cdot 2H_2O$ was placed in a 100-ml, volumetric flask. The copper salt was then heated in a muffle furnace at 421 °C overnight to give 0.1093 g (26.32%) of dark brown product. IR (cm^{-1}) (KBr): 3040(vw), 2897(vw), 2827(vw), 2342(vw), 1793(vw), 1653(vw), 1522(vw), 1384(w), 1359(vw), 1179(vw), 1081(vw), 880(vw), 824(vw), 735(vw), 594(s), 462(m).

Pyrolysis of PAO^{2-} Salts

Pyrolysis of $[(H_3C)_4N]^+[Cu(PAO^-)(PAO^{2-})(H_2O)]^- \cdot H_2O$

A sample of 2.6242 g of $[(H_3C)_4N]^+[Cu(PAO^-)(PAO^{2-})(H_2O)]^- \cdot H_2O$ was placed in a 250-ml, Erlenmeyer flask. The copper salt was then heated in a muffle furnace at 314 °C overnight to give 0.5804 g (22.12%) of a black product. IR (cm^{-1}) (KBr): 3016(vw), 2766(vw), 1890(vw), 1521(vw), 1383(vw), 1118(vw), 549(m), 460(w).

Pyrolysis of $[H_3C(H_2C)_{15}NH_3]^+[Fe(PAO^-)(PAO^{2-})]^-$ at 574°C

A sample of 1.5033 g of $[H_3C(H_2C)_{15}NH_3]^+[Fe(PAO^-)(PAO^{2-})]^-$ was placed in a 250-ml, Erlenmeyer flask and heated to 574 °C in a muffle furnace overnight to yield 0.2540 g (16.90%) of red-brown product. IR (cm^{-1}) (KBr): 3853(vw, sharp), 3438(w, br), 3059(vw), 2859(vw), 2339(vw), 1506(vw), 1389(vw), 1247(w), 1155(w), 1037(vw), 914(vw), 625(s), 481(m), 420(vw).

Pyrolysis of $[H_3C(H_2C)_{15}NH_3]^+[Zn(PAO^-)(PAO^{2-})(H_2O)]^-$ at 101°C

A sample of 2.0037 g of $[H_3C(H_2C)_{15}NH_3]^+[Zn(PAO^-)(PAO^{2-})(H_2O)]^-$ was placed in a 250-ml, Erlenmeyer flask. This PAO salt was then heated in a muffle furnace at 101 °C overnight to yield 1.9118 g (95.41%) of white product. IR (cm^{-1}) (KBr): 3263(m), 2922(s), 2852(s), 1759(vw), 1629(m), 1582(m), 1468(m), 1362(m), 1214(m), 1114(w), 1078(m), 1024(w), 980(vw), 905(vw), 855(w), 838(w), 773(m), 745(w), 726(w), 663(vw), 552(vw), 492(w), 420(vw), 407(vw).

Sintering of $[H_3C(H_2C)_{15}NH_3]^+[Zn(PAO^-)(PAO^{2-})(H_2O)]^-$ at 140°C

A sample of 1.5191 g of $[H_3C(H_2C)_{15}NH_3]^+[Zn(PAO^-)(PAO^{2-})(H_2O)]^-$, previously heated at 101°C, was placed in a 250-ml, Erlenmeyer flask. This PAO salt was then heated in a muffle furnace at 140 °C overnight to yield 1.1981 g (78.87%) of white, glassy product. IR (cm^{-1}) (KBr): 3255(m), 3144(w), 2921(vs), 2851(vs), 1638(m), 1468(w), 1354(m), 1211(w), 1114(m), 862(w), 771(m), 721(w), 663(vw), 551(vw), 503(vw), 419(vw), 406(vw).

Sintering of $[H_3C(H_2C)_{15}NH_3]^+[Zn(PAO^-)(PAO^{2-})(H_2O)]^-$ at 208°C

A sample of 0.8174 g of $[H_3C(H_2C)_{15}NH_3]^+[Zn(PAO^-)(PAO^{2-})(H_2O)]^-$, previously heated at 140°C, was placed in a 250-ml, Erlenmeyer flask. This PAO salt was then heated in a muffle furnace at 208°C overnight to yield 0.5530 g (67.65%) of dark brown, glassy product. IR (cm^{-1}) (KBr): 3319(w), 2936(m), 2858(m), 2729(w), 2682(w), 2315(vw), 2216(vw), 2026(vw), 1913(vw), 1714(w), 1468(w), 1351(w), 1242(vw), 1074(vw), 964(vw), 721(vw), 541(vw), 409(vw).

Sintering of $[H_3C(H_2C)_{15}NH_3]^+[Zn(PAO^-)(PAO^{2-})(H_2O)]^-$ at 411°C

A sample of 0.5463 g of $[H_3C(H_2C)_{15}NH_3]^+[Zn(PAO^-)(PAO^{2-})(H_2O)]^-$, previously heated at 208°C, was placed in a 250-ml, Erlenmeyer flask. This PAO salt was then

heated in a muffle furnace at 411°C overnight to give 0.1672 g (30.61%) of white, crystalline product. IR (cm^{-1}) KBr): 3504(vw, br), 2387(vw), 1520(vw), 1379(vw), 882(vw), 238(m), 530(m), 442(w), 406(vw).

Pyrolysis of $[H_3C(H_2C)_{15}NH_3]^+[Ce(PAO^-)_2(PAO^{2-})(H_2O)]^-$ at 289°C

In a 250-ml, Erlenmeyer flask was placed 3.0077 g of $[H_3C(H_2C)_{15}NH_3]^+[Ce(PAO^-)_2(PAO^{2-})(H_2O)]^-$ in a muffle furnace and heated to 289 °C overnight to yield 0.7614 g (25.32%) of a yellow product. IR (cm^{-1}) (KBr): 3424(m, br), 1507(m), 1384(m), 1060(vw), 846(vw), 721(vw), 551(w), 464(w), 406(vw).

Acidity and Basicity Measurements

The acidities and basicities of all metal oxides prepared were determined from Langmuir adsorption isotherms of an adsorbate (a titrating agent).[75] The equilibrium concentration (*C*) of the adsorbate was determined from the difference in UV absorption before and after the adsorption of the titrating agent on the metal oxide (adsorbent). In practice, 10 ml of the titrating agent solution was added to a specific amount of the adsorbent in a 20-ml vial. This mixture was then magnetically stirred overnight. Filtering this mixture through a membrane filter, and then measuring the UV absorption at the λ_{max} of the adsorbate, gave *C*, and hence the amount of the titrating agent adsorbed per unit mass of investigated adsorbent (*X*). The number of acidic or basic sites on the surface of the adsorbent expressed in μmol/g is equal to the amount of adsorbate adsorbed by the adsorbent in the monolayer (X_m), which, in turn, is equal to the reciprocal of the slope of the straight line obtained from the plot of *C*/*X* versus *C* according to Langmuir equation:[75]

$$\frac{C}{X} = \frac{b}{X_m} + \frac{C}{X_m} \quad \text{(Eq. 2.4)}$$

where *b* is a characteristic constant of the adsorbent under study and is determined experimentally. Cyclohexylamine (pK_a = 10.64,[76] λ_{max} = 226 nm[77]) dissolved in cyclohexane and chloranil (electron affinity = 2.40 eV, λ_{max} = 288 nm)[78] dissolved in acetonitrile were used to measure the acidity of the adsorbent. Phenol (pK_b = 4.11,[76] λ_{max} = 271.6 nm[77]) dissolved in cyclohexane was used to measure the basicity of the adsorbent.

2.3. RESULTS AND DISCUSSION

All of the PAO metal salts and complexes were prepared in this investigation by ligand exchange process in an aqueous medium at room temperature as shown in the following equation:

$$MX_n\,(aq) + nNaO_2CC(=NOH)CH_3\,(aq) \xrightarrow[25\ ^oC]{} nNaX\,(aq) + M[O_2CC(=NOH)CH_3]_n \quad \text{(Eq. 2.5)}$$

where X = SO_4^{2-}, NO_3^-, H_3CCOO^-, or Cl^- exchanges with PAO^- to form precipitates with most metals and crystals with the others.

PAO^- Salts of Main Group Elements

The alkaline earth metal salts of PAO^- were synthesized and characterized by spectroscopic methods including IR, NMR, and by XRD, which resulted in a different pattern for each salt, indicating that each one has its own unique structure.[6] These structural differences partially influenced the decomposition temperatures.[6,14] The magnesium PAO^- salt structure, illustrated in Figure 2.6, was determined in this investigation, and confirmed the preceding conclusion concerning the structural variations in that it has a completely different crystalline lattice than that observed for the calcium salt.[6] The magnesium ion center lies in a pseudo-octahedral environment, i.e.

has a coordination number of six, where three coordination sites are occupied by the oxygen atoms of three water molecules with bond lengths of 2.075(3), 2.058(3), 2.066(3) Å corresponding to Mg(1)—O(21), Mg(1)—O(22), Mg(1)—O(23), respectively (see Table 2.7), which are comparable to those found in magnesium acetate tetrahydrate $[Mg(O_2CCH_3)_2(H_2O)_4]$[79] where two water molecules are attached to Mg^{2+} at a distance of 2.0577(9) and the other two at a distance of 2.1091(8) Å. The differences in the Mg—O bond lengths for the magnesium complexes is due to the variation in the distortion of the octahedron environment of the Mg^{2+}, which in turn is a consequence of the different ligands, PAO^- and H_3CCOO^-, the different ligating mode of both ligands, and the different natures of the H-bonding in both salts. The coordination in the magnesium sphere of $Mg(PAO)_2(H_2O)_3 \cdot 2H_2O$ is completed by two ligands of PAO^-, where one of them is monodentate attached through the deprotonated hydroxyl oxygen atom of carboxylate moiety, Mg(1)—O(91), having a distance of 2.061(3) Å. This distance is close to that found in magnesium acetate tetrahydrate (2.0761(8) Å),[79] where the acetate is also coordinated to the Mg^{2+} in a monodentate fashion. This monodentate PAO^- ligand shows partial delocalization of the negative charge because of the slight large difference (0.026 Å) in the bond length of the two carbon-oxygen bonds of the carboxylate moiety, O(91)—C(91) = 1.268(3) Å & O(92)—C(91) = 1.242(2) Å. The longer distance of the former bond can be ascribed to the fact that O(91) oxygen atom is bonded to the magnesium ion center. The bond distances of the remaining bonds in the monodentate PAO^-, C(91)—C(92), C(92)—C(93), C(92)—N(94), and N(94)—O(94), are, respectively, 1.529(3), 1.486(4), 1.289(3), and 1.416(3) Å. The other PAO^- chelates the magnesium center to form a five-membered metallacycle, which is similar to that previously found in

the $Na(PAO)\cdot H_2O$[18] and $Ca(PAO)_2\cdot H_2O$[6] structures. However, the bond length of the magnesium—oximino nitrogen atom contact, Mg(1)—N(4), has a bond distance of 2.217(3) Å, that is much smaller than those reported for sodium[14] and calcium[6] derivatives (2.440(2),[14] and 2.503(2)[6] Å, respectively).

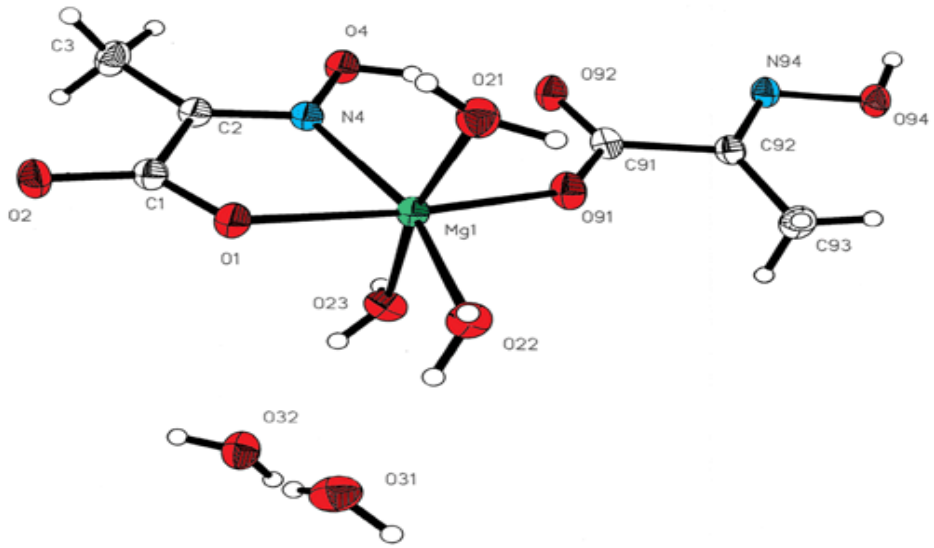

Figure 2.6. Crystal structure of $Mg(PAO)_2(H_2O)_3\cdot 2H_2O$

Table 2.7. Bond Distances (Å) for $Mg(PAO)_2(H_2O)_3\cdot 2H_2O$

Mg(1)—O(1)	2.114(3)	Mg(1)—N(4)	2.217(3)
Mg(1)—O(91)	2.061(3)	Mg(1)—O(21)	2.075(3)
Mg(1)—O(22)	2.058(3)	Mg(1)—O(23)	2.066(3)
O(1)—C(1)	1.259(3)	O(2)—C(1)	1.264(2)
C(1)—C(2)	1.524(3)	C(2)—C(3)	1.472(4)
C(2)—N(4)	1.297(2)	N(4)—O(4)	1.385(3)
O(91)—C(91)	1.268(3)	O(92)—C(91)	1.242(3)
C(91)—C(92)	1.529(3)	C(92)—C(93)	1.486(4)
C(92)—N(94)	1.289(3)	N(94)—O(94)	1.416(3)

Numbers in parentheses are estimated standard deviations in the least significant digits.

Moreover, the magnesium-oxygen atom of the deprotonated hydroxyl group of the carboxyl moiety, Mg(1)—O(1), having a bond length of 2.114(3) Å, is also much smaller than those published for both sodium[14] and calcium[6] derivatives (2.490(2),[14] and 2.513(1)[6] Å, respectively). The smaller bond lengths of M—N and M—O (M = Na, Ca, or Mg) observed for the so-formed N,O-chelate five-membered ring in the Mg derivative reflect the smaller size of the hexa-coordinated Mg^{2+} (0.720 Å)[80] in comparison to the equal size (1.12 Å)[80] of the hepta-coordinated Na^{1+} and the octa-coordinated Ca^{2+}. Moreover, the different coordination environment and number of each metal cation, and the different ligating modes adopted by PAO^- in each salt play a role. The carboxyl group of the N,O-chelate PAO^- in the magnesium salt has almost equal C—O bond lengths, O(1)—C(1) = 1.259(3) Å & O(2)—C(1) = 1.264(2) Å, indicating the full delocalization of the negative charge on the carboxylate moiety. Comparing these bond distances with typical C—O (1.36 Å), and C═O (1.23 Å) bond lengths demonstrates that carboxylate carbon-oxygen bonds have intermediate distances between the single and double carbon-oxygen bond lengths.[81] This affirms the deduction of the complete negative charge delocalization. A similar full delocalization of the negative charge of the carboxylate moiety of the N,O-chelate PAO^- was also observed earlier in the $Na(PAO)\cdot H_2O$ salt.[14,15] The values of the bond lengths for the rest of the bonds in the five-membered ring are 1.524(3), 1.472(4), 1.297(2), and 1.385(3) Å for C(1)—C(2), C(2)—C(3), C(2)—N(4), and N(4)—O(4), respectively. These are also similar to those reported for the PAO^- complexes of Na^{1+} (1.515(2), 1.487(2), 1.281(2), and 1.396(2) Å, respectively),[14] Ca^{2+} (1.624(2), 1.487(3), 1.275(2), and 1.392(2) Å, respectively),[6] Ni^{2+} (1.50(2), 1.47(2), 1.28(2), and 1.38(1) Å, respectively),[21] and Cu^{2+} (1.49(1), 1.47(1),

1.27(1), and 1.360(8) Å, respectively).[20] The similarity between each of these bonds suggests that the different metal ion centers have only a slight effect on the geometry of the N,O-chelated PAO^- ligand.

The Mg^{2+} ion center has a distorted octahedral environment due to the N,O-chelate adopted by one of the PAO^- ligand to create a five-membered metallacycle, leading to decline of the O(1)—Mg(1)—N(4) angle from 90° to *ca*. 74.0(1)° (see Table 2.8), which in turn reflects the rigidity of the O═C—C═N fragments of the PAO^- ion.[18] This bite angle of N,O-chelate PAO^- is larger than those observed in sodium[14] and calcium[6] derivatives [64.08(5),[14] and 62.28(5)°,[6] respectively], and similar to that observed in Ni^{2+} related complex [76.8(3)°],[21] but smaller than those noticed in the relevant $Co^{3+}(Im)_2$,[18] $Co^{3+}(Py)_2$,[18] and Cu(II)[20] complexes [83.46(7),[18] 82.78(5),[18] and 82.0(2)°,[20] respectively]. The metallacycle atoms are almost coplanar, as can be inferred from the angles around each corner atom (N(4), C(2), C(1), and O(1)) forming the metallacycle. The angles around the C(91), the carbon atom of the carboxylate moiety of the monodentate PAO^- have the values of 118.1(2)°, 117.1(2)°, and 124.7(2)°, which makes the bonds around the C(91) center almost coplanar. The bonds around the C(92), the carbon atom of the oximino moiety of the monodentate PAO^-, are also almost coplanar because of the angles of 115.5(2)°, 118.4(2)°, and 126.1(2)°. As a consequence, the carboxylate and oximino moieties of the monodentate PAO^- are coplanar. The other angles around the Mg^{2+} ion center vary from 86.3(1)° to 172.8(1)° reflecting the distortion of the octahedral sphere around the magnesium.

Table 2.8. Interbond Angles (^{o}) for $Mg(PAO)_2(H_2O)_3 \cdot 2H_2O$

O(1)—Mg(1)—N(4)	74.0(1)	O(1)—Mg(1)—O(91)	172.8(1)
N(4)—Mg(1)—O(91)	98.9(1)	O(1)—Mg(1)—O(21)	93.8(1)
N(4)—Mg(1)—O(21)	97.7(1)	O(91)—Mg(1)—O(21)	86.3(1)
O(1)—Mg(1)—O(22)	89.2(1)	N(4)—Mg(1)—O(22)	162.8(1)
O(91)—Mg(1)—O(22)	98.0(1)	O(21)—Mg(1)—O(22)	86.5(1)
O(1)—Mg(1)—O(23)	94.5(1)	N(4)—Mg(1)—O(23)	91.4(1)
O(91)—Mg(1)—O(23)	86.4(1)	O(21)—Mg(1)—O(23)	169.1(1)
O(22)—Mg(1)—O(23)	86.5(1)	Mg(1)—O(1)—C(1)	119.6(1)
O(1)—C(1)—O(2)	124.3(2)	O(1)—C(1)—C(2)	116.4(1)
O(2)—C(1)—C(2)	119.3(2)	C(1)—C(2)—C(3)	120.4(1)
C(1)—C(2)—N(4)	113.8(2)	C(3)—C(2)—N(4)	125.7(2)
Mg(1)—N(4)—C(2)	116.0(1)	Mg(1)—N(4)—O(4)	128.2(1)
C(2)—N(4)—O(4)	115.7(2)	Mg(1)—O(91)—C(91)	140.0(2)
O(91)—C(91)—O(92)	124.7(2)	O(91)—C(91)—C(92)	117.1(2)
O(92)—C(91)—C(92)	118.1(2)	C(91)—C(92)—C(93)	118.4(2)
C(91)—C(92)—N(94)	115.5(2)	C(93)—C(92)—N(94)	126.1(2)
C(92)—N(94)—O(94)	113.8(2)		

Numbers in parentheses are estimated standard deviations in the least significant digits.

The unit cell contains two $Mg(PAO)_2(H_2O)_3$ complexes connected via two intermolecular hydrogen-bonds between the N,O-chelate PAO^- carboxylate oxygen atom [O(1)]. The latter is attached to a magnesium ion center of one complex molecule, and a proton of the water molecule, which is marked by O(22) coordinated to the magnesium center on the other complex molecule as illustrated by dashed lines in the following Figure 2.7:

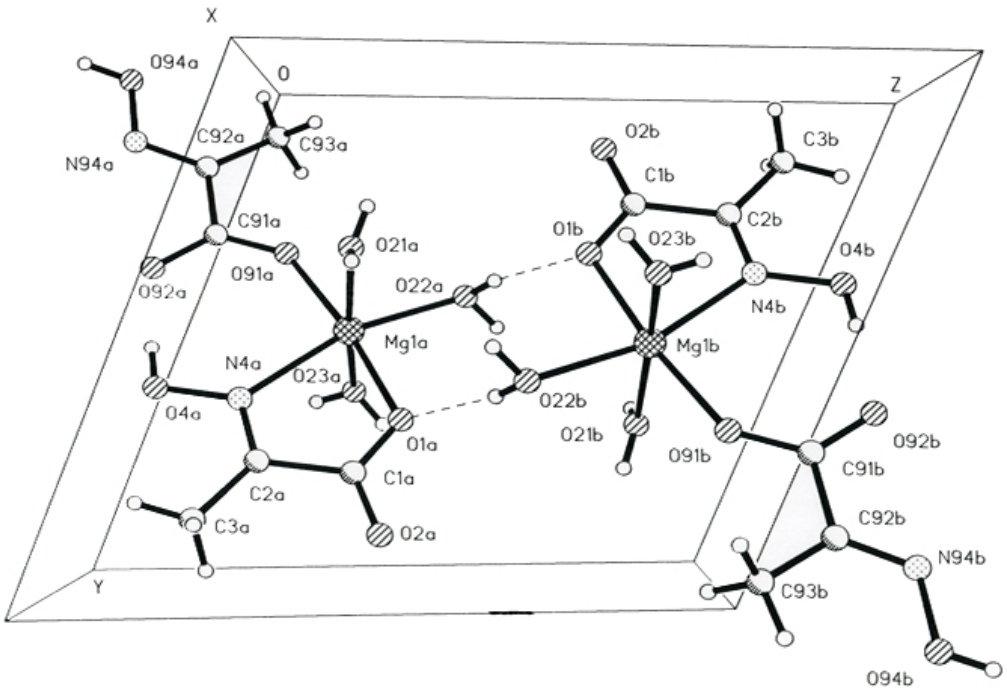

Figure 2.7. A view of the unit cell contents of $[Mg(PAO)_2(H_2O)_3]$ complex molecules joined by hydrogen bonds, denoted by the dashed lines

As shown in Figure 2.7, there are two ancillary water solvent molecules for each complex molecule occupying the available voids in the unit cell, and forming hydrogen bonds between the two complex molecules contained within the unit cell. These water molecules also form hydrogen bonds that join the complexes within the unit cell to complexes in the adjacent unit cells. Each complex in the unit cell is also linked to another complex in a neighboring unit cell via two hydrogen bonding connections between a water molecule ligating to the adjacent magnesium ion center of a complex and the monodentate PAO^- carboxylate oxygen atom that is not bonded to the magnesium ion center in the other complex molecule in the adjacent unit cell. The resultant of this hydrogen bond is an extended 3-dimensional network, as depicted in Figure 2.8.

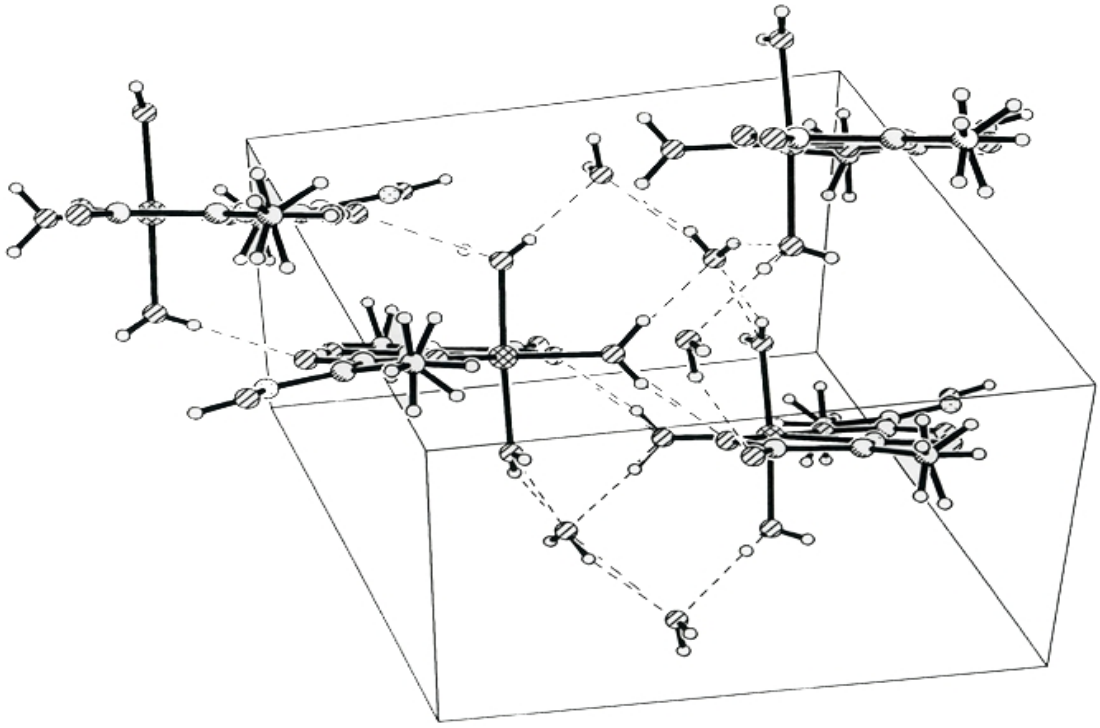

Figure 2.8. Hydrogen-bonded $[Mg(PAO)_2(H_2O)_3 \cdot 2H_2O]$ units within the unit cell and adjacent unit cells. The dashed lines represent the hydrogen-bonds

Spectroscopic Characterization of PAO^- Salts of Main Group Elements

Both IR and solid-state ^{13}C NMR spectroscopy techniques were utilized to describe the main group element salts of PAO^- prepared in this investigation. The important distinguishing IR vibrational frequencies are displayed in Table 2.9. The bands attributable to the vibrational frequencies of C═N and N—O groups were identified on the basis of earlier work by Russian scientists[20-21] who synthesized HPAO and PPAO enriched with the ^{15}N isotope, which caused splitting of the $\nu_{(C=N)}$ band at 1660 cm^{-1} into two bands at 1660 cm^{-1} and 1645 cm^{-1} in the IR spectra of both α-oximinocarboxylic acids. The $\nu_{(N—O)}$ at 1045 cm^{-1} for HPAO was split into two bands at 1045 cm^{-1} and 1030 cm^{-1}, and the $\nu_{(N—O)}$ at 1023 cm^{-1} for PPAO was split into two bands at 1023 cm^{-1} and

1008 cm^{-1}. A remarkable character of the IR spectra of PAO^- salts is that the asymmetric stretch of the carboxylate group decreases significantly by 72-76 cm^{-1} and its symmetric

Table 2.9. Distinctive IR Vibrational Frequencies (cm^{-1}) of the Salts of Main Group Elements of PAO^-

Compound	$\nu_{(C=N)}$	$\nu_{as(COO)}$	$\nu_{s(COO)}$	$\Delta\nu_{(COO)}$[a]	$\nu_{(N-O)}$
HPAO[b]	1654 (1652)	1695 (1696)	1420 (1420)	275 (276)	1043 (1048)
$Mg(PAO)_2(H_2O)_3\cdot 2H_2O$[c]	1672 (1674)	1623 (1647)	1370 (1394)	253 (253)	1063 (1045)
$HOAl(PAO)_2\cdot 2H_2O$[d]	1684 (1692)	1653 (1654)	1368 (1366)	285 (288)	1091 (1041)
$Pb(PAO)_2\cdot 2H_2O$[d]	1660 (1664)	1619 (1619)	1394 (1399)	225 (220)	1035 (1033)
$Na(PAO)\cdot H_2O$[b]	1661	1599	1375	224	1008
$Ca(PAO)_2\cdot 2H_2O$[c]	1675	1617 1640	1386 1418	231 222	1038

[a] $\Delta\nu(COO) = \nu_{as}(COO) - \nu_s(COO)$. [b] Values in parenthesis are from reference 14

[c] Values for $Mg(PAO)_2\cdot 2H_2O$ are from reference 6

[d] Values for $Al(PAO)_3\cdot EtOH$ and for $Pb(OH)(PAO)\cdot 1.89H_2O$ are from reference 15

Vibration stretch by 21-54 cm^{-1} in comparison to the parent acid, HPAO

These observations, which are common for the carboxylates of metals,[82] are attributed to the deprotonation, delocalization of the negative charge in the carboxylate moiety and its coordination to the metal center. The stretching vibrations of C═N groups in these salts, where the metal ion center is bonded to the nitrogen atom of the oximino group of PAO^-, are comparable to those observed in the protonated form of PAO^-,[14] which agrees with the data reported previously for the light alkali metal (Li, Na, and K),[14] alkaline earth metal,[6] and the divalent 3d transition metal (Mn, Co, Ni, Cu, Zn) salts of PAO^-.[23] The $\nu_{(N—O)}$ stretching frequency increases by 20-48 cm^{-1} except for the lead

derivative in which the corresponding frequency declines slightly by 8 cm^{-1}, as compared to that observed for the parent acid, HPAO. The observed increase in the $\nu_{(N—O)}$ frequency stretch is similar to that observed for the some of the first row transition metal PAO^- complexes[23] but is opposite the trend realized for the alkali[14] and the earth alkaline[6] metal derivatives, in which a decrease in this frequency is observed. The lowering of the $\nu_{(N—O)}$ frequency stretch observed in the lead compound may be ascribed to the weak coordination of the oximino nitrogen atom to the metal ion center, similar what was observed for the alkali[14] and earth alkaline[6] salts. The existence of IR absorption bands in the 820-860 cm^{-1} region are assigned to the vibrations of water molecules coordinated to the metal ion center,[23] while the broad bands at higher wave number than 2600 cm^{-1} are suggestive of the existence of hydrogen bonds in the crystalline structure[23] of these compounds in Table 2.9. Such conclusions regarding the coordinated water molecules to the metal ion center and hydrogen bonds on the basis of IR spectra are evidenced by the crystal structure of $Mg(PAO)_2(H_2O)_3 \cdot 2H_2O$ (see p. 54).

The difference between the asymmetric and symmetric stretching frequencies of the carboxylate group, $\Delta\nu_{(COO)}$, is a function of the coordination modes (monodentate, chelate, and bridging) of the carboxylate.[83] The monodentate mode usually has the highest $\Delta\nu_{(COO)}$. For the PAO^- ligand, this remains true, the $\Delta\nu_{(COO)}$ was found to descend as follows:[7]

$$\text{monodentate, bridging, chelate} \xrightarrow[\text{decreasing of } \Delta\nu_{(COO)}]{}$$

The monodentate has a $\Delta\nu_{(COO)} > 250$ cm^{-1}, the bridging has $225 < \Delta\nu_{(COO)} < 250$, and the chelate has a $\Delta\nu_{(COO)} < 200$ cm^{-1}. On this basis, it can be concluded that the PAO^-

ligand carboxylate group adopts a monodentate configuration in coordination in both of its salts of magnesium and aluminum, while it is bridging in the lead compound. This inference, based on the IR spectra, concerning the coordination mode of carboxylate, is consistent with the X-ray single crystal structural determination of $Mg(PAO)_2(H_2O)_3 \cdot 2H_2O$ (see p. 54), which revealed that the carboxylate groups of both of the PAO^- ligands are monodentate. However, one PAO^- ligand also chelates to the Mg^{2+} ion center with its oximino nitrogen atom. The IR spectrum shows only one set of asymmetric and symmetric stretches of the carboxylate group (Table 2.9), which may be assigned to the N, O-chelate PAO^- because they are close to the frequencies observed in the calcium[6] and sodium[14] derivatives with the same type of chelate. The stretches corresponding to the PAO^- group, which is only attached to Mg^{2+} through its carboxylate moiety in a monodentate fashion, are not distinguishable in the IR, presumably because they lie very close to the bands of the carboxylate of the N, O-chelate PAO^-, and hence require an IR instrument with a higher resolution to separate these bands. The $\nu_{as(COO)}$ observed for the aluminum salt is higher than the corresponding frequency observed in compounds having N,O-chelate PAO^- by 30-54 cm^{-1}, which indicates that the PAO-ligand is only attached to Al^{3+} through the oxygen atom of the deprotonated hydroxyl of the carboxylate moiety as also concluded from the $\Delta\nu_{(COO)}$. This is, in addition, supported by the result obtained by the solid state ^{13}C NMR CPMAS spectroscopy (see p. 63). Accordingly, a possible structure of the aluminum compound can be proposed as follows in Figure 2.9:

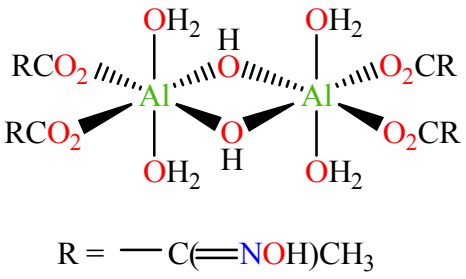

Figure 2.9. A suggested structure of $HOAl(PAO)_2 \cdot 2H_2O$

The $\nu_{as(COO)}$ observed for the lead salt, on the other hand, is similar to those observed in sodium[14] and calcium[6] salts, which implies that the PAO^- is coordinated to the lead ion center as an N,O-chelate. The other oxygen of the carboxylate moiety is attached to a neighboring lead ion center, serving as a bridge between two Pb^{2+} ions.

The solid state ^{13}C NMR CPMAS spectra are very instructive because the chemical shifts are quite sensitive to the local electron density changes in the PAO^- ligand, resulting from the deprotonation of the HPAO and the coordination mode of PAO^- to the metal ion center. Moreover, this spectroscopic technique is capable of resolving the peaks, owing to the existence of various binding modes of the carboxylate moiety. The chemical shifts for each compound are given in Table 2.10. The solid-state ^{13}C chemical shifts for HPAO are similar to those obtained from liquid $^{13}C\{^1H\}$ NMR using dimethyl-d_6 sulfoxide as a solvent. The methyl carbon, which has a chemical shift range from 8.4 to 13.9 ppm, is slightly influenced by the deprotonation of HPAO and the coordination of PAO^- to the metal ion center, as indicated by shifting of its signal upfield by 1.9-3.0 ppm and downfield by 0.0-2.5 ppm from the corresponding peaks of HPAO (11.4 ppm). However, both of the oximino and carboxylate carbons have chemical shifts that are more affected by the deprotonation and complexation. The signal of the oximino carbon is

shifted downfield by 3.0-10.7 ppm in comparison to that of HPAO resonance at 149.0 ppm. In contrast, the peak of the carboxylate carbon is shifted downfield by 1.9-6.2 ppm with respect to the HPAO resonance at 167.0 ppm. The ^{13}C NMR CPMAS spectrum of $Mg(PAO)_2(H_2O)_3 \cdot 2H_2O$ is in accordance with its X-ray structure determination in that it displays two sets of peaks due to the existence of two different ligating PAO^- carboxylates.

Table 2.10. Solid-State ^{13}C NMR CPMAS Chemical Shifts (ppm) of the Salts of Main Group Elements of PAO^-

Compound	CH_3	C=N	COO
HPAO[a]	11.4 (10.9)	149.0 (148.9)	167.0 (166.0)
$Mg(PAO)_2(H_2O)_3 \cdot 2H_2O$	9.5, and 11.5	154.2	170.1, and173.2
$HOAl(PAO)_2 \cdot 2H_2O$	8.4	152.0	168.9
$Pb(PAO)_2 \cdot 2H_2O$	11.4,12.2, and 13.9	155.4, and159.7	170.1
$Na(PAO) \cdot H_2O$[b]	12.2	153.5	171.7
$Ca(PAO)_2 \cdot H_2O$[c]	11.4, and 12.1	153.5	168.6, and 171.6

[a]Values for HPAO $^{13}C\{^1H\}$ NMR (DMSO-d_6) referenced to TMS in parenthesis are from reference 14.
[b]From reference 14.
[c]From reference 6.

Two peaks at 9.5 ppm and 11.5 ppm are assigned to two methyl carbon atoms residing in two different electronic environments. A set of double peaks are also observed for the two carboxylate carbons at 170.1 ppm and 173.2 ppm. However, there is only one peak for the oximino carbons at 154.2 ppm. The signals at 11.5 ppm and 173.2 ppm may be assigned to the N,O-chelate PAO^- due to their similarity to those observed in

the sodium[14] salt of PAO^- (12.2 and 171.7 ppm, respectively) and those noticed in the calcium[6] derivative (12.1 and 171.6 ppm, respectively). Hence, the signals at 9.5 ppm and 170.1 ppm can be assigned to the monodentate PAO^- ligand. The carbons of the oximino groups have their signals unresolved, probably because of their high electronic asymmetry and interaction with quadrapolar ^{14}N, which leads to one broad signal.[6] The ^{13}C NMR CPMAS spectrum of $HOAl(PAO)_2 \cdot 2H_2O$ consists only of one set of signals that indicates the existence of one type of monodentate of PAO^- coordinated to the Al^{3+} ion center. The chemical shifts are not similar to those observed for the compounds containing the N, O-chelate PAO^- ligand type, especially the methyl carbon which has a peak shifted upfield from that of the parent acid. The carboxylate carbon has a chemical shift close to that of the free acid. On the other hand, the chemical shifts of aluminum salts are similar to those for the monodentate PAO^- carboxylate in the magnesium salt. Therefore, it can be inferred that the PAO^- carboxylate is monodentate in the aluminum salt, suggesting the structure shown in Figure 2.9 (see p. 63). The ^{13}C NMR CPMAS spectrum of $Pb(PAO)_2 \cdot 2H_2O$ is complicated compared to the spectrum of the other compounds prepared in this investigation. The spectrum of the lead compound is composed of three signals assigned to the methyl carbons, two signals of the oximino carbons, and one signal to the carboxylate carbons. Accordingly, the methyl carbons are found in three different electronic environments, and the oximino carbons exist in two different electronic environments, while the carboxylate carbons lie in similar electronic environment. The chemical shifts at 12.2 ppm and 155.4 ppm for the methyl and oximino carbons, respectively, are close to those observed for the sodium[14] and calcium[6]

derivatives. This may imply that this PAO^- is the N, O-chelate type with its second carboxylate oxygen bridging adjacent lead ions.

Thermal Behavior of PAO^- Salts of Main Group Elements

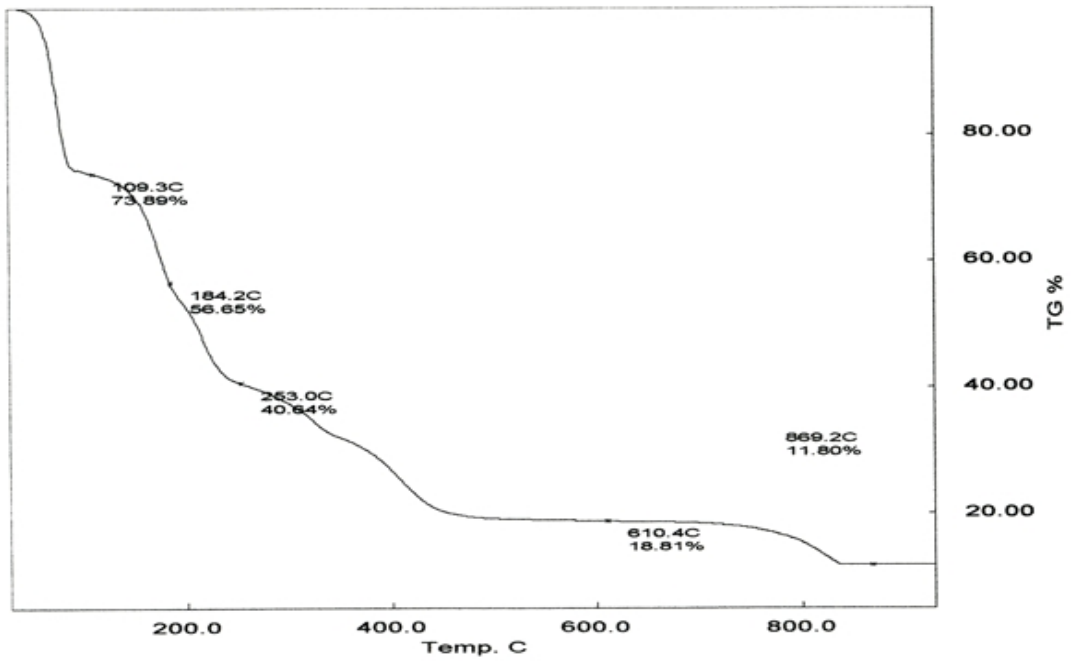

Figure 2.10. The TGA trace for $Mg(PAO)_2(H_2O)_3 \cdot 2H_2O$, contaminated with NaCl, in dry air with a heating rate of 1 ^oC/min

Figure 2.10 displays the TGA of $Mg(PAO)_2(H_2O)_3 \cdot 2H_2O$, contaminated with NaCl. The TGA trace is made up of seven steps leading to weight loss. The first weight change step, beginning at around 60^{o}C, corresponds to a loss of four water molecules. The same weight loss was observed upon drying the magnesium salt under vacuum for 3 nights or dehydrating at 80^{o}C. The IR spectra of the products from both dehydration experiments still showed distinctive bands for the PAO^- ligand, indicating that the ligand was un-decomposed during dehydration. The second step, with a start at 110^{o}C, is a complete dehydration of the salt and the beginning of the destruction of the ligand as indicated by the mass loss and the IR analysis of the decomposition product obtained

after heating at 175°C. The successive step has an onset at 200°C and results in formation of carbonate as can be inferred from the weight change. The IR spectra of the solid products at 220°C and 250°C are similar to that published for authentic sample of magnesium carbonate.[84] The formation of magnesium carbonate was also confirmed by the evolution of bubbles of CO_2 gas when the 250°C decomposition product was treated with concentrated HCl. This observation is in agreement with the previous study of the thermal pyrolysis of $Mg(PAO)_2 \cdot 2H_2O$ to magnesium carbonate.[6] Moreover, it was shown that the entire alkali and alkaline earth PAO^- derivatives decompose to their corresponding carbonates.[6,14] The next step in the pyrolysis is the decomposition of the magnesium carbonate to give magnesium oxide that starts around 400°C. The formation of magnesium oxide is evidenced by the mass loss and by the IR analysis of the decomposition product obtained at 450°C. The last step in the TGA trace is due to calcination of MgO and existence of the halide phase of sodium chloride. The MgO obtained at 500, 600, 700, 800, and 900°C was white, and crystalline, as indicated by XRD analysis. However, the crystalline MgO was contaminated with NaCl, as indicated by the XRD pattern of the pyrolysis product obtained at 600°C. The MgO was found to be nanocrystalline, as revealed by XRD measurements of crystallite size. The MgO obtained at 500, 600, and 900 °C had an average crystallite size of 3.8, 6.2, and 90.1 nm, respectively, with a maximum of relative frequency of 2.2, 28.7, and 46.9 nm, respectively.

The TGA diagram of pure $Mg(PAO)_2(H_2O)_3 \cdot 2H_2O$ derived from $Mg(OH)_2$ is depicted in Figure 2.11. It can be seen that the TGA trace is composed of three weight-loss steps. The first one has an offset at 51°C, corresponding to complete dehydration of

the magnesium salt, i.e. a loss of five water molecules as deduced from the percentage of mass remained at 113^{o}C. However, existence of sodium chloride does not allow for this whole dehydration of the magnesium salt, but rather only four water molecules are lost as explained above. The material obtained upon heating to 113^{o}C was found to be crystalline as proved by XRD analysis. The XRD pattern of this anhydrous material is different from that of the starting magnesium PAO^{-} salt, implying a change in the crystalline phase upon dehydration. In addition, the ^{13}C NMR CPMAS of the anhydrous phase of magnesium PAO^{-} supported the result from XRD analysis. The chemical shifts are dramatically shifted upfield, comparing to those of the hydrous form of magnesium PAO^{-} salt. Therefore, it can be inferred that dehydration led to a crystalline structure which made all the carbons of the PAO^{-} ligand resided in more shielded electronic environment. The methyl carbon atoms are observed at -2.8 and -0.1 ppm, indicating the existence of two different methyl side groups of the two PAO^{-} ligands. The carboxylate carbons have a peak at 159.3 ppm. The signal of the oximino carbons is broad and located at 143.4 ppm. This broadness can be ascribed to the interacation with quadrapolar ^{14}N and to their high electronic asymmetry.

The second step starts around 150^{o}C and it is due to the decomposition of the two PAO^{-} ligands to give magnesium carbonate as indicated by the weight% remained at 304 ^{o}C. The last step is ascribed to the decomposition of magnesium carbonate to yield magnesium oxide at 399^{o}C. XRD analysis of the magnesium oxide obtained at the latter temperature revealed the existence of a nanocrystalline phase with an average of crystallite size of 2.2 nm and maximum of relative frequency of 1.3 nm.

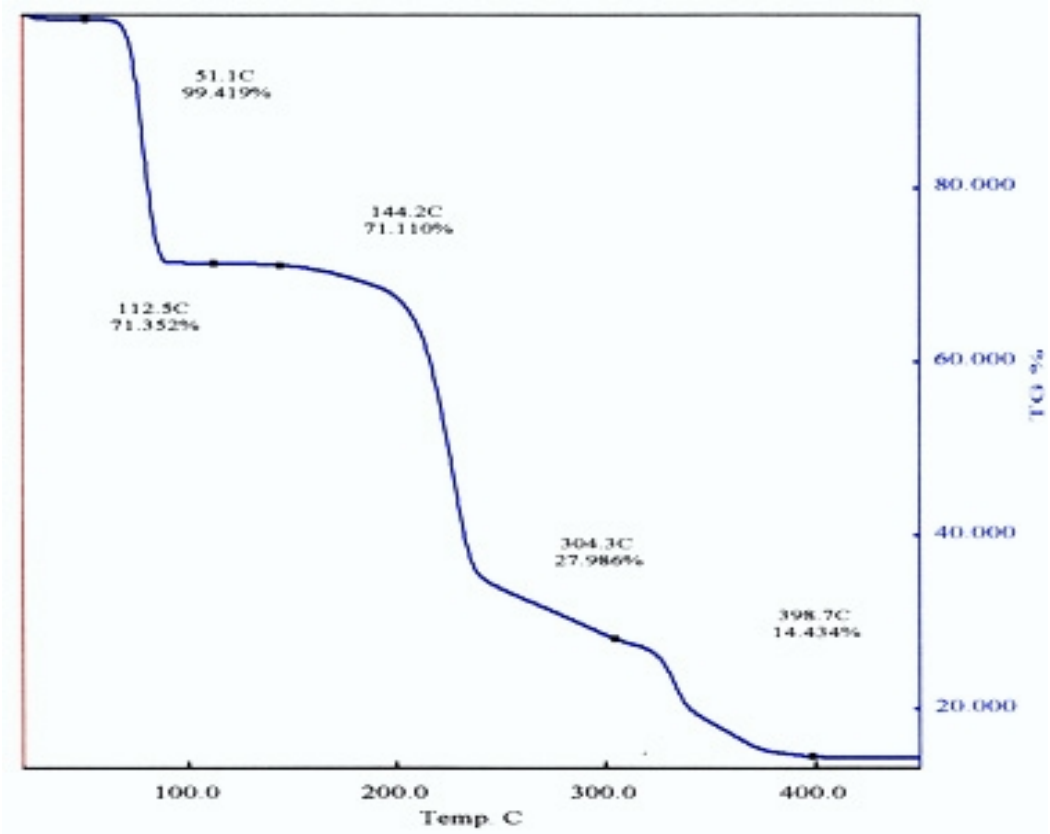

Figure 2.11. The TGA trace for pure $Mg(PAO)_2(H_2O)_3 \cdot 2H_2O$ in dry air with a heating rate of 1 ^oC/min

The thermal behavior of the aluminum PAO^- salt differs markedly from that exhibited by the magnesium salt. The aluminum salt does not thermally decompose in stepwise fashion, but rather it decomposes in one step (Figure 2.12) to produce nanocrystalline, amorphous, aluminum oxide (alumina) at 300^{o}C, as confirmed by XRD analysis and a morphology study by SEM (Figure 2.13). The weight loss of the salt when heated to 100^{o}C corresponds to dehydration (see the pyrolysis part of the Experimental section of this chapter). The IR spectrum of the product obtained at this temperature indicates the existence of PAO^- ligand. Heat treatments of the salt at 125^{o}C, 150^{o}C, 200^{o}C, and 250^{o}C cause the decomposition of the PAO^- ligand as can be inferred from the weight change observed from bulk pyrolysis. The XRD pattern of the product

obtained at 150°C produced a non-crystalline substance. The product obtained at 450°C was alumina as confirmed by the weight loss. The XRD spectrum of the product obtained at 400°C consists of very broad peaks, an indication of a nanocrystalline phase, that matches alumina with a primitive, orthorhombic (a = 7.934, b = 7.956, and c = 11.711 Å) unit cell.

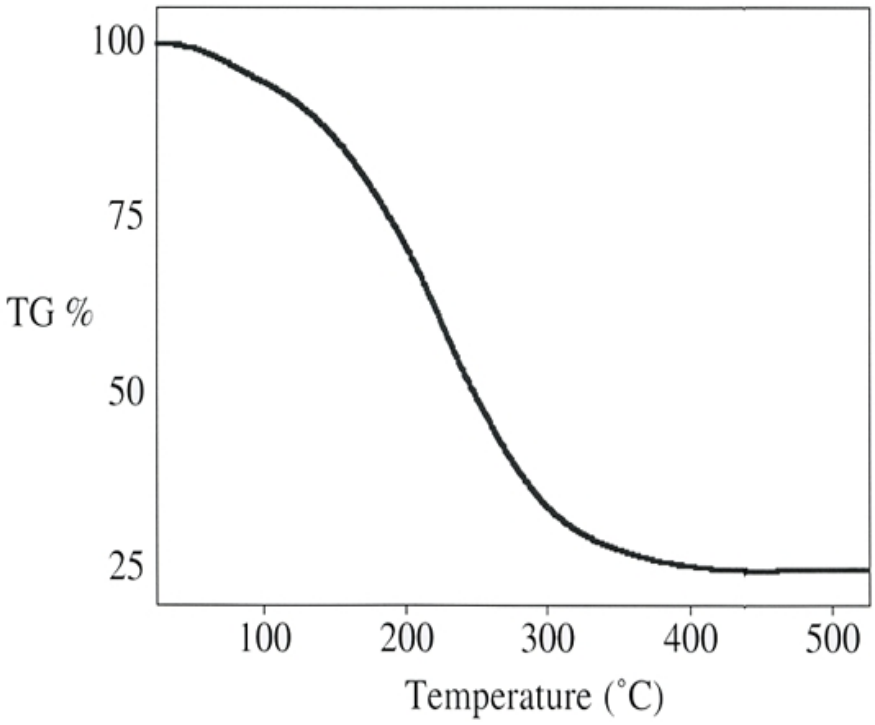

Figure 2.12. The TGA trace for $HOAl(PAO)_2 \cdot 2H_2O$ in dry air with a heating rate of 1 °C/min

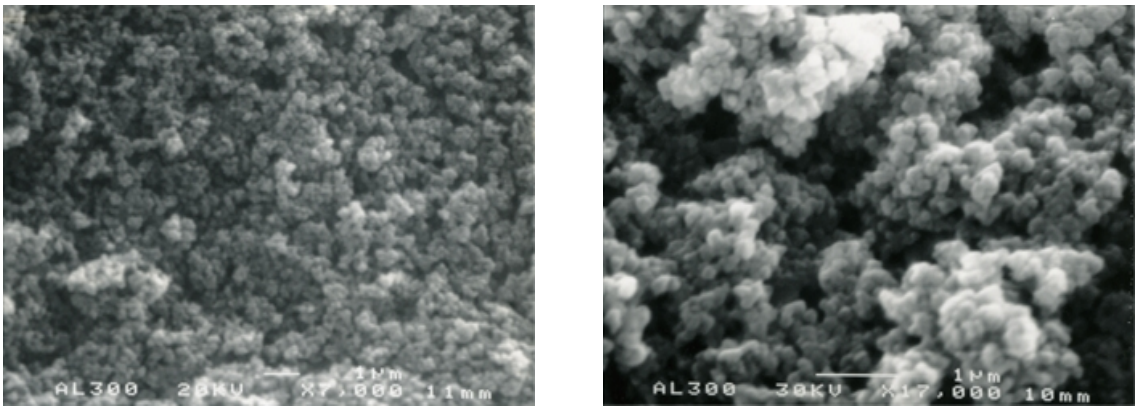

Figure 2.13. SEM electromicrographs of $HOAl(PAO)_2 \cdot 2H_2O$ heated to 300 ^oC

Surprisingly, heating the aluminum salt to 600^{o}C, led to the formation of an alumina phase with cubic unit cell (a transition alumina) and broad peaks, suggesting the presence of nanocrystalline material. On the other hand, corundum alumina phase was obtained upon calcinations at 900^{o}C, and the XRD pattern peaks were sharp, implying a highly crystalline material (see Figure 2.14).

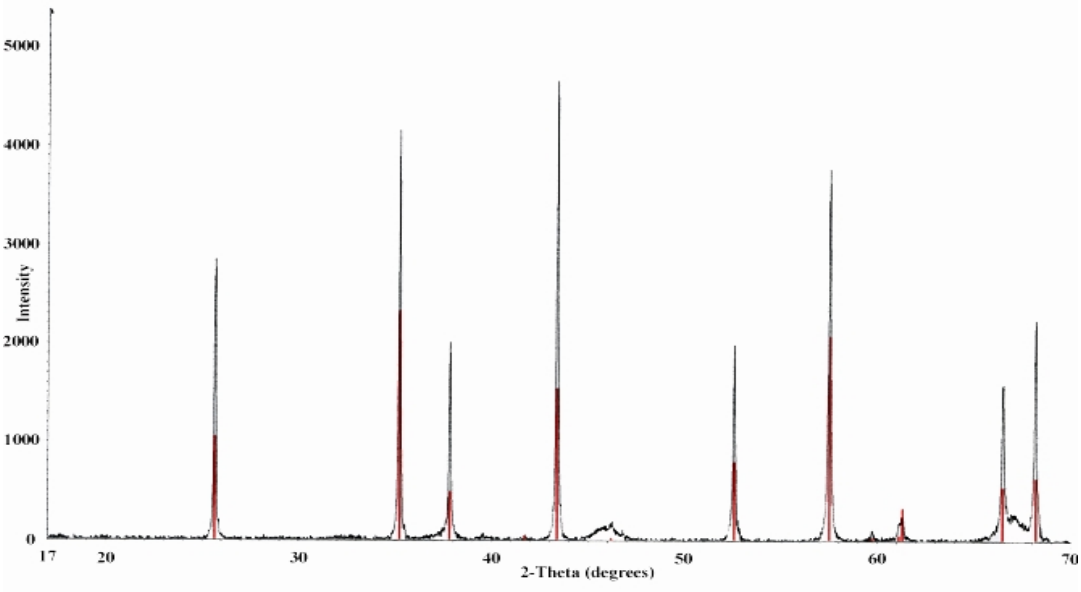

Figure 2.14. The XRD pattern of $HOAl(PAO)_2 \cdot 2H_2O$ calcined at 900 ^oC

Textural and Surface Acid-Base Properties of Main Group Element Oxides

Table 2.11 summarizes the chemical and textural properties of MgO obtained from pyrolysis of $Mg(PAO)_2(H_2O)_3{\cdot}2H_2O$ at 900 ^oC and compares them to data for MgO produced from other sources.[77,85] The specific surface area in m^2/g is denoted by S_{BET}, while both of acidity and basicity are given in units of μmol/g. Division of the values of acidity and basicity by the S_{BET} gives the acidity and basicity per surface area (μmol/ m^2).

The MgO obtained from the sintering of commercially available $Mg(OH)_2$ source has a surface area that is 10 to 11 times as large as those of MgO yielded from the calcination of $Mg(PAO)_2(H_2O)_3{\cdot}2H_2O$ and $Mg_4(OH)_2(CO_3)_3{\cdot}3H_2O$. The latter sources, however, gave MgO with comparable surface areas upon pyrolysis. All of the three sources, on the other hand, lead to the formation of MgO with predominantly basic surfaces. This is due to the presence of the strong Brønsted and Lewis base oxide-sites. Of course, the weakness of the Mg^{2+} ions as Lewis acids is known.[86] The basicity of MgO is demonstrated by its ability to deprotonate water molecules (Eq. 2.6):

$$MgO + H_2O \longrightarrow Mg(OH)_2 \qquad \text{(Eq. 2.6)}$$

The MgO derived from the $Mg(OH)_2$ has the largest number of basic sites per mass unit, which is almost 9 and 5 times of those of MgO produced from the PAO and carbonate sources, respectively. The basic carbonate produced MgO with surface basic site populations per gram almost twice the amount of PAO-derived MgO. However, the basicity is best compared as a function of surface area. The MgO derived from the basic carbonate has the largest population of surface basic sites, 1.6 to 2 times as large as those of MgO from the other two sources. The number basic sites of the MgO from $Mg(PAO)_2$

source is higher than those of the MgO derived from the $Mg(OH)_2$ by around 20%. The variations in these textural and acid-base features for the magnesium oxides produced in each case are attributed to chemical differences among the sources and the heat treatment that the precursor was subjected to give the final desired oxide.

Table 2.11 . Chemical and Textural Properties of MgO

Source of MgO	Calcination Temperature (^oC)	S_{BET} (m^2/g)	Acidity (μmol/g)	Basicity (μmol/g)	Acidity (μmol/ m^2)	Basicity (μmol/ m^2)	References
$Mg(PAO)_2(H_2O)_3 \cdot 2H_2O$	900	21.75		28.7		1.32	this work
Commercially available $Mg(OH)_2$	500	241	123	254	0.51	1.05	75
Synthesized $Mg_4(OH)_2(CO_3)_3 \cdot 3H_2O$	500	24	< 1	51	< 0.04	2.13	83

The surface area was measured for the alumina product obtained at different calcination temperatures of $HOAl(PAO)_2 \cdot 2H_2O$. The S_{BET} decreases, as expected, with increasing temperature due to sintering of smaller particles to form larger particles or agglomerates. The decline of S_{BET} with the elevation of temperature of calcination is almost linear as illustrated in Figure 2.15.

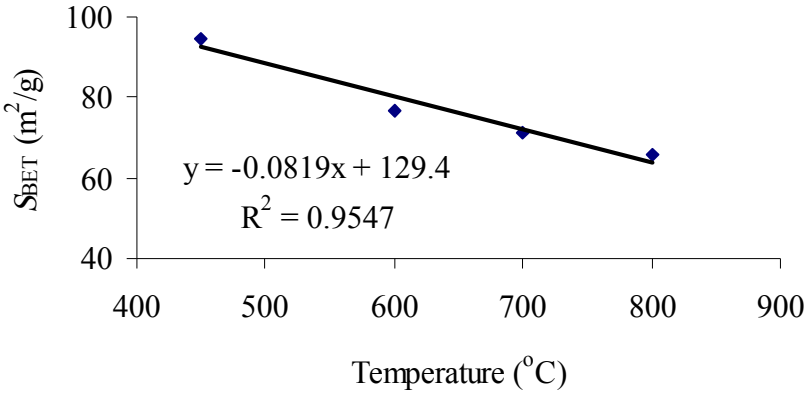

Figure 2.15. Change of S_{BET} with temperature for calcined $HOAl(PAO)_2 \cdot 2H_2O$

PAO^- Salts of Group 12 Metals

A group 12 metal salts of PAO^- were prepared and characterized by spectroscopic methods, including IR, NMR, and by XRD analyses. Each salt had a different XRD pattern indicating that each had a unique structure (Figure 2.16). These structural differences may partially influence the decomposition temperatures (see below for the thermal behavior discussion of these salts). However, $Zn(PAO)_2 \cdot 2H_2O$ has an XRD pattern similar to those of Fe, Co, Ni, and Cu derivatives of PAO^-, implying that all those four complexes are isostructural (see the result and discussion of PAO^- salts of divalent

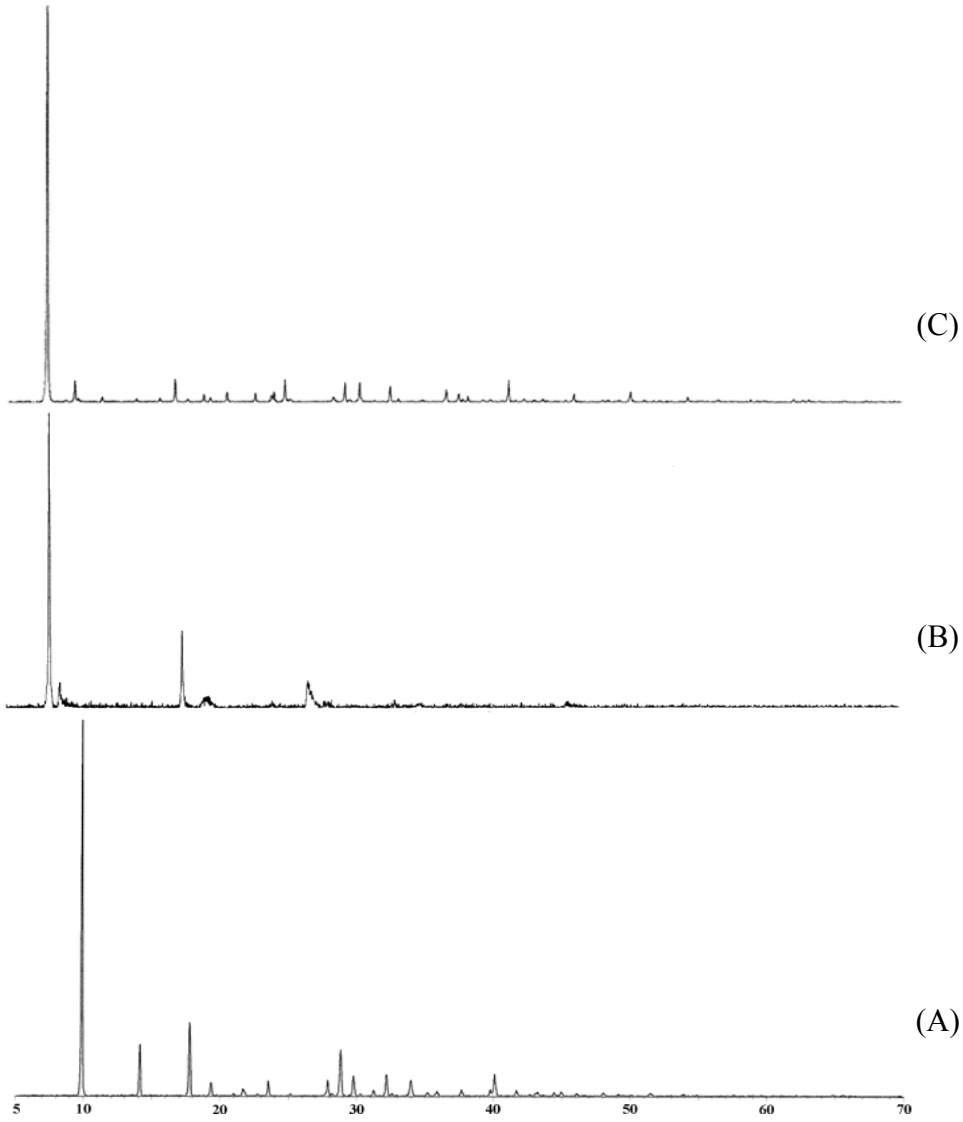

Figure 2.16. The XRD patterns of (A) $Zn(PAO)_2 \cdot 2H_2O$, (B) $Cd(PAO)_2$, and (C) $Hg(PAO)_2$

3d transition metals). This conclusion regarding the structure of zinc complex on the basis of XRD analysis is confirmed by single crystal X-ray determination of its structure. The zinc PAO^- salt structure is illustrated in Figure 2.17.

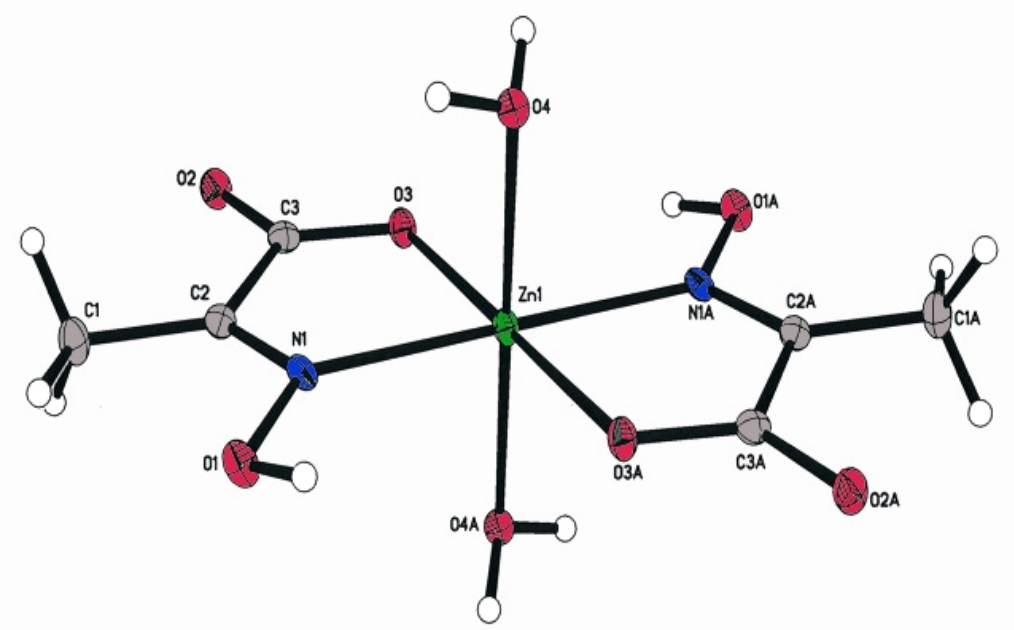

Figure 2.17. Crystal structure of $Zn(PAO)_2 \cdot 2H_2O$ drawn at 50% level

The zinc ion center lies in a pseudo-octahedral environment, i.e. is a six-coordinate, where two coordination sites are occupied by the oxygen atoms of two water molecules with bond length of 2.1746(10) Å corresponding to Zn(1)—O(4)A, and Zn(1)—O(4) (see Table 2.12), which are comparable to those found in zinc acetate dihydrate $[Zn(O_2CCH_3)_2(H_2O)_2]$ where two water molecules are attached to Zn^{2+} at a distance of 1.987 Å.[87] The differences in the Zn—OH_2 bond lengths for the zinc complexes is due to the variation in the distortion of the octahedron environment of the Zn^{2+}, which in turn is a consequence of the different ligands, PAO^- and H_3CCOO^-, the different ligating mode of both ligands and the different natures of the H-bonding in both salts.

Table 2.12. Bond Distances (Å) for $Zn(PAO)_2.2H_2O$

Zn(1)-O(3)	2.0386(11)	O(3)-C(3)	1.2745(19)
Zn(1)-O(3)#1	2.0386(11)	O(4)-H(4D)	0.8772
Zn(1)-N(1)#1	2.1673(13)	O(4)-H(4E)	0.8798
Zn(1)-N(1)	2.1673(13)	N(1)-C(2)	1.2790(19)
Zn(1)-O(4)#1	2.1746(10)	C(1)-C(2)	1.483(2)
Zn(1)-O(4)	2.1746(10)	C(1)-H(1A)	0.9800
O(1)-N(1)	1.3910(15)	C(1)-H(1B)	0.9800
O(1)-H(1)	0.8766	C(1)-H(1C)	0.9800
O(2)-C(3)	1.2321(18)	C(2)-C(3)	1.527(2)

Numbers in parentheses are estimated standard deviations in the least significant digits.
Symmetry transformations used to generate equivalent atoms: #1 -x+1,-y+1,-z+1

The coordination in the zinc sphere of $Zn(PAO)_2(H_2O)_2$ is completed by two ligands of PAO^-, where both of them chelate the zinc center to form a five-membered metallacycle attached through the nitrogen atom, Zn(1)—N(1) and Zn(1)—N(1A), having a distance of 2.1673(13) and through the deprotonated hydroxyl oxygen atom of carboxylate moiety, Zn(1)—O(3) and Zn(1)—O(3A), having a distance of 2.0386(11) Å. These distances are close to that found in zinc acetate dihydrate 2.179(4) and 2.189(5) Å, where the acetate is also coordinated to the Zn^{2+} in a bidentate fashion.[87] This bidentate PAO^- ligand shows partial delocalization of the negative charge because of the slight large difference (0.0424 Å) in the bond length of the two carbon-oxygen bonds of the carboxylate moiety, O(3)—C(3) = 1.2745(19) Å & O(2)—C(3) = 1.2321(18) Å. The

longer distance of the former bond can be ascribed to the fact that O(3) oxygen atom is bonded to the zinc ion center. The PAO^- chelates the zinc center to form a five-membered metallacycle, which is similar to that previously found in the $Na(PAO)\cdot H_2O$,[14] $Ca(PAO)_2\cdot H_2O$,[6] $Ce(PAO)_3$,[1,3] and $Y(PAO)_3(DMSO)(H_2O)\cdot H_2O$[15] structures. However, the bond length of the zinc—oximino nitrogen atom contact, Zn—N, has a bond distance of 2.1673(13) Å that is much smaller than those reported for sodium[14] and calcium[6] derivatives (2.440(2)[14] and 2.503(2)[6] Å, respectively). Also, the oxygen atoms of the deprotonated hydroxyl groups of the carboxyl moieties, Zn(1)—O(3) and Zn(1)—O(3)A, have a bond length of 2.0386(11) Å, which is also much smaller than those published for both sodium[14] and calcium[6] derivatives (2.490(2)[14] and 2.513(1)[6] Å, respectively). The smaller bond lengths of M—N and M—O (M = Na, Ca, or Zn) observed for the so-formed N,O-chelate five-membered ring in the Zn derivative reflect the smaller size of the hexa-coordinated Zn^{2+} (0.740 Å)[80] in comparison to the equal size (1.12 Å)[80] of the hepta-coordinated Na^{1+} and the octa-coordinated Ca^{2+}. Moreover, the different coordination environment and number of each metal cation and the different ligating modes adopted by PAO^- in each salt play a role. The carboxyl group of the N, O-chelate PAO^- in the zinc salt has C—O bond lengths, O(2)—C(3) = 1.2321(18) Å and O(3)—C(3) = 1.2745(19) Å. Comparing these bond distances with typical C—O (1.36 Å), and C═O (1.23 Å) bond lengths demonstrates that carboxylate carbon-oxygen bonds have intermediate distances between the single and double carbon-oxygen bond lengths.[81] The values of the bond lengths for the rest of the bonds in the five-membered ring are 1.483(2),1.527(2), 1.2790(19), and 1.3910(15) Å for C(1)—C(2), C(2)—C(3), C(2)—N(1), and N(1)—O(1), respectively. These are also similar to those reported for the PAO^-

complexes of Na^{1+} (1.487(2), 1.515(2), 1.281(2), and 1.396(2) Å, respectively),[14] Ca^{2+} (1.487(3), 1.624(2), 1.275(2), and 1.392(2) Å, respectively),[6] Ni^{2+} (1.47(2), 1.50(2), 1.28(2), and 1.38(1) Å, respectively),[21] and Cu^{2+} (1.47(1), 1.49(1), 1.27(1), and 1.360(8) Å, respectively).[20] The similarity between each of these bonds suggests that the different metal ion centers have only a slight effect on the geometry of the N,O-chelated PAO^- ligands.

The Zn^{2+} ion center has a distorted octahedral environment due to the N,O-chelate adopted by the PAO^- ligands to create a five-membered metallacycle, leading to decline of the O(3)—Zn(1)—N(1) and O(3)A—Zn(1)—N(1)A angle from 90° to *ca*. 77.34(4)° (see Table 2.13), which in turn reflects the rigidity of the O═C—C═N fragments of the PAO^- ion.[18] This bite angle of N,O-chelate PAO^- is larger than those observed in sodium[14] and calcium[6] derivatives [64.08(5),[14] and 62.28(5)°,[6] respectively], and similar to that observed in Ni^{2+} related complex [76.8(3)°],[21] but smaller than those noticed in the relevant $Co^{3+}(Im)_2$,[18] $Co^{3+}(Py)_2$,[18] and Cu(II)[20] complexes [83.46(7),[18] 82.78(5),[18] and 82.0(2)°,[20] respectively]. The metallacycle atoms are almost coplanar, as can be inferred from the angles around each corner atom (N(1), C(2), C(3), and O(3) and N(1)A, C(2)A, C(3)A, and O(3)A) forming the metallacycle. The other angles around the Zn^{2+} ion center vary from 88.92(4)° to 180.0° reflecting the distortion of the octahedral sphere around the zinc.

Table 2.13. Interbond Angles (^{o}) for $Zn(PAO)_2 \cdot 2H_2O$

O(3)-Zn(1)-O(3)#1	180.0	Zn(1)-O(4)-H(4E)	111.6
O(3)-Zn(1)-N(1)#1	102.66(4)	H(4D)-O(4)-H(4E)	112.3
O(3)#1-Zn(1)-N(1)#1	77.34(4)	C(2)-N(1)-O(1)	114.16(11)
O(3)-Zn(1)-N(1)	77.34(4)	C(2)-N(1)-Zn(1)	114.34(9)
O(3)#1-Zn(1)-N(1)	102.66(4)	O(1)-N(1)-Zn(1)	131.32(9)
N(1)#1-Zn(1)-N(1)	180.0	C(2)-C(1)-H(1A)	109.5
O(3)-Zn(1)-O(4)#1	89.95(4)	C(2)-C(1)-H(1B)	109.5
O(3)#1-Zn(1)-O(4)#1	90.05(4)	H(1A)-C(1)-H(1B)	109.5
N(1)#1-Zn(1)-O(4)#1	91.08(4)	C(2)-C(1)-H(1C)	109.5
N(1)-Zn(1)-O(4)#1	88.92(4)	H(1A)-C(1)-H(1C)	109.5
O(3)-Zn(1)-O(4)	90.05(4)	H(1B)-C(1)-H(1C)	109.5
O(3)#1-Zn(1)-O(4)	89.95(4)	N(1)-C(2)-C(1)	126.84(13)
N(1)#1-Zn(1)-O(4)	88.92(4)	N(1)-C(2)-C(3)	113.92(12)
N(1)-Zn(1)-O(4)	91.08(4)	C(1)-C(2)-C(3)	119.23(12)
O(4)#1-Zn(1)-O(4)	180.0	O(2)-C(3)-O(3)	125.75(14)
N(1)-O(1)-H(1)	107.5	O(2)-C(3)-C(2)	116.97(13)
C(3)-O(3)-Zn(1)	116.99(9)	O(3)-C(3)-C(2)	117.27(12)
Zn(1)-O(4)-H(4D)	108.8		

Numbers in parentheses are estimated standard deviations in the least significant digits.
Symmetry transformations used to generate equivalent atoms: #1 -x+1,-y+1,-z+1

The unit cell contains one $Zn(PAO)_2(H_2O)_2$ complex connected via hydrogen-bonds to other complexes in the adjacent unit cells (Table 2.14). The coordinated water molecules are involved in this H-bond network. The water molecules form hydrogen bonds between their oxygen atoms and the oxime protons on adjacent complexes and complementary bonds between one of the water's protons and the metal-coordinated carboxylate hydroxyl deprotonated oxygen on the adjoining complexes. The second proton of each water molecule forms a hydrogen bond to the uncoordinated carboxylate carbonyl oxygen of a metal complex on the adjacent complex so that the zinc complexes are linked into sheets along the yz-plane (Figure 2.18).

Table 2.14. Hydrogen Bonds for $Zn(PAO)_2 \cdot 2H_2O$ [Å and ^{o}]

D-H...A	d(D-H)	d(H...A)	d(D...A)	<(DHA)
O(1)-H(1)...O(4)#2	0.88	1.81	2.6891(15)	175.6
O(4)-H(4E)...O(2)#3	0.88	1.73	2.6092(15)	173.8
O(4)-H(4D)...O(3)#4	0.88	1.82	2.6177(15)	149.7

Numbers in parentheses are estimated standard deviations in the least significant digits.
Symmetry transformations used to generate equivalent atoms: #1 -x+1,-y+1,-z+1 #2 -x+2,-y+1,-z+1 #3 -x+1,-y,-z+1 #4 x+1,y,z

The resultant of this hydrogen-bonding is an extended 3-dimensional network, which can account for the sparingly soluble $Zn(PAO)_2 \cdot 2H_2O$.

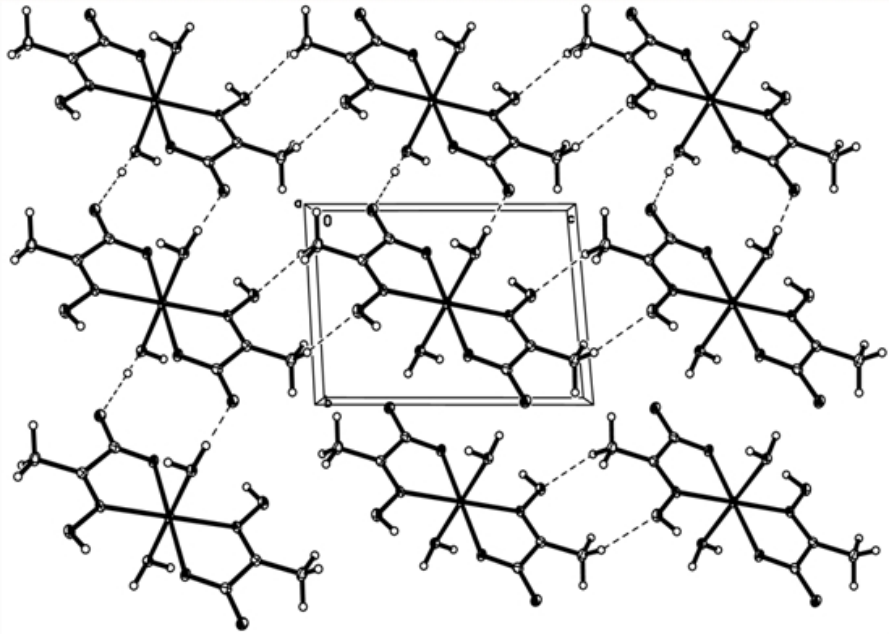

Figure 2.18. A perspective view of the zinc complex sheet along the yz-plane

Spectroscopic Characterization of PAO^- Salts of Group 12 Metals

Both IR and solid-state ^{13}C NMR spectroscopic techniques were used to characterize the group 12 element salts of PAO^- prepared in this work. The important distinctive infrared vibrational frequencies are displayed in Table 2.15.

Table 2.15. Distinctive IR Vibrational Frequencies (cm^{-1}) of the Salts of Group 12 Elements of PAO^-

Compound	$\nu_{(C=N)}$	$\nu_{as(COO)}$	$\nu_{s(COO)}$	$\Delta\nu_{(COO)}$	$\nu_{(N-O)}$
$Zn(PAO)_2 \cdot 2H_2O$	1675	1653	1391	262	1054
$Cd(PAO)_2$	1678	1634	1371	263	1065
$Hg(PAO)_2$	1656	1610	1379	231	1073 1011

As seen for the PAO^- salts of main group elements, two of the characteristics of the IR spectra of the PAO^- salts are that the asymmetric vibrational stretch of the carboxylate group decreases significantly by 42-85 cm^{-1} and its symmetric vibration stretch by 29-49 cm^{-1} in comparison to the parent acid, HPAO. This phenomenon is common for the carboxylates of metals and is attributed to the deprotonation and delocalization of the negative charge in the carboxylate moiety and its coordination to the metal center.[82] The stretching vibrations of C═N in these salts are comparable to that observed for HPAO in agreement with the data reported previously for the light alkali metal (Li, Na, and K),[14] alkaline earth metal,[6] and the divalent 3d transition metal (Mn, Co, Ni, Cu, Zn) salts of PAO^-.[23] The $\nu_{(N—O)}$ stretching frequency increases by 11-30 cm^{-1} compared to that observed for the parent acid, HPAO. This increase in the $\nu_{(N—O)}$ frequency stretch is similar to that observed for some of the first row transition metal PAO^- complexes[23] and is opposite the trend observed for the alkali[14] and the alkaline earth[6] metal derivatives. These showed a decrease in the N—O frequency with respect to HPAO. This difference may be due to much stronger interaction of the nitrogen atom with transition metal centers. This would lead to strengthening of the N—O bond through inductive effects. The IR spectrum of the mercury complex shows two bands for $\nu_{(N—O)}$, indicating the existence of two types of the coordination of the PAO^- ligand. This conclusion is consistent with the result of solid-state ^{13}C NMR spectroscopy (*vide infra*). One of these frequencies of $\nu_{(N—O)}$ is lower than that seen for HPAO by 32 cm^{-1}. Such a decrease was noticed previously in the alkali,[14] alkaline earth,[6] and lead salts (see above). The existence of IR absorption bands in the 820-860 cm^{-1} region are attributed to as vibrations of water molecules coordinated to the metal ion center,[23] while the broad bands

at wave numbers higher than 2600 cm^{-1} are suggestive of the existence of hydrogen bonds in these compounds.[23] The difference between the asymmetric and symmetric stretching frequencies of the carboxylate group, $\Delta\nu_{(COO)}$ indicates that the coordination mode of the carboxylate moiety of the PAO^- ligand is monodentate[81] in both the zinc and cadmium compounds. It may also be concluded that the PAO^- is bound to the metal ion center through its nitrogen atom of the oximino group to form N, O-chelate five-membered metallacycles as evidenced from the $\nu(C{=}N)$ in the IR spectra.

The $\Delta\nu_{(COO)}$ calculated for the mercuric compound corresponds to a bridging carboxylate.[81] This conclusion regarding the coordination of the PAO^- ligands coordinated to the Hg^{2+} is supported by the similarity between the $\nu_{as(COO)}$ = 1610 cm^{-1} and $\nu_{s(COO)}$ = 1379 cm^{-1} for the mercuric salt with those reported for the sodium (1599 cm^{-1} and 1375 cm^{-1}, respectively)[14] and calcium (1617 cm^{-1} and 1386 cm^{-1}, respectively)[6] derivatives. These both contain PAO ligands that have carboxylates that bridge two adjacent metal ions. However, the two different N—O stretches suggest that there are two different coordination modes for the PAO^- ligands, one in which the nitrogen is coordinated to the metal and one where it is not. The absorption at 1073 cm^{-1} can be assigned to an N, O chelating PAO while the one at 1011 cm^{-1} could be due to a non-chelating O-bonded PAO ligand.

The solid-state ^{13}C chemical shifts for each of the group 12 metal salts of PAO^- are shown in Table 2.16. The methyl carbon has a chemical shift range from 11.0 to 12.6 ppm, and is slightly affected by the deprotonation of HPAO and the coordination of PAO^- to the metal ion center, as indicated by its signal shifted upfield by 0.4 ppm or downfield by 1.2 ppm from the corresponding peak of HPAO (11.4 ppm). The oximino carbons,

however, have chemical shifts reflecting considerable influence of deprotonation and complexation since the signals for these carbons are downfield shifted by 5.9-9.2 ppm relative to the HPAO resonance (149.0 ppm). The carboxylate carbon peak, unexpectedly, was shifted slightly upfield by 0.1-3.6 ppm from the HPAO resonance at 176.0 ppm. This is opposite the downfield shifting reported for this carbon in the alkali[14] and alkaline earth[6] compounds. The difference probably arises from the influence of the d-electrons of the transition metals that can back donate into the π* system of the carboxylate. In terms of purely inductive effects, this would shield the carboxylate carbons but there is also likely to be a strong influence of paramagnetic effects. Notably, there is also a monotonic decrease in the chemical shift of the carboxylate as Group 12 is descendent.

Table 2.16. Solid-State ^{13}C NMR CPMAS Chemical Shifts (ppm) of the Salts of Group 12 Elements of PAO$^-$

Compound	CH_3	C=N	COO
$Zn(PAO)_2 \cdot 2H_2O$	11.0	157.6	166.5
$Cd(PAO)_2$	11.4	154.9	167.5
$Hg(PAO)_2$	12.6	158.2	164.0 and 166.4

The ^{13}C NMR CPMAS spectrum of $Zn(PAO)_2 \cdot 2H_2O$ consists only of one set of signals indicating the existence of one type of monodentate of PAO$^-$ coordinated to the Zn^{2+} ion center. The chemical shifts are similar to those observed for the compounds containing the N,O-chelate PAO$^-$ ligand type in the sodium,[14] calcium[6] and magnesium (this work) salts. Therefore, it can be inferred that the PAO$^-$ forms the N, O-chelate in

the zinc salt in agreement with the conclusions drawn from the IR and XRD spectra, and structural determination by X-ray single crystal. The ^{13}C NMR CPMAS spectrum of $Cd(PAO)_2$ also displays only one set of signals at positions similar to those observed in zinc, sodium,[14] calcium,[6] and magnesium compounds, and hence the PAO^- ligand is coordinated to the Cd^{2+} ion center through its oximino nitrogen atom and the oxygen atom of the deprotonated hydroxyl of the carboxylate moiety, a conclusion that is in accord with the IR spectral results. The mercury complex, on the other hand, has two peaks for the carboxylate carbon dwelling in two different electronic environments, accounting for the existence of two kinds of ligations of PAO^- ligand. The resonance of the methyl carbon at 12.6 ppm and that of carboxylate carbon at 166.4 ppm are similar to those found in sodium (12.2 and 171.7 ppm, respectively)[14] and calcium (12.1 and 171.6 ppm, respectively).[6] Consequently, it can be said that this PAO^- ligand in the mercuric salts adopts the N,O,O-chelate-bridge mode. The other carboxylate carbon of the other PAO^- ligand has a chemical shift at 164 ppm, which is close to those observed in both of zinc and cadmium derivatives, and thus it might be ascribed to N, O-chelate mode. The methyl and oximino carbons atoms signals were not resolved in the recorded spectrum due to the broadness of their peaks and presumably due to the electronic asymmetry resulted from the different modes of coordination of both PAO^- ligands to Hg^{2+} ion center. All of these deductions from the ^{13}C NMR CPMAS spectrum regarding the structure of $Hg(PAO)_2$ are parallel to those revealed by the IR spectroscopic investigation.

Thermal Behavior of PAO^- Salts of Group 12 Metals

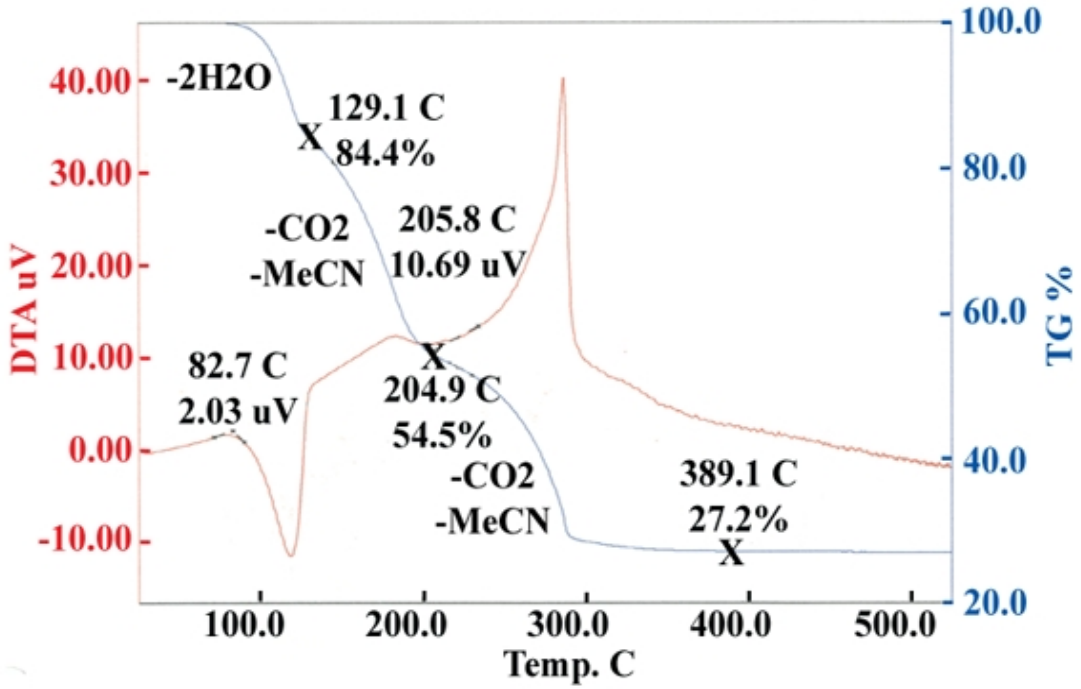

Figure 2.19. The TGA and DTA traces for $Zn(PAO)_2 \cdot 2H_2O$ in dry air with a heating rate of 1 ^oC/min

The TGA and DTA investigations of $Zn(PAO)_2 \cdot 2H_2O$ are depicted in Figure 2.19. As can be seen, the zinc salt decomposes in a stepwise fashion. The first weight change step, beginning at around 80^oC, corresponds to an endothermic process of losing the two crystallization water molecules. This relatively high temperature of removal of water molecules is an indication of the coordination of these water molecules to the Zn^{2+} ion center, as proposed on the basis of IR, NMR, XRD, and X-ray single crystal analyses (see above Figure 2.17). The second step, with a start at 130^oC, is a slightly exothermic for decarboxylation and a lost of an acetonitrile owing to the decomposition of one of the PAO^- ligand as indicated by the mass loss. The following step is extremely exothermic and has an onset at 206^oC referring to the dissociation of the remaining PAO^- ligand to

oxide (the major product) and to carbonate (very small amount) by the loss of carbon dioxide and acetonitrile molecules, as can be inferred from the weight variation and the IR and solid-state ^{13}C CPMAS NMR spectra of the decomposition products at 290 (Figure 2.20). The last step is pyrolysis of this carbonate to oxide and sintering of the oxide particles. The formation of zinc oxide as the final product of pyrolysis of the zinc PAO^- salt is in accord with the preceding study of the thermal decomposition of $Zn(PAO)_2 \cdot 2H_2O$.[23]

To gain a deeper insight into the thermolytic behavior of the zinc salt, IR and solid-state ^{13}C CPMAS NMR techniques were employed besides the TGA and DTA studies. The solid-state ^{13}C CPMAS NMR instrumentation was demonstrated to be a very efficient, informative tool to probe the mechanism of the pyrolysis of this PAO^- compound and to confirm the results of the TGA experiment. The solid-state ^{13}C CPMAS NMR spectra recorded for the pyrolysis products yielded at 150°C, 200°C, and 290°C are shown in Figure 2.20. The spectrum of the product obtained at 150°C still displays the distinctive peaks for the PAO^- ligand but broader and with less intensities than those for the thermally untreated salt. The observation of two signals for the methyl carbon is a sign of the existence of two carbons in two different electronic environments. The IR spectrum of this product, in addition, verify the existence of the PAO^- ligand [$\nu_{as(COO)}$ = 1618, $\nu_{s(COO)}$ = 1367, $\nu_{(N-O)}$ = 1075 cm^{-1}]. The signals noted in the spectrum of the 200°C-pyrolysis product refer to the existence of PAO^- ligand (10.3 ppm, 158.0 ppm, and 171.2 ppm) and of acetamide [$H_3CC(=O)NH_2$] at 22.3 ppm for the methyl carbon and 181.7 ppm for the amide carbon, which are comparable to those observed for an authentic sample in D_2O of acetamide (22.11 and 178.06 ppm, respectively).[44]

However, the IR spectrum is difficult to interpret and to predict the existence of these species. The product obtained at a calcination temperature of 290°C displays a small, broad peak at 166.9 ppm which matches with that of zinc carbonate synthesized according to the procedure reported in the literature.[61] The bands seen in IR spectrum of the 290°C-product at 1521 cm^{-1} and 1362 cm^{-1} can be assigned for the $\nu_{as(COO)}$ and $\nu_{s(COO)}$ stretches of carbonate anion, respectively, because they are similar to those obtained for the synthesized $ZnCO_3$ (1500 cm^{-1} and 1387 cm^{-1}, respectively). It seems this carbonate is amorphous because it is not detected by the XRD (see Figure 2.21). The amount of material formed at this temperature is very small, lying on the surface of the ZnO, because no bubbles of CO_2 were noted upon treatment with concentrated HCl.

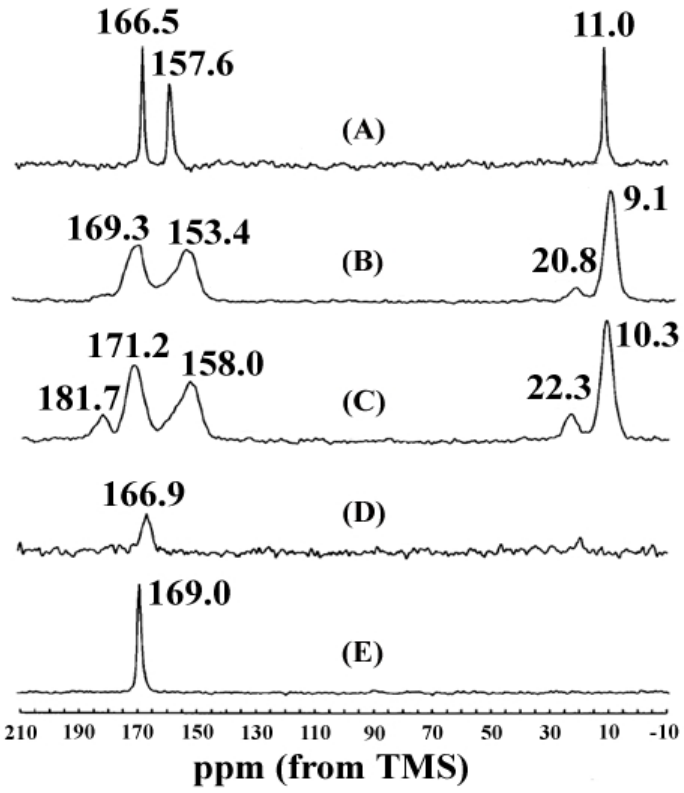

Figure 2.20. Solid-state ^{13}C CPMAS NMR spectra of $Zn(PAO)_2 \cdot 2H_2O$ heated to (A) 25°C, (B) 150°C, (C) 200°C, and (D) 290°C. (E) is the spectrum of synthesized $ZnCO_3$

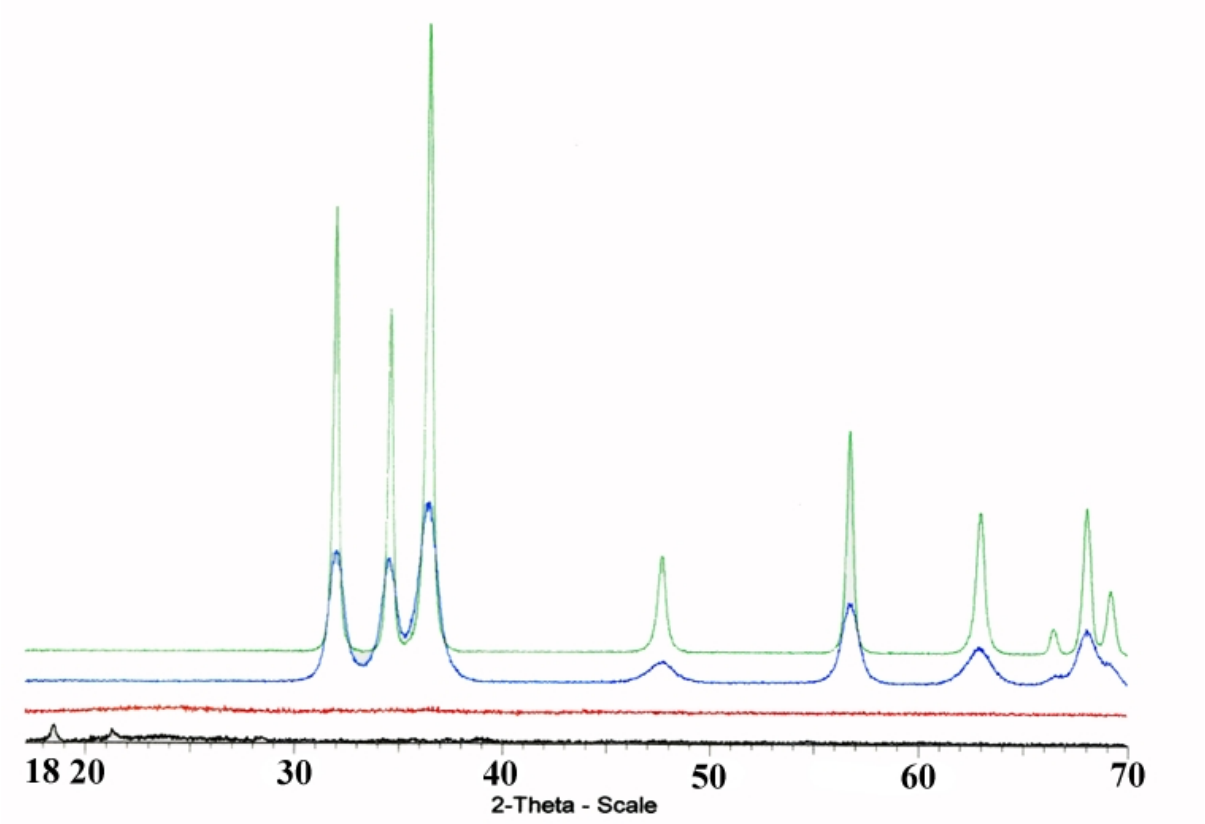

Figure 2.21. XRD patterns of $Zn(PAO)_2 \cdot 2H_2O$ heated to 150, 200, 290, and 389°C

The XRD spectra recorded for the products resulted from the calcinations of $Zn(PAO)_2 \cdot 2H_2O$ at 150°C, 200 °C, 290°C, and 389°C are shown in Figure 2.21. Clearly, the products obtained at 150 °C (black) and 200 (red) °C are amorphous. The product obtained at 290 °C (blue) has broad peaks which match with those of zincite, ZnO (no peaks for zinc carbonate) and are superimposable on those of the product produced at 389 °C (green) with sharper peaks, implying a zincite phase having larger crystallites than those of the 290°C-product. The crystallite size measurements by XRD also confirms that the zincite produced at 290°C has an average crystallite size of 6.2 nm, which is much smaller than that of the zincite obtained at 389°C (24.6 nm) as shown in Figure 2.22. Moreover, TEM images prove that the particle size is smaller for the ZnO obtained

at 290°C in comparison to that of ZnO obtained at 389°C (*vide infra* Figure 2.23). Investigation of the morphology of $Zn(PAO)_2 \cdot 2H_2O$ and its pyrolysis products produced at various calcination temperatures 150 °C, 200 °C, 290 °C, and 389°C revealed that the morphology of the original zinc PAO^- complex, rod-like shape was maintained in the pyrolysis products. In contrast, the particle size increased with increasing the temperature of calcinations due to sintering of the particles, except those at 150°C had smaller particles than those of the $Zn(PAO)_2 \cdot 2H_2O$ (Figure 2.24). The surface area measurements are consistent with this increasing trend observed for particle size. The S_{BET} declines with increasing the temperature of pyrolysis, except the S_{BET} of the product obtained at 150°C which is higher than that of the starting material, $Zn(PAO)_2 \cdot 2H_2O$ and represents a maximum of S_{BET}. The latter may occur because its decomposition starts at this point to yield smaller particles than those of $Zn(PAO)_2 \cdot 2H_2O$ (Figure 2.25).

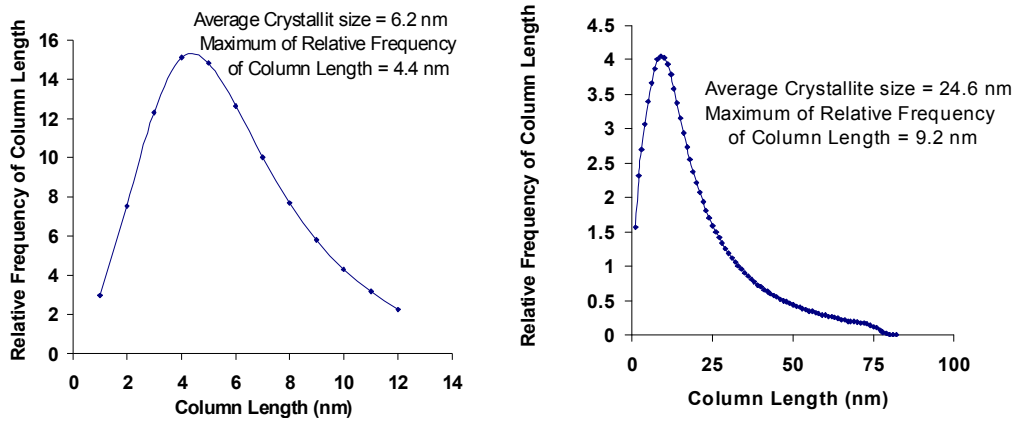

Figure 2.22. Crystallite size measurements by XRD of ZnO obtained at 290 °C (left) and at 389 °C (right)

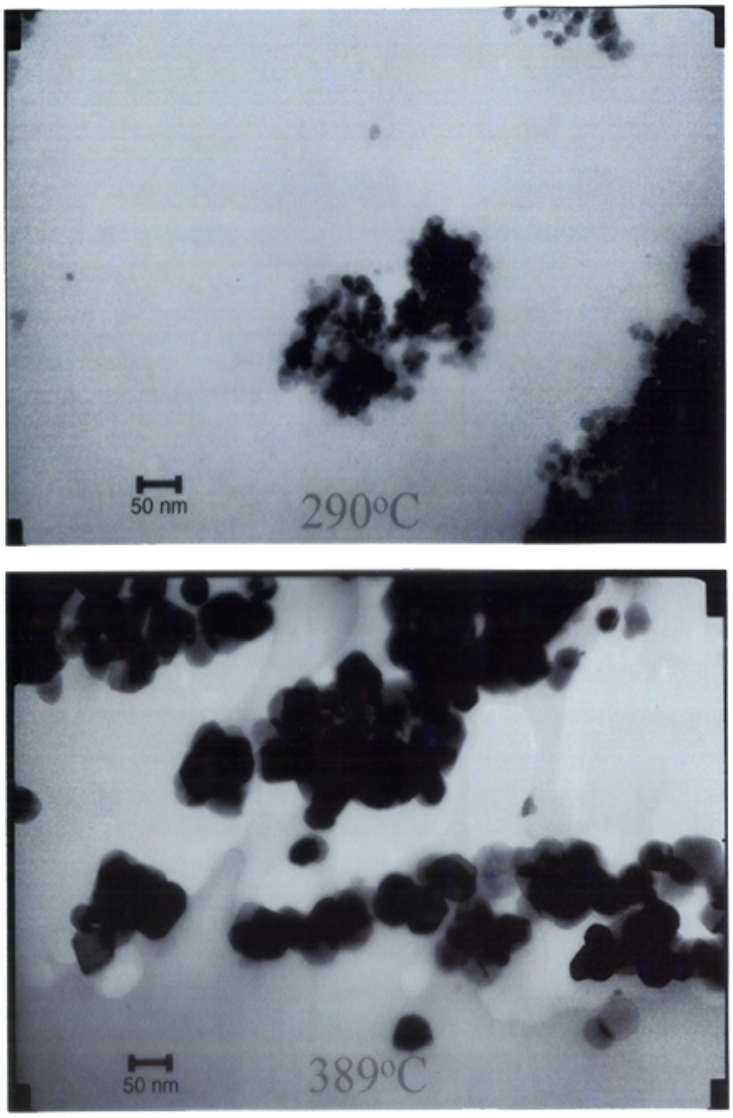

Figure 2.23. TEM images of ZnO particles obtained at 290°C (top) and at 389°C (bottom)

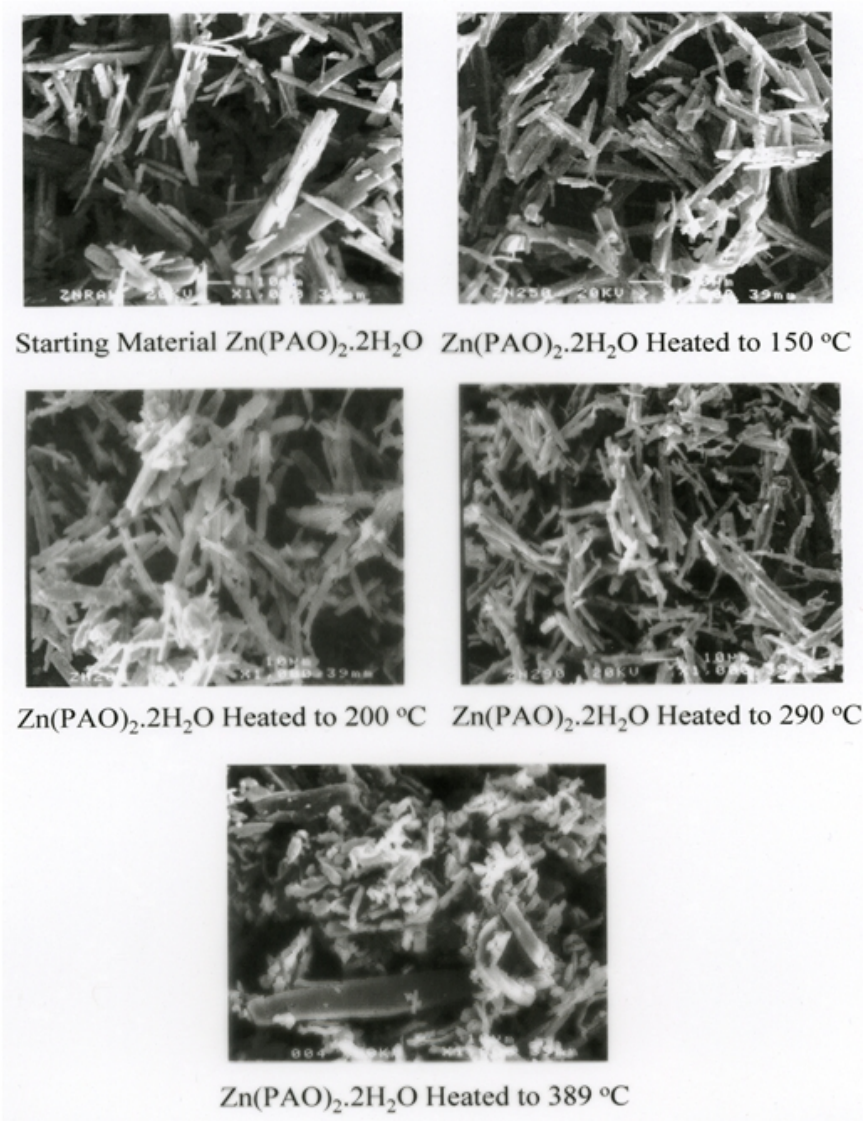

Figure 2.24. SEM electromicrographs of $Zn(PAO)_2 \cdot 2H_2O$ and its pyrolysis products

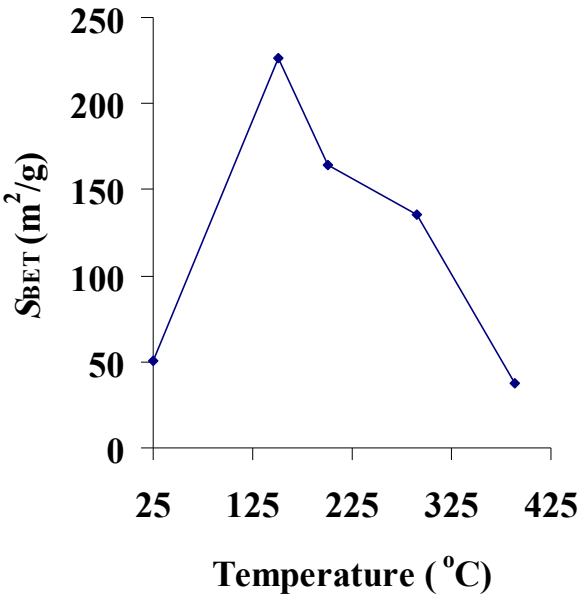

Figure 2.25. Variation of specific surface area (S_{BET}) with temperature for $Zn(PAO)_2 \cdot 2H_2O$

The $Cd(PAO)_2$ and $Hg(PAO)_2$ systems have completely different thermal behaviors from each other and from that exhibited by $Zn(PAO)_2 \cdot 2H_2O$, which is partially attributed to the variation in their own structures. The cadmium salt does not show a dehydration step because it does not contain water molecules of crystallization, but the process begins with the decomposition of the PAO^- ligand at 200°C in two steps to give highly crystalline cadmia (CdO) upon calcination at 400°C, as indicated by the sharp peaks of its XRD pattern (not shown here). The mercuric compound, on the other hand, decomposes gradually over a wide range of temperature to give mercury metal as the final product at 300°C.

The group 12 metal salts of PAO^- have their thermal decomposition temperature increased with increasing the ionic radius of the metal ion on going down the group, as

illustrated diagrammatically in Figure 2.26. This observed trend follows the ionic model based on lattice enthalpies, predicting that large anion salt becomes more stable and has higher decomposition temperature when the ionic radius of the metal ion increases.[88] The obeying of the group 12 metal salts of PAO^- this ionic model, however, is contradictory to the deviation of the thermal behavior of both of alkali[14] and alkaline earth[6] derivatives from this model. In addition, comparing the thermal decomposition temperature of each compound in the group 12 with those of compounds of the alkali and alkaline earths in

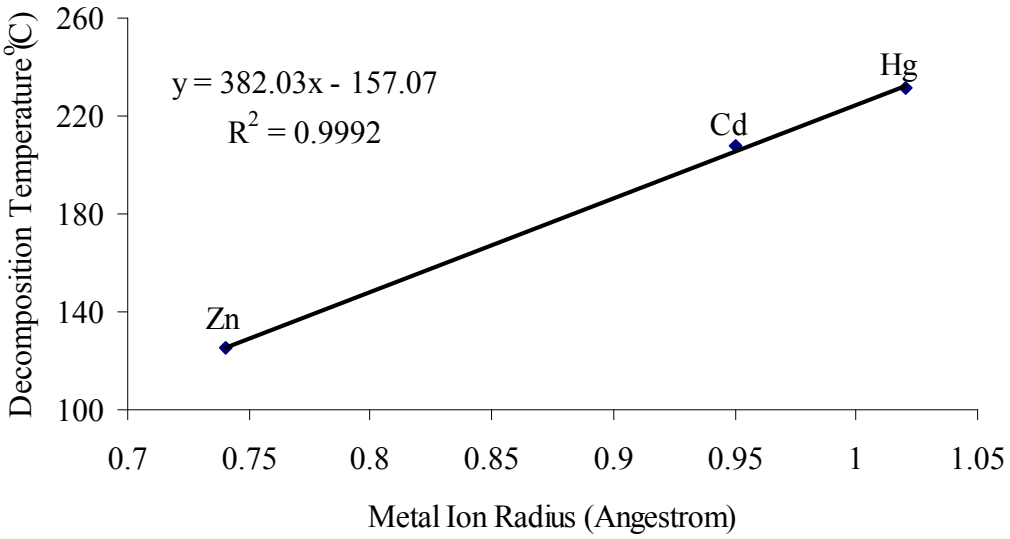

Figure 2.26. Decomposition temperature in ^oC of the divalent group 12 metal 2-hydroxyiminpropanoates as a function of the metal ion radius

the same period shows that decomposition temperatures increase with decreasing the metal ion radius in the same period, except the metals of the fourth period which show a maximum with calcium compound as seen in Figure 2.27. This trend of increasing the decomposition temperature on going from left to right in both periods 4 and 5 contradicts the ionic model notion which forecasts that the highly charged cation lowers the decomposition temperature of the salt of the large anion.[88]

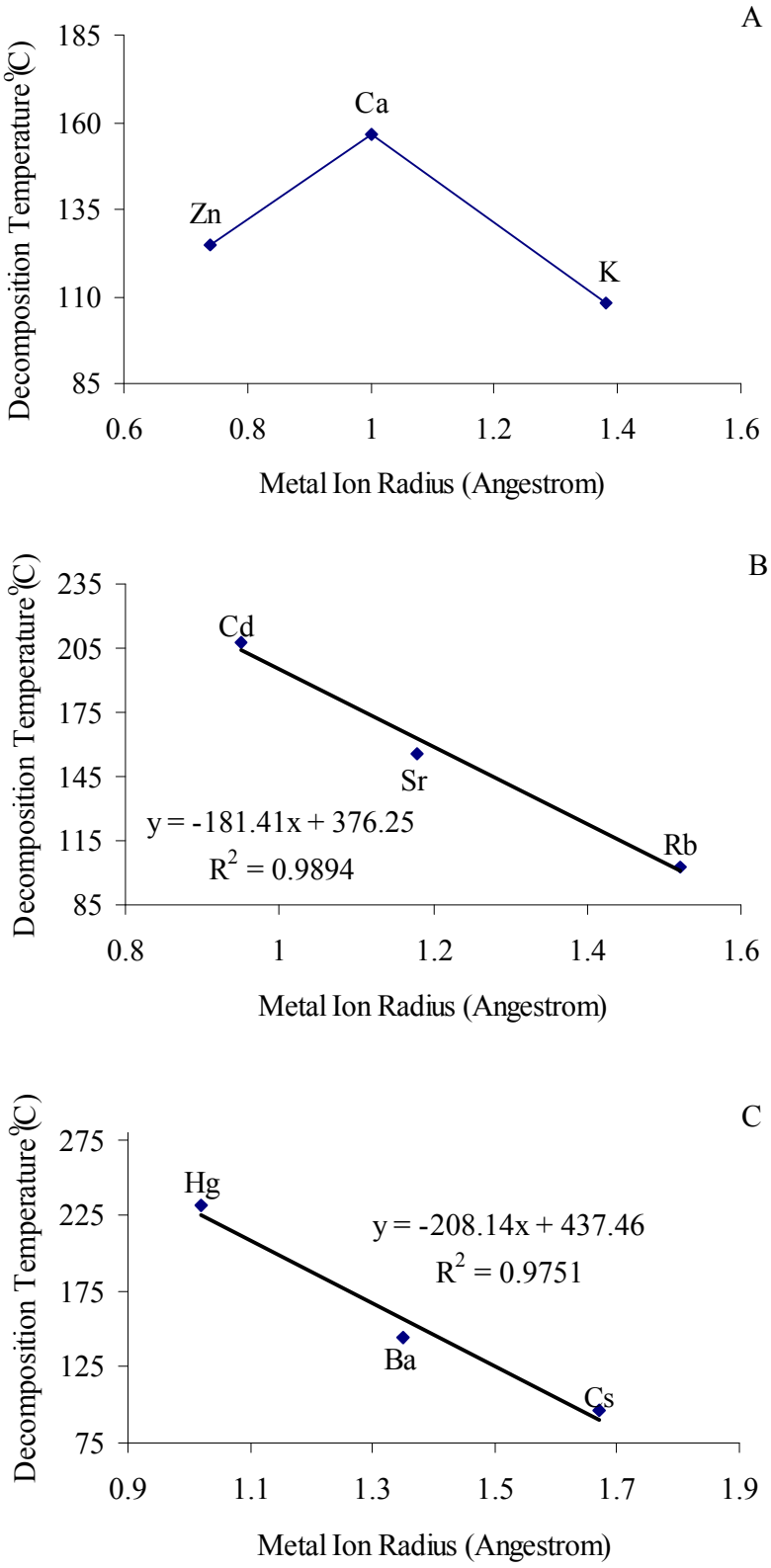

Figure 2.27. Decomposition temperatures versus the ionic radius of PAO^- complexes of metals of periods (A) 4, (B) 5, and (C) 6

Thus, decreasing the decomposition temperature on going from calcium to zinc is consistent with the ionic model, while increasing the decomposition temperature on going from potassium to calcium is contrary to it. (All of the ionic radii in Figures 2.26 and 2.27 are taken for the metal ion with coordination number 6 from reference 80).

Textural and Surface Acid-Base Properties of Group 12 Metal Oxides

Table 2.17 summarizes the chemical and textural properties of ZnO obtained from pyrolysis of $Zn(PAO)_2{\cdot}2H_2O$ at 389^{o}C and compares them to data published in the literature.[75] The acidity and basicity are expressed in μmol/g and μmol/ m^2 units. The ZnO obtained from the sintering of the $Zn(PAO)_2{\cdot}2H_2O$ source has almost S_{BET} 19 times as large as that of ZnO obtained from the calcination of a commercially available $Zn(OH)_2$ source. The ZnO derived from the first source has larger number of basic sites per mass unit, which is almost 14 times of those of ZnO produced from the second source. The basicity as function of the surface area, however, differs markedly from the trend exhibited by the basicity per mass unit. The ZnO derived from the second source has a population of surface basic sites which is 23.5% more than those of the ZnO derived from the first source. The ZnO originating from the second source is not acidic at all and is extremely basic, while the one derived from the first source is highly acidic in that its acidity exceeds its basicity by almost 61% per gram and/or per square meter. The variations in these textural and acid-base features for the zinc oxides produced in each case are undoubtedly ascribed to the differences among sources and their fabrication methods and to the heat treatment that the precursor was subjected to to give the final desired oxide.

Table 2.17. Chemical and Textural Properties of ZnO

Source of ZnO	Calcination Temperature (^oC)	S_{BET} (m^2/g)	Acidity (μmol/g)	Basicity (μmol/g)	Acidity (μmol/ m^2)	Basicity (μmol/ m^2)	References
$Zn(PAO)_2 \cdot 2H_2O$	389	37.37	147.82	57.04	3.95	1.53	this work
Commercially available $Zn(OH)_2$	500	2	---	4	---	2	75

PAO^- Salts of Divalent 3d Transition Metals

The complexes of PAO^- were synthesized and characterized by IR and by XRD which showed that not only the cobalt, nickel, copper, and zinc complexes were isostructural as previously claimed by Skopenko *et al.*,[23] but also that the iron complex had the same structure of these complexes as confirmed through our investigation (Figure 2.28). The manganese complex gave a completely different XRD pattern which agreed with the prediction of Skopenko *et al.*[23] in that manganese compound was not isostructural to the Co^{2+}, Ni^{2+}, Cu^{2+}, and Zn^{2+} derivatives which was confirmed later by the crystal structure determination of the manganese complex.[19] The latter was totally different from the structure determined by single crystal X-ray crystallography for Cu complex in this work (Figure 2.29).[7] The copper complex of PAO^- has a pseudo-octahedral cupric ion center ligated to two molecules of water trans to each other and chelated to PAO^- ligands adopting the N,O-chelate mode, whereas the oximino moieties lie trans to each other around the Cu^{2+} ion center, and all the non-hydrogen atoms of these PAO^- ligands are coplanar. Accordingly, the copper complex belongs to the point group of D_{2h}. The arrangement of the PAO^- ligands in $Cu(PAO)_2 \cdot 2H_2O$ is contrary to the cis arrangement noted for the oximino moieties in the potassium[8] and the pyridinium[20] copper salts containing PAO^- and PAO^{2-} ligands, $K^+[Cu^{II}(PAO)_2]^-$ and $[HPy]^+[Cu^{II}(PAO)_2]^-$, coordinated to the Cu^{2+} center in square planar geometry. This cis arrangement is also a result of the hydrogen-bond bridging of the oximino hydroxyl group of PAO^- and its deprotonated analogous of PAO^{2-}, where the hydrogen atom is located in the middle between the two oxygen atoms of the oximino groups to endow a high symmetry to the anion $[Cu^{II}(PAO)_2]^-$.[8,20]

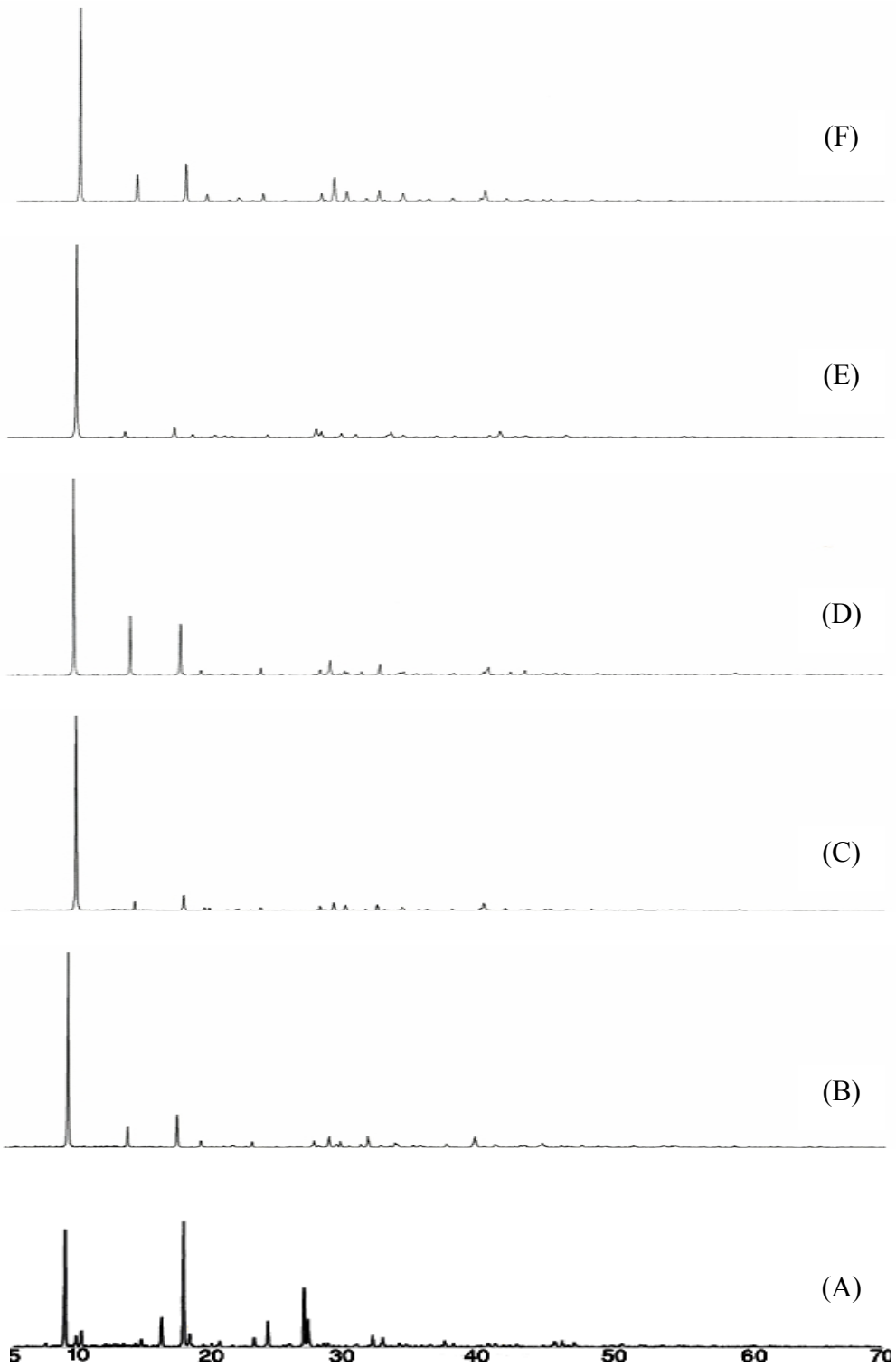

Figure 2.28. XRD patterns of (A) $Mn_4(PAO)_8 \cdot 2H_2O$, (B) $Fe(PAO)_2 \cdot 2H_2O$, (C) $Co(PAO)_2 \cdot 2H_2O$, (D) $Ni(PAO)_2 \cdot 2H_2O$, (E) $Cu(PAO)_2 \cdot 2H_2O$, (F) $Zn(PAO)_2 \cdot 2H_2O$

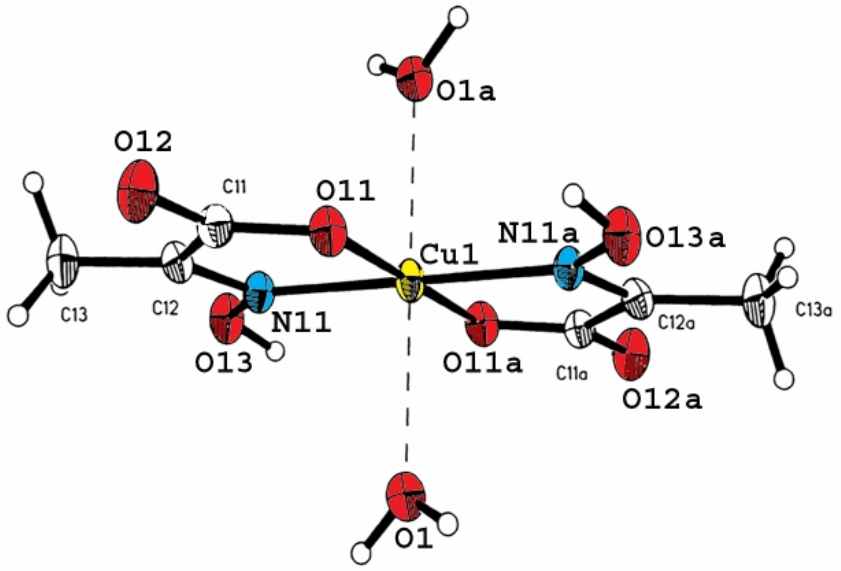

Figure 2.29. Crystal structure of $Cu(PAO)_2 \cdot 2H_2O$

The bond lengths and angles for the $Cu(PAO)_2 \cdot 2H_2O$ complex are summarized in Table 2.18 and Table 2.19. Comparing the Cu—N distance in the $Cu(PAO)_2 \cdot 2H_2O$ complex with its analogs found in the $K^+[Cu^{II}(PAO)_2]^-$ salt[8] and in the $[HPy]^+[Cu^{II}(PAO)_2]^-$ salt[20] shows that the Cu—N bond in the former compound [2.044(5) Å] is longer than those in the potassium and pyridinium salts [1.942,[8] 1.925 Å,[20] respectively], which may account for the greater negative charge on the nitrogen atom in the latter salts because of the removal of a proton from the oxime and the square planar geometry of the deprotonated salt. Moreover, the Cu—N bonds in the $K^+[Cu^{II}(PAO)_2]^-$ and $[HPy]^+[Cu^{II}(PAO)_2]^-$ salts are very comparable to that found in a prototypical, square planar, copper dimethylglyoximate (1.93-1.96 Å).[56] The effect of deprotonation of the PAO^- ligand to form a PAO^{2-} ligand does not only reduce the Cu—N bond length, but also results in decreasing of the N—O and the C═N distances. The N—O bond

decreases from 1.393(6) Å in $Cu(PAO)_2 \cdot 2H_2O$ to an average of 1.355(3) Å[8] and 1.353(8) Å[20], respectively, in the potassium and pyridinium copper salts, while the C═N bond contracts from 1.301(7) Å to an average of 1.28(3) Å[8] and 1.28(1) Å,[20] respectively. The carboxylate O—Cu contacts for $Cu(PAO)_2 \cdot 2H_2O$, $K^+[Cu^{II}(PAO)_2]^-$, and $[HPy]^+[Cu^{II}(PAO)_2]^-$ are identical within experimental error and fall within the range of 1.93-2.03 Å, observed in other copper carboxylates.[81] The Cu—OH_2 distance in $Cu(PAO)_2 \cdot 2H_2O$ is 2.482(5) Å, which is significantly longer than that observed in the dihydrate of cupric acetate (2.1613(17) Å),[89] indicating a much weaker binding of the water molecule in the PAO^- complex.

The observation of monodentate carboxylates in $Cu(PAO)_2 \cdot 2H_2O$, $K^+[Cu^{II}(PAO)_2]^-$, and $[HPy]^+[Cu^{II}(PAO)_2]^-$ is in sharp contrast with other reported PAO^- structures for $Na(PAO) \cdot H_2O$,[14] $Ca(PAO)_2 \cdot H_2O$,[6] and $Ce(PAO)_3$[1,3] in which the carboxylates bridge adjacent metal centers. This monodentate nature of the carboxylate in the copper complex is reflected in the large variation in the two carboxylate C—O distances (6.9 %) indicating significant double bond character in the shorter bond to the uncoordinated oxygen. By comparison, the percentage difference in the carboxylate bonds for $Na(PAO) \cdot H_2O$[14] and $Ca(PAO)_2 \cdot H_2O$[6] is only 0.32% and 1.3%, respectively.

Table 2.18. Bond Distances (Å) for $Cu(PAO)_2 \cdot 2H_2O$

Cu(1)—O(1)	2.482(5)	C(12)—C(13)	1.474(8)
Cu(1)—O(11)	1.944(5)	Cu(1)—N(11)	2.044(8)
O(11)—C(11)	1.293(7)	O(12)—C(11)	1.240(7)
O(13)—N(11)	1.393(6)	C(11)—C(12)	1.531(7)
C(12)—N(11)	1.301(8)		

Numbers in parentheses are estimated standard deviations in the least significant digits.
Symmetry transformation used to generate equivalent atoms (A): -x, -y, -z.

The extremely low solubility of $Cu(PAO)_2 \cdot H_2O$ in water can be accounted for by the extensive network of strong hydrogen bonds that tie together the individual copper complexes (Figure 2.30). Since the copper ions sit on the corners of the unit cell, the copper complexes are stacked in chains along the a-axis. The metal complexes in each of these chains are tied together by a network of hydrogen bonds that involve the coordinated water molecules. Within each chain, the water molecules form hydrogen bonds between their oxygen atoms and the oxime protons on adjacent complexes and complementary bonds between one of the water's protons and the metal-coordinated carboxylate oxygen on the adjoining complexes. The second proton of each water molecule forms a hydrogen bond to the uncoordinated carboxylate oxygen of a metal complex on the adjacent chain so that the chains are linked into sheets along the b-axis.

Table 2.19. Interbond Angles (^{o}) for $Cu(PAO)_2 \cdot 2H_2O$

O(1)—Cu(1)—N(11)	91.3(2)	C(13)—C(12)—N(11)	126.8(5)
O(1)—Cu(1)—N(11A)	88.7(2)	Cu(1)—N(11)—C(12)	114.8(3)
O(1)—Cu(1)—O(1A)	180.0	O(13)—N(11)—C(12)	113.0(4)
O(1)—Cu(1)—O(11)	88.7(2)	O(11)—Cu(1)—N(11A)	98.7(2)
O(1)—Cu(1)—O(11A)	91.3(2)	O(11A)—Cu(1)—N(11A)	81.3(2)
O(11)—Cu(1)—N(11)	81.3(2)	O(11)—C(11)—O(12)	125.1(5)
N(11)—Cu(1)—O(11A)	98.7(2)	O(12)—C(11)—C(12)	117.8(5)
Cu(1)—O(11)—C(11)	115.2(3)	C(11)—C(12)—N(11)	111.6(4)
O(11)—C(11)—C(12)	117.1(4)	Cu(1)—N(11)—O(13)	132.1(3)
C(11)—C(12)—C(13)	121.6(5)		

Numbers in parentheses are estimated standard deviations in the least significant digits.

(A)

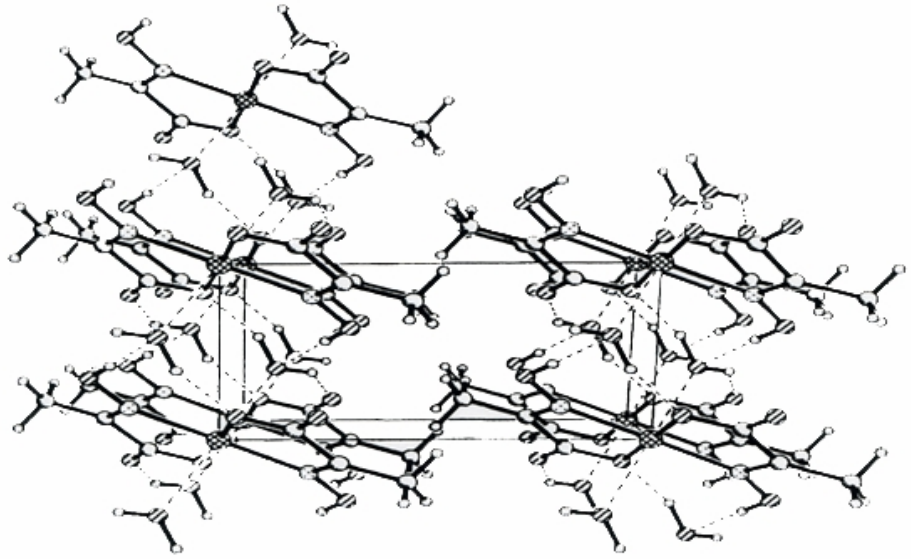

(B)

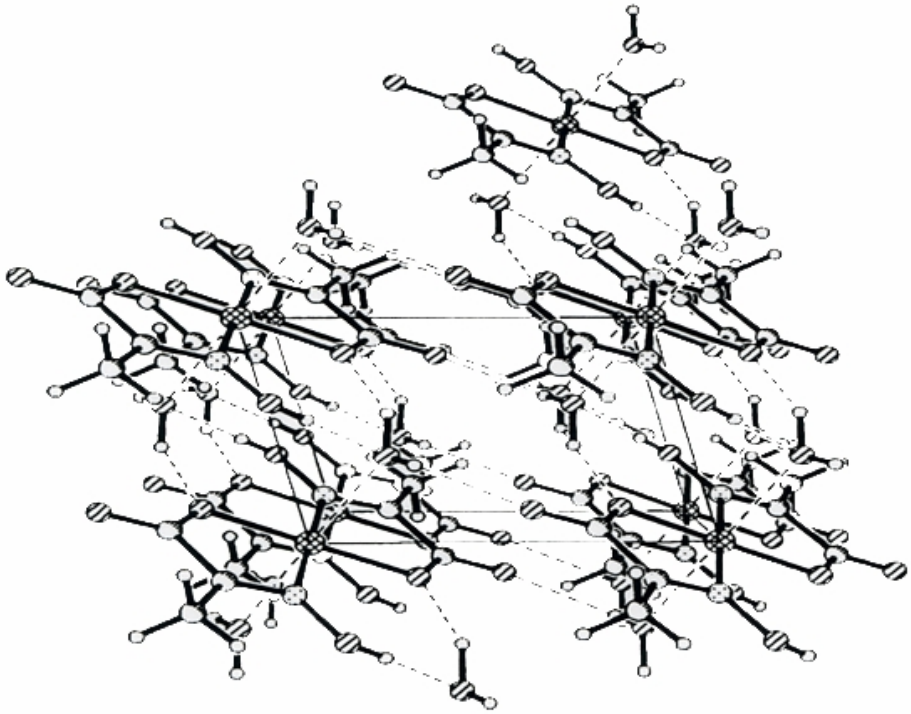

Figure 2.30. Perspective view of (A) the stacked chains of the copper complexes along the a-axis and (B) the extensive network of hydrogen bonds tying the copper complexes

Spectroscopic Characterization of PAO^- Salts of Divalent 3d Transition Metals

The IR was recorded for these compounds and the characteristic absorption bands are summarized and compared to those previously reported in Table 2.20. A marked characteristic of the IR spectra of PAO^- complexes was that the asymmetric vibrational stretch of the carboxylate group decreased significantly by 40-63 cm^{-1} and its symmetric vibrations stretch by 25-55 cm^{-1} in comparison to the parent acid, HPAO.

Table 2.20. Distinctive IR Vibrational Frequencies (cm^{-1}) of the PAO^- Salts of Divalent 3d Transition Metals

Compound	$\nu_{(C=N)}$	$\nu_{as(COO)}$	$\nu_{s(COO)}$	$\Delta\nu_{(COO)}$	$\nu_{(N-O)}$
$Mn_4(PAO)_8 \cdot 2H_2O$[a]	1667 (1670)	1633 (1620)	1370 (1400)	263 (220)	1069 (1060)
$Fe(PAO)_2 \cdot 2H_2O$[b]	1668 (1668)	1650 (1647)	1389 (1395)	261 (252)	1045 (1043)
$Co(PAO)_2 \cdot 2H_2O$[a]	1669 (1670)	1651 (1645)	1390 (1395)	261 (250)	1050 (1060)
$Ni(PAO)_2 \cdot 2H_2O$[a]	1672 (1670)	1655 (1650)	1395 (1395)	260 (255)	1058 (1060)
$Cu(PAO)_2 \cdot 2H_2O$[c]	1674 (1660)	1632 (1638)	1365 (1369)	267 (269)	1085 (1077)

[a, b, c]Values in parenthesis are from references 23, 15, and 7, respectively.

Such observations are common for the carboxylates of metals and are attributed to the deprotonation, delocalization of the negative charge in the carboxylate moiety and its coordination to the metal center.[82] The stretching vibrations of C=N in these complexes, where the metal ion center is bonded to the nitrogen atom of the oximino group of PAO^-, are comparable to those observed in the protonated form of PAO^-, which agrees with the data reported previously for these complexes of divalent 3d transition metals,[23] the light alkali metal (Li, Na, and K),[14] and alkaline earth metal salts.[6] The $\nu_{(N—O)}$ stretching

frequency increased by 2-42 cm^{-1} compared to that observed for the parent acid, HPAO. The noted increase in the $\nu_{(N—O)}$ frequency stretch may be attributed to the strong coordination of the oximino nitrogen atom to the transition metal ion center in these PAO^- complexes and opposite to the trend realized for the alkali[14] and the alkaline earth [6] metal derivatives in which a decrease in this frequency was observed. The existence of IR absorption bands in the 820-860 cm^{-1} region are referred to the vibrations of water molecules coordinated to the metal ion center,[23] while the broad bands at higher wave number (> 2600 cm^{-1}) are suggestive of the existence of H-bonds in the crystalline structure of these compounds[23] (Table 2.20). Such conclusions regarding the coordinated water molecules to the metal ion center and H-bonds on the basis of IR spectra is evidenced by the crystal structure of $Cu(PAO)_2 \cdot 2H_2O$ obtained in this work[7] (*vide supra*), and by the crystal structure of $Mn_4(PAO)_8 \cdot 2H_2O$ reported in literature.[19] The difference between the asymmetric and symmetric stretching frequencies of the carboxylate group, $\Delta\nu$(COO), suggests that the coordination mode of the carboxylate moiety of the PAO^- ligand is monodentate[81] in the complexes of Fe^{2+}, Co^{2+}, Ni^{2+}, and Cu^{2+}. At the same time the PAO^- is bound to the metal ion center through its nitrogen atom of the oximino group to form N, O-chelate five-membered metallacycles, as evidenced from the $\nu_{(C=N)}$ in the IR spectra. Moreover, XRD spectra of Fe^{2+}, Co^{2+}, and Ni^{2+} derivatives are similar to those recorded for the copper compound, which had its structure determined (see above), implying that all of the Fe^{2+}, Co^{2+}, and Ni^{2+} compounds have the same structure as determined for the Cu complex. Accordingly, a likely structure of the Fe^{2+}, Co^{2+}, and Ni^{2+} complexes is as follows (Figure 2.31):

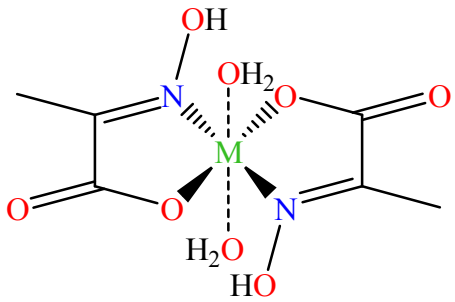

M = Fe^{2+}, Co^{2+}, or Ni^{2+}

Figure 2.31. Suggested structure of iron, cobalt, and nickel PAO^- complexes based on their IR and XRD spectra

On the other hand, the $\Delta\nu_{(COO)}$ calculated for the manganese compound corresponds to the existence of two types of coordination modes of the PAO^- ligand to the Mn^{2+} ion center. The one with $\Delta\nu_{(COO)}$ = 220 cm^{-1} is a bridging carboxylate[83] via chelating the metal ion center with its oximino nitrogen atom, i.e. N, O, O-chelate-bridge. The other one has a $\Delta\nu_{(COO)}$ = 263 cm^{-1}, corresponding to N, O-chelate PAO- ligand. This conclusion, on the basis of IR spectrum, regarding the coordination of both of the PAO^- ligands coordinated to the Mn^{2+} is supported by the observation of these modes of coordination in the structure of the manganese complex determined by single crystal X-ray crystallography.[19]

Thermal Behavior of PAO^- Salts of Divalent 3d Transition Metals

The TGA trace of $Mn_4(PAO)_8 \cdot 2H_2O$ is displayed in Figure 2.32. As can be seen, there are two distinctive decomposition steps. The first takes place over the range of 147-200°C, resulting in a weight loss of around 39.5% of mass, which accounts for the lost of two water molecules and decomposition of one PAO^- ligand. However, the mass loss was found to be 69.5% when carrying out bulk pyrolysis in the muffle furnace (see above

section 2.3 of this Chapter). The difference between the TGA and the bulk pyrolysis in the percentage of the remaining mass can be ascribed to the fact that heat process during the TGA analysis is fast, and thus not enough time is allowed for the material to pyrolyze at this temperature. The latter mass loss resulting from the bulk pyrolysis may be ascribed to deaquation and complete decomposition of the PAO^- ligand. No dehydration step is observed before 147°C, implying that the two water molecules are tightly bounded to the Mn^{2+} ion centers.

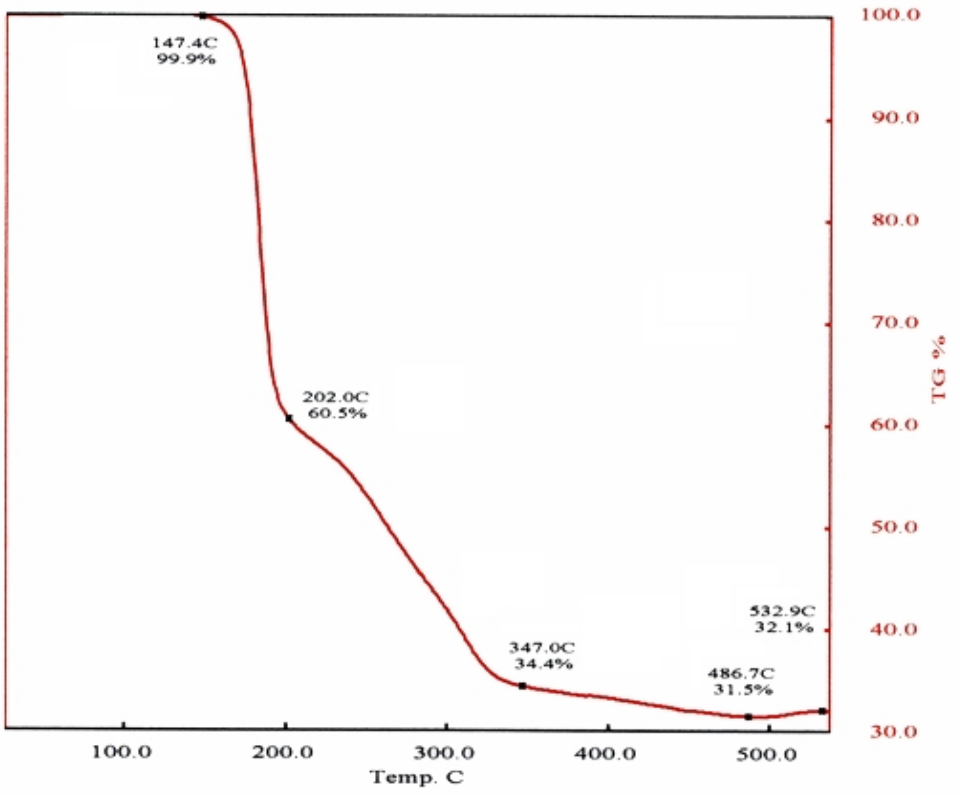

Figure 2.32. The TGA trace for $Mn_4(PAO)_8.2H_2O$ in dry air with a heating rate of 1 °C per minute

The XRD spectrum of the solid obtained at 200°C superimposes on that of the hausmannite phase of manganite, $[Mn^{II}]_{tet}[Mn^{III}_2]_{oct}O_4$. In addition, the peaks of this

XRD spectrum are broad, indicating the existence of nanocrystalline phase of manganite. Measurement of the crystallite size by XRD confirmed this prediction where the crystallite size was found to be 6.3 nm. The second step starts at around 220°C and finishes at 487°C. On the basis of bulk pyrolysis in the muffle furnace at 347°C, the weight change is owing to the dehydroxylation of the manganite surface because the mass decreases only by 3.91% upon raising temperature from 200°C to 347°C. The X-ray analysis of the solid, produced at 347°C, revealed the co-existence of the hausmannite phase of manganite and manganese oxide Mn_5O_8 ($Mn^{II}_2Mn^{IV}_3O_8$). The formation of the latter metastable manganese oxide phase takes place via the oxidation of manganite manganese (III) to manganese (IV) as illustrated in the following chemical equation.[90-93]

$$Mn_3O_4\ (s) + 2/5O_2\ (g) \longrightarrow 3/5Mn_5O_8\ (s) \qquad \text{(Eq. 2.7)}$$

The X-ray spectrum of the solid, obtained at 347°C, is composed of broad peaks of crystallite size of 7.4 nm. On the other hand, according to the TGA trace, the mass change is 26% upon heating the manganese complex to the latter temperature. This mass loss would correspond to a dissociation of the other PAO^- ligand to carbon dioxide and acetonitrile. The increase in weight mass around 500°C is due to the oxidation of the manganite Mn^{2+} to Mn^{3+} and reduction of Mn_5O_8 to manganese trioxide, as shown in the following chemical equations:[90,91]

$$Mn_3O_4\ (s) + 1/4O_2\ (g) \longrightarrow 3/2Mn_2O_3\ (s) \qquad \text{(Eq. 2.8a)}$$

$$3/5Mn_5O_8\ (s) \longrightarrow 3/20O_2\ (g) + 3/2Mn_2O_3\ (s) \qquad \text{(Eq. 2.8b)}$$

The summation of these two equations is an oxidation to manganese trioxide as follows:

$$Mn_3O_4\ (s) + 3/5Mn_5O_8\ (s) + 1/10O_2\ (g) \longrightarrow 3Mn_2O_3\ (s) \qquad \text{(Eq. 2.8c)}$$

The formation of Mn_2O_3 was confirmed by XRD investigations of the decomposition products obtained at 478°C and 533°C. Moreover, the only crystalline phase observed in these XRD patterns is that of Mn_2O_3. The crystallite sizes, measured by XRD, were found to be 32.1 nm and 49.8 nm for Mn_2O_3 obtained at 478°C and 533°C, respectively. Interestingly, heating the manganese complex at 200°C under nitrogen gives a rhodochrosite synthesized phase of manganese carbonate having a hexagonal unit cell as proved by XRD analysis. Acetamide was identified by GC/MS as a byproduct of this decomposition under N_2. Such a product may result from the hydrolysis of the $H_3CC{\equiv}N$ generated by the thermolysis of the PAO^- ligand.

Figure 2.33 displays the TGA and DTA thermograms of the PAO^- derivative of ferrous cation. The TGA trace is not multi step like that observed for zinc complex, but rather is more similar to that noticed for the manganese compound in that the complex undergoes dehydration and ligand dissociation at the same time. This step takes place over a range of temperature between 100°C and 200°C. The loss of water molecules starts at a temperature close to 100°C, indicating the strong binding of these water molecules to the ferrous ion center. The weight lost at 132°C is 16%, corresponding to a lost of two water molecules. This latter temperature can also be taken as the temperature at which the anhydrous complex of ferrous cation is formed. Interestingly, comparing to the PAO complex of zinc, dehydrated at 80°C and completely dehydrated at 129°C, it can be inferred that the aqua ligand is more strongly coordinated to the ferrous center.

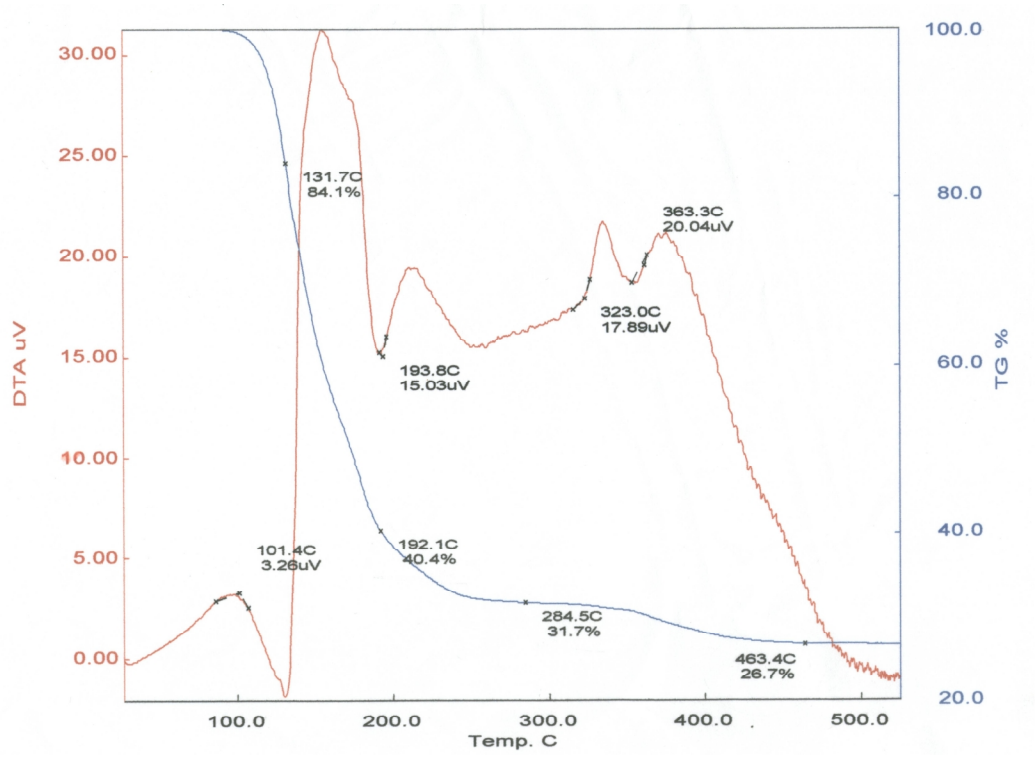

Figure 2.33. The TGA and DTA traces for $Fe(PAO)_2 \cdot 2H_2O$ in dry air with a heating rate of 1 ^oC/min

These facts derived from the TGA investigation regarding deaquation support the structure proposed for the ferrous PAO complex on the basis of its IR and XRD spectra analyses. The removal of the ligated water is an energy consuming process as reflected by the endothermic peak in the DTA trace. The PAO ligand decomposition can be said to start at a temperature higher than 132^oC. The DTA shows this step is accompanied with the release of a large amount of energy, as indicated by a dramatically exothermic peak. This exothermic behavior can be accounted for by the evolution of carbon dioxide and acetonitrile/acetamide resulted from the decomposition of the PAO ligand. The iron oxide thus resulted from the pyrolysis of the PAO complex seems to undergo two successive weight loss steps accompanied with three consecutive, exothermic steps as revealed by the TGA and DTA investigation. However, the mass difference is small

between the beginning weight and the end weight of each of these two steps. The mass loss can be ascribed to the dehydration of the hydroxyl groups existing on the surface of the iron oxide and/or conversion of maghemite phase (γ-Fe_2O_3) to hematite phase (α-Fe_2O_3). The former phase was observed in the X-ray spectrum of the pyrolysis product of the ferrous PAO complex at 197^{o}C under an air stream. However, upon the pyrolysis of the ferrous PAO complex in air atmosphere at 285^{o}C, hematite (α-Fe_2O_3) and maghemite (γ-Fe_2O_3) were detected by X-ray while at 463^{o}C hematite (α-Fe_2O_3) was the only detected phase of iron oxide by XRD (Figure 2.34). The latter result is logical because the *alpha* phase is the most thermodynamically stable phase of iron oxide under the oxidation conditions. The XRD analysis of the crystallite size of the hematite obtained at 197 ^{o}C, 285 ^{o}C, and 463 ^{o}C reveals that the crystallite size increases with increasing the temperature, as also reflected by increasing the sharpness of the peaks in the XRD spectra. The average crystallite sizes are 3.0, 1.3, and 30.0 nm with size distribution of 4.2, 2.7, 24.9 nm (full width at half height, FWHM) for the iron oxide obtained at 197 ^{o}C, 285 ^{o}C, and 463 ^{o}C, respectively.

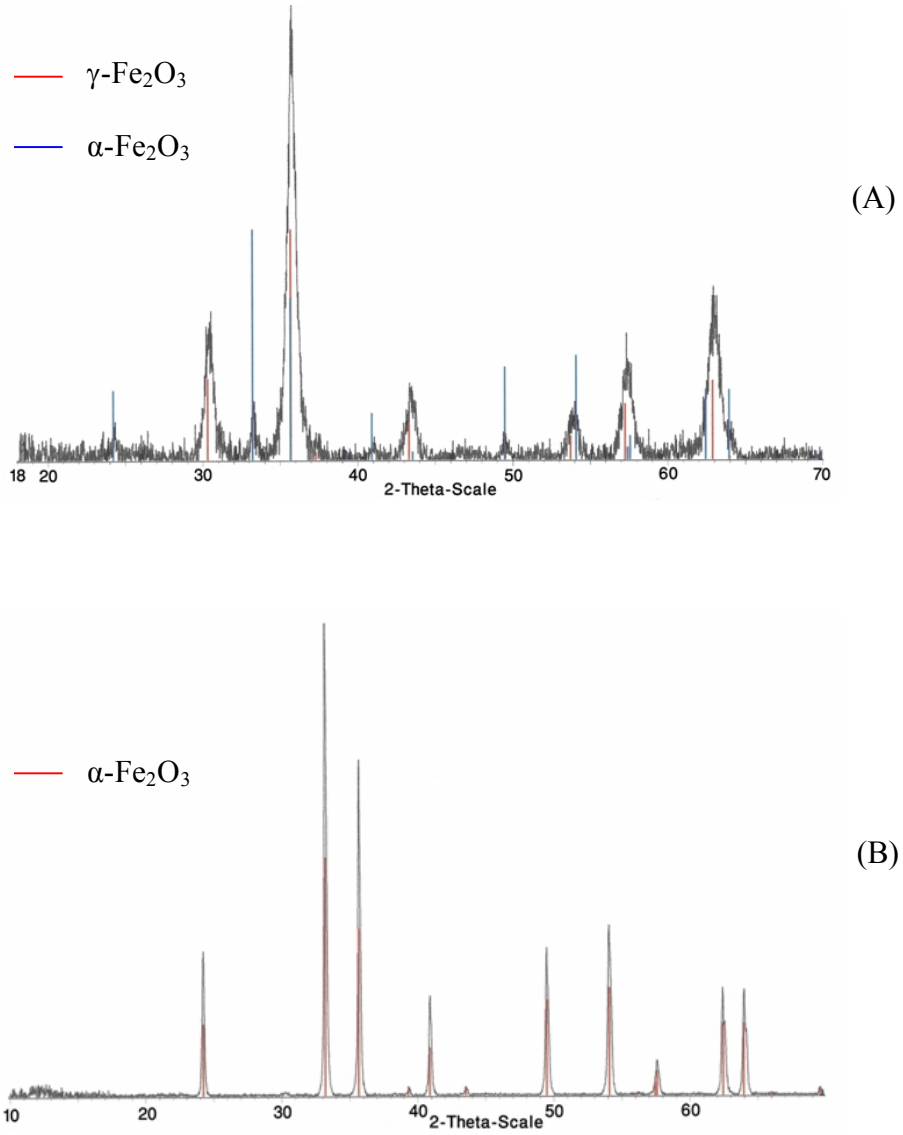

Figure 2.34. The XRD spectra for $Fe(PAO)_2 \cdot 2H_2O$ heated under air stream to (A) 285 ^oC and (B) 463 ^oC

In Figure 2.35, the TGA trace of the cobalt PAO complex is depicted. It is obvious that this TGA resembles those of nickel and zinc derivatives in which the complex is decomposed in stepwise fashion. The first step refers to the dehydration process of the cobalt complex with an onset at 100^{o}C. After the completion of the deaquation process at 149^{o}C, the weight of the complex changes by 18%, which corresponds to the loss of two water molecules. The relative high temperature of

dehydration indicates that these water molecules are ligated to the cobaltous cation center. This attachment of water molecules to the cobalt ion center, concluded from the TGA, agrees with the structure suggested for $Co(PAO)_2 \cdot 2H_2O$ on the basis of its IR and XRD spectra. The occurrence of the deaquation of the cobalt complex over a range of 100^oC-149^oC may indicate a stronger binding of the water molecules to the cobaltous center compared to ferrous and zinc centers with ranges of dehydration of 100^oC-132^oC and 80^oC-129^oC, respectively. The second step is assigned to the thermal dissociation of one of the PAO ligand. The third step refers to the pyrolysis of the other PAO ligand. In each of the second and third decomposition step, the weight lost is owing to the evolution of a molecule of carbon dioxide and a molecule of acetonitrile.

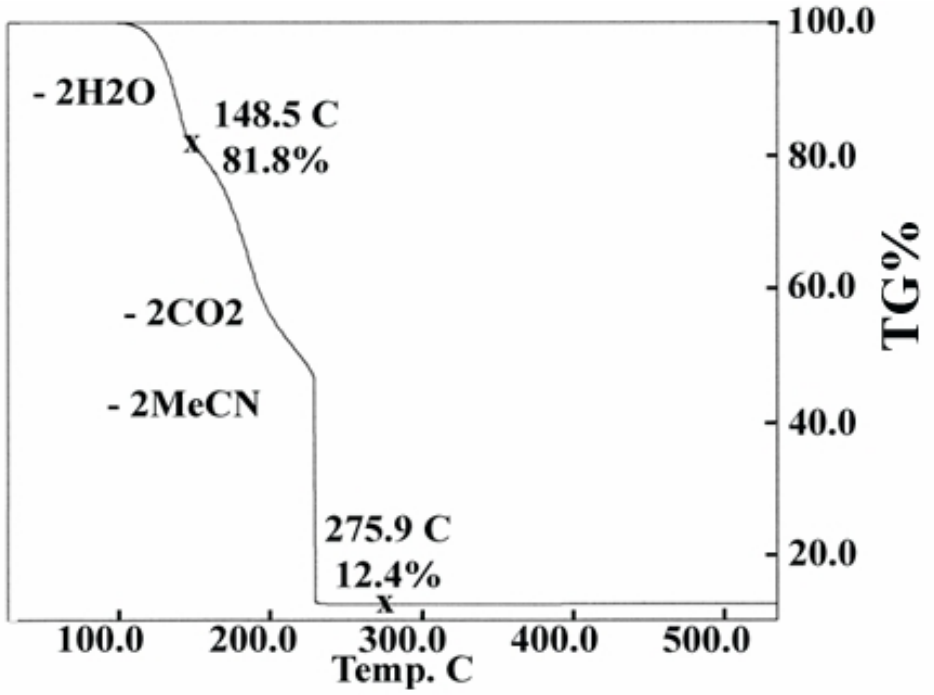

Figure 2.35. The TGA trace for $Co(PAO)_2 \cdot 2H_2O$ in dry air with a heating rate of 1 ^oC/min

The final product of the pyrolysis of the cobalt PAO complex at 276 ^{o}C was found to be a cobaltosic oxide ($Co^{II}Co^{III}_2O_4$), as defined by the XRD analysis (Figure 2.36). The peaks in the XRD spectrum are broad, indicating the existence of a nanocrystalline phase.

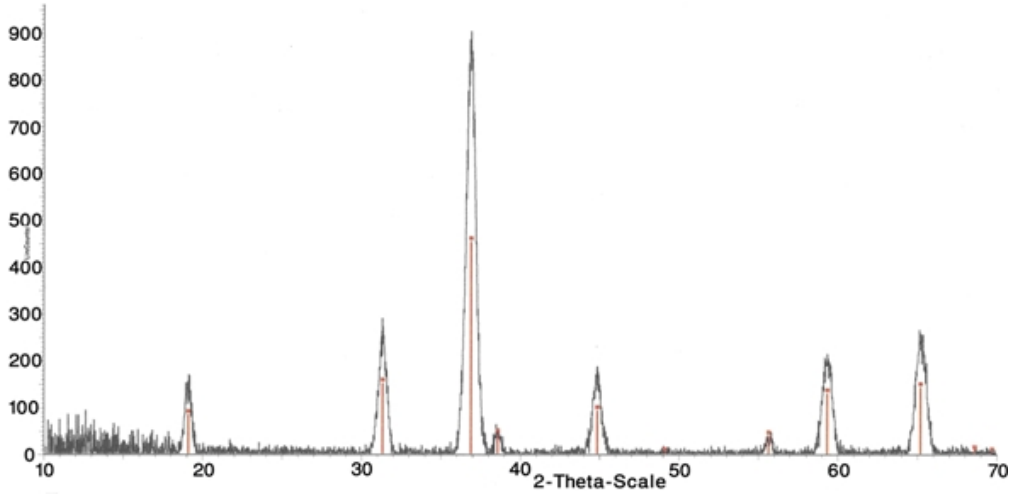

Figure 2.36. The XRD spectrum for $Co(PAO)_2 \cdot 2H_2O$ heated under air stream to 276 ^{o}C

Measurement of the crystallite size by the XRD confirms this expectation, where the average crystallite size was found to be 6.4 nm with a narrow distribution (5.8 nm full width at half height, FWHM) (Figure 2.37).

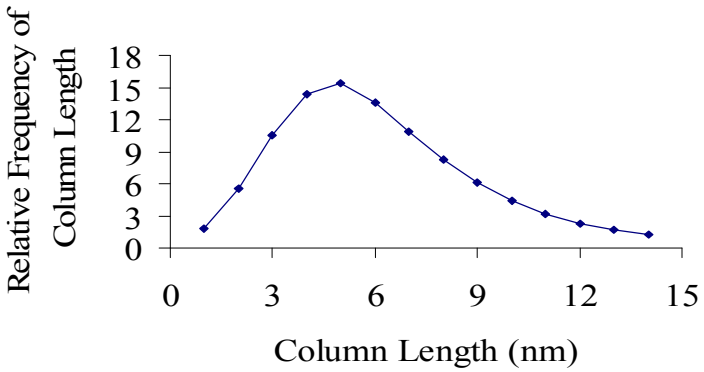

Figure 2.37. Crystallite size of Co_3O_4 obtained under air stream at 276 ^{o}C

The morphology of the Co_3O_4 thus obtained was studied by SEM (Figure 2.38) revealing that the particles have a rod-like shape and are porous. These two morphological features (the nanometric size and porosity) endow the Co_3O_4 with a relatively high BET surface area of 58.76m^2/g.

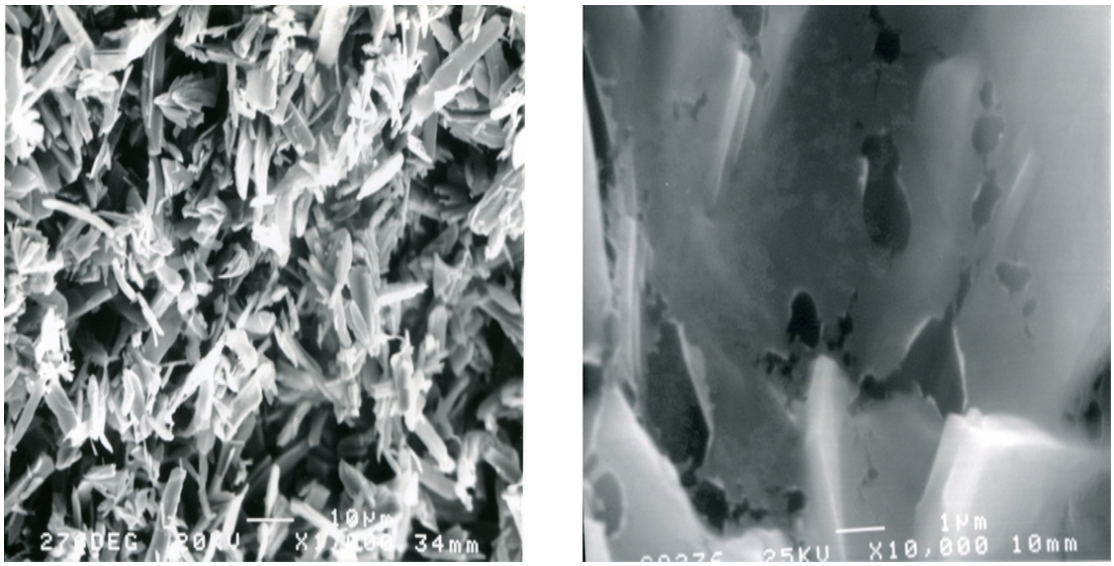

x 1,000 **x 10,000**

Figure 2.38. The SEM electromicrographs of Co_3O_4 obtained at 276 ^oC

The TGA and DTA thermograms of the nickel PAO complex are shown in Figure 2.39. It can be noticed that the TGA trace is made up of three steps. The first one is attributed to the deaquation of the complex. This step has an onset at 100^{o}C and an end around 169^{o}C. This dehydration step results in weight loss of 19%, which corresponds to the loss of two water molecules. Again, the relative high temperature range at which the dehydration occurs is an implication of the strong binding of these water molecules to the nickelous cation center. In addition, it can be deduced that the bond between ligated

water and the Ni (II) center is much stronger than that found in iron (II), cobalt (II), and zinc complexes. As expected, the dehydration step requires adsorption of some of the energy in order to take place, reflected by the endothermic peak in the DTA trace. These facts drawn from the removal of the water molecules step are in agreement with the structure predicted for $Ni(PAO)_2 \cdot 2H_2O$ on the basis of its IR and XRD spectrum. The second step, following the loss of coordinated water molecules, is due to the decomposition of one PAO ligand and is responsible for weight loss of 27.5%, which is attributed to the loss of a molecule of carbon dioxide and a molecule of acetonitrile. The third step corresponds to a weight loss of 21.4% and it can be ascribed to the loss of a molecule of carbon dioxide and a molecule of acetonitrile resulting from the decomposition of the other PAO ligand. The second and third steps are exothermic as revealed by the DTA investigation. The general pattern of TGA of the nickel PAO complex is very similar to those observed for cobalt and zinc derivatives.

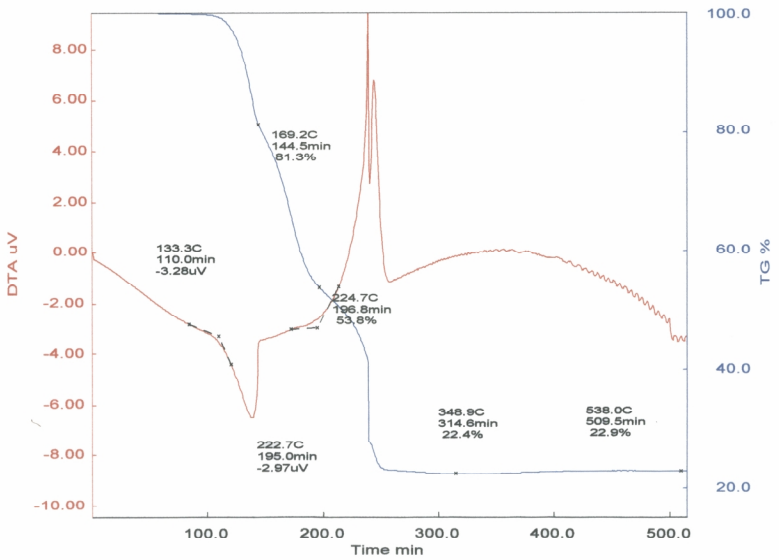

Figure 2.39. The TGA and DTA traces for $Ni(PAO)_2 \cdot 2H_2O$ in dry air with a heating rate of 1 ^oC/min

Bulk pyrolysis of the nickel complex at 340 ^{o}C led to the formation of nickel oxide and nickel metal along with nickel carbonate, as revealed by XRD analysis (Figure 2.40A). Formation of nickel metal can be attributed to a radical oxidation mechanism in which PAO^- ligand undergoes decarboxylation and formation of the radical $[OHN{=}C{-}CH_3]^{\cdot}$, which is converted either to dimethylglyoxime or acetaldoxime. Nickel oxide, however, was found to be the pyrolysis product after heating $Ni(PAO)_2{\cdot}2H_2O$ at 538^{o}C overnight, as confirmed by XRD analysis of the solid remain (Figure 2.40B).

Pyrolysis of $Ni(PAO)_2{\cdot}2H_2O$ at 340^{o}C in a pressure tube allowed a greater insight into its thermal decomposition mechanism through the analysis of the confined products. The analysis of the off-gases by GC-MS revealed the detection of carbon dioxide. The analysis of the crystals accumulated on the walls of the tube by XRD showed the existence of crystalline ammonium bicarbonate. Washing the remaining contents of the tube after removal of the latter crystals with methanol and then analysis of this alcoholic extract by GC-MS led to detection of acetamide and acetic acid. Acetamide might have resulted from the hydrolysis of acetonitrile produced during the pyrolysis course of the PAO^- ligand. Further hydrolysis of acetamide would be responsible for the formation of acetic acid and ammonium cation. The hydrolysis of nitriles is a well-known synthetic path to carboxylic acids in the discipline of organic chemistry. Bicarbonate anion is readily formed by the hydrolysis of carbon dioxide. Acetamide, however, could be formed through a Beckmann rearrangement, as it is discussed in detail in Chapter 3. It appears that the thermal decomposition of the nickel complex is complicated and diverse mechanistic pathways can be followed to reach the final products.

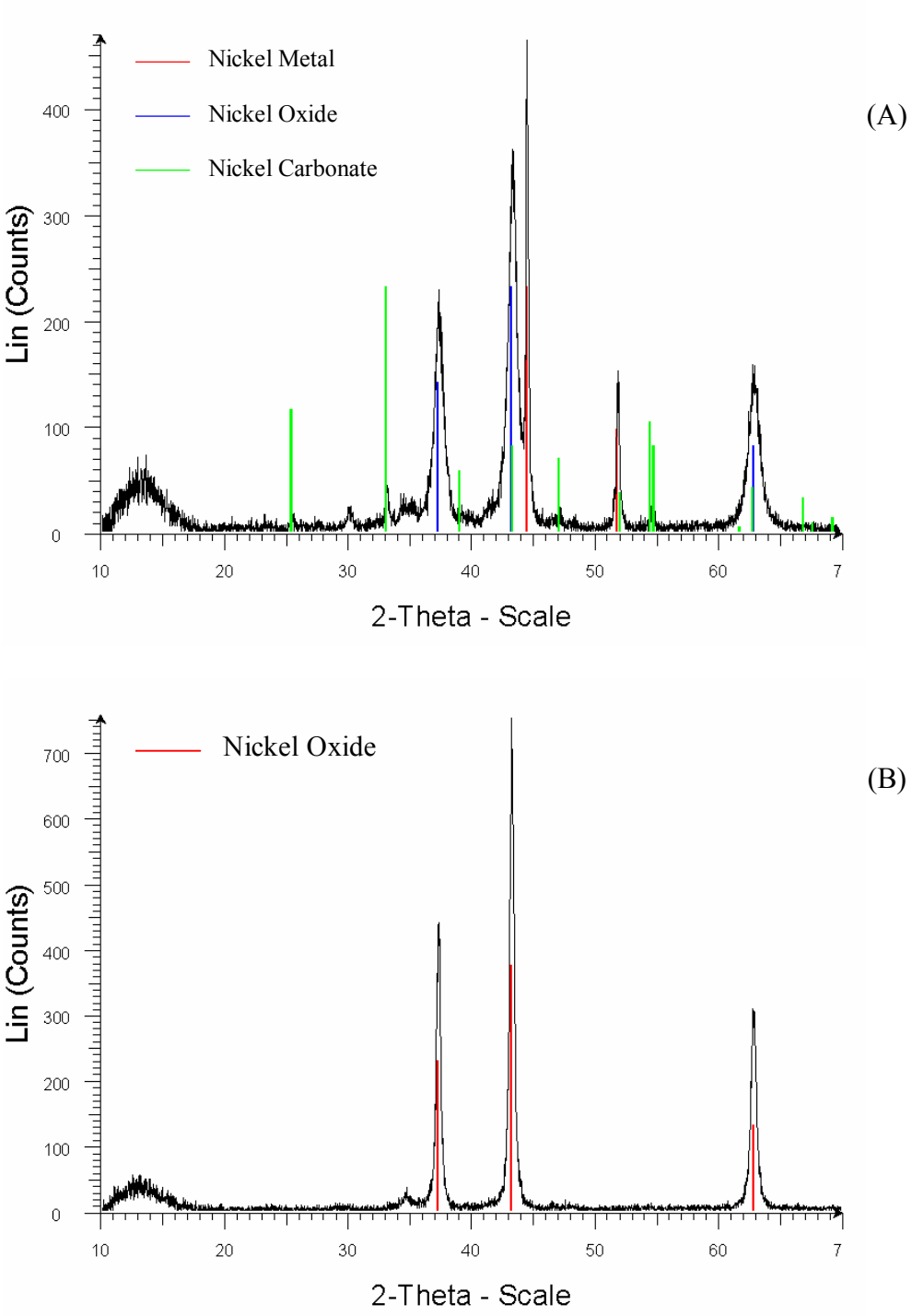

Figure 2.40. The XRD spectra for $Ni(PAO)_2 \cdot 2H_2O$ heated to (A) 340 ^oC and (B) 538 ^oC

The TGA and DTA of $Cu(PAO)_2 \cdot 2H_2O$ analyses are shown in Figure 2.41. The TGA trace is composed of two weight losses. The first of these occurs over the range of 54°C to 100°C, results in loss of 11.9% of the mass, and corresponds to dehydration of the complex. By comparison, dehydration of $Cu_2(O_2CCH_3)_4 \cdot 2H_2O$ was previously reported to occur over the range 100-180°C, indicating that the waters are much less loosely bound in $Cu(PAO)_2 \cdot 2H_2O$. In addition, the temperature range at which $Cu(PAO)_2 \cdot 2H_2O$ dehydrates is lower than those for the ferrous, cobaltous, nickelous, and zinc derivatives, indicating that the water molecules bind more weakly to the cupric center. This weak coordination of the aqua ligand to the cupric center in the $Cu(PAO)_2 \cdot 2H_2O$ can be attributed to Jahn-Teller distortion, a common, well-known phenomenon observed for octahedral-coordinated cupric ion center. Accordingly, the Jahn-Teller distortion in $Cu(PAO)_2 \cdot 2H_2O$ is a tetragonal elongation along the z-axis. The second weight loss is due to decomposition of the ligand and has an onset temperature of 148°C and is complete at 290°C. Thus, the decomposition of $Cu(PAO)_2$ has an onset temperature that is 52°C lower than that of $Cu_2(O_2CCH_3)_4$, which decarboxylates over the range 200-290°C.

The XRD analysis of the ceramic residue from a bulk sample of $Cu(PAO)_2 \cdot 2H_2O$ pyrolyzed under nitrogen yielded a mixture of cuprous and cupric oxides. The formation of cuprous oxide suggested a second mechanism of decomposition other than that shown in Figure 3.1 in Chapter 3. Analysis of the organic byproducts of the thermal decomposition by GC/MS demonstrated that, in addition to the expected acetonitrile, the pyrolysis reaction also produced acetoxime and dimethylglyoxime. These products are likely derived from the radical decomposition pathway shown in Figure 2.42.

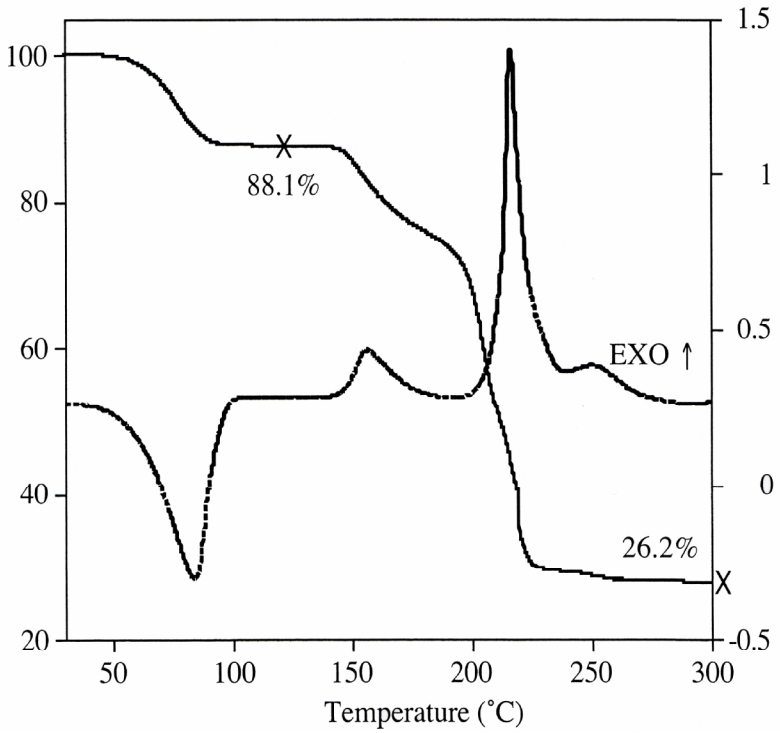

Figure 2.41. The TGA and DTA traces for $Cu(PAO)_2 \cdot 2H_2O$ in dry air with a heating rate of 1 ^{o}C/min

Cupric carboxylates are particularly prone to undergoing decarboxylation via a redox process leading to the formation of cuprous salts or copper metal. The competing thermal decomposition mechanisms likely account for the complex shape of the TGA trace for the pyrolysis step. Also, it is likely that the products from the radical pathway account for the relatively high temperature for complete removal of organics as compared to other 2-oximinopropionate complexes.

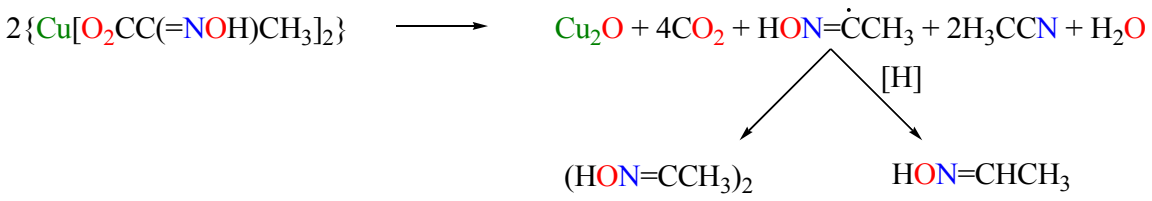

Figure 2.42. Radical pyrolysis pathway of $Cu(PAO)_2$

Heating $Cu(PAO)_2 \cdot 2H_2O$ in an aqueous suspension to reflux was found to almost completely convert it to cuprous oxide, albeit rather slowly, indicating that the radical decomposition pathway is favored at lower temperatures. DTA (Figure 2.41) indicates that the dehydration process is endothermic. The thermal decomposition step is slightly better resolved in the DTA trace and three separate exotherms can be identified, an initial one from 148-181^oC and two overlapping exotherms in the range 196-267^oC.

Pyrolysis of bulk sample of $Cu(PAO)_2 \cdot 2H_2O$ at 220^oC (approximately the most exothermic point in the thermal decomposition) in air produces a voluminous brown-black solid. The XRD analysis (Figure 2.43) demonstrated that the only detectable crystalline product present was the tenorite phase of cupric oxide. No cuprous oxide was observed since it would have been readily oxidized to cupric oxide by ambient oxygen under the experimental conditions used.

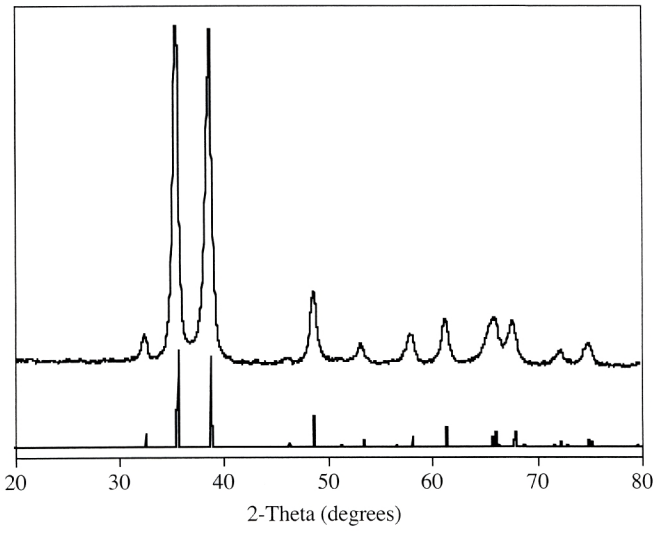

Figure 2.43. The XRD spectrum for $Cu(PAO)_2 \cdot 2H_2O$ heated under air stream to 220 ^oC

Crystallite size analysis (Figure 2.44) of the pattern yielded an average crystallite size of 8.9 nm while the crystallite size with highest frequency is 1.6 nm. Thus, there is a large size-distribution but very small particles predominate. SEM (Figure 2.45) shows that the particles are aggregated into filamentous clusters. BET surface area analysis demonstrated a surface area of 21.7m^2/g. By comparison, commercial cupric oxide powders have surface area of 3.1-3.4m^2/g while the one prepared by low-pressure spray pyrolysis, a favored method for synthesis of nanoparticulate powders, was reported to yield a material with a surface area of 17m^2/g using copper acetate as the copper source. Thus, it may be concluded that complexes of 2-oximinopropionates are promising precursors for nanoparticulate metal oxides with high surface areas. It is likely that dispersing the metal complex in air or in an inert solvent before pyrolysis will yield powders with less agglomeration and higher surface areas.

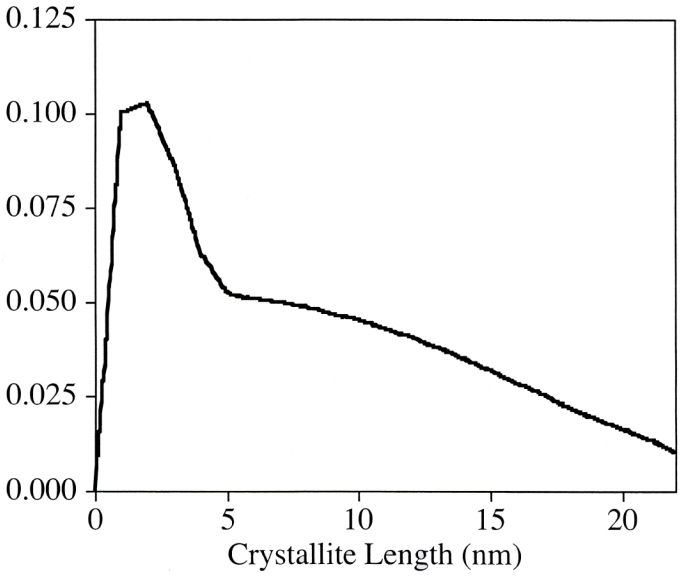

Figure 2.44. Crystallite size of CuO obtained under air stream at 220 ^{o}C

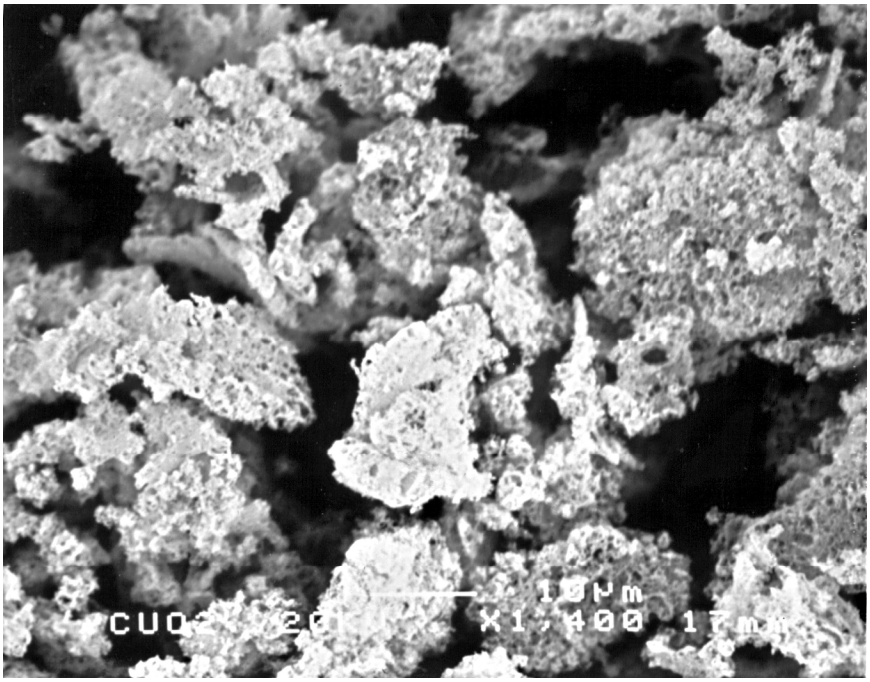

Figure 2.45. SEM electronmicrograph of CuO obtained under air at 220 ^{o}C

PAO^{-} Salts of Some Trivalent Lanthanides

The cerium and praseodymium derivatives were prepared and characterized by IR and XRD spectroscopy. The crystal structure of the praseodymium complex was also established by single crystal X-ray diffraction spectroscopy (Figure 2.46).

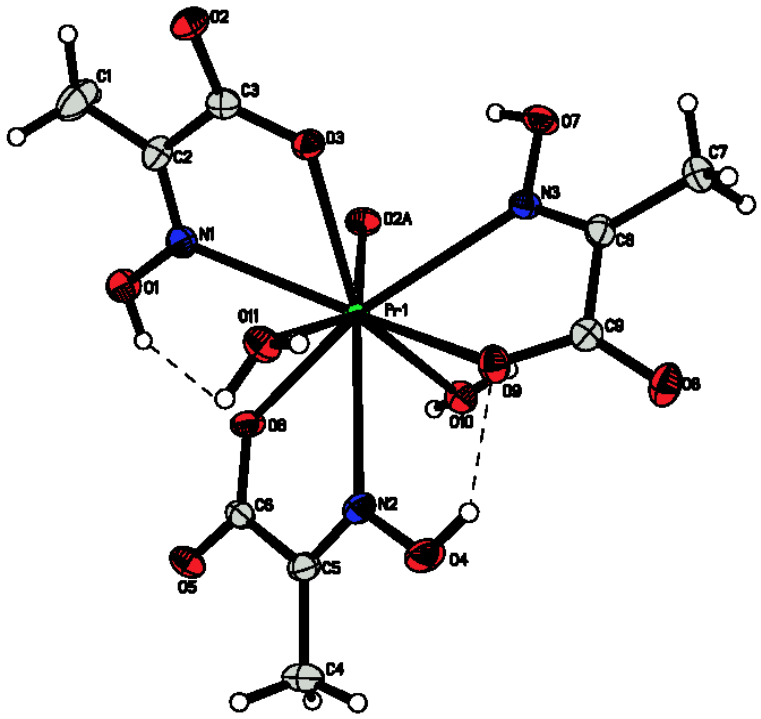

Figure 2.46. Crystal structure of $Pr(PAO)_3(H_2O)_2$ drawn at 50% level

It is demonstrated by the latter technique that the praseodymium and the cerium complexes are not isostructural, opposing the previous claim based on their XRD patterns.[15] The praseodymium (III) ion center has a coordination number of nine, where two coordination sites are occupied by the oxygen atoms of two water molecules with bond length of 2.4730(12) and 2.5272(12) Å corresponding to Pr(1)—O(10), and Pr(1)—O(11) (see Table 2.21). These values are comparable to that found in praseodymium acetate monohydrate [$Pr(O_2CCH_3)_3(H_2O)$], where the water molecule is attached to Pr^{3+} at a distance of 2.541(3) Å.[94]

Table 2.21. Bond Distances (Å) for $Pr(PAO)_3(H_2O)_2$

Pr(1)-O(2)#1	2.4228(12)	O(10)-H(10D)	0.837(4)
Pr(1)-O(9)	2.4597(13)	O(10)-H(10E)	0.837(4)
Pr(1)-O(6)	2.4611(14)	O(11)-H(11D)	0.839(4)
Pr(1)-O(10)	2.4730(12)	O(11)-H(11E)	0.839(4)
Pr(1)-O(3)	2.5064(11)	N(1)-C(2)	1.278(2)
Pr(1)-O(11)	2.5272(12)	N(2)-C(5)	1.275(2)
Pr(1)-N(1)	2.6726(16)	N(3)-C(8)	1.277(2)
Pr(1)-N(2)	2.6767(12)	C(1)-C(2)	1.485(3)
Pr(1)-N(3)	2.7358(15)	C(1)-H(1A)	0.9800
O(1)-N(1)	1.387(2)	C(1)-H(1B)	0.9800
O(1)-H(1D)	0.8400	C(1)-H(1C)	0.9800
O(2)-C(3)	1.244(2)	C(2)-C(3)	1.512(2)
O(2)-Pr(1)#2	2.4229(12)	C(4)-C(5)	1.493(2)
O(3)-C(3)	1.263(2)	C(4)-H(4A)	0.9800
O(4)-N(2)	1.3749(19)	C(4)-H(4B)	0.9800
O(4)-H(4D)	0.8400	C(4)-H(4C)	0.9800
O(5)-C(6)	1.237(3)	C(5)-C(6)	1.511(3)
O(6)-C(6)	1.279(2)	C(7)-C(8)	1.496(2)
O(7)-N(3)	1.3751(18)	C(7)-H(7A)	0.9800
O(7)-H(7D)	0.8400	C(7)-H(7B)	0.9800
O(8)-C(9)	1.236(3)	C(7)-H(7C)	0.9800
O(9)-C(9)	1.273(2)	C(8)-C(9)	1.519(3)

Numbers in parentheses are estimated standard deviations in the least significant digits. Symmetry transformations used to generate equivalent atoms: #1 x+1/2,-y+1/2,z, #2 x-1/2,-y+1/2,z .

The differences in the Pr—O bond lengths for the praseodymium complexes is due to the variation in the distortion of the coordination environment of the Pr^{3+}, which in turn is a consequence of the different ligands, PAO^- and H_3CCOO^-, the different ligating mode of both ligands, and the different natures of the H-bonding in both salts. Six of the coordination sites in the praseodymium sphere of $Pr(PAO)_3(H_2O)_2$ are occupied by three ligands of PAO^-, where each of them chelates the praseodymium center to form a five-membered metallacycle, attached through the nitrogen atom, Pr(1)—N(1), Pr(1)—N(2) and Pr(1)—N(3) having a distance of 2.6726(16), 2.6767(12) and 2.7358(15) Å, respectively, and through the deprotonated hydroxyl oxygen atom of carboxylate moiety, Pr(1)—O(3), Pr(1)—O(6) and Pr(1)—O(9) having a distance of 2.5064(11), 2.4611(14) and 2.4597(13) Å, respectively. These distances are close to that found in praseodymium acetate monohydrate Pr(1)—O(1), Pr(1)—O(2), Pr(1)—O(3), and Pr(1)—O(4) having a distance of 2.411(3), 2.516(3), 2.580(3), and 2.601(3) Å, respectively, where the acetate is also coordinated to the Pr^{3+} in a bidentate fashion.[92] However, the bond distances between the Pr^{3+} center and the N-dentate and the O-dentate of the PAO^- ligand, as expected, are shorter than their analogues in the cerium(III)[15] derivative due to the smaller ionic radius of the nona-coordinated Pr^{3+} (1.179 Å)[80] than that of the nona-coordinated Ce^{3+} (1.196 Å).[80] The coordination in the praseodymium sphere of $Pr(PAO)_3{\cdot}2H_2O$ is completed by a bridging carboxylate carbonyl oxygen atom from an adjacent molecule, Pr(1)—O(2A) with a distance of 2.4228(12) Å, resembling the carboxylate carbonyl oxygen bridge observed in the structures of sodium,[14] calcium,[6] manganese,[19] yttrium,[15] and cerium[1,3] PAO^- complexes. Such a bridge was also observed in the structure of praseodymium triacetate monohydrate.[94] The Pr(1)—O(2A),

surprisingly, is shorter than the Pr(1)—O(3), Pr(1)—O(6), Pr(1)—O(9) bonds. A similar observation was also reported for the structures of praseodymium triacetate monohydrate[92] and PAO^- complexes of cerium(III)[15] and calcium.[6] However, the bond length of the bridge in the sodium derivative of PAO^- is found to be longer in comparison to the non-bridging bond.[14] The bidentate N,O-chelate PAO^- ligands show partial delocalization of the negative charge because of the slight large difference (0.019, 0.042 and 0.037 Å) in the bond lengths of the two carbon-oxygen bonds of each carboxylate moiety, O(2)—C(3) = 1.244(2) Å, O(3)—C(3) = 1.263(2) Å, O(5)—C(6) = 1.237(3) Å, O(6)—C(6) = 1.279(2) Å, O(8)—C(9) = 1.236(3) Å and O(9)—C(9) = 1.273(2) Å. The longer distances of the O(3)—C(3), O(6)—C(6), and O(9)—C(9) bonds can be ascribed to the fact that O(3), O(6) and O(9) oxygen atoms are bonded to the praseodymium ion center. The O(2)—C(3) bond is longer than its analogs O(5)—C(6) and O(8)—C(9) because O(2) atom functions as a bridge to a neighboring praseodymium center. The PAO^- chelates the praseodymium center to form a five-membered metallacycle, which is similar to that previously found in the $Na(PAO)\cdot H_2O$,[14] $Ca(PAO)_2\cdot H_2O$,[6] $Mn_4(PAO)_8\cdot 2H_2O$,[19] $Y(PAO)_3(DMSO)(H_2O)\cdot 2H_2O$,[15] and $Ce(PAO)_3$[1,3] structures. However, the bond lengths of the praseodymium—oximino nitrogen atom contacts, Pr(1)—N(1), Pr(1)—N(2) and Pr(1)—N(3) have bond distances of 2.6726(16), 2.6767(12) and 2.7358(15) Å, respectively, that are much longer than those reported for sodium[14] and calcium[6] derivatives (2.440(2)[14] and 2.503(2)[6] Å, respectively), but shorter than that noticed for the cerium complex (2.821(3) Å).[15] The oxygen atoms of the deprotonated hydroxyl groups of the carboxyl moieties, Pr(1)—O(3), Pr(1)—O(6) and Pr(1)—O(9), have bond lengths of 2.5064(11), 2.4611(14) and 2.4597(13) Å,

respectively, which are about the length as those published for sodium,[14] calcium,[6] and cerium[15] derivatives (2.490(2),[14] 2.513(1),[6] and 2.507(2) Å,[15] respectively). The longer bond lengths of M—N and the similar bond lengths of M—O (M = Na, Ca, or Pr) observed for the so-formed N,O-chelate five-membered ring in the Pr derivative reflect the larger size of the nona-coordinated Pr^{3+} (1.179 Å)[80] in comparison to the equal size (1.12 Å)[78] of the hepta-coordinated Na^{1+} and the octa-coordinated Ca^{2+}. Moreover, the different coordination environment and number of each metal cation and the different ligating modes adopted by PAO^- in each salt play a role. The carboxyl group of the N,O-chelate PAO^- in the praseodymium salt has almost equal C—O bond lengths, O(2)—C(3) = 1.244(2) Å, O(3)—C(3) = 1.263(2) Å, O(5)—C(6) = 1.237(3) Å, O(6)—C(6) = 1.279(2) Å, O(8)—C(9) = 1.236(3) Å and O(9)—C(9) = 1.273(2) Å, indicating the full delocalization of the negative charge on the carboxylate moiety. Comparing these bond distances with typical C—O (1.36 Å), and C═O (1.23 Å) bond lengths demonstrates that carboxylate carbon-oxygen bonds have intermediate distances between the single and double carbon-oxygen bond lengths.[79] This affirms the deduction of the complete negative charge delocalization. A similar full delocalization of the negative charge of the carboxylate moiety of the N,O-chelate PAO^- was also observed earlier in the $Na(PAO)\cdot H_2O$ salt.[14,15] The values of the bond lengths for the rest of the bonds in the three five-membered rings are C(2)—C(3), C(2)—C(1), C(2)—N(1), N(1)—O(1), C(5)—C(6), C(5)—C(4), C(5)—N(2), N(2)—O(4), C(8)—C(9), C(8)—C(7), C(8)—N(3), N(3)—O(7) are, respectively, 1.512(2), 1.485(3), 1.278(2), 1.387(2), 1.511(3), 1.493(2), 1.275(2), 1.3749(19), 1.519(3), 1.496(2), 1.277(2), and 1.3751(18) Å, respectively. These are also similar to those reported for the PAO^- complexes of Na^{1+} (1.487(2), 1.515(2),

1.281(2), and 1.396(2) Å, respectively),[14] Ca^{2+} (1.487(3), 1.624(2), 1.275(2), and 1.392(2) Å, respectively),[6] Ni^{2+} (1.47(2), 1.50(2), 1.28(2), and 1.38(1) Å, respectively),[21] and Cu^{2+} (1.47(1), 1.49(1), 1.27(1), and 1.360(8) Å, respectively).[20] The similarity between each of these bonds suggests that the different metal ion centers have only a slight effect on the geometry of the N,O-chelated PAO^- ligands. It is clear from the above discussion that the same coordination number, the existence of three metallacycles due to the three N,O-chelate PAO^- ligands, and the existence of bridging carboxylate carbonyl oxygen are the common features between the Ce^{3+} and Pr^{3+} PAO^- complexes. The main differences, on the other hand, between these two complexes are the existence of two ligating water molecules in the coordination sphere of the Pr^{3+}, while there is no any water molecules coordinated to the Ce^{3+} center.[15] In addition, the latter ion center completes its coordination by three bridging carboxylate carbonyl oxygen atoms from adjacent molecules,[1,3,15] while there is only one of such bridge in the Pr^{3+} complex.

The Pr^{3+} ion center has a distorted polyhedron environment due to the N,O-chelate adopted by the PAO^- ligands to create a five-membered metallacycle, leading to narrow biting angles, O(3)—Pr(1)—N(1), O(6)—Pr(1)—N(2) and O(9)—Pr(1)—N(3), *ca*. 60.46(4), 60.22(5) and 60.52(4)^o, respectively (see Table 2.22), which in turn reflects the rigidity of the O═C—C═N fragments of the PAO^- ion.[18] These bite angles of N,O-chelate PAO^- ligands are comparable to those observed in sodium[14], calcium[6], yttrium,[15] and cerium[15] derivatives [64.08(5),[14] 62.28(5),[6] 62.6(3)-64.3(3),[15] and 58.76(8)^o,[15] respectively], smaller than those observed in Ni^{2+},[21] $Co^{3+}(Im)_2$,[18] $Co^{3+}(Py)_2$,[18] and Cu(II)[20] complexes [76.8(3),[21] 83.46(7),[18] 82.78(5),[18] and 82.0(2)^o,[20] respectively], and

larger than those reported for $Pr(O_2CCH_3)_3(H_2O)$, having bite angles of 50.1(1) and 50.2(1)°.[94]

Table 2.22. Interbond Angles (°) for $Pr(PAO)_3(H_2O)_2$

O(2)#1-Pr(1)-O(9)	130.04(4)	Pr(1)-O(11)-H(11E)	121.0(11)
O(2)#1-Pr(1)-O(6)	89.88(4)	H(11D)-O(11)-	103.1(12)
O(9)-Pr(1)-O(6)	125.09(4)	C(2)-N(1)-O(1)	113.79(15)
O(2)#1-Pr(1)-O(10)	73.58(4)	C(2)-N(1)-Pr(1)	121.45(12)
O(9)-Pr(1)-O(10)	79.83(4)	O(1)-N(1)-Pr(1)	123.02(11)
O(6)-Pr(1)-O(10)	78.19(4)	C(5)-N(2)-O(4)	114.56(13)
O(2)#1-Pr(1)-O(3)	80.69(4)	C(5)-N(2)-Pr(1)	122.00(12)
O(9)-Pr(1)-O(3)	100.51(4)	O(4)-N(2)-Pr(1)	123.40(10)
O(6)-Pr(1)-O(3)	124.98(4)	C(8)-N(3)-O(7)	112.93(14)
O(10)-Pr(1)-O(3)	145.48(4)	C(8)-N(3)-Pr(1)	118.92(11)
O(2)#1-Pr(1)-O(11)	145.67(4)	O(7)-N(3)-Pr(1)	128.01(10)
O(9)-Pr(1)-O(11)	76.05(4)	C(2)-C(1)-H(1A)	109.5
O(6)-Pr(1)-O(11)	89.68(5)	C(2)-C(1)-H(1B)	109.5
O(10)-Pr(1)-O(11)	139.51(4)	H(1A)-C(1)-H(1B)	109.5
O(3)-Pr(1)-O(11)	71.64(4)	H(11D)-O(11)-	103.1(12)
O(2)#1-Pr(1)-N(1)	71.36(5)	C(2)-N(1)-O(1)	113.79(15)
O(9)-Pr(1)-N(1)	151.31(5)	C(2)-N(1)-Pr(1)	121.45(12)
O(6)-Pr(1)-N(1)	65.14(5)	O(1)-N(1)-Pr(1)	123.02(11)
O(10)-Pr(1)-N(1)	128.33(5)	C(5)-N(2)-O(4)	114.56(13)

Table 2.22. (Continued)

O(3)-Pr(1)-N(1)	60.46(4)	C(5)-N(2)-Pr(1)	122.00(12)
O(11)-Pr(1)-N(1)	77.40(5)	O(4)-N(2)-Pr(1)	123.40(10)
O(2)#1-Pr(1)-N(2)	137.38(4)	C(8)-N(3)-O(7)	112.93(14)
O(9)-Pr(1)-N(2)	65.15(4)	C(8)-N(3)-Pr(1)	118.92(11)
O(6)-Pr(1)-N(2)	60.22(5)	O(7)-N(3)-Pr(1)	128.01(10)
O(10)-Pr(1)-N(2)	71.12(4)	C(2)-C(1)-H(1A)	109.5
O(3)-Pr(1)-N(2)	140.64(4)	C(2)-C(1)-H(1B)	109.5
O(11)-Pr(1)-N(2)	69.35(4)	H(1A)-C(1)-H(1B)	109.5
N(1)-Pr(1)-N(2)	114.57(5)	C(2)-C(1)-H(1C)	109.5
O(2)#1-Pr(1)-N(3)	72.48(4)	H(4B)-C(4)-H(4C)	109.5
O(9)-Pr(1)-N(3)	60.52(4)	N(2)-C(5)-C(4)	126.38(17)
O(6)-Pr(1)-N(3)	152.54(4)	N(2)-C(5)-C(6)	113.05(15)
O(10)-Pr(1)-N(3)	76.70(4)	C(4)-C(5)-C(6)	120.56(16)
O(3)-Pr(1)-N(3)	73.82(4)	O(5)-C(6)-O(6)	125.05(19)
O(11)-Pr(1)-N(3)	116.82(5)	O(5)-C(6)-C(5)	118.28(17)
N(1)-Pr(1)-N(3)	124.89(4)	O(6)-C(6)-C(5)	116.66(17)
N(2)-Pr(1)-N(3)	120.28(5)	C(8)-C(7)-H(7A)	109.5
N(1)-O(1)-H(1D)	109.5	C(8)-C(7)-H(7B)	109.5
C(3)-O(2)-Pr(1)#2	152.63(11)	H(7A)-C(7)-H(7B)	109.5
C(3)-O(3)-Pr(1)	125.25(10)	C(8)-C(7)-H(7C)	109.5
N(2)-O(4)-H(4D)	109.5	H(7A)-C(7)-H(7C)	109.5
C(6)-O(6)-Pr(1)	128.02(13)	H(7B)-C(7)-H(7C)	109.5

Table 2.22. (Continued)

N(3)-O(7)-H(7D)	109.5	N(3)-C(8)-C(7)	126.49(16)
C(9)-O(9)-Pr(1)	125.70(11)	N(3)-C(8)-C(9)	113.47(16)
Pr(1)-O(10)-H(10D)	113.2(10)	C(7)-C(8)-C(9)	120.03(16)
Pr(1)-O(10)-H(10E)	117.9(13)	O(8)-C(9)-O(9)	125.49(18)
H(10D)-O(10)-H(10E)	103.5(11)	O(8)-C(9)-C(8)	118.14(18)
Pr(1)-O(11)-H(11D)	115.6(11)	O(9)-C(9)-C(8)	116.36(17)

Numbers in parentheses are estimated standard deviations in the least significant digits.

The metallacycle atoms are almost coplanar, as can be inferred from the angles around each corner atom of each metallacycle (N(1), C(2), C(3), O(3), N(2), C(5), C(6), O(6), N(3), C(8), C(9), and O(9)). The other angles around the Pr^{3+} ion center vary from 65.14(5)^{o} to 152.63(11)^{o} reflecting the distortion of the nine coordination geometry around the praseodymium. The unit cell contains four $Pr(PAO)3(H_2O)_2$ complexes connected via the carboxylate carbonyl oxygen bridge (O(2A)), forming a 2-dimension sheet along the zy-plane. Intermolecular hydrogen bonds along the a-axis and c-axis (Table 2.23) are responsible for the connection of the parallel sheets to result in a 3-dimension network (Figure 2.47). In addition, there are two intramolecular hydrogen bonds within each praseodymium complex (Table 2.23).

Table 2.23. Hydrogen Bonds for Pr(PAO)3(H2O)2 (Å and o)

D-H...A	d(D-H)	d(H...A)	d(D...A)	<(DHA)
O(1)-H(1D)...O(6)	0.84	1.97	2.657(2)	138.1
O(4)-H(4D)...O(9)	0.84	1.95	2.6378(18)	138.9
O(7)-H(7D)...O(3)#1	0.84	1.88	2.7112(17)	171.4
O(10)-H(10D)...O(8)#3	0.837(4)	1.948(5)	2.7701(18)	166.9(12)
O(10) -H(10E)...O(5)#4	0.837(4)	1.830(5)	2.6653(19)	176.1(17)
O(11)-H(11D)...O(5)#5	0.839(4)	2.052(7)	2.870(2)	164.9(18)
O(11)-H(11E)...O(8)#6	0.839(4)	1.959(5)	2.7897(19)	170.5(17)

Numbers in parentheses are estimated standard deviations in the least significant digits.
Symmetry transformations used to generate equivalent atoms: #1 x+1/2,-y+1/2,z
#2 x-1/2,-y+1/2,z #3 -x+1,-y+1,z+1/2 #4 -x+1,-y+1,z-1/2 #5 -x,-y+1,z-1/2
#6 -x,-y+1,z+1/2

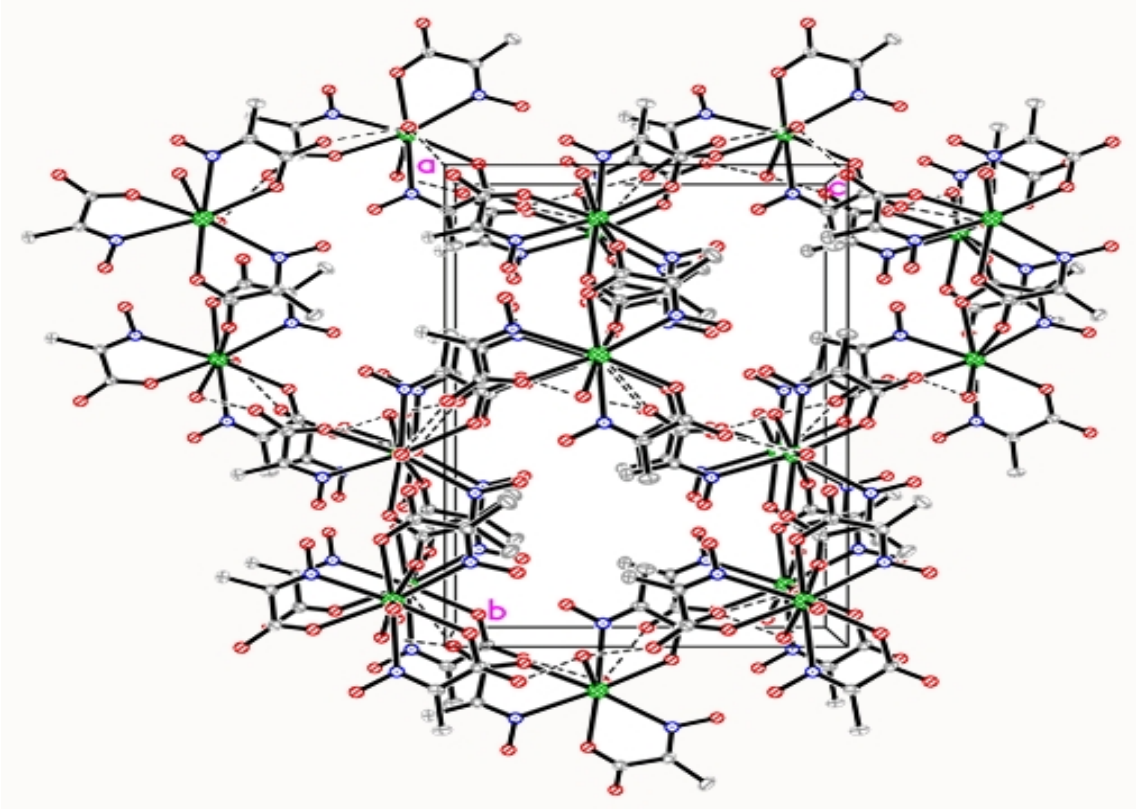

Figure 2.47. Perspective view of the 3-D network of $Pr(PAO)_3(H_2O)_2$ along the a-axis

The percentage difference in the length of the bonds of the carboxylate bridging two Pr^{3+} centers is 1.50%, which is comparable to its analog observed in the calcium derivative (1.3%).[6] In contrast, this percentage is larger for the other non-bridging carboxylates (2.91% and 3.28%), indicating more double bond character in their carbonyl bonds.

The sparing solubility of the PAO^- complex of praseodymium (III) in aqueous medium can be ascribed to the strong carboxylate carbonyl bridge and to the extensive network of strong hydrogen bonds that bind together the individual praseodymium complexes (Figure 2.47).

Spectroscopic Characterization of PAO^- Salts of Some Trivalent Lanthanides

Table 2.24 displays the characteristic IR absorption bands for the cerium and praseodymium complexes. The IR analysis of these complexes shows lowering in the asymmetric stretches by 29-62 cm^{-1} comparing to the parent acid HPAO.

Table 2.24. Distinctive IR Vibrational Frequencies (cm^{-1}) of the PAO^- Salts of Some Trivalent Lanthanides

Compound	$\nu_{(C=N)}$	$\nu_{as(COO)}$	$\nu_{s(COO)}$	$\Delta\nu_{(COO)}$	$\nu_{(N-O)}$
$Ce(PAO)_3$	1686	1666 1633	1469 1414	197 219	1058
$Pr(PAO)_3(H_2O)_2$	1688	1666 1640	1412 1468	254 172	1060

Such observation is common for the carboxylates of metals and is due to the deprotonation and delocalization of the negative charge in the carboxylate moiety and its coordination to the metal center.[82] The $\Delta\nu_{(COO)}$ calculated for the cerium compound is a

characteristic of a bridging carboxylate, which is in agreement with its structure determined previously by X-ray single crystal study.[1,3] The $\Delta\nu_{(COO)}$ calculated for the praseodymium compound with a value of 254 cm^{-1} is attributed to the monodentate carboxylate, while that of 172 cm^{-1} is referred to the bridging one. Once again, this deduction, based on IR analysis, is parallel with the crystallographic structural determination of the praseodymium complex by single crystal X-ray. The $\nu_{(C=N)}$ vibration stretch in these two complexes, where the oximino nitrogen atom is bonded to the metal ion center, is shifted towards higher wave numbers by 32-34 cm^{-1} in comparison to the parent acid, HPAO. This observation may be accounted for the high oxophilicity of the f-block elements. This fact is also responsible for the observed blue shift in the $\nu_{(N-O)}$ in these two complexes by 15-17 cm^{-1} as compared to HPAO. The existence of broad bonds at higher wave number (> 2600 cm^{-1}) in the IR spectrum of the praseodymium complex indicates the existence of H-bonds in its crystalline structure. This conclusion regarding the H-bonds on the basis of IR is reinforced by the determined crystal structure of $Pr(PAO)_3(H_2O)_2$.

Thermal Behavior of PAO^- Salts of Some Trivalent Lanthanides

The thermal behavior of the cerium complex was previously investigated. The final product was found to be ceria, CeO_2,[1] which was demonstrated to be formed according the thermal mechanism described in Chapter 3. In addition, the off gases analysis by GC-MS revealed a synchronous evolution of carbon dioxide, acetonitrile, and water.

The thermal behavior of the praseodymium derivative was studied in this work. The TGA trace of $Pr(PAO)_3(H_2O)_2$ is shown in Figure 2.48. The compound does not

undergo any weight loss before 136.4°C. However, after this temperature, a massive weight loss of 45.44% occurs upon heating to 306°C, which is due to dehydration and decomposition of two PAO^- ligands. A weight loss of 20% takes place when heated to 500°C. This latter weight change may be ascribed to the loss of the third PAO^-ligand. The XRD analysis of the solid obtained upon pyrolysis at 512°C revealed the existence of a crystalline phase of hexapraseodymium undecaoxide, Pr_6O_{11} ($Pr^{III}_2Pr^{IV}_4O_{11}$).

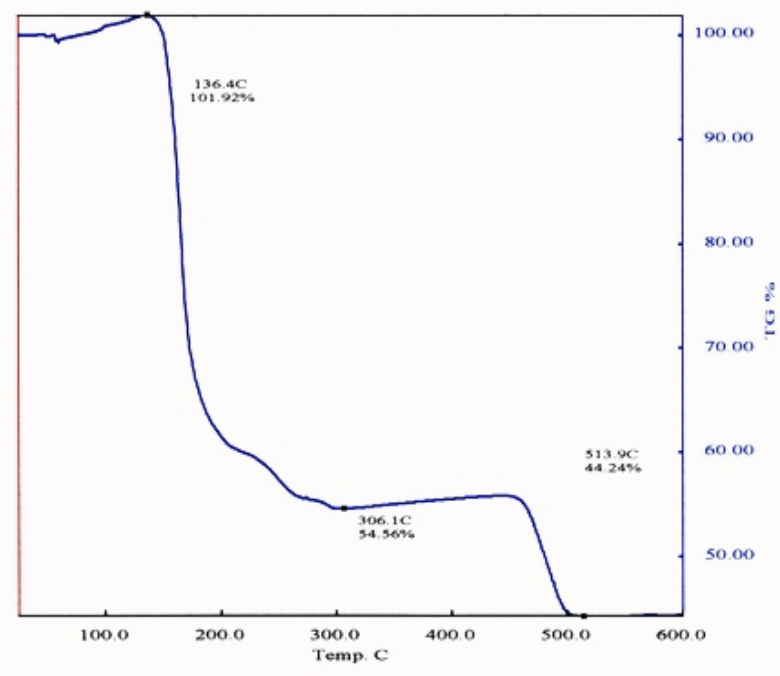

Figure 2.48. The TGA trace of $Pr(PAO)_3(H2O)_2$ complex

PAO^{2-} Salts

The dianion form of PAO^{2-} ligand was readily obtained by the deprotonation of the oximino hydroxyl group of a coordinated PAO^- ligand to a metal cation center using either a hydroxide or an amine base.[8,18,20-22] This process is facilitated by the fact that the positively charged metal cation center exercises the function of an electron-withdrawing group. This fact was supported by the measurement of the pK_a of an aqueous solution of

$Cu(PAO)_2 \cdot 2H_2O$; it was found to be similar to that of acetic acid.[7] Furthermore, the deprotonation of the oximino hydroxyl makes dramatic changes in the symmetry and the structure of the obtained metal-PAO-based anion, as confirmed by X-ray crystallography studies in this investigation and in the previous reported studies.[8,18,20-22] Preparation of PAO^{2-} salts is a convenient synthetic route for the preparation of a two-metal single precursor for the preparation of binary metal oxides, too. In this chapter, the PAO^{2-} salts were utilized to prepare metal-PAO-based anions with a quaternary ammonium counteraction attempting to prepare mesoporous metal oxides. The metal-PAO-based anion compounds were characterized by IR and XRD, which showed spectra that were totally different from their corresponding, starting PAO^- complexes. In addition, the crystal structure of the salt, based on copper-PAO-anion and tetramethyl ammonium, $[(H_3C)_4N]^+[Cu(PAO^-)(PAO^{2-})(H_2O)]^- \cdot H_2O$, was determined by single-crystal X-ray diffraction (Figure 2.49). The copper (II) center in the cuprate anion resides in a pseudo-square pyramidal. The apical position of the pyramid is occupied by water molecule at a distance from Cu^{2+} center of 2.3343(10) Å (Table 2.25). This latter Cu—OH_2 is shorter than the one observed in $Cu(PAO)_2 \cdot 2H_2O$ (2.482(5) Å),[7] but longer than its corresponding in $Cu_2(O_2CCH_3)_4 \cdot 2H_2O$ (2.1613(17) Å).[89] Consequently, the water molecule binds stronger to the Cu^{2+} in the cuprate anion as compared to the one in the PAO^- complex but weaker than that in the acetate complex.

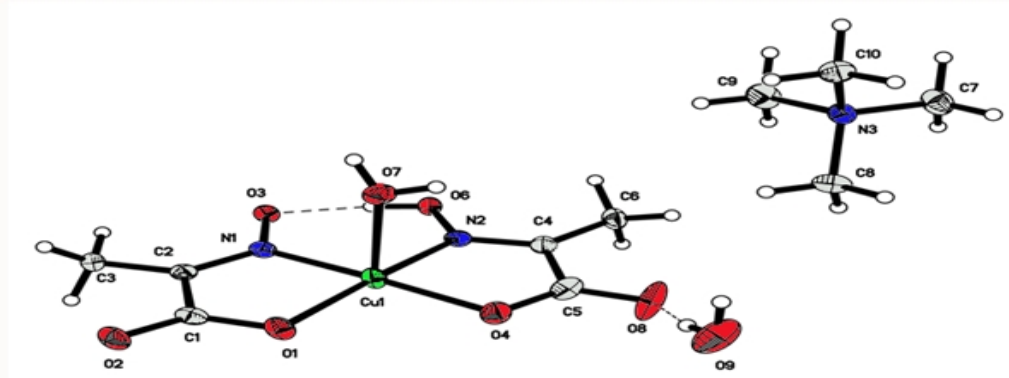

Figure 2.49. Crystal structure of $[(H_3C)_4N][Cu(PAO^-)(PAO^{2-})(H_2O)]\cdot H_2O$ drawn at 50% level

The four equatorial positions in the square base are occupied by the PAO^- and PAO^{2-} ligands, forming two semi symmetrical, coplanar five-membered metallacycles, opposing to each other and sharing the Cu^{2+} vertex. The N,O-chelate mode is adopted by both ligands where the two oximino moieties are cis to each other around the Cu^{2+} ion center. This latter conformation allows the formation of an intramolecular H-bond between the oximino hydroxyl group of the PAO^- ligand with the deprotonated oxygen of the oximino hydroxyl group of the PAO^{2-} ligand (═N−O−H---O−N═). This H-bond between the two oxime oxygen atoms endows an extra stabilization to the cuprate complex and leads to the formation of a pseudo six-membered metallacycle. However, the bridging proton is localized very near the O(6), resulting in asymmetric O—H bonds (O(6)—H = 0.893(4) Å, H---O(3) = 1.588(4) Å, O(6)---O(3) = 2.4773(12) Å, O(6)—H---O(3) = 173.2(17)^o) (Table 2.26). Such an intramolecular H-bond connecting two oximino oxygen atom has been observed in several complexes based on oximino-containing ligands.[8,12,18,20,22,47-59] Moreover, this H-bond bridge can be regarded as a characteristic feature for the oximino complexes.

Table 2.25. Bond Distances (Å) for $[(H_3C)_4N][Cu(PAO^-)(PAO^{2-})(H_2O)]\cdot H_2O$

Cu(1)-N(1)	1.9452(11)	C(4)-C(5)	1.5080(19)
Cu(1)-O(1)	1.9549(9)	C(6)-H(6A)	0.9800
Cu(1)-N(2)	1.9609(10)	C(6)-H(6B)	0.9800
Cu(1)-O(4)	1.9644(10)	C(6)-H(6C)	0.9800
Cu(1)-O(7)	2.3343(10)	N(3)-C(9)	1.4913(16)
O(1)-C(1)	1.2893(15)	N(3)-C(10)	1.4940(18)
O(2)-C(1)	1.2296(16)	N(3)-C(7)	1.4954(17)
O(3)-N(1)	1.3568(13)	N(3)-C(8)	1.4982(17)
O(4)-C(5)	1.2708(18)	C(7)-H(7A)	0.9800
O(6)-N(2)	1.3551(13)	C(7)-H(7B)	0.9800
O(6)-H(6D)	0.893(4)	C(7)-H(7C)	0.9800
O(7)-H(7D)	0.888(3)	C(8)-H(8A)	0.9800
O(7)-H(7E)	0.888(3)	C(8)-H(8B)	0.9800
O(8)-C(5)	1.2358(17)	C(8)-H(8C)	0.9800
N(1)-C(2)	1.2841(16)	C(9)-H(9A)	0.9800
N(2)-C(4)	1.2798(15)	C(9)-H(9B)	0.9800
C(1)-C(2)	1.5115(17)	C(9)-H(9C)	0.9800
C(2)-C(3)	1.4837(17)	C(10)-H(10A)	0.9800
C(3)-H(3A)	0.9800	C(10)-H(10B)	0.9800
C(3)-H(3B)	0.9800	C(10)-H(10C)	0.9800
C(3)-H(3C)	0.9800	O(9)-H(9E)	0.887(3)
C(4)-C(6)	1.4948(17)	O(9)-H(9D)	0.887(3)

Numbers in parentheses are estimated standard deviations in the least significant digits.

Table 2.26. Hydrogen Bonds for $[(H_3C)_4N][Cu(PAO^-)(PAO^{2-})(H_2O)]\cdot H_2O$ [Å and °]

D-H...A	d(D-H)	d(H...A)	d(D...A)	<(DHA)
O(6)-H(6D)...O(3)	0.893(4)	1.588(4)	2.4773(12)	173.2(17)
O(6)-H(6D)...N(1)	0.893(4)	2.265(11)	3.0066(14)	140.3(14)
O(9)-H(9E)...O(8)	0.887(3)	1.898(4)	2.7786(16)	171.8(19)
O(7)-H(7D)...O(3)#1	0.888(3)	1.885(3)	2.7687(13)	173.6(8)
O(7)-H(7E)...O(9)#2	0.888(3)	1.938(4)	2.8154(15)	169.4(12)
O(9)-H(9D)...O(4)#2	0.887(3)	2.435(8)	3.2829(17)	160.0(18)

Numbers in parentheses are estimated standard deviations in the least significant digits.
Symmetry transformations used to generate equivalent atoms: #1 -x+1,y+1/2,-z+1
#2 -x+2,y+1/2,-z+2

The bond distance between the Cu^{2+} and the oxime nitrogen dentate of PAO^{2-}, Cu—N(1), has a length of 1.9452(11) Å, which is comparable to its analogs observed in the cuprate anionic complex $[Cu(PAP^{3-})]^{-1}$ in $[Cu(Im)_4(H_2O)_2][Cu(PAP^{3-})]_2\cdot 2H_2O$[95] and in $[Li(H_2O)_4]$ $[Cu(PAP^{3-})]\cdot 2H_2O$[96] ($PAP^{3-}$ = $H_3CC(=NOH)C(=O)N^-(CH_2)_3N^-C(=O)C(=NO^-)CH_3$, Im = imidazole), and in the dinuclear copper(II) cationic complex $[Cu(Hpab)]_2^{2+}$ in $Cu(Hpab)_2\cdot(H_2O)_4(ClO_4)_2$[97,98] (Hpab=$H_3CC(=NOH)C(=O)NH(CH_2)_4NHC(=O)C(=NO)CH_3$) (1.957(2),[95] 1.954(4),[96] and 1.934(2)[97,98] Å, respectively). The length of the bond between the Cu^{2+} and the oxime nitrogen atom of PAO^-, Cu—N(2), is 1.9609(10) Å, which is close to its corresponding bonds observed in the aforementioned cuprate anion and the cationic copper(II) complexes (1.971(2),[95] 1.962(4),[96] and 1.957(2) Å,[97,98] respectively). The Cu—N(1) bond is slightly shorter than Cu—N(2) due to the greater negative charge on

N(1), as a result of the deprotonation of its hydroxyl group. The Cu—O(1), the bond between the Cu^{2+} and the carboxylate hydroxyl oxygen atom of PAO^{2-}, has a distance of 1.9549(9) Å, which is shorter than the Cu—O(4) with a distance of 1.9644(10) Å, the connecting bond between the Cu^{2+} and the carboxylate hydroxyl oxygen atom of PAO^{-}. Again, the shortness of the former bond can be ascribed to the greater negative charge born by the PAO^{2-}. The Cu—N(1), Cu—N(2), Cu—O(1), and Cu—O(4) bonds in the $[(H_3C)_4N][Cu(PAO^{-})(PAO^{2-})(H_2O)]\cdot H_2O$ are longer than their analogs found in the $[HPy]^{+}[Cu(PAO)_2]^{-}$ salt (1.925, 1.942, 1.913, and 1.946 Å, respectively).[20] The latter bonds are shorter because of the Cu^{2+} has a coordination number of 4 and a square planar geometry in the $[HPy]^{+}[Cu(PAO)_2]^{-}$ salt. The influence of deprotonation of PAO^{-} ligand to form PAO^{2-} ligand does not only decrease the bond length of Cu—N bond, but also reduces the N—O and the C═N contacts. The N—O bonds in the $[Cu(PAO^{-})(PAO^{2-})(H_2O)]^{-}$ anion (1.3568(13) and 1.3551(13) Å) are comparable to those observed in the pyridinium cuprate salt (1.360 and 1.345 Å),[20] and shorter than those found in $Cu(PAO)_2\cdot 2H_2O$ (1.393(6) Å).[7] The C═N bonds in the $[Cu(PAO^{-})(PAO^{2-})(H_2O)]^{-}$ anion (1.2841(16) and 1.2798(15) Å) are similar to those found in the pyridinium cuprate salt (1.27(1) and 1.293(9) Å),[20] but shorter than those encountered in $Cu(PAO)_2\cdot 2H_2O$ (1.301(8) Å).[7] In addition, the length of Cu—N, N—O and C═N bonds in $[(H_3C)_4N][Cu(PAO^{-})(PAO^{2-})(H_2O)]\cdot H_2O$ are similar to their corresponding bonds found in bis(dimethylglyoximato)copper(II).[56] This similarity is probably due to the fact that the Cu^{2+} resides in a pseudo square pyramidal environment of coordination number of 5.[56] The monodentate carboxylates of PAO^{-} and PAO^{2-} ligands display partial delocalization of their negative charge, as reflected by the slight large difference in the

bond lengths of the C—O bonds of each carboxylate moiety (0.0350 and 0.0597 Å, respectively). This conclusion regarding the delocalization of the carboxylate charge is supported by the fact that all the carbon-oxygen bonds have intermediate distances between the C—O bond (1.36 Å) and the C═O bond (1.23 Å). The values of the bond lengths for the rest of the bonds in the five-membered rings created by PAO^{2-} and PAO^{-} are 1.5115(17), 1.4837(17), 1.5080(19), and 1.4948(17) Å for C(1)—C(2), C(2)—C(3), C(4)—C(5), and C(4)—C(6), respectively. The bond lengths of these bonds are similar to their analogs found in bis(dimethylglyoximato)copper(II),[56] the PAO^{-} complexes of Na^{1+},[14] and Ca^{2+},[6] and the PAO^{-}-PAO^{2-} complexes of Cu^{2+},[20] and Ni^{2+}.[21]

The Cu^{2+} ion center in the cuprate anion $[Cu(PAO^{-})(PAO^{2-})(H_2O)]$ reside above the mean square basal plane [N(1)O(1)O(4)N(2)] by 0.1158 Å in the direction of the axially-bound water molecule. Consequently, the water oxygen is above this mean square basal plane by 2.4476 Å. The mean deviation of the atoms of the square basal plane from planarity is only 0.0082 Å. The largest deviation from planarity for the five-membered ring created by the PAO^{2-} ligand is 0.0937 Å at C(2), while that for the five-membered ring created by the PAO^{-} ligand is 0.0503 Å at C(5). These measurements emphasize the near planarity of each five-membered ring.

The Cu^{2+} ion center has a distorted square pyramidal environment due to the existence of two five-membered metallacycle rings, leading to deviation of the angles subtended at the copper ion center from the ideal value of 90^{o} (Table 2. 27). The bite angle of N,O-chelate PAO^{-} [N(2)—Cu(1)—O(4)] is $81.56(4)^{o}$, while that of N,O-chelate PAO^{2-} [N(1)—Cu(1)—O(1)] is $82.85(4)^{o}$, reflecting the rigidity of the O═C—C═N fragment of PAO ions. These bite angles are comparable to those found in the

pyridinium cuprate salt (82.0(2)^{o} and 83.4(2)^{o}, respectively)[20] and in $Cu(PAO)_2 \cdot 2H_2O$ (81.3(2)^{o}).[7] The other two angles around the Cu^{2+} ion center in the square base of the pyramid have the values of 94.79(4)^{o} and 99.99(4)^{o} for [N(1)—Cu(1)—N(2)] and [O(1)—Cu(1)—O(4)], respectively. These latter angles are similar to their analogs found in the pyridinium cuprate anion (95.1(3)^{o} and 99.3(2)^{o}, respectively).[20] Interestingly, the sum of the angles is 359.19^{o} around the Cu^{2+} ion center in the square base of the pyramid of $[Cu(PAO^{-})(PAO^{2-})(H_2O)]^{-}$. This summation of angles would be 360^{o} if the square base was thoroughly planar. Thus, the square base can be inferred that is almost planar since it deviates slightly from the ideal value.

Table 2.27. Interbond Angles (^{o}) for $[(H_3C)_4N][Cu(PAO^{-})(PAO^{2-})(H_2O)] \cdot H_2O$

N(1)-Cu(1)-O(1)	82.85(4)	O(4)-C(5)-C(4)	117.07(11)
N(1)-Cu(1)-N(2)	94.79(4)	C(4)-C(6)-H(6A)	109.5
O(1)-Cu(1)-N(2)	172.48(5)	C(4)-C(6)-H(6B)	109.5
N(1)-Cu(1)-O(4)	172.90(5)	H(6A)-C(6)-H(6B)	109.5
O(1)-Cu(1)-O(4)	99.99(4)	C(4)-C(6)-H(6C)	109.5
N(2)-Cu(1)-O(4)	81.56(4)	H(6A)-C(6)-H(6C)	109.5
N(1)-Cu(1)-O(7)	95.44(4)	H(6B)-C(6)-H(6C)	109.5
O(1)-Cu(1)-O(7)	92.60(4)	C(9)-N(3)-C(10)	109.18(11)
N(2)-Cu(1)-O(7)	94.74(4)	C(9)-N(3)-C(7)	109.54(10)
O(4)-Cu(1)-O(7)	90.95(4)	C(10)-N(3)-C(7)	109.01(10)
C(1)-O(1)-Cu(1)	112.61(8)	C(9)-N(3)-C(8)	109.01(11)
C(5)-O(4)-Cu(1)	113.05(9)	C(10)-N(3)-C(8)	110.27(10)

Table 2.27. (Continued)

N(2)-O(6)-H(6D)	99.7(10)	C(7)-N(3)-C(8)	109.82(11)
Cu(1)-O(7)-H(7D)	115.1(6)	N(3)-C(7)-H(7A)	109.5
Cu(1)-O(7)-H(7E)	113.1(8)	N(3)-C(7)-H(7B)	109.5
H(7D)-O(7)-H(7E)	107.4(10)	H(7A)-C(7)-H(7B)	109.5
C(2)-N(1)-O(3)	120.84(10)	N(3)-C(7)-H(7C)	109.5
C(2)-N(1)-Cu(1)	115.28(9)	H(7A)-C(7)-H(7C)	109.5
O(3)-N(1)-Cu(1)	123.73(7)	H(7B)-C(7)-H(7C)	109.5
C(4)-N(2)-O(6)	119.59(10)	N(3)-C(8)-H(8A)	109.5
C(4)-N(2)-Cu(1)	115.82(8)	N(3)-C(8)-H(8B)	109.5
O(6)-N(2)-Cu(1)	124.55(7)	H(8A)-C(8)-H(8B)	109.5
O(2)-C(1)-O(1)	124.78(12)	N(3)-C(8)-H(8C)	109.5
O(2)-C(1)-C(2)	118.99(11)	H(8A)-C(8)-H(8C)	109.5
O(1)-C(1)-C(2)	116.22(10)	H(8B)-C(8)-H(8C)	109.5
N(1)-C(2)-C(3)	126.23(12)	N(3)-C(9)-H(9A)	109.5
N(1)-C(2)-C(1)	112.71(10)	N(3)-C(9)-H(9B)	109.5
C(3)-C(2)-C(1)	121.04(11)	H(9A)-C(9)-H(9B)	109.5
C(2)-C(3)-H(3A)	109.5	N(3)-C(9)-H(9C)	109.5
C(2)-C(3)-H(3B)	109.5	H(9A)-C(9)-H(9C)	109.5
H(3A)-C(3)-H(3B)	109.5	H(9B)-C(9)-H(9C)	109.5
C(2)-C(3)-H(3C)	109.5	N(3)-C(10)-H(10A)	109.5
H(3A)-C(3)-H(3C)	109.5	N(3)-C(10)-H(10B)	109.5
H(3B)-C(3)-H(3C)	109.5	H(10A)-C(10)-H(10B)	109.5

Table 2.27. (Continued)

N(2)-C(4)-C(6)	125.71(11)	N(3)-C(10)-H(10C)	109.5
N(2)-C(4)-C(5)	111.89(11)	H(10A)-C(10)-H(10C)	109.5
C(6)-C(4)-C(5)	122.30(11)	H(10B)-C(10)-H(10C)	109.5
O(8)-C(5)-O(4)	124.68(14)	H(9E)-O(9)-H(9D)	107.5(10)
O(8)-C(5)-C(4)	118.21(13)		

Numbers in parentheses are estimated standard deviations in the least significant digits.

The axial water molecule does not stand perpendicularly to the square base, as can be inferred from the value of the angles among the water and the equatorial arms of the base [95.44(4), 92.60(4), 94.74(4), and 90.95(4)^{o} for N(1)—Cu(1)—O(7), O(1)—Cu(1)—O(7), N(2)—Cu(1)—O(7), and O(4)—Cu(1)—O(7), respectively]. The angle between two arms opposite to each other in the square base is not straight angle [172.48(5) and 172.90(5)^{o} for O(1)—Cu(1)—N(2) and N(1)—Cu(1)—O(4), respectively] because the Cu^{2+} is slightly above the plane of the base as explained previously (*vide supra*). The metallacycle atoms of each five-membered ring are almost coplanar, as reflected by the angles around each corner atom [N(1), C(2), C(1), and O(1) for PAO^{2-}, and N(2), C(4), C(5), and O(4) for PAO^{-}] (see Table 2.27). All the angles around the carbon of the methyl side chain of PAO^{2-} and PAO^{-} ligands have the value of 109.5^{o} as expected for an ideal tetrahedral array.

The tetramethylammonium cation has the expected tetrahedral geometry. The N—C lengths range from 1.4913(16) to 1.4982(17) Å and the C—N—C angles from 109.01(10) to 110.27(10)^{o} with average values of 1.4947(17) Å and 109.47(11)^{o},

respectively (Table 2.25 and Table 2.27). These crystallographic values regarding the tetramethylammonium cation are similar to those reported previously in literature.[99-101]

The cuprate anion is H-bonded through the carboxylate carbonyl oxygen of its PAO^- ligand to a water solvent molecule [O(9)—H(9E)---O(8), Table 2.26] occupying the voids between the voluminous $[Cu(PAO^-)(PAO^{2-})(H_2O)]^-$ structural units (Figure 2.50). The latter water molecule is also H-bonded to the carboxylate deprotonated hydroxyl oxygen of PAO^- ligand of cuprate anion generated by symmetry [O(9)—H(9D)---O(4)#2, Table 2.26]. The axial water coordinated to the Cu^{2+} center of the cuprate anion also participates in the formation of two H-bonds, as shown in Table 2.26 and Figure 2.50, which lead along with the other H-bonds to the connection of the 2-D sheets of the cuprate complex and hence the creation of a 3-D network.

The cuprate anions are bonded by unusual long Cu---O(3) contact, leading to a creation of a zigzag ribbon of the cuprate complex along the structure of $[H_3C)_4N][Cu(PAO^-)(PAO^{2-})(H_2O)]\cdot H_2O$ (Figure 2.51). This Cu—O(3) has a length of 2.902 Å, which is much longer than the average contact between the Cu^{2+} center and the carboxylate hydroxyl deprotonated oxygen in the anionic complex by 0.943 Å and longer than the bond between the copper(II) center and the apical coordinated water by 0.568 Å.

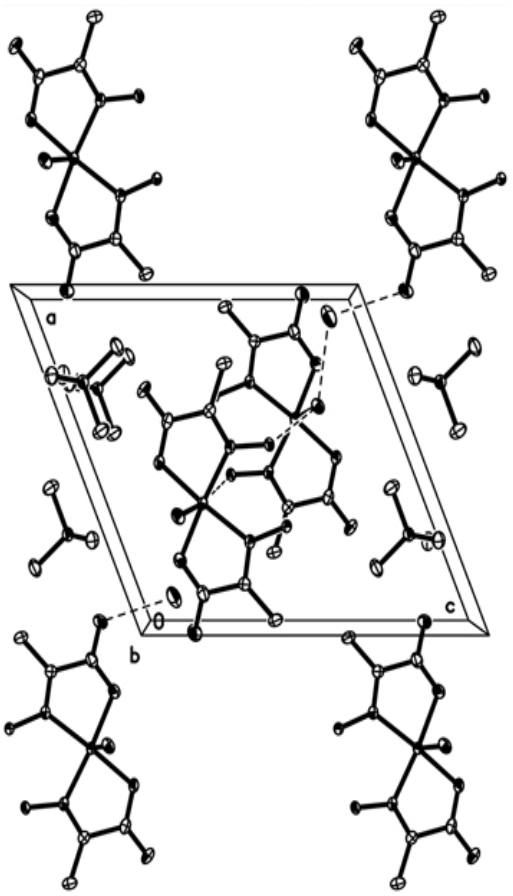

Figure 2.50. A view along the b-axis of the network showing some of the hydrogen bonds connecting the cuprate anions and the crystallization water molecules in $[(H_3C)_4N][Cu(PAO^-)(PAO^{2-})(H_2O)]\cdot H_2O$

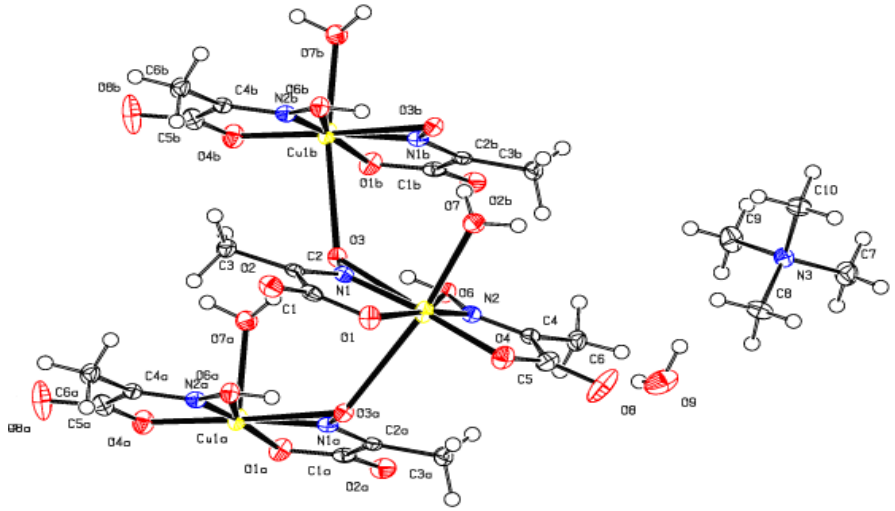

Figure 2.51.A perspective view of the cuprate anion ribbon $[Cu(PAO^-)(PAO^2(H_2O)]$

This long-range bonding or interaction requires the Cu^{2+} ion center to have a coordination number of six and a distorted pseudo octahedral environment. The zigzag nature of the ribbon is dictated by the apical coordinated water molecule. A longer bond interaction than Cu---O(3) was reported previously in the crystal structure of $Cu(Hpab)_2 \cdot (H_2O)_4(ClO_4)_2$ between the Cu^{2+} and the amide oxygen of the parallel complex (3.535(2) Å).[97,98] Accordingly, the long-range copper-oxygen interaction is stronger in $[(H_3C)_4N][Cu(PAO^-)(PAO^{2-})(H_2O)] \cdot H_2O$ than in $Cu(Hpab)_2 \cdot (H_2O)_4(ClO_4)_2$ on the basis of the length of the contact.

Spectroscopic Characterization of PAO^{2-} Salts

The IR and XRD spectroscopy techniques were used to characterize the mono metal cation salts of PAO^{2-} synthesized in this work. The XRD spectra of all the salts in the range of 10.0-70.0 for 2θ prove their crystalline nature. Moreover, the observation of some peaks in their low angle X-ray diffraction patterns in the range of 1.3-10.0 for 2θ is an indication of long-range order of the crystalline phase in these compounds. All of the XRD patterns, in both ranges of 2θ, were found to be qiute different from those of the starting metal ion PAO^- complex and that of hexadecylamine in the same range of 2θ. The latter comparison of XRD patterns helps affirm the formation of the new crystalline phase of PAO^{2-}.

Table 2.28 displays the important distinguishing IR vibrational frequencies. A marked characteristic of the IR spectra of PAO^{2-} is that the asymmetric stretch of the carboxylate group decreases significantly by 64-78 cm^{-1} and its symmetric vibration stretch by 57-78 cm^{-1} in comparison to the free acid, HPAO.

Table 2.28. Distinctive IR Vibrational Frequencies (cm^{-1}) of the Salts of PAO^{2-}

Compound	$\nu_{(C=N)}$	$\nu_{as(COO)}$	$\nu_{s(COO)}$	$\Delta\nu_{(COO)}$	$\nu_{(N-O)}$
$[(H_3C)_4N][Cu(PAO)(PAO^{2-})(H_2O)].H_2O$	1658	1632	1342	290	1129
$[H_3C(CH_2)_{15}NH_3][Fe(PAO)(PAO^{2-})]$	1657	1631	1355	276	1116
$[H_3C(CH_2)_{15}NH_3][Zn(PAO)(PAO^{2})(H_2O)]$	1632	1617	1362	255	1078
$[H_3C(CH_2)_{15}NH_3][Ce(PAO)_2(PAO^{2})(H_2O)]$	1605	-----	1363	-----	1046

These observations, which are common for the carboxylate of metals, are due to the deprotonation, delocalization of the negative charge in the carboxylate moiety, and its coordination to the metal ion center.[80] The differences between the asymmetric and symmetric stretching frequencies of the carboxylate groups, $\Delta\nu_{(COO)}$, have values greater than 250 cm^{-1}, implying that the carboxylates in these compounds are monodentate. This conclusion is consistent with the crystal structure determined for the copper(II) PAO^{2-} salt. The positions of $\nu_{(N—O)}$ absorption stretching peaks confirm the coordination of the oximino nitrogen atom to the metal ion center. The $\nu_{(N—O)}$ is blue-shifted by 3-86 cm^{-1} in the IR spectra of the PAO^{2-} salts in comparison to the parent acid, HPAO. The deprotonation of the oximino hydroxyl group is also accounted for the large shift of $\nu_{(N—O)}$ band toward higher frequencies (shorter wavelength) in these salts. Such interpretation is supported by the preceding studies which showed that coordination of the oximino group resulted in a hypsochromic (blue) shift of $\nu_{(N—O)}$, and it became greater upon its deprotonation.[8,12,22] The stretching vibrations of C═N groups in the salts of Cu^{2+} and Fe^{2+} are comparable to those reported for HPAO and its salts of light alkali,[14] alkaline

earth,[6] and the divalent 3d transition metals.[23] However, the peaks for C═N in the salts of zinc and cerium are subjected to a bathochromic (red) shift. Such observation was reported previously for some dianion of 2-hydroxyiminocarboxylic acids.[8,12] The band of C═N in the cerium salt is highly red-shifted and broaden, so that the $\nu_{as(COO)}$ band was masked and could not be distinguished. It was difficult in the IR spectra of these compounds, unfortunately, to distinguish the stretching of bands of the amine N—H due to the presence of (—OH) groups of oximino moiety and of water molecules. The C—N bands are located in the frequency range of 1000-1200 cm^{-1}, as expected.

Thermal Behavior of PAO^{2-} Salts

The TGA trace of $[(H_3C)_4N][Cu(PAO)(PAO^{2-})(H_2O)].H_2O$ is composed of two weight-loss steps that finally lead to the formation of *tenorite* phase of cupric oxide, as confirmed by IR and XRD spectroscopies. The first step can be attributed to the loss of two water molecules (the coordinated one to the copper(II) center and the crystallization one) and a molecule of tetramethylammonium cation on the basis of the percentage of weight remaining (~ 71%). The second step is due to the decomposition of the PAO^- and PAO^{2-} ligands to give CuO, as supported by the mass remained percentage (21.1 %). The copper(II) oxide obtained upon pyrolysis at 314 ^oC was found to have a very low specific surface areas of 6.6569m^2/g. In addition, the XRD pattern in the range of 2θ of 1.3-10^o is amorphous, indicating that this CuO is not mesoporous.

The iron derivative of PAO^{2-}, $[H_3C(CH_2)_{15}NH_3][Fe(PAO)(PAO^{2-})]$, decomposes according to a TGA trace consisted of three weight-loss steps to yield eventually hematite (α-Fe_2O_3) at 574^{o}C. The sum of the weight lost in the first two steps refers to the loss of the *n*-hexamethylammonium ion $[n\text{-}CH_3(CH_2)_{15}NH_3]^+$, implying a stepwise

decomposition of this cation during the decomposition of the complex. The third step is due to the decomposition of the PAO^- and PAO^{2-} ligands to give the final product of hematite. The surface area of this hematite is 19.5603m^2/g, which is almost 66 times the surface area of the starting complex (0.2985m^2/g). The low surface area of hematite indicates that it is not mesoporous. This conclusion was confirmed via the XRD analysis in the small angle range (1.3-10.0^o) which did not show any peaks. On the other hand, the starting complex diffracts the X-ray beams in this range of angle, implying a long-range order of the complex in crystalline phase, but not implying the existence of mesoporous phase due to its low surface area.

The zinc complex, $[H_3C(CH_2)_{15}NH_3][Zn(PAO)(PAO^{2-})]$, decomposes in four steps according to its TGA trace. The first one is ascribable to dehydration (loss of one water molecule) of the zinc complex on the basis of weight loss at 101^{o}C (97% is the wt% remaining). This high temperature of dehydration is an implication of the coordination of the water molecule to the zinc ion center. The second and third steps may account for the loss of *n*-hexamethylammonium ion $[n\text{-}CH_3(CH_2)_{15}NH_3]^+$ and one of the PAO ligands, as can be inferred from wt% remaining (~31%) at 208^{o}C. The fourth step represents the decomposition of the other PAO ligand to yield zinc oxide, as proved by XRD analysis and percentage of weight remaining (~15%). The surface area of the zinc complex is very low (0.7364m^2/g), while that of the dehydrated phase, obtained at 101 ^{o}C, is 0.2482m^2/g. The XRD patterns in the 2θ range of (1.3-10^o) and (10-70^o) of both the zinc complex and its dehydrated phase are similar, indicating that the structure of original complex is maintained intact after the dehydration process. The X-ray diffractions in the low angle range along with the low surface areas imply a long-range

order in the crystalline phase of the zinc complex and its anhydrous form, but not the existence of mosoporous phase. The XRD patterns, on the other hand, of the pyrolysis product, obtained at 140^{o}C, in the 2θ ranges (1.3-10.0^{o}) and (10-70^{o}) are different from those of the zinc complex and its dehydrated form, indicating a change in the crystalline phase upon increase the temperature from 100 to 140 ^{o}C. The surface area of the material produced at 140 ^{o}C is 1.8264m^{2}/g.

The cerium complex dissociates to cerianite phase of ceria ($Ce^{IV}O_2$) in two weight-loss steps. The first one is due to the loss of a water molecule coordinated to the Ce^{3+} ion center, as indicated by the percentage of weight remaining (~ 97%). This dehydration step takes place around 80^{o}C. The second step refers to the decomposition of the *n*-hexamethylammonium ion [*n*-$CH_3(CH_2)_{15}NH_3]^+$ and the three PAO ligands of the anhydrous cerium complex to ceria. The XRD analysis in the 2θ range (10-70^{o}) confirmed the formation of nanocrystalline ceria, obtained by thermal decomposition at 289^{o}C, as reflected by the broad peaks of the spectrum. However, no peaks in the XRD pattern of this ceria in the range of 2θ range (1.3-10.0^{o}), indicating the absence of a long-range order crystalline phase. The surface area is subjected to a dramatic change upon the pyrolysis of the cerium complex (0.7295m^{2}/g) at 289 ^{o}C to yield CeO_2 (29.8248m^{2}/g). The high surface area of ceria can be ascribed to the ease of the thermal decomposition of the cerium complex which is facilitated by the ease of oxidation of Ce^{3+} to Ce^{4+} by oxygen.

The failure to prepare mesoporous metal oxide could be attributed to the lack of micelle formation by *n*-hexadecylammonium cations in the low polarity medium of methanol. Instead the cation molecules gather to form bimolecular (bilayer) sheets,

where their $(—NH_3)^+$ polar heads are connected to the PAO metallate anion by hydrogen bonds. The non-polar hydrocarbon tails of the cation chains are bound by van der Waals forces. Such arrangement results in bidimensional, layered crystalline structure.

2.4. CONCLUSION

Metal salts and complexes based on PAO ligand are demonstrated to form 3-dimensional polymeric and network crystalline materials via both covalent and hydrogen bonds. The latter hydrogen bonds facilitate the crystallization process of these compounds and are partially responsible for the low solubility in aqueous medium of some of them. The PAO compounds, furthermore, are very suitable precursors for the fabrication of high surface area, nanocrystalline metal oxide ceramics for catalysis and environmental purposes for instance. The utility of these complexes for the latter applications arises from their low thermal stabilities, which is due to the binding mode of the PAO ligand, the formation of strained fiver-membered metallacycles, and the crystalline structures adopted.

Each PAO complex has its own thermal decomposition pathway, as reflected by the variation of the concomitant products with the oxide. In addition, holding the pyrolysis under nitrogen gas instead of air stream led to different products. The PAO complexes are also acidic as evidenced by the ability to deprotonate their oximino hydroxyl groups to form metallate anions.

REFERENCES

1. A. W. Apblett, G. D. Georgieva, J. T. Mague, and E. J. Matta, "Low-Temperature Precursors for Ceramic Oxide Catalysts", *Ceram. Trans.*, **1997,** *73*, 105-113.

2. A. W. Apblett and G. D. Georgieva, "Low-Temperature Precursors for Titanium Oxide", *Phosphorus, Sulfur, Silicon Relat. Elem.*, **1994,** *93-94*, 479-480.

3. A. W. Apblett, G. D. Georgieva, and J. T. Mague, "Incorporation of Radionuclides into Mineral Phases via a Thermally Unstable Complexant Ligands", *Mat. Res. Soc. Symp. Proc.,* **1993,** *294*, 123-128.

4. A. W. Apblett, J. Lei, and G. D. Georgieva, "Molecular Design of Carboxylic Precursors for Zirconia", *Mat. Res. Soc. Symp. Proc.,* **1992,** *271*, 77-82.

5. G. Occupati, and L. Pratt, "Some Reactions of the Carbonyl Group in Co-ordinated Keto-carboxylates", *J. Chem. Soc., Dalton Trans.,* **1973,** 1699-1701.

6. A. W. Apblett, G. D. Georgieva, and J. T. Mague, "Spectroscopic and Thermochemical Investigation of Alkaline Earth Metal Salts of 2-Oximinopropionate", *Can. J. Chem.,* **1997,** *75* (5), 483-490.

7. A. W. Apblett, A. Bagabas, and E. M. Holt, "X-ray Crystal Structure, Spectroscopic Analysis, and Thermal Chemistry of Copper(II) 2-Oximinopropionate", *Polyhedron,* Submitted for publication.

8. K. Malek, M. Vala, J. Kozlowska, L. M. Proniewicz, "Solid State Study of the Copper(II) Complex of 2-Hydroxyiminopropionic Acid", *New J. Chem.,* **2004,** *28* (4), 477-483.

9. A. A. Mokhir, E. Gumienna-Kontecka, J. Swiatek-Kozlowska, E. G. Petkova, I. O. Fritsky, L. Jerzykiewicz, A. A. Kapshuk, and T. Y. Sliva, "Study of Complex Formation with 2-Hydroxyiminocarboxylates: Specific Metal Binding Ability of 2-(4-Methylthiazol-2-yl)-2-(hydroxyimino)acetic Acid", *Inorg. Chim. Acta,* **2002,** *329*, 113-121.

10. A. Dobosz, N. M. Dudarenko, I. O. Fritsky, T. Glowiak, A. Karaczyn, H. Kozlowski, T. Y. Sliva, and J. Swiatek-Kozlowska, "N-Bonding of the Hydroxamic Function in Nickel(II) and Copper(II) Complexes with 2-(Hydroxyimino)propanohydroxamic Acid", *J. Chem. Soc., Dalton Trans.,* **1999,** 743-749.

11. T. Y. Sliva, A. Dobosz, L. Jerzykiewicz, A. Karaczyn, A. M. Moreeuw, J. Swiatek-Kozlowska, T. Glowiak, and H. Kozlowski, "Copper(II) and Nickel(II) Complexes with Oxime Analogues of Amino Acids. Potentiometric, Spectroscopic, and X-ray Studies of Complexes with 2-Cyano-2-(hydroxyimino)acetic Acid and its Ethane-1,2-diamine Derivatives", *J. Chem. Soc., Dalton Trans.,* **1998,** 1863-1867.

12. T. Y. Sliva, R. D. Lampeka, "Structure of Anionic Mixed-Ligand Nickel Complex Containing 2-Hydroxyimino-3-phenylpropionic Acid", *Ukr. Chem. J.,* **1998,** *64* (9), 6-8.

13. S. M. Harben, P. D. Smith, R. L. Beddoes, D. Collison, and C. D. Garner, "Rhenium and Molybdenum Oxo-Complexes Containing Ligands related to N-hydroxyiminodipropionic Acid", *J. Chem. Soc., Dalton Trans.*, **1997,** 2777-2784.

14. A. W. Apblett, G. D. Georgieva, and J. T. Mague, "Synthesis and Spectroscopic and Thermal Decomposition Studies of Alkali Metal Salts of 2-Oximinopropionate", *Inorg. Chem.,* **1997,** *36* (12), 2656-2661.

15. G. D. Georgieva "Metal Carboxylate Precursors for Ceramic Materials and Waste Forms for Radionuclides" Ph.D. Dissertation, Tulane University, New Orleans, 1995.

16. R. D. Lampeka, N. M. Dudarenko, and V. V. Skopenko, "*trans*-Bis(2-hydroxyiminopropionato-*N,O*)dimethanolnickel(II) Dimethanol Solvate, $[Ni\{CH_3C(NOH)COO\}_2(CH_3OH)_2]\cdot 2CH_3OH$", *Acta Crystallogr., Sect. C,* **1994,** *50* (5), 706-708.

17. R. Lampeka, R. Bergs, R. Krämer, K. Polborn, W. Beck, "Metal Complexes with Biological Important Ligands, LXIX [1]. Half-Sandwich Complexes of Cobalt(III), Rhodium(III), Iridium(III), and Ruthenium(II) with Anions of α-Hydroxyimino Acids", *Z. Naturforsch., B: Chem. Sci.,* **1994,** *49* (2), 225-232.

18. R. D. Lampeka, Z. D. Uzakbergenova, and V. V. Skopenko, "Spectroscopic and X-ray Investigation of Cobalt(III) Complexes with 2-Oximinocarboxylic Acids", *Z. Naturforsch., B: Chem. Sci.,* **1993,** *48* (4), 409-417.

19. V. V. Skopenko, T. Y. Sliva, Y. A. Simonov, A. A. Dvorkin, N. D. Mazus, R. D. Lampeka, and T. I. Malinovski, "The Structure of Manganese(II) Complex with 2-(Hydroxyimino)propionic Acid", *Russ. J. Inorg. Chem.,* **1990,** *35* (7), 993-995.

20. Y. A. Simonov, T. Y. Sliva, M. D. Mazus, A. A. Dvorkin, and R. D. Lampeka, "The Synthesis and Structure of Complexes of Copper(II) with 2-Hydroximinopropionic Acid", *Russ. J. Inorg. Chem.,* **1989,** *34* (4), 489-491.

21. A. A. Dvorkin, Y. A. Simonov, T. Y. Sliva, R. D. Lampeka, M. D. Mazus, V. V. Skopinko, and T. I. Malinovskii, "Preparation and Structure of a Binuclear Mixed-Ligand Complex of Nickel(II) with 2-(Hydroxyimino)propionic Acid and Imidazole", *Russ J. Inorg. Chem.,* **1989,** *34* (10), 1475-1478.

22. R. D. Lampeka, T. Y. Sliva, V. V. Skopenko, "Different-Ligand 2-Oximinocaroxylates of Manganese(II), Nickel(II), Copper(II), and Zinc", *Soviet Prog. Chem.,* **1993,** *59* (1), 3-8.

23. V. V. Skopenko, R. D. Lampeka, T. Y. Sliva, and D. I. Sakhov, "2-Oximinopropionates of Certain Metals", *Soviet Prog. Chem.,* **1990,** *56* (7), 675-678.

24. R. D. Lampeka, V. V. Skopenko, T. Y. Sliva, and H. Hennig, "2-Oximino-3-phenylpropionates of Certain 3d-Metals", *Soviet Prog. Chem.,* **1988,** *54* (7), 675-678.

25. T. Y. Sliva, R. D. Lampeka, G. V. Vladyko, Ye. I. Boreko, L. V. Korobchenko, "2-Oximocarboxylates of Some Metals and Their Antiviral Activity", *Khimiko-Farmatsevticheskii Zhurn.,* **1992,** *26* (7-8), 56-58.

26. A. Ahmad and I. D. Spenser, "The conversion of α-Keto Acids and of α-Keto Acid Oximes to Nitriles in Aqueous Solution", *Can. J. Chem.,* **1961,** *39* (6), 1340-1359.

27. A. Ahmad, "A Facile Conversion of α-Oximino-Acids to Nitriles", *Synthesis,* **1976,** *6*, 418.

28. S. Ali, M. H. Bhatti, M. Mazhar, F. Shahnaz, and S. Mahmood, "Thermal Analysis and Pyrolysis of Biologically Active α-Oximino Acids", *J. Saudi Chem. Soc.,* **1998,** *2* (2), 97-100.

29. M. Katyal and R. P. Singh, "Determination of Copper by Phenyl Pyruvic Acid Oxime", *Current Sci.,* **1962,** *31* (9), 373-374.

30. M. Katyal and R. P. Singh, "Reaction of Phenylpyruvic Acid Oxime with Cations", *J. Indian Chem. Soc.,* **1963,** *40* (6), 491-492.

31. M. Katyal and R. P. Singh, "Precipitation of Copper-Phenyl Pyruvic Acid Oxime Complex from Homogeneous Solution", *Current Sci.,* **1965,** *34* (1), 17-18.

32. Q. Haider, A. Ahmad, V. N. Mehrotra, E. B. Singh, "A Rapid Method for the Gravimetric Determination of Copper(II) in Presence of Cadmium(II) by α-Keto Acid Oxime", *J. Indian Chem. Soc.,* **1975,** *52* (9), 881-882.

33. A. Ahmad, Q. Haider, V. N. Mehrotra, E. B. Singh, "Analytical Application of *p*-Methoxyphenylpyruvic Acid Oxime in Separation and Determination of Copper(II) and Zinc(II) in Brass", *Indian J. Tech.,* **1975,** *13* (1), 43-45.

34. J. K. Maurin, "Resonance-Assisted Hydrogen Bonds Between Oxime and Carboxyl Groups. II. The Tetrameric Structure of Pyruvic Acid Oxime", *Acta Crystallogr., Sect. C,* **1995,** *51* (10), 2111-2113.

35. J. K. Maurin, "Oxime-Carboxyl Hydrogen Bonds: The Preferred Interaction Determining Crystal Packing of Carboxyoximes", *Acta Crystallogr., Sect. B,* **1998,** *54* (6), 866-871.

36. K Borszeky, T. Mallat, R. Aeschiman, W. B. Schweizer, and A. Baiker, "Enantioselective Hydrogenation of Pyruvic Acid Oxime to Alanine on Pd/Alumina", *J. Catal.,* **1996,** *161* (1), 451-458.

37. T. Y. Sliva, Y. A. Simonov, R. D. Lampeka, A. A. Dvorkin, and M. D. Mazus, "Crystal and Molecular Structure of $[HPy]^{+}[CH_3C(NOH)CO_2]^{-}$ $.CH_3C(NOH)CO_2H$", *J. Struct. Chem.,* **1991,** *32* (3), 439-441.

38. R. Bartnik and B. Orlowska, "Isonitrosoketones. Part XII. A Study of ^{13}C Shieldings and $^{13}C—^{15}N$ Couplings in *E* and *Z* Isomers of Isonitrosoketones", *Pol. J. Chem.,* **1988,** *62* (4-6), 433-443.

39. G. C. Levy and G. L. Nelson, "Carbon-13 NMR Study of Aliphatic Amides and Oximes. Spin-Lattice Relaxation Times and Fast Internal Motions", *J. Am. Chem. Soc.,* **1972,** *94* (14), 4897-4901.

40. G. E. Hawkes, K. Herwig, and J. D. Roberts, "Nuclear Magnetic Resonance Spectroscopy. Use of Carbon-13 spectra to Establish Configurations of Oximes", *J. Org. Chem.,* **1974,** *39* (8), 1017-1028.

41. G. W. Buchanan, and B. A. Dawson, "A Study of $^{13}C—^{15}N$ Couplings and Revised ^{13}C Shieldings in ^{15}N-enriched *E*-acetophenone Oximes", *Can. J. Chem.,* **1976,** *54* (5), 790-794.

42. G. W. Buchanan, and B. A. Dawson, "Sign Reversal of Geminal $^{13}CH_3—C—^{15}N$ Coupling in Configurationally Isomeric Fragments", *Can. J. Chem.,* **1977,** *55* (9), 1437-1439.

43. G. W. Buchanan, and B. A. Dawson, "Stereochemical Analysis of Aromatic Oximes. $^{13}C—^{15}N$ Nuclear Spin Coupling and ^{13}C Shieldings as Conformational Probes", *Can. J. Chem.,* **1978,** *56* (16), 2200-2204.

44. T. Saito, K. Hayamizu, M. Yanagisawa and O. Yamamoto. SDBS Web. http://www.aist.go.jp/RIODB/SDBS/menu-e.html (accessed Aug 2003).

45. A. W. Apblett Oklahoma State University, Stillwater, OK. Personal Communication, 1998.

46. D. A. Skoog, D. M. West, and F. J Holler "Fundamentals of Analytical Chemistry" 7th ed.; Saunders College Publishing: Philadelphia, 1996; pp A-8-A-9.

47. X. Solans, M. Font-Bardia, C. López and S. Alvarez, "Anhydrous *trans*-(Aniline)chlorobis(dimethylglyoximato)cobalt(III)", *Acta Crystallogr., Sect. C,* **1996,** *52* (1), 63-66.

48. L. Xu, D. Xu, Y. Xu and J. Gu, "Diamminebis[dimethylglyoximato(1-)]cobalt(III) Fluoborate and Perchlorate", *Acta Crystallogr., Sect. C*, **1996,** *52* (5), 1119-1122.

49. Y. Inouye, T. Kambe and M. Tada, "(Benzenethiolato-*S*)(4-*tert*-butylpyridine-*N*) bis(dimethylglyoximato-*N,N*)cobalt(III) and (4-*tert*-Butylpyridine-*N*)bis (dimethylglyoximato-*N,N*)(4-methoxybenzenethiolato-*S*)cobalt(III), *Acta Crystallogr., Sect. C*, **1998,** *54* (7), 945-947.

50. L. E. Godycki and R. E. Rundle, "The Structure of Nickel Dimethylglyoxime", *Acta Crtystallogr.,* **1935,** *6* (6), 487-494.

51. H. Endres and M. Schendzielorz, "Squaric Acid Salts of Bis(oxamide oxime)nickel(II): the 1:1 Salt $[C_4O_4]^{2-}.[Ni(C_2H_6N_4O_2)_2]^{2+}$ and the salt $[C_4O_4]^{2-}.[Ni(C_2H_5N_4O_2)(C_2H_6N_4O_2)]^{+}$", *Acta Crystallogr., Sect. C,* **1983,** 39 (11), 1528-1530.

52. E. Bua and G. Schiavinato, "Analisi Strutturistica Della Cudimetilgliossima. – Nota I. Interpretazione dei roentgenfotogrammi. –Determinazione Della Cella elementare e del Gruppo Spaziale", *Gazz. Chim. Ital.,* **1951,** *81*, 212-218.

53. E. Bua and G. Schiavinato, "Analisi Strutturistica Della Cu-dimetilgliossima. – Nota II. Analisi Fourier-Patterson", *Gazz. Chim. Ital.,* **1951,** *81*, 847-855.

54. S. Bezzi, E. Bua, and G. Schiavinato, "Analisi Strutturistica Della Cu-dimetilgliossima. –Nota III. – Analisi Fourier-Bragg preliminare", *Gazz. Chim. Ital.,* **1951,** *81*, 856-867.

55. E. Frasson, R. Zannetti, R. Bardi, S. Bezzi, and G. Giacometti, "Non Planar Coordination in a Cu^{++} Complex", *J. Inorg. Nucl. Chem.,* **1958,** *8* (6), 452-457.

56. E. Frasson, R. Bardi, and S. Bezzi, "Structure of Copper-Dimethylglyoxime at Low Temperature", *Acta Crystallogr.,* **1959,** *12* (3), 201-205.

57. H. Endres, N. Genc, and D. Nothe, "The Catena Structure and EPR Properties of Bis(oxamide oximato)cooper(II)-Oxamide Oxime, $[Cu(C_2H_5N_4O_2)_2].C_2H_6N_4O_2$", *Acta Crystallogr., Sect. C,* **1983,** *39* (6), 701-703.

58. R. Ruiz, J. Sanz, B. Cervera, F. Lloret, M. Julve, C. Bois, J. Faus, and M. C. Munoz, "Oximato Complexes. Part 1. Solution Study, Synthesis, Structure, Spectroscopic and Magnetic Properties of Polynuclear Copper(II) Complexes Containing Dimethylglyoxime", *J. Chem. Soc., Dalton Trans.,* **1993,** 1623-1628.

59. R. Ruiz, J. Sanz, B. Cervera, F. Lloret, M. Julve, J. Faus, C. Bois, and M. C. Munoz, "Oximato Complexes. Part 2. Dinuclear Dimethylglyoximeato Complexes of Copper(II) with a New Co-ordination Mode of the Oximate Ligand", *J. Chem. Soc., Dalton Trans.,* **1993,** 3035-3039.

60. A. Isaacs, J. Daintith, and E. Martin "Oxford Concise Science Dictionary" 3rd ed.; Oxford University Press: Oxford, 1996; p 382.

61. F. Wagenknecht and R. Juza "Zinc, Cadmium, Mercury" In *Handbook of Preparative Inorganic Chemistry,* 2nd ed., G. Brauer, Ed.; Academic Press: New York, 1965; Vol. 2, pp 1086-1087.

62. S. Zhang, C. L. Czekaj, and W. T. Ford, "Enhancement of Polarization Transfer under High-Speed MAS Using Quasi-Adiabatic Cross-Polarization Sequence", *J. Magn. Reson. A,* **1994,** *111*, 87-92.

63. A. E. Bennett, C. M. Rienstra, M. Auger, K. V. Lakshmi, and R. G. Griffin, "Heteronulear Decoupling in Rotating Solids", *J. Chem. Phys.,* **1995,** *103* (16), 6951-6958.

64. Siemens, "XSCANS V2.0 Technical Reference", Siemens Analytical X-ray Instrument, Inc.: Madison, WI, 1990.

65. Siemens, "XSCANS Users Manual", Siemens Analytical X-ray Systems; Madison. WI, 1991.

66. Siemens, "P3/P4-PC Diffractometer Program, Ver. 4.27", Siemens Analytical X-ray Systems; Madison. WI, 1991.

67. G. M. Sheldrick, "Phase annealing in *SHELX*-90: direct methods for larger structures", *Acta Crystallogr., Sect. A,* **1990,** *46* (6), 467-473.

68. G. M. Sheldrick "A Computer Program for Crystal Structure Determination" University of Cambridge: Cambridge, England, 1976.

69. G. M. Sheldrick "SHELX86: A Computer Program for Crystal Structure Determination" University of Göttingen: Göttingen, Germany, 1986.

70. J. W. Jeffery "Methods in X-ray Crystallography" Academic Press: London, 1971.

71. G. M. Sheldrick "SHELX97: Program for the Refinement of Crystal Structures" University of Göttingen: Göttingen, Germany, 1997.

72. J. A. Ibers and W.A. Hamilton "International Tables for X-ray Crystallography" Kynoch Press, Birmingham, England, 1974; Vol. IV.

73. Bruker SMART (version 5.625), GEMINI (version 1.0), and SAINT-plus (version 6.29), Bruker AXS Inc.: Madison, Wisconsin, 2002.

74. Bruker SHELXTL (version 6.12), Bruker AXS Inc.: Madison, Wisconson, 1997.

75. M. A. Aramendia, V. Borau, C. Jimenez, J. M. Marinas, and F. Rodero, "Acidity Determination of Several Catalysts by Various Procedures", *Colloids Surf.,* **1984,** *12* (3-4), 227-238.

76. T. W. G. Solomons "Organic Chemistry" 6th ed.; John Wiley & Sons, Inc.: New York, 1996; pp 902 and 970.

77. M. A. Aramendia, V. Borau, C. Jimenez, J. M. Marinas, and F. J. Romero, "Vapour-Phase Reaction of Acetophenone with Methanol or Dimethyl Carbonate on Magnesium Oxide and Magnesium Phosphates", *J. Catal.,* **1999,** *183* (1), 119-127.

78. K. Sreekumar, T. Raja, B. P. Kiran, S. Sugunan, and B. S. Rao, "Selective *N*-monomethylation of Aniline over $Zn_{1-x}Ni_xFe_2O_4$ (x = 0, 0.2, 0.5, 0.8, and 1) type system", *Appl. Catal. A*, **1999,** Vol. 182, No 2, pp. 327-336.

79. D. E. Irish, J. Semmler, N. J. Taylor, and G. E. Toogood, "Structure of Magnesium Diacetate Tetrahydrate", *Acta Crystallogr., Sect. C,* **1991,** *47* (11), 2322-2324.

80. W. L. Jolly "Modern Inorganic Chemistry" McGraw-Hill, Inc.: Singapore, 1991; pp. 592-597.

81. R. C. Mehrotra and R. Bohra "Metal Carboxylates" Academic Press: New York, 1983.

82. A. L. Smith "Applied Infrared Spectroscopy: Fundamentals, Techniques, and Analytical Problem-Solving" In *Chemical Analysis: A Series of Monographs on Analytical Chemistry and Its Applications,* P. J. Elving, J. D. Winefordner, and I. M. Kolthoff, Eds.; John Wiley & Sons: New York, 1979; Vol. 54, pp 286-314.

83. G. B. Deacon and R. J. Phillips, "Relationships between the carbon-oxygen stretching frequencies of carboxylato complexes and the type of carboxylate coordination", *Coord. Chem. Rev.,* **1980,** *33* (3), 227-250.

84. S. Kinugasa, K. Tanabe, and T. Tamura. SDBS Web. http://www.aist.go.jp/RIODB/SDBS/menu-e.html (accessed Sep 2003).

85. M. A. Aramendia, V. Borau, C. Jimenez, J. M. Marinas, F. J. Romero, J. A. Navio, and J. Barrios, "Modification of the Activity of $Mg_3(PO_4)_2$ in the Gas-Phase Conversion of Cyclohexanol by Addition of Sodium Carbonate", *J. Catal.,* **1995,** *157* (1), 97-108.

86. B. A. Morrow, "Surface Groups on Oxides", *Stud. Surf. Sci. Catal.,* **1990,** *57A*, A202.

87. T. Ishioka, Y. Shibata, M. Tkahashi, I. Kanesaka, Y. Kitagawa, K. T. Nakamura, "Vibrational Spectra and Structures of Zinc Carboxylates. I. Zinc Acetate Dihydrate", *Spectrochim. Acta,* **1998,** *A 54* (12), 1827-1836.

88. D. F. Shriver, P. W. Atkins, and C. H. Langford "Inorganic Chemistry" 2nd ed.; Oxford University Press: Great Britain, 1994; pp 174-176.

89. G. M. Brown and R. Chidambaram, "Dinuclear Copper(II) Acetate Monohydrate: A Redetermination of the Structure by Neutron-Diffraction Analysis", *Acta Crystallogr., Sect. B,* **1973,** *29* (11), 2393-2403.

90. V. Berbenni, A. Marini, "Oxidation Behavior of Mechanically Activated Mn_3O_4 by TGA/DSC/XRPD", *Mater. Res. Bull.,* **2003,** *38* (14), 1859-1866.

91. B. Gillot, M. Guendouzi, M. Laarj, "Particle Size Effects on the Oxidation-Reduction Behavior of Mn_3O_4 Hausmannite", *Mater. Chem. Phys.,* **2001,** *70* (1), 54-60.

92. A. Punnoose, H. Magnone, M. S. Seehra, "Synthesis and Antiferromagnetism of Mn_5O_8", *IEEE Transac. Mag.*, **2001,** *37* (4), 2150-2152.

93. S. Fritsch, J. Sarrias, A. Rousset, G. U. Kulkarni, "Low-Temperature Oxidation of Mn_3O_4 Hausmannite", *Mater. Res. Bull.,* **1998,** *33* (8), 1185-1194.

94. S. Ganapathy, V. P. Chacko, R. G. Bryant, M. C. Etter, "Carbon CP-MASS NMR and X-ray Crystal Structure of Paramagnetic Lanthanide Acetate", *J. Am. Chem. Soc.,* **1986,** *108* (12), 3159-3165.

95. I. O. Fritsky, J. Kozlowska, A. Dobosz, T. Y. Sliva, N. M. Dudarenko, "Hydrogen Bonded Supramolecular Structures of Cationic and Anionic Module Assemblies Containing Square-Planar Oximate Complex Anions", *Inorg. Chim. Acta,* **2004,** *357* (12), 3746-3752.

96. A. M. Duda, A. Karaczyn, I. O. Fritsky, T. Glowiak, E. V. Prisyazhnaya, T. Y. Sliva, J. Kozlowska, "Co-ordination of Copper(II) and Nickel(II) ions by a Novel Open Chain Oxime Ligand", *J. Chem. Soc., Dalton Trans.,* **1997,** *20,* 3853-3859.

97. I. O. Fritsky, H. Kozlowski, E. V. Prisyazhnaya, A. Karaczyn, V. A. Kalibabchuk, T. Glowiak, "A Short Intramolecular Hydrogen Bond Is a Key Factor in the Self-Assembly of a Dimeric Complex with a 22-Membered Metallamacrocyclic Cavity", *J. Chem. Soc., Dalton Trans.,* **1998,** *10,* 1535-1536.

98. I. O. Fritsky, H. Kozlowski, E. V. Prisyazhnaya, Z. Rzaczynska, A. Karaczyn, T. Y. Sliva, T. Glowiak, "Co-ordination Ability of Novel Tetradentate Amide-and-Oxime Ligands: Differential Binding to Cu^{II} and Ni^{II}", *J. Chem. Soc., Dalton Trans.,* **1998,** *21,* 3629-3633.

99. S. M. Jessen, "Structure of Tetramethylammonium Hydrogen Phthalate", *Acta Crystallogr., Sect. C,* **1990,** *46* (8), 1513-1515.

100. N. Ohama, M. Machida, "Structure of Tetramethylammonium Dihydrogenorthophosphate Monohydrate", *Acta Crystallogr., Sect. C,* **1987,** *43* (5), 962-964.

101. S. Drobez, L. Golic, I. Leban, "Structure of Tetramethylammonium Hydrogen Maleate", *Acta Crystallogr., Sect. C,* **1987,** *41* (10), 1503-1505.

CHAPTER 3

3. PYRUVIC ACID OXIME COMPLEXES PYROLYSIS MECHANISM

3.1. INTRODUCTION

The low temperature thermal decomposition, exhibited by the salts of pyruvic acid oxime (PAO) ligand, ranges between 76-250^{o}C, and results in nanocrystalline, high surface area metal oxides.[1] This remarkable feature of these compounds deserves to be investigated mechanistically in order to understand the responsible electronic and geometrical factors for this phenomenon. Ultimately, the results can lead to the design of thermally unstable coordination compounds for the synthesis of nanostructured materials with unprecedented chemical and physical attributes for electrical, magnetic, optical, sensorial, and catalytic applications. Such thermally unstable compounds can provide a simple, cost-effective, and low energy route for the fabrication of the nano-materials that are desired for the technological and industrial advancements.

It has been demonstrated that PAO compounds dissociate to generate water, acetonitrile, and carbon dioxide along with metal oxides, hydroxides, or carbonates depending on the metal center, as illustrated in the following chemical equation:[1-8]

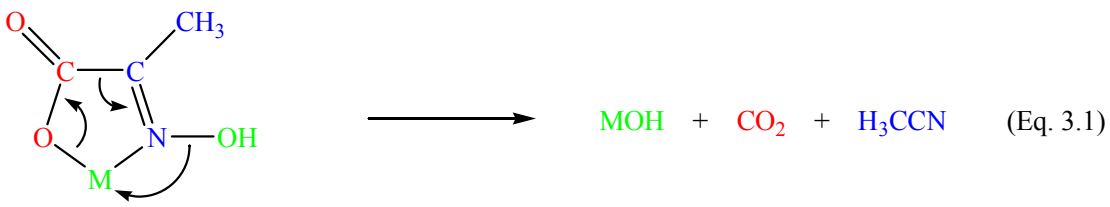

(Eq. 3.1)

The coordination mode of the PAO ligand to the metal center is undoubtedly a key factor in determining the stability of its complexes. Single crystal X-ray crystallography structures of a variety of PAO complexes, reported previously in the literature and performed during this work, reflect this fact explicitly through demonstration of the presence of strained five-membered metallacycles.[1-4,6,8-16] This causes Pitzer strain (ring strain), due to the ligation of the PAO ligand to the metal center via the nitrogen atom of the oximino moiety and the deprotonated hydroxyl oxygen atom of the carboxylate moiety, as described in Chapter 2. Another structural factor that has to be taken into consideration for thermal stability of PAO compounds is the formation of polymeric materials or networks by the formation of bridges between two metal ion centers. This can be caused by formation of bridging carboxylate or hydrogen-bonding interactions between carboxylate oxygen atoms and oximino hydroxyl groups or waters of hydration.[1-4,6,8-16]

The influence of the bidentate type mode adopted by the PAO ligand in its complexes on the thermal behavior has been detected through thermal gravimetric analysis (TGA), differential thermal analysis (DTA), differential scanning calorimetry (DSC), and tandem TGA-MS analysis.[1-8] The latter investigation revealed that the gases produced during the thermal decomposition of PAO complexes were evolved simultaneously, implying a concerted decomposition mechanism (Figure 3.1).[1,4,6,7] Such a mechanism, proposed by Apblett and Georgieva,[1,6,7] could involve a simultaneous rearrangement of electron pairs within a six-membered O,O metallacycle transition state (Equation 3.2 b).[1] This requires rotation around the C=N bond but would be expected to be a low-energy pathway after such rearrangement. Alternatively, a higher energy

pathway for extrusion of carbon dioxide and acetonitrile from the five-membered ring is possible (Equation 3.2 a).[1]

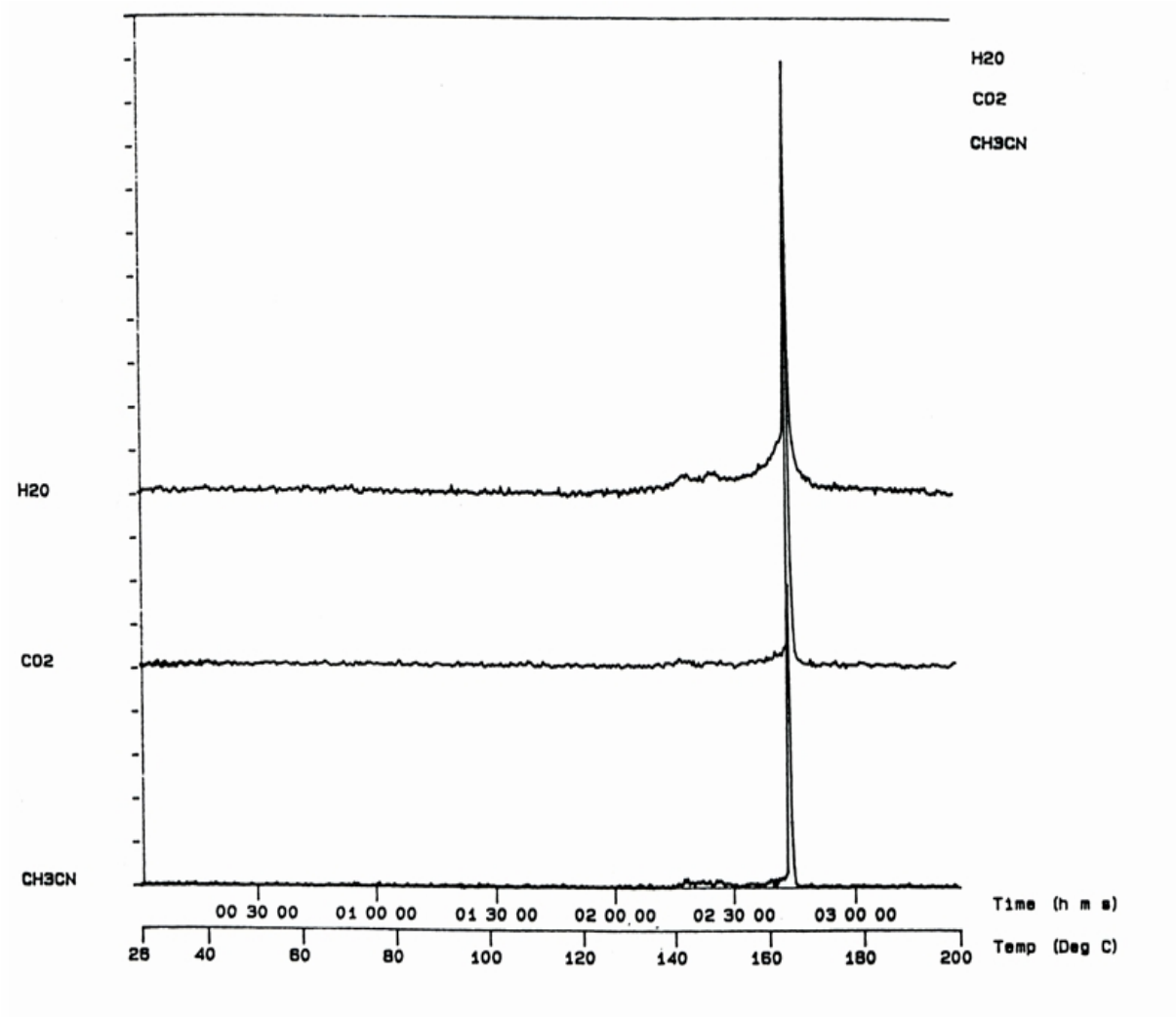

Figure 3.1. Synchronous production of acetonitrile, carbon dioxide, and water during the thermal decomposition of $Ce(PAO)_3$. Adapted from the literature[1]

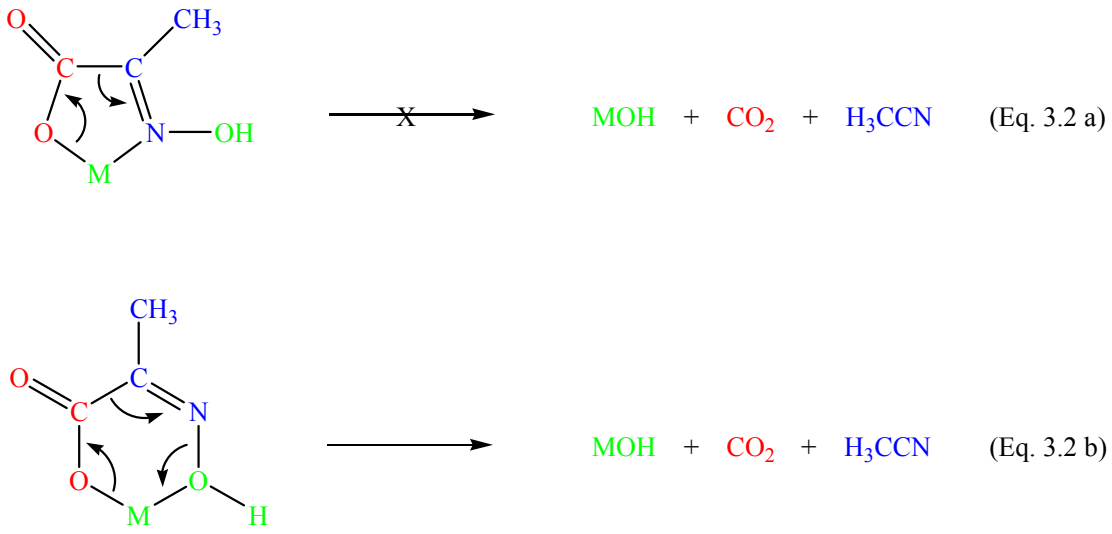

The formation of the six-membered ring requires the isomerization of the coordinated *E*-isomer of PAO ligand to its *Z*-isomer, which should be preceded by the breaking of the N-metal dative bond at an elevated temperature.[1] Supportive evidences of the Apblett-Georgieva mechanism are the isomerization of *E*-benzoyl formic acid oxime, *E*-$C_6H_5C(=NOH)COOH$, to the *Z*-configuration at 120°C,[17] the decomposition of the α-oximinocarboxylic acids to their corresponding nitriles and carbon dioxide by a similar proposed mechanism involving the same cyclic intermediate or transition state shown in equation 3.2b,[17] and a correlation of the strength of the N-metal bond with increased decomposition temperature.[1] For example, the thermal stability decreases linearly down the alkali and alkaline earth groups, i.e. with increasing ionic radius of the metal cation.[1-3] This is opposite the trend predicted by the ionic model and is opposite the observed trend for the carbonate of these metals.[18] Ring strain would increase with the ionic radius of the metal ion and this would be expected to weaken the N—metal bond and make formation of the six-membered metallacycle more favorable.[1-3] Theoretical energetic calculations based on the MM3 model for $M[H_3CC(=NOH)COO]$

species supported the responsibility of the Pitzer strain for the trends in thermodynamic stability of these salts.[1] The above discussion also showed the influence of the cationic radius on the thermal stability of these PAO compounds. However, comparing the pyrolysis temperature of PAO salts of alkali and alkaline earth having similar ionic radii revealed that the alkaline earth derivative possessed a higher thermal stability, reflecting the impacts of metal ion center charge on both thermodynamic stability and on covalent character of these compounds.[1,3]

In spite of the success of the Apblett-Georgieva mechanism in providing a logical, plausible pathway for the thermal decomposition of PAO complexes, it did not explain how the *E*-conformation might be converted to its *Z*-isomer. There are, however, two possible routes for the conversion of anti (*E*) oxime isomer to its syn (*Z*) isomer.[19] The first one is the Ashbrook mechanism,[20] which is based on the formation of a nitrone intermediate (II) during the isomerization process of an aromatic *o*-hydroxyoxime as shown in equation 3.3.[19,20]

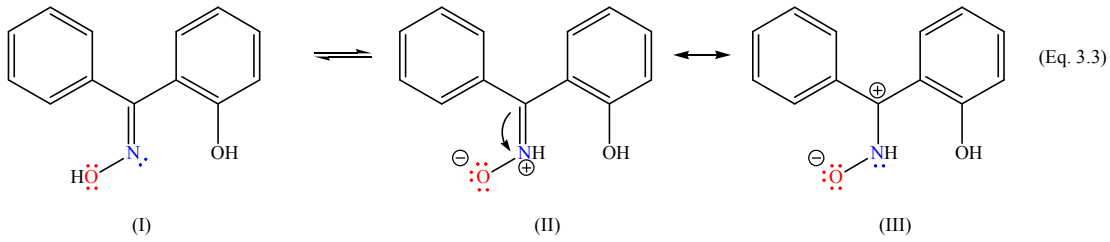

(I) (II) (III) (Eq. 3.3)

The occurrence of such mechanism relies strongly upon the substituents on the oxime carbon to stabilize the positive charge developed on this carbon atom in structure (III). Electron donating groups (EDG) will stabilize both of II and III structures. Existence of alkyl groups, the poorest EDG, only is not enough for stabilization of the positive charge on the oxime carbon of an aliphatic oxime, and hence the formation of III is difficult.

Consequently aliphatic oximes are mainly present in their oxime isomeric form.[19] *E*-PAO ligand, on this basis, cannot isomerize to its *Z*-form due to the presence of the electron withdrawing group (EWD), carboxylate, and thus, transformation of the five-membered ring to the intermediate or transition state six-membered ring in Apblett-Georgieva mechanism will not happen through the Ashbrook path of oxime isomerization.

The second possible avenue for isomerization of an oxime is the oxime-nitroso tautomerism in which the oxime hydroxyl proton migrates to the carbon holding the nitroso group (Equation 3.4).[19] Such mechanism is well-established in literature.[21-31]

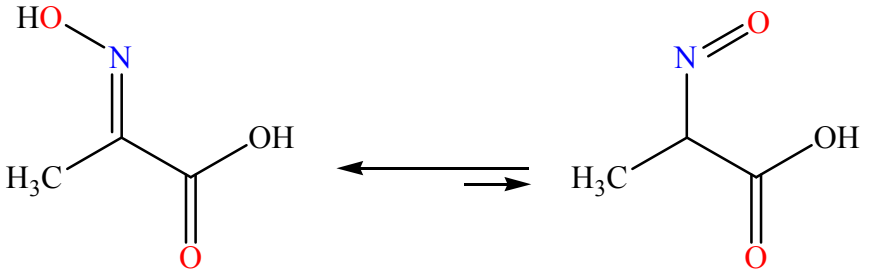

(Eq. 3.4)

The oxime is the predominant tautomer at room temperature because nitroso compounds are destabilized in the presence of α-hydrogens. However, at high temperatures, the equilibrium concentration of nitroso tautomer becomes quite considerable due to shifting of the equilibrium towards the right side. Characteristic features of the nitroso tautomer are the flexibility of free rotation about the C−N bond and the simplicity of its formation without the requirement of formal charge separation, elucidating the quicker isomerization of oximes upon raising the temperature.[19] Accordingly, this mechanism is more likely to facilitate the isomerisation of *E*-PAO to its *Z*-isomer during the Apblett-Georgieva mechanism for the pyrolysis of PAO complexes. The verification of the *E*-*Z*

isomerization via oxime-nitroso tautomerization[19] within the thermal decomposition of PAO complexes can be done by *in situ* measurements of ^{1}H and ^{13}C magnetic resonance (PMR and CMR) spectra in order to monitor the resonance changes of the oxime hydroxyl proton and the oxime carbon while heating the PAO complex from room temperature to its decomposition temperature determined from the TGA or DSC study.

In this investigation acetamide, $H_3CC(=O)NH_2$, and in some cases acetic acid, $H_3CC(=O)OH$, carbon dioxide, CO_2, and acetonitrile, $H_3CC{\equiv}N$, were detected during thermal dissociation of $Zn(PAO)_2{\cdot}2H_2O$ in air, $Mn_4(PAO)_8{\cdot}2H_2O$ under nitrogen, $Co(PAO)_2{\cdot}2H_2O$ under helium, and hydrolysis of $Cu(PAO)_2{\cdot}2H_2O$. A reasonable mechanistic interpretation for the formation of acetamide and acetic acid, based on Beckmann rearrangement,[32] decarboxylation, and hydration processes, was presented.

3.2. EXPERIMENTAL

Pressure tubes (30 ml) were placed in a cylindrical, digitally controlled furnace set at the suitable temperature for thermal decomposition of the PAO salt. The latter solid was contained in the pressure tube and purged under the desired inert gas using Schlenk techniques for 4 hours. The PAO complexes of manganese(II), cobalt(II), copper(II), zinc(II) were prepared and pyrolyzed as described previously in Chapter 2. Tandem gas chromatography-mass spectroscopy technique was used to identify the gas products of the thermal decomposition of these compounds. Acetamide was obtained as white crystals upon performing the pyrolysis of Mn and Co derivatives of PAO using the pressure tube. Addition of methylene chloride helped dissolve acetamide and, hence, separated it from the metal-containing solid. Subsequent GC-MS analysis of the methylene chloride extract confirmed the formation of acetamide as a decomposition

product of these two compounds. Solid-state ^{13}C nuclear magnetic spectroscopy also detected acetamide and zinc carbonate from the thermal decomposition of zinc PAO complex. The XRD and IR techniques were used to confirm the identity of the metal-containing solid.

3.3. RESULTS AND DISCUSSION

A plausible mechanism for the formation of acetamide upon the pyrolysis of PAO complexes can be based on the Beckmann's rearrangement[32] of the ketoximic form of *E*-PAO to its *N*-substituted amide isomer by the migration of the carboxylate group from the oxime carbon to the oxime nitrogen. This would be followed by decarboxylation (Equation 3.5 a), or vice versa, i.e. the loss of a molecule of carbon dioxide takes place first and then the rearrangement leads to the production of acetamide (Equation 3.5 b).

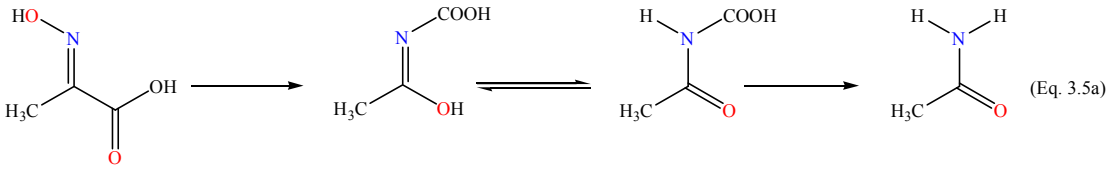

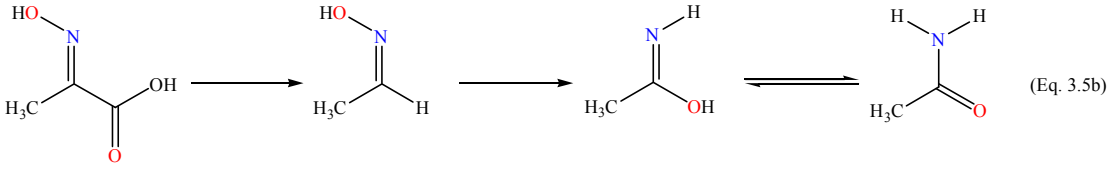

A dissociation of the oxygen-metal bond is required to take place whether or not the rearrangement or the decarboxylation precedes the other one. However, the former route takes place through the formation of N-bearing carboxylate compounds that finally, upon decarboxylation, gives acetamide. On the other hand, the other route starts with the loss of CO_2 to produce Z-acetaldoxime, which undergoes a Beckmann's rearrangement to yield acetamide. In addition, it is quite possible that the acetamide comes from the

hydrolysis of acetonitrile, resulted from the decomposition of PAO ligand according to equation 3.1.

In the case of the manganese derivative of PAO, the formation of manganese(II) carbonate and acetamide occurred. The observation of the latter can be attributed to the above mechanism based on a Beckmann rearrangement, followed by decarboxylation, while carbonate anion may be formed from the reaction of carbon dioxide from decarboxylation process with the water formed from the decomposition of PAO ligand according to equation 3.1. A similar explanation can be given for the formation of acetamide and zinc carbonate during the thermal decomposition of the PAO complex of zinc.

Pyrolysis of $Co(PAO)_2 \cdot 2H_2O$ under helium gave carbon dioxide, acetonitrile, acetamide, and acetic acid. The first two products are produced according to equation 3.1. Acetamide associated with carbon dioxide upon Beckmann's rearrangement and decarboxylation of PAO ligand. Acetic acid can be either obtained by a hydrolysis reaction of acetonitrile or acetamide. Such hydrolysis reactions are well-known synthetic pathways in organic chemistry for the production of carboxylic acids from nitriles and amide.

In case of hydrolysis of the copper(II) derivative of PAO, the copper(II) is reduced to copper(I) in the form of Cu_2O, indicating that this reduction process is radical, i.e. includes the transfer of one electron. The PAO ligand is expected to be the reducing agent that provides the transferred electron to copper(II). A possible radical resulted from the oxidation of PAO is $[HON{=}CCH_3]^{\cdot}$ species, which either may be hydrogenated to give acetaldoxime or may be coupled with itself to dimethylglyoxime. A supportive

evidence of the latter fate is the previous observation of Dr. Apblett of dimethylglyoxime formation when nickel or copper derivative of PAO were thermally decomposed under nitrogen, where the reduced form of the metal, nickel or copper metal, respectively, besides the corresponding metal(II) oxide, were obtained.[8,33]

3.4. CONCLUSION

The thermal decomposition of PAO metal complexes involves the conversion of the *E*-isomer of the PAO ligand at high temperatures to its *Z*-isomer to form a six-membered ring transition state, which allows the simultaneous evolution of carbon dioxide, acetonitrile, and water. Such isomerization could take place via oxime-nitroso tautomerism. In addition, depending on the metal and the atmosphere under which the pyrolysis is executed, acetamide, acetic acid, metal carbonate or oxide, and the metal itself are detected as products. A Beckmann rearrangement or hydrolysis of acetonitrile can be responsible for the formation of acetamide. Acetic acid might be formed from the hydrolysis of either acetonitrile or acetamide. Carbonate is formed upon the reaction of carbon dioxide with water, which are produced from the thermal decomposition process. The formation of the metal is likely associated with radical oxidation of the PAO ligand.

To probe the thermal decomposition process and gain insight on its mechanism, *in situ* measurements of ^{1}H and ^{13}C magnetic resonance (PMR and CMR) spectra are proposed for future work.

REFERENCES

1. G. D. Georgieva "Metal Carboxylate Precursors for Ceramic Materials and Waste Forms for Radionuclides" Ph.D. Dissertation, Tulane University, New Orleans, 1995.

2. A. W. Apblett, G. D. Georgieva, and J. T. Mague, "Synthesis and Spectroscopic and Thermal Decomposition Studies of Alkali Metal Salts of 2-Oximinopropionate", *Inorg. Chem.,* **1997,** *36* (12), 2656-2661.

3. A. W. Apblett, G. D. Georgieva, and J. T. Mague, "Spectroscopic and Thermochemical Investigation of Alkaline Earth Metal Salts of 2-Oximinopropionate", *Can. J. Chem.,* **1997,** *75* (5), 483-490.

4. A. W. Apblett, G. D. Georgieva, J. T. Mague, and E. J. Matta, "Low-Temperature Precursors for Ceramic Oxide Catalysts", *Ceram. Trans.,* **1997,** *73*, 105-113.

5. A. W. Apblett and G. D. Georgieva, "Low-Temperature Precursors for Titanium Oxide", *Phosphorus, Sulfur, Silicon Relat. Elem.,* **1994,** *93-94*, 479-480.

6. A. W. Apblett, G. D. Georgieva, and J. T. Mague, "Incorporation of Radionuclides into Mineral Phases via a Thermally Unstable Complexant Ligands", *Mat. Res. Soc. Symp. Proc.*, **1993,** *294*, 123-128.

7. A. W. Apblett, J. Lei, and G. D. Georgieva, "Molecular Design of Carboxylic Precursors for Zirconia", *Mat. Res. Soc. Symp. Proc.*, **1992,** *271*, 77-82.

8. A. W. Apblett, A. Bagabas, and E. M. Holt, "X-ray Crystal Structure, Spectroscopic Analysis, and Thermal Chemistry of Copper(II) 2-Oximinopropionate", *Polyhedron,* Submitted for publication.

9. A. Dobosz, N. M. Dudarenko, I. O. Fritsky, T. Glowiak, A. Karaczyn, H. Kozlowski, T. Y. Sliva, and J. Swiatek-Kozlowska, "N-Bonding of the Hydroxamic Function in Nickel(II) and Copper(II) Complexes with 2-(Hydroxyimino)propanohydroxamic Acid", *J. Chem. Soc., Dalton Trans.,* **1999,** 743-749.

10. S. M. Harben, P. D. Smith, R. L. Beddoes, D. Collison, and C. D. Garner, "Rhenium and Molybdenum Oxo-Complexes Containing Ligands related to N-hydroxyiminodipropionic Acid", *J. Chem. Soc., Dalton Trans.,* **1997,** 2777-2784.

11. R. D. Lampeka, N. M. Dudarenko, and V. V. Skopenko, "*trans*-Bis(2-hydroxyiminopropionato-*N,O*)dimethanolnickel(II) Dimethanol Solvate, $[Ni\{CH_3C(NOH)COO\}_2(CH_3OH)_2]\cdot 2CH_3OH$", *Acta Crystallogr., Sect. C,* **1994,** *50* (5), 706-708.

12. R. Lampeka, R. Bergs, R. Krämer, K. Polborn, W. Beck, "Metal Complexes with Biological Important Ligands, LXIX [1]. Half-Sandwich Complexes of Cobalt(III), Rhodium(III), Iridium(III), and Ruthenium(II) with Anions of α-Hydroxyimino Acids", *Z. Naturforsch., B: Chem. Sci.,* **1994,** *49* (2), 225-232.

13. R. D. Lampeka, Z. D. Uzakbergenova, and V. V. Skopenko, "Spectroscopic and X-ray Investigation of Cobalt(III) Complexes with 2-Oximinocarboxylic Acids", *Z. Naturforsch., B: Chem. Sci.,* **1993,** *48* (4), 409-417.

14. V. V. Skopenko, T. Y. Sliva, Y. A. Simonov, A. A. Dvorkin, N. D. Mazus, R. D. Lampeka, and T. I. Malinovski, "The Structure of Manganese(II) Complex with 2-(Hydroxyimino)propionic Acid", *Russ. J. Inorg. Chem.,* **1990,** *35* (7), 993-995.

15. Y. A. Simonov, T. Y. Sliva, M. D. Mazus, A. A. Dvorkin, and R. D. Lampeka, "The Synthesis and Structure of Complexes of Copper(II) with 2-Hydroximinopropionic Acid", *Russ. J. Inorg. Chem.,* **1989,** *34* (4), 489-491.

16. A. A. Dvorkin, Y. A. Simonov, T. Y. Sliva, R. D. Lampeka, M. D. Mazus, V. V. Skopinko, and T. I. Malinovskii, "Preparation and Structure of a Binuclear Mixed-Ligand Complex of Nickel(II) with 2-(Hydroxyimino)propionic Acid and Imidazole", *Russ J. Inorg. Chem.,* **1989,** *34* (10), 1475-1478.

17. A. Ahmad and I. D. Spenser, "The conversion of α-Keto Acids and of α-Keto Acid Oximes to Nitriles in Aqueous Solution", *Can. J. Chem.,* **1961,** *39* (6), 1340-1359.

18. D. F. Shriver, P. W. Atkins, and C. H. Langford "Inorganic Chemistry" 2nd ed.; Oxford University Press: Great Britain, 1994; pp 174-176.

19. M. E. Keeney, I. Asare, "Thermal Stability of LIX63 Oxime", *Hydrometallurgy,* **1984,** *12* (2), 255-265.

20. A. W. Ashbrook, "Commercial Chelating Solvent Extraction Reagents. I. Purification and Isomer Separation of 2-Hydroxyoximes", *J. Chromatogr.,* **1975,** *A 105* (1), 141-150.

21. A. Srinivasan, N. Kebede, J. E. Saavedra, A. V. Nikolaitchik, D. A. Brady, E. Yourd, K. M. Davies, L. K. Keefer, J. P. Toscano, "Chemistry of the Diazeniumdiolates. 3. Photoreactivity", *J. Am. Chem. Soc.,* **2001,** *123* (23), 5465-5472.

22. R. Glaser, R. K. Murmann, and C. L. Barnes, "Why Do Nitroso Compounds Dimerize While Their Oxime Tautomers Do Not? A Structural Study of the *Trans*-Dimer of 2-Chloro-2-methyl-3-nitrosobutane and Higher Level ab Initio

Study of Thermodynamics Stabilities and Electronics Structures of Isomers of Diazene Dioxides", *J. Org. Chem.,* **1996,** *61* (3), 1047-1058.

23. S. A. Bajue, P. Dasgupta, R. B. Jordan, G. C. Lalor, "Kinetics of the Formation and Dissociation of Some Nitrosonaphtholsulfonate Complexes of Nickel(II)", *Inorg. Chem.,* **1985,** *24* (5), 726-731.

24. R. K. Norris and S. Sternhell, "Tatomerism and *Syn-Anti* Isomerism in the *p*-Nitrosophenol-*p*-benzoquinone Monoxime System", *Tetrahedron Lett.,* **1967,** *8* (2), 97-101.

25. H. Uffmann, "Isomerism of Benzoquinone Oximes. II. Stereoisomerism and Tautomerism of 1,4-beznoquinone Oximes", *Z. Naturforsch., B: Chem. Biochem. Biophys. Biol.,* **1967,** *22* (5), 491-502.

26. R. K. Norris and S. Sternhell, "Nuclear Magnetic Resonance Spectra of *p*-Nitrosophenol and its Methyl Derivatives", *Aust. J. Chem.,* **1966,** *19* (5), 841-860.

27. H. Uffmann, "Isomerie von Benzochinonoximen", *Tetrahedron Lett.,* **1966,** *7* (38), 4631-4637.

28. S. Marcinkiewicz, J. Green, "Paper Chromatography and Chemical Structure. VI. Tautomerism and Intramolecular Hydrogen Bonding in the Same Molecule. *O-Nitrosophenols*", *J. Chromatogr.,* **1963,** *A 10,* 366-371.

29. J. Green, S. Marcinkiewicz, "Paper Chromatography and Chemical Structure. V. Tautomerism. The Determination of Tautomeric Equilibrium by Paper Chromatography. Thienol and *p*-Nitrosophenols", *J. Chromatogr.,* **1963,** *A 10,* 354-365.

30. L. C. Andrson, R. L. Yanke, "The Tautomerism of Quinoneoxime-para-nitrosophenol Systems", *J. Am. Chem. Soc.,* **1934,** *56* (3), 732-735.

31. L. C. Andrson, M. B. Geiger, "The Tautomerism of Quinoneoxime and Para-nitrosophenol", *J. Am. Chem. Soc.,* **1932,** *54* (8), 3064-3070.

32. P. Sydes "A Guidebook to Mechanism in Organic Chemistry" 6th ed.; Longman Group Limited: Great Britain, 1986; pp 123-126.

33. A. W. Apblett Oklahoma State University, Stillwater, OK. Personal Communication, 1999.

CHAPTER 4

4. CATALYTIC CLAISEN-SCHMIDT CONDENSATION USING NANOPARTICULATE $Zn(PAO)_2 \cdot 2H_2O$-DERIVED ZINC OXIDE

4.1. INTRODUCTION

The Claisen-Schmidt condensation is an "aldol-type" reaction used for carbon-carbon bond formation. It leads to the production of an α,β-unsaturated aldehyde or ketone upon the condensation of an aromatic aldehyde with an aliphatic aldehyde or ketone in the presence of a basic (e.g. HO^- and EtO^-) or an acidic (e.g. HCl) catalyst.[1,2] The condensation is exemplified in the following chemical equations:[1,3]

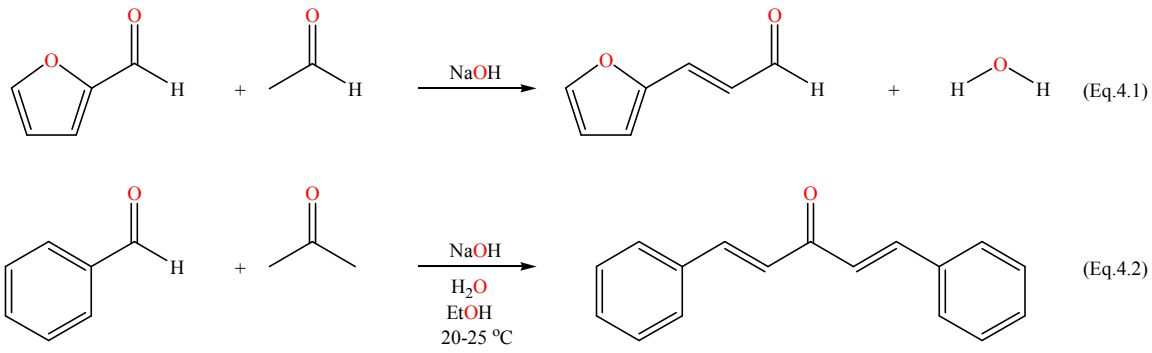

This kind of aldehyde-ketone condensation also represents the simplest method for the synthesis of an important class of naturally-occurring materials, called benzylideneacetophenones, also known as chalcones. These are generally prepared by catalytically-basic condensation of equimolar quantities of the appropriate substitute

benzaldehyde with the suitable substituted acetophenone.[2] Chalcones have wide important chemical, industrial, and pharmacological applications besides their biological activities and preparative usefulness for other compounds. They have been used as artificial sweeteners,[2] stabilizer against heat, photoprotectors against visible and ultraviolet light and light-induced aging,[2] photoreactive materials,[4-8] color photography,[2] scintillators,[2,9] polymerization catalysts,[2] analytical reagents,[2] coordinating ligands,[10,11] fluorescent whitening agents,[2] organic brightening additives,[2] anti-oxidants,[12-15] anti-inflammatories,[16-20] anti-cancer,[13,14,21-26] anti-malarials,[27-32] anti-leishmanial,[27,33-35] anti-bacterial,[36] anti-fungal,[37] and anti-AIDS.[11,38] They are useful for the synthesis of several compounds such as flavanones,[2,39-41] flavanols,[2,39] flavans,[2,39] flavones,[2,39] isoflavones,[2,39] aurones,[2,39,40] benzils,[2] heterocyclic epoxychalcones,[2,42,43] benzylacetophenones,[2] dihydrochalcones,[2,40] substituted allyl alcohols,[2] phenylindenes,[44] and quinolines.[45] The simplest and the parent member of the chalcone compounds is the 1,3-diphenyl-2-propen-1-one, also called benzylideneacetophenone or chalcone, obtained from the condensation of benzaldehyde with acetophenone in the presence of either an acidic or a basic catalyst as follows:[1,2]

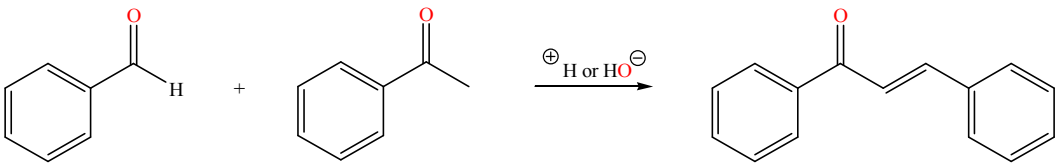

(Eq. 4.3)

A remarkable feature of the Claisen-Schmidt condensation reaction is its stereochemistry that usually leads to an *E*-α,β-unsaturated aldehyde or ketone, i.e. the carbonyl group and the bulkier substituent at the β-carbon atom are trans to each other.[1,3,42,43,46-52] This observed stereoselectivity can be accounted for by two reasons.

First, the steric hindrance interaction between the planar enolate anion and the large group attached to β-carbon in the conformation (II) of the enolate anion is reduced in comparison to conformation (I) (Equation 4.4). Consequently, conformation (II) is energetically preferred over conformation (I).[3,42,43,50-52] Second, the favorable transition state (III) (see Equation 4.4) produces the *E*-isomer because the large two substitute groups are not eclipsed[53] and there is no interference with coplanarity of the enolate system. It was found that the second factor had greater importance.[43,50-52]

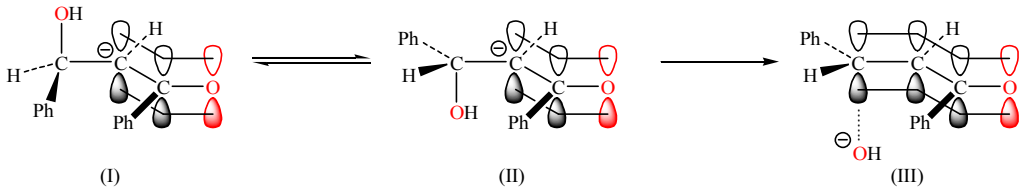

(Eq. 4.4)

Beside the Claisen-Schmidt Condensation reaction, chalcones can be synthesized by various methods such as Witting reaction,[2,54-56] Photo-Fries reaction,[2,57] Friedel-Crafts acylation of benzene with cinnamoyl chloride,[2] coupling reactions between cinnamoyl chloride and phenylboronic acids or benzoyl chloride and phenylvinylboronic acids (Suzuki reaction),[58] and thermal decomposition of α-diazoacetophenone.[59] However, the Claisen-Schmidt condensation is still the easiest and the most suitable one.[2]

Both homogeneous and heterogeneous catalysts were used for the fabrication of chalcones by the Claisen-Schmidt condensation reaction. The homogeneous catalysis conditions have been extensively employed, investigated, and are still being improved. Solutions of alkali (e.g. NaOH, NaOEt) in water, alcohol, or water/alcohol mixtures were the first homogeneous catalysts employed to promote the condensation at a temperature in the range of 25-50 ^{o}C.[1-3] Complete reaction required several hours to a week,

depending on the reaction temperature.[2] However, the yield of the desired chalcone decreases due to the disproportionation of aldehyde to alcohol and carboxylate (Cannizzaro reaction) under these conditions.[60] Benzal diacetate can be used instead of the aldehyde to avoid a Cannizaro reaction.[61] Moreover, methanol is preferred over ethanol as a co-solvent to prevent the discoloration and the aldol polymerization that may be caused by the oxidation of ethanol to acetaldehyde during the reaction. This discoloration and polymer formation are more likely to take place if the ethanolic alkali solution is heated or given opportunity to stand for a long time.[3] Acid catalysts were found to be better condensing catalyst agents than the alkali ones in the cases of phenols and phenol esters.[1] α-Alkylchalcones, Ar′C(O)C(R)═CHAr,[1] cyanomethylchalcones,[2] and hydroxynitrochalcones[2] were obtained readily using HCl as a catalyst. Phosphoryl chloride was shown to be a better catalyst than alkali for the production 2′-hydroxy-5-acetamidochalcones.[2] Other basic and acidic catalysts have been utilized for the synthesis of chalcones such as magnesium *t*-butoxide,[62] potassium-graphite intercalate (KC_8),[2] anhydrous aluminum chloride,[63] boron trifluoride,[64] titanium tetrachloride,[65] boric anhydride,[2] boric acid,[66] borax,[2] amino acids,[2] Grignard reagents,[2,67] phenyllithium,[68] organocadmium compounds (e.g. diphenyl cadmium and diethyl cadmium),[2] bis(p-methoxyphenyl)telluroxide,[69] calix[n]arenes/aqueous NaOH,[70] and lithium bis(trimethylsilyl)amide.[71] Generally, it is concluded from the investigation of the kinetics of the Claisen-Schmidt condensation that the reaction favors the acid catalysis conditions in the presence of an electron-withdrawing group (EWG) substitute on the ketone and/or an electron-donating group (EDG) substituent on the aldehyde.[2] In contrast, basic catalysts are superior if there is an EWG substituent on the aldehyde.[2]

However, both the EDG and EWG substituents in the aldehydic and ketonic components have generally the same effect on the yield of chalcone whether the reaction is catalyzed by an acid or a base promoter.[1] EWG substituents lead to higher yields because they accelerate the dehydration of the intermediate ketol to a greater extent than its retrogression to the reactants (decomposition of the ketol to the starting aldehyde and ketone).[1] Also, no intermediate ketols have been isolated under the acidic conditions because irreversible dehydration of ketols to chalcones is favored by the acid catalysts.[1] Thus, most ketols isolated so far have been prepared under mild basic conditions (e.g. aqueous ethanolic sodium phosphate).[1]

Heterogeneous catalysis of the Claisen-Schmidt condensation reaction have been recently exploited for the formation of chalcones on the surfaces of various simple solid inorganic materials such as alumina,[72] barium hydroxide,[73-77] hydrotalcites,[78-81] zeolites,[81,82] modified clays (e.g. ion-exchanged montmorillonite),[83] agar-agar gel-KOH (gel entrapped base catalyst),[84] cationic surfactant-aqueous NaOH (e.g. cetyltrimethylammonium chloride, sulfate, and hydroxide),[85] natural phosphate,[86] calcined sodium nitrate/natural phosphate,[87,88] calcined lithium nitrate/natural phosphate,[89] and imprinted polymers based on vinylpyridine-styrene-divinylbenzene copolymer.[90] Irradiation of the reaction mixture with ultrasound, in addition, gives better yields and reduces the reaction temperature.[91-93] The heterogeneous catalysis systems are preferred over the conventional homogeneous techniques because the formers require mild conditions, give improved yields and selectivity of the desired product, and need only simple manipulation and easy experimental set-up and work-up.[84,86]

In this investigation, nanocrystalline zinc oxide was prepared as described previously in Chapter 2, and was used to promote the heterogeneous Claisen-Schmidt condensation reaction of benzaldehyde with acetophenone under solvent-free conditions at 150^{o}C. Only a very small amount of the catalyst was needed for the completion of the reaction in several hours. To the best of our knowledge, zinc oxide was used for the first time by us in such application.

4.2. EXPERIMENTAL

Acetophenone [$H_3CC(O)C_6H_5$ (TCI)], benzaldehyde [C_6H_5CHO (Aldrich)], *t*-chalcone [$C_6H_5C(O)CH{=}CHC_6H_5$ (Aldrich)], dodecane [$H_3C(CH_2)_{10}CH_3$, 99+% (Aldrich)], phenol [C_6H_5OH (EM Science)], cyclohexylamine [$C_6H_{11}NH_2$ (Aldrich)], and cyclohexane [C_6H_{12}, reagent grade (Fisher Scientific)] were used-as-received without further purification. ZnO was obtained upon pyrolysis of $Zn(PAO)_2{\cdot}2H_2O$ at 389 ^{o}C as described previously in Chapter 2. A Hewlett Packard G1800A Gas Chromatograph-Mass Spectrometer GC-MS, equipped with 30 m x 0.25 mm HP5 column (crosslinked 5% PhMe silicone), was used to analyze the products of reactions catalyzed by prepared ZnO. The temperature program used was an initial hold of 2 min at 35^{o}C, a ramp of 5^{o}C/min to 170^{o}C, and a final hold of 5 min. The helium flow rate was 1 ml/min and the injection port was set at 250^{o}C.

A solvent-free mixture of acetophenone (0.8429 g, ~ 7 mmol), and benzaldehyde (0.8656 g, ~ 8 mmol) was placed in a 100-ml, glass media jar sealed with a Teflon-lined high-temperature resistant cap. A drop (0.0151 g) of this solution was taken, diluted with 23.99 g of an internal standard solution of highly pure dodecane/CH_2Cl_2 ($\approx$1:10000) in a 20-ml vial, and labeled as t = 0 hr. Then ZnO (0.08540 g, ~ 5 wt% of reactants) was

added to the reactants solution in the glass jar. This sealed reaction system was placed in a digitally-controlled oven at 150^{o}C to start the reaction. Several samples were taken at different intervals, diluted with the internal standard solution of highly pure dodecane/CH_2Cl_2, and then 1-µl samples were injected into a GC/MS. The glass jar reactor was cooled to room temperature before removing every sample. Response factors for the reactants and the products were determined using a solution containing these compounds along with dodecane as an internal standard. These were subsequently used to determine the reactants and product concentrations of the samples. Comparing the mass spectra of the reactants and the product to those available in the NIST database helped identify them. Verification of the product identity was established by the determination of the retention times of standard samples of the reactants and products. A pseudo first order procedure was followed to determine the reaction order with respect to both of the reactants, acetophenone and benzaldehyde. Thus, a mole ratio of 1:20 of one of the reactants to the other was employed at the same above reaction conditions mentioned. In order to calculate the reaction rate constant (k) and the reaction activation energy (E_a), the coupling reaction was performed at 110^{o}C and 130^{o}C with a mole ratio of 7 mmol acetophenone to 8 mmol benzaldehyde. To explore the extent of the catalyst's lifetime, the catalyst was reused to catalyze the same reaction at 130^{o}C.

Acidity and Basicity Measurements

The acidity and basicity of ZnO were measured by adsorption of cyclohexylamine and phenol from cyclohexane, respectively, according to the procedure outlined in Chapter 2.

4.3. RESULTS AND DISCUSSION

Figure 4.1 shows the Langmuir adsorption isotherms of the acidity (A) and basicity (B) of ZnO. These two surface properties of ZnO were discussed in detail in Chapter 2. The important conclusion that can be drawn is that while significant numbers of basic sites and acidic sites are present, the surface acidity predominates. This is unusual for ZnO and could be expected to strongly influence the catalytic activity. Therefore, the catalysis of a crossed aldol condensation of acetophenone with benzaldehyde at 150^{o}C was investigated using $Zn(PAO)_2$-derived ZnO to yield *t*-chalcone (Equation 4.5). Since the Claisen-Schmidt condensation can be expected to give an alkene with acid catalysts, the formation of chalcone reflects the acidity of the ZnO.

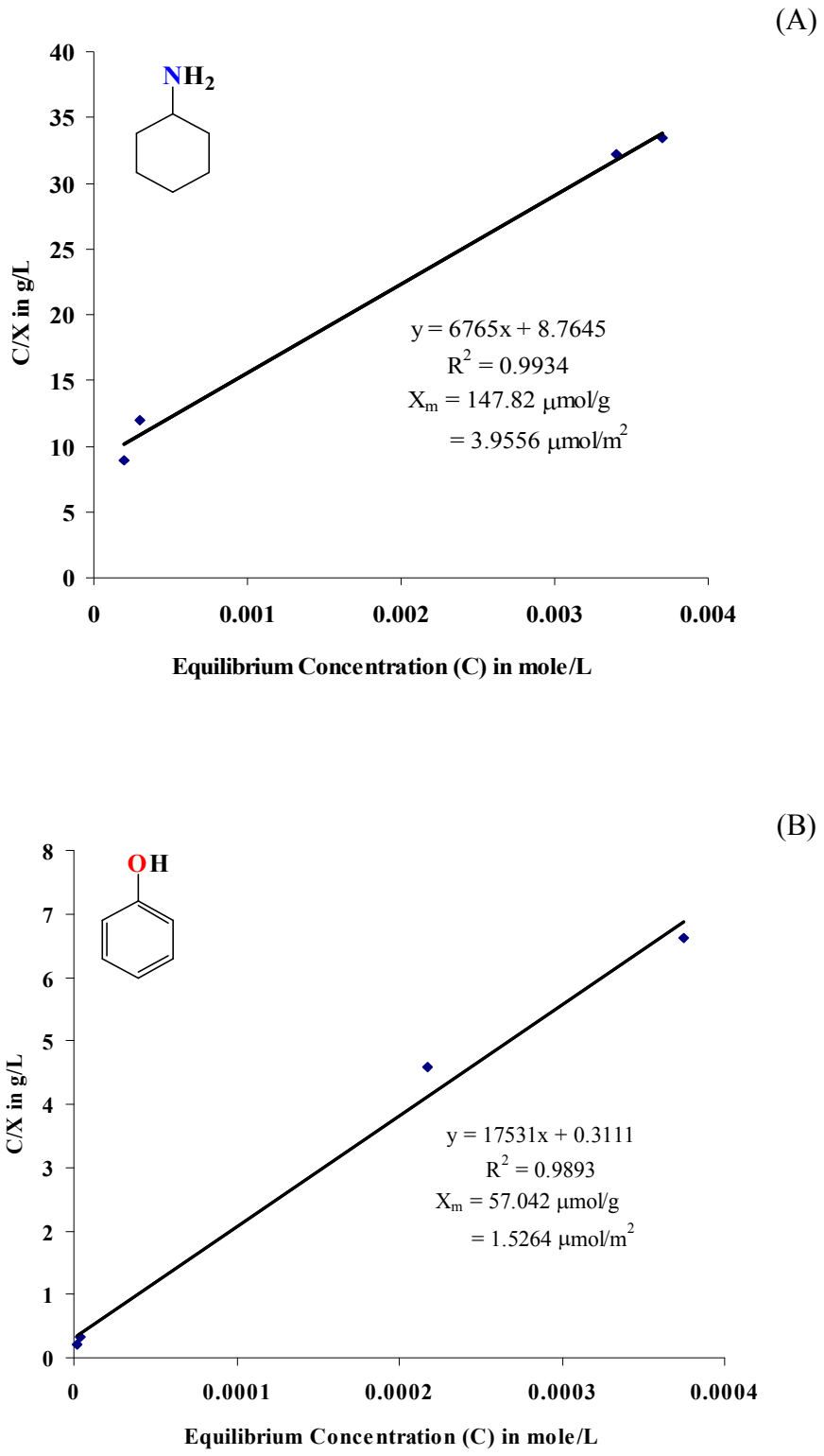

Figure 4.1. Langmuir adsorption isotherm of (A) acidity and (B) basicity of ZnO

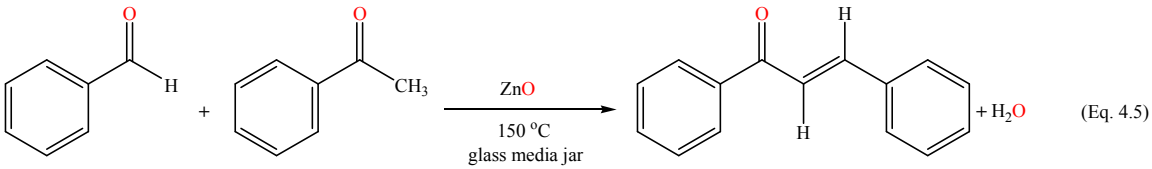

(Eq. 4.5)

The coupling reaction between acetophenone and benzaldehyde gave exclusively *t*-chalcone in 90% yield after an 8-hour run at 150°C. The IR and solid state ^{13}C NMR analyses of the catalyst used in the reaction confirm the formation of zinc benzoate on the surface of ZnO. Such observation implies that benzoic acid is formed during the reaction and then is adsorbed on the surface of the ZnO catalyst causing the neutralization of some of the basic sites. The origin of the benzoic acid is most likely to be the direct oxidation of benzaldehyde by oxygen as shown in equation 4.6:

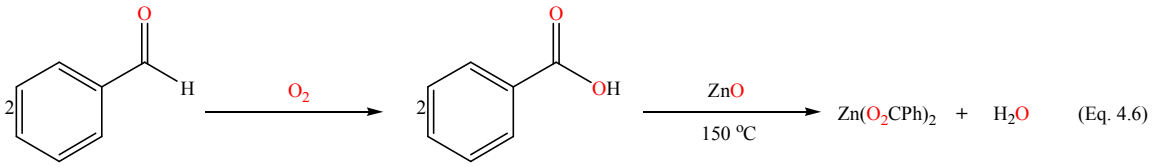

(Eq. 4.6)

The ease of oxidation of benzaldehyde by this route is well-established[94] and would be expected to be rapid with elevation of temperature. No benzyl alcohol, $PhCH_2OH$, was detected in the reaction mixture, indicating that benzaldehyde did not undergo a Cannizzaro reaction[94] which would also produce benzoic acid. Investigation of the catalytic activity of ZnO at 150°C as a function of the mole fraction (X) of reactants shows that the consumption of benzaldehyde is larger than that of acetophenone during the reaction period (Figure 4.2). This observation is consistent with the fact that benzaldehyde is also consumed for the production of benzoic acid. It is noteworthy to emphasize that no hydroxyketone (ketol) intermediate was observed or isolated under the

reaction conditions employed, even at lower temperature. This observation implies that the acidic sites on the oxide surface are responsible for the condensation reaction, because the ketol intermediate has been obtained under basic condensation only. However, the absence of the ketol intermediate does not exclude the basic sites on the surface of the catalyst from any role or participation in the catalytic process.

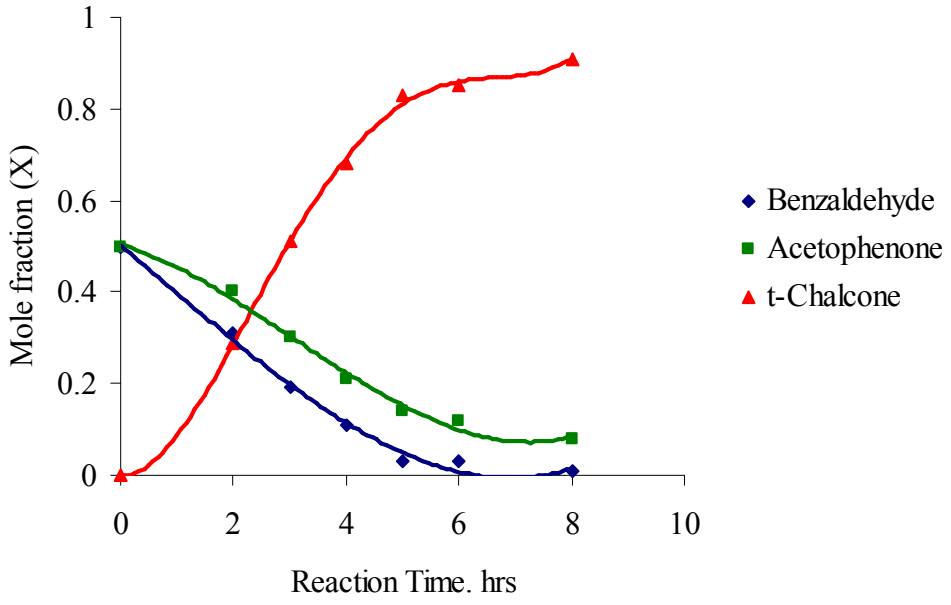

Figure 4.2. Mole fraction (X) of reactants and product versus time at 150°C

The kinetic aspects of the reaction were studied and revealed that the process has an overall order of 2, as evidenced by the sketch of the natural logarithm of the mole fraction ratio of acetophenone/benzaldehyde versus time (Figure 4.3). By using 20 times excess of each reagent, it was determined that the reaction was first order in acetophenone and first order in benzaldehyde (Figure 4.4). The pseudo rate constant (k_{pse}) of acetophenone is very similar to that of benzaldehyde. This may imply a similar adsorption strength of each reactant on the catalyst surface, i.e. the surface coverage (θ)

of the catalyst by each reactant. The results regarding the kinetics of the condensation of benzaldehyde and acetophenone promoted at 150°C by ZnO prepared in this study is similar to that observed for the reaction catalyzed at 28°C by H_2SO_4/HO_2CCH_3.[95] The latter reaction was found to be first order in each reactant and a second order overall.[95] It may be concluded from the kinetic aspects of the reaction that the condensation step, not the dehydration step of the ketol intermediate, is the rate-limiting step.

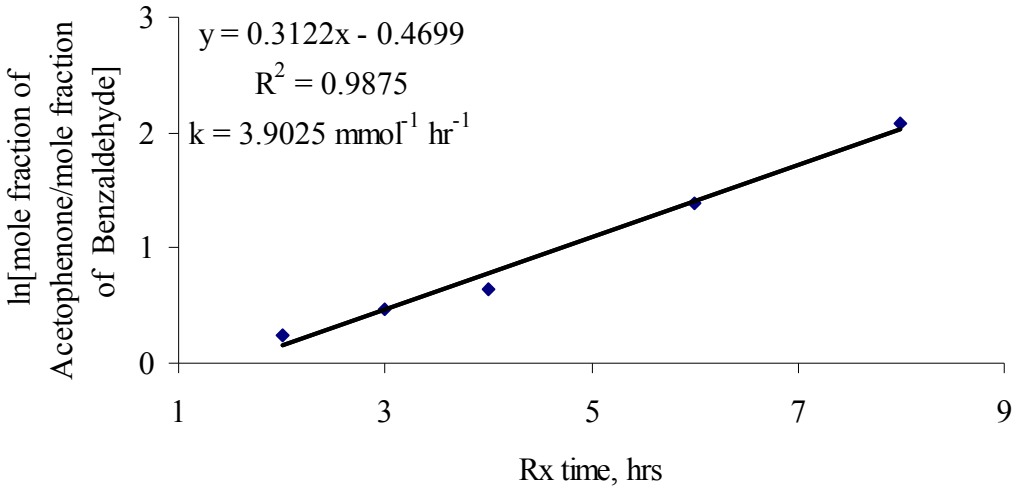

Figure 4.3. Second-order plot for the Claisen-Schmidt condensation between acetophenone and benzaldehyde catalyzed by 5 wt% reactants ZnO at 150°C

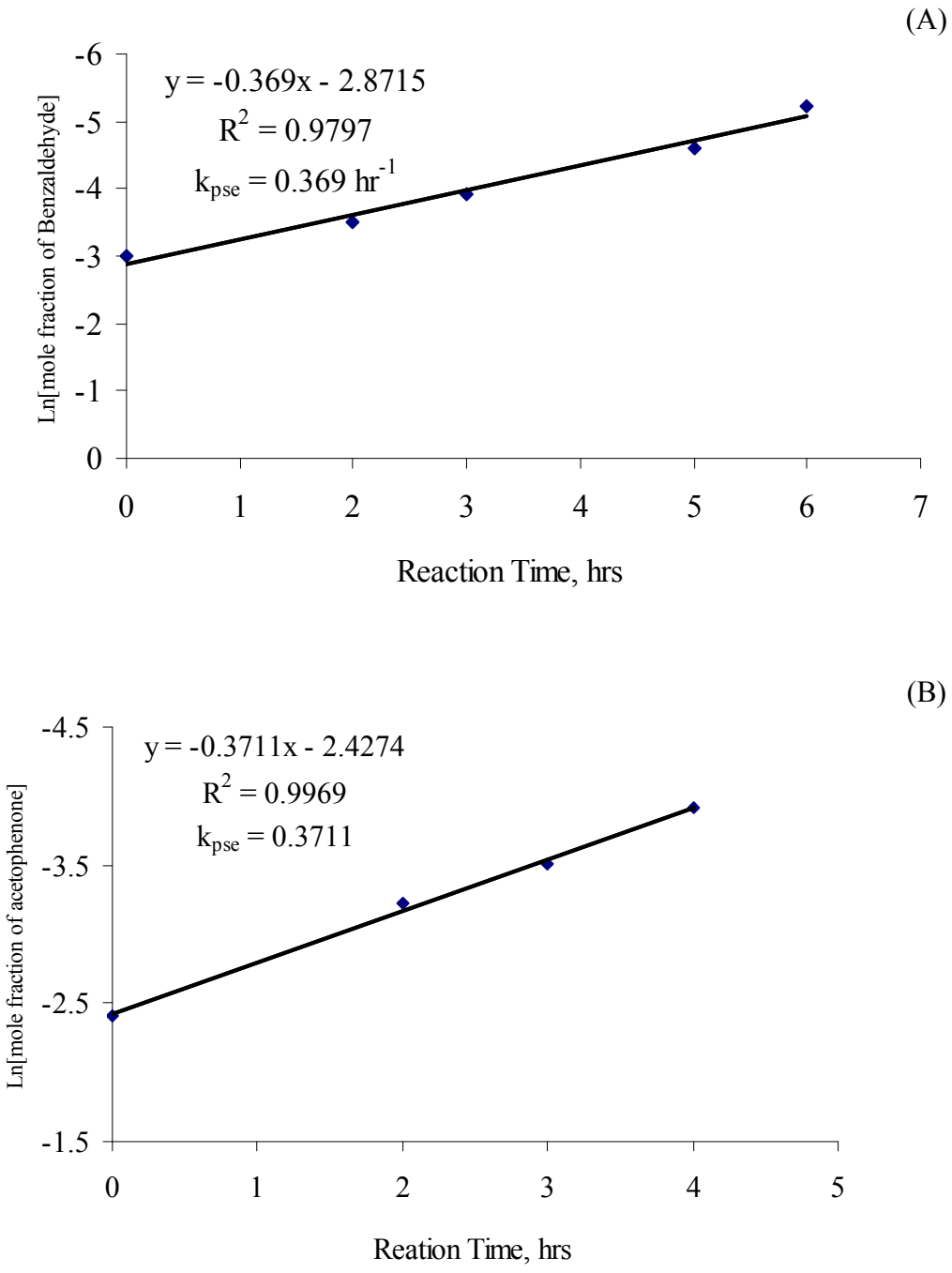

Figure 4.4. Pseudo first-order reaction in (A) acetophenone and (B) benzaldehyde

The reaction was also performed at 130°C, and it was found that the reaction was second-order overall and first-order in each reactant as concluded from the plot in Figure 4.5. The rate constant at 130°C is 71% less than that observed at 150°C.

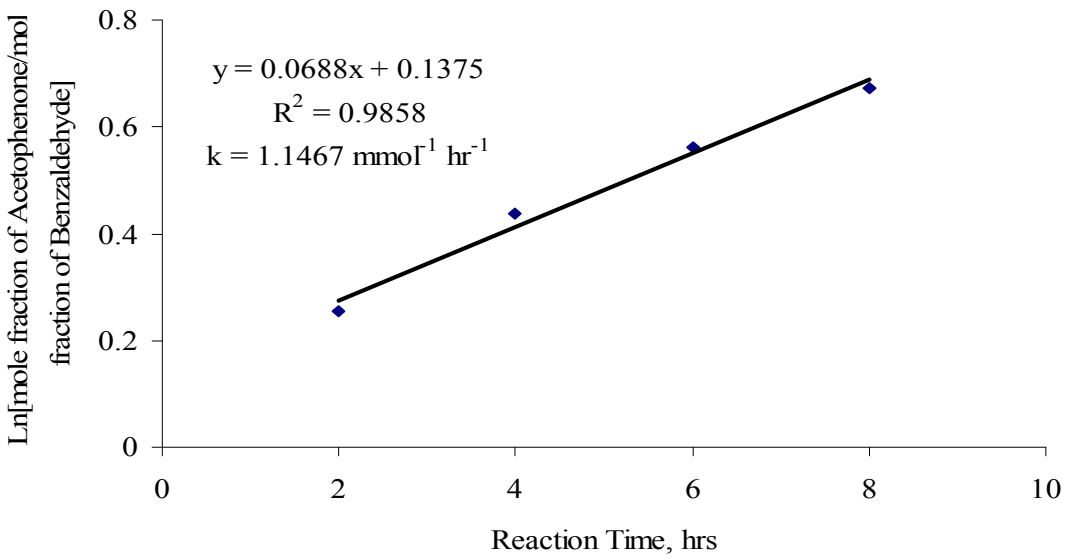

Figure 4.5. Second-order plot for the Claisen-Schmidt condensation between acetophenone and benzaldehyde catalyzed by 5 wt% reactants ZnO at 130°C

The catalytic activity of the catalyst at this temperature was monitored through the variation of mole fraction (X) of both of reactants and products as a function of the reaction run time (Figure 4.6).

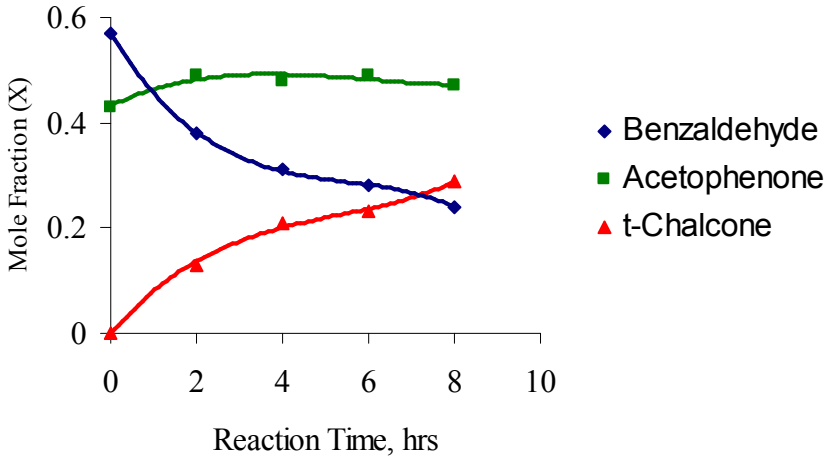

Figure 4.6. Change of the mole fraction (X) of reactants and products with time at 130°C

Investigation of the kinetic aspects of the reaction at 110°C revealed that the reaction was much slower in comparison to the reaction at 150°C, where the rate constant at the latter temperature is 78% greater than the former temperature. This is also confirmed by the smaller change of mole fraction of reactants and product at 110°C during the same period of time compared to those noted at 150°C and 130°C (Figure 4.7). However, the reaction still obeys the second-order mixed case and is a first order in each of both of reactants (Figure 4.8).

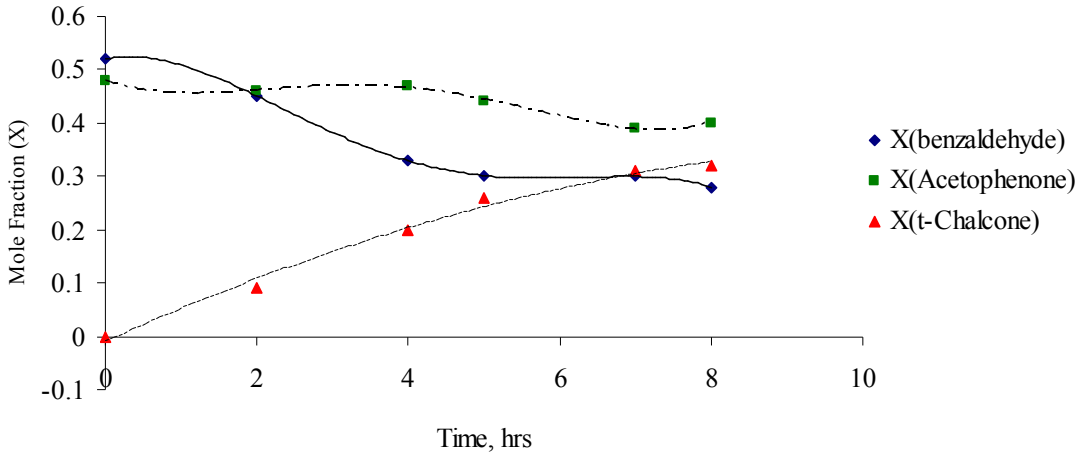

Figure 4.7. Variation of mole fraction (X) of reactant and product at 110°C with time

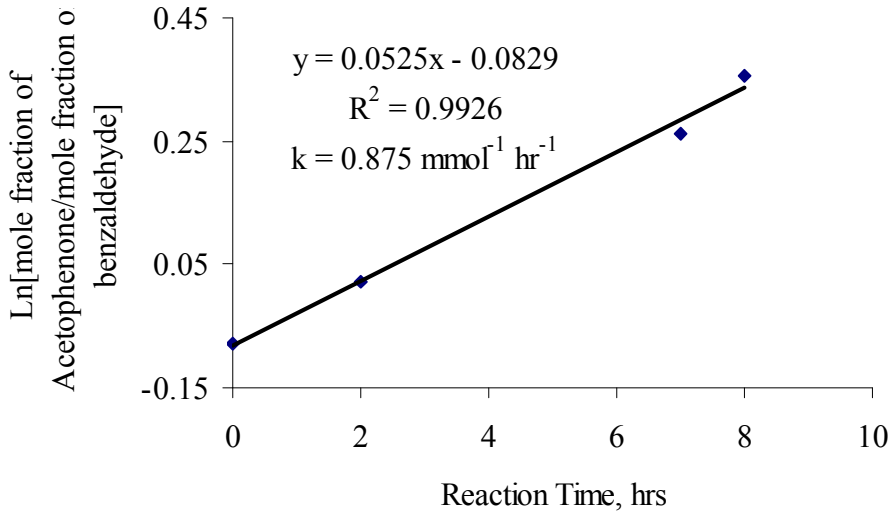

Figure 4.8. Second-order for the aldol condensation between acetophenone and benzaldehyde at 110°C promoted by 5 wt% reactants ZnO

Variation of the reaction temperature allowed the determination of activation energy (E_a) on the basis of Arrhenius equation. Plotting the natural logarithm (ln) of the rate constant (k) versus the reciprocal of the absolute temperature resulted in a straight line and E_a was calculated from the slope to be 49.77kJ/mol (Figure 4.9).

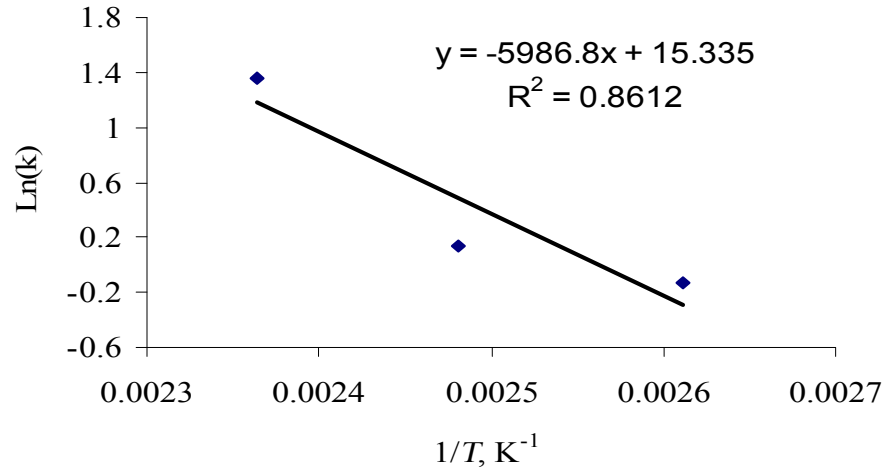

Figure 4.9. The Arrhenius plot for the Claisen-Schmidt Condensation between acetophenone and benzaldehyde catalyzed by 5 wt% reactants ZnO

To test the activity and the life time of the catalyst used, the ZnO utilized to catalyze the reaction at 130^{o}C was reused for the promotion of the reaction at the same temperature. The yield of *t*-chalcone after 8 hours is poor (23%), indicating the reaction becomes very slow owing to the conversion of ZnO, the active catalyst, to zinc benzoate, the inactive or the less active form of the catalyst. Thus, reactivation and regeneration of the catalyst by its combustion under air or oxygen for the conversion of benzoate to oxide is a necessary step for the utilization of the catalyst once again. Alternatively, performance of the reaction in an inert gas will likely prevent catalyst deactivation and excess benzaldehyde consumption.

4.4. CONCLUSION

Zinc oxide has been exploited for the first time for the Claisen-Schmidt condensation of benzaldehyde with acetophenone. The zinc oxide thus prepared in this study is nanocrystalline, and acidic. Such properties may endow the oxide with unprecedented chemical behavior in catalysis. It has been shown that the reaction rate is proportional to the first power of the concentration of each reactant, implying that the rate-limiting step is the condensation step. At 150^{o}C, the chalcone yield was 90% after an 8-hour run. Higher temperature, therefore, should speed up the reaction and increase the yield in a shorter period of time. However at 150^{o}C, the reaction was limited by competitive consumption of benzaldehyde by a side oxidation reaction. The use of a greater excess of benzaldehyde, or changing the amount of the catalyst has not been investigated during this work. However, the additional benzaldehyde and changing the amount to zinc oxide may profoundly affect the reaction rate because the catalyst is consumed and converted to the less active material zinc benzoate.

REFERENCES

1. A. T. Nielsen and W. J. Houlihan "The Aldol Condensation" In *Organic Reactions;* A. C. Cope, R. Adams, A. H. Blatt, V. Boekelheide, T. L. Cairns, D. J. Cram, and H. O. House, Eds.; John Wiley & Sons, Inc.: New York, 1968; Vol. 16, pp 2 and 44-47.

2. D. N. Dhar "The Chemistry of Chalcones and Related Compounds"; John Wiley & Sons, Inc.: New York, 1981.

3. H. O. House "Modern Synthetic Reactions" In *The Organic Chemistry Monograph Series;* R. Breslow, P. D. Bartlett, D. Curtin, W. S. Johnson, J. D. Roberts, and R. B. Woodward, Eds.; W. A. Benjamin, Inc.: Menlo Park, California, 1972; pp 632-653.

4. B. H. Lee, J. H. Kim, M. J. Cho, S. H. Lee, and D. H. Choi, "Photochromic Behavior of Spiropyran in the Photoreactive Polymer Containing Chalcone Moieties", *Dyes and Pigments,* **2004,** *61* (3), 235-242.

5. J. H. Kim, S. Y. Ban, S. Kaihua, and D. H. Choi, "Photochromic Behavior of New Bifunctional Copolymer Containing Spiropyran and Chlacone Moiety in the Side Chain", *Dyes and Pigments,* **2003,** *58* (2), 105-112.

6. J. Indira, P. P. Karat, and B. K. Sarojini, "Growth, Characterization, and Nonlinear Optical Property of Chalcone Derivative", *J. Crystal Growth,* **2002,** *242* (1-2), 209-214.

7. K. H. Jung, S.Hyun, D. Song, and D. Shin, "The Characteristics of Polyimide Photoalignment Layer with Chalcone Derivatives Produced by Linear Polarized UV Light", *Opt. Mater.,* **2002,** *21* (1-3), 663-666.

8. D. Song, K. Jung, J. Moon, and D. Shin, "Photochemistry of Chalcone and the Application of Chalcone-Derivatives in Photo-Alignment layer of Liquid Crystal Display", *Opt. Mater.,* **2002,** *21* (1-3), 667-671.

9. N. DiCesare and J. R. Lakowicz, "Chalcone-Analogue Fluorescent Prfobes for Saccharides Signaling Using the Boronic Acid Group", *Tetrahedron Lett.,* **2002,** *43* (14), 2615-2618.

10. K. Zutin, V. M. Nogueira, A. E. Mauro, P. Melnikov, and A. Iluykhin, "Synthesis, Electrochemical Behavior and X-ray Crystal and Molecular Structures of [Fe(diene)$(CO)_2PPh_3$] (diene = Chalcone, Sorbic Acid)", *Polyhedron,* **2001,** *20* (9-10), 1011-1016.

11. L. Mishra, R. Sinha, H. Itokawa, K. F. Bastow, Y. Tachibana, Y. Nakanishi, N. Kilgore, and K. Lee, "Anti-HIV and Cytotoxic Additives of Ru(II)/Ru(III)

Polypyridyl Complexes Containing 2,6-(2′-Benzimidazolyl)-Pyridine/Chalcone as Co-Ligand", *Bioorg. Med. Chem.,* **2001,** *9* (7), 1667-1671.

12. C. Nakamura, N. Kawasaki, H. Miyataka, E. Jayachandran, I. H. Kim, K. L. Kirk, T. Taguchi, Y. Takeuchi, H. Hori, and T. Satoh, "Synthesis and Biological Activities of Fluorinated Chalcone Derivatives", *Bioorg. Med. Chem.,* **2002,** *10* (3), 699-706.

13. S. Mukherjee, V. Kumar, A. K. Prasad, H. G. Raj, M. E. Bracke, C. E. Olsen, S. C. Jain, and V. S. Parmar, "Synthesis and Biological Activity Evaluation Studies on Novel 1,3-Diarylpropenones", *Bioorg. Med. Chem.,* **2001,** *9* (2), 337-345.

14. C. Furman, J. Lebeau, J. Fruchart, J. Bernier, P. Duriez, N. Cotelle, and E. Teissier, "Di-tert-Butylhdroxylated Flavonoids Protect Endothelial Cells Against Oxidized LDL-Induced Cytotoxicity", *J. Biochem. Mol. Toxicol.,* **2001,** *15* (5), 270-278.

15. R. J. Anto, K. Sukumaran, G. Kuttan, M. N. A. Rao, V. Subbaraju, and R. Kuttan, "Anticancer and Antioxidant Activity of Synthetic Chalcones and Related Compounds", *Cancer Lett.,* **1995,** *97* (1-4), 33-37.

16. J. Rojas, M. Paya, J. N. Dominguez, and M. L. Ferrandiz, "The Synthesis and Effect of Fluorinated Chalcone Derivatives on Nitric Oxide Production", *Bioorg. Med. Chem. Lett.,* **2002,** *12* (15), 1951-1954.

17. F. Herencia, M. P. Lopez-Garcia, A. Ubeda, and M. L. Ferrandiz, "Nitric Oxide-Scavenging Properties of Some Chalcone Derivatives", *Nitric Oxide,* **2002,** *6* (2), 242-246.

18. H. Hsieh, L. Tsao, J. Wang, and C. Lin, "Synthesis and Anti-Inflammatory Effect of Chalcones", *J. Pharm. Pharmcol.,* **2000,** *52* (2), 163-171.

19. F. Herencia, M. L. Ferrandiz, A. Ubeda, J. N. Dominguez, J. E. Charris, G. M. Lobo, and M. J. Alcaraz, "Synthesis and Anti-Inflammatory Activity of Chalcone Derivatives", *Bioorg. Med. Chem. Lett.,* **1998,** *8* (10), 1169-1174.

20. J. F. Ballesteros, M. J. Sanz, A. Ubeda, M. A. Miranda, S. Iborra, M. Paya, and M. J. Alcaraz, "Synthesis and Pharmacological Evaluation of 2'-Hydroxychalcones and Flavones as Inhibitors of Inflammatory Mediators Generation", *J. Med. Chem.,* **1995,** *38* (14), 2794 – 2797.

21. K. Monostory, V. Tamasi, L. Vereczkey, and P. Perjesi, "A Study on CYP1A Inhibitory Action of *E*-2-(4′-Methoxybenzylidene)-1-benzosuberone and Some Related Chalcones and Cyclic Chalcone Analogues", *Toxicology,* **2003,** *184* (2-3), 203-210.

22. G. Saydam, H. H. Aydin, F. Sahin, O. Kucukoglu, E. Erciyas, E. Terzioglu, F. Buyukkececi, and S. B. Omay, "Cytotoxic and Ihibitory Effects of 4,4′-Dihydroxy Chalcone (RVC-588) on Proliferation of Human Leukemic HL-60 Cells", *Leuk. Res.*, **2003,** *27* (1), 57-64.

23. F. Bois, C. Beney, A. Boumendjel, A. Mariotte, G. Conseil, and A. Peitro, "Halogenated Chalcones with High-Affinity Binding to P-Glycoprotein: Potential Modulators of Multidrug Resistance", *J. Med. Chem.,* **1998,** *41* (21), 4161-4164.

24. A. T. Kostova, C. Abeygunawardana, and P. Talalay, "Chemoprotective Properties of Phenylpropenoids, Bis(benzylidene)cycloalkanones, and Related Michael Reaction Acceptors: Correlation of Potencies as Phase 2 Enzyme Inducers and Radical Scavengers", *J. Med. Chem.,* **1998,** *41* (26), 5287 – 5296.

25. L Wattenberg, "Chalcones, Myo-Inositol and Other Novel Inhibitors of Pulmonary Carcinogenesis", *Lung Cancer,* **1996,** *14* (1), 152.

26. M. L. Edwards, D. M. Stemrick, and P. S. Sunkara, "Chalcones: A New Class of Antimitotic Agents", *J. Med. Chem.,* **1990,** *33* (7), 1948-1954.

27. M. Liu, P. Wilairat, S. L. Croft, A. L. Tan, and M. Go, "Structure-Activity Relationships of Antileshmanial and Antimalarial Chalcones", *Bioorg. Med. Chem.,* **2003,** *11* (13), 2729-2738.

28. X. Wu, P. Wilairat, and M. Go, "Antimalarial Activity of Ferrocenyl Chalcones", *Bioorg. Med. Chem. Lett.,* **2002,** *12* (17), 2299-2302.

29. J. N. Dominguez, J. E. Charris, G. Lobo, N. G. Dominguez, M. M. Moreno, F. Riggione, E. Sanchez, J. Olson, and P. J. Rosenthal, "Synthesis of Quinolinyl Chalcones and Evaluation of Their Antimalarial Activity", *Eur. J. Med. Chem.,* **2001,** *36* (6), 555-560.

30. M. Liu, P. Wilairat, and M. Go, "Antimalarial Alkoxylated and Hydroxylated Chalcones: Structure-Activity Relationship Analysis", *J. Med. Chem.,* **2001,** *44* (25), 4443-4452.

31. V. J. Ram, A. S. Saxena, S. Srivastava, and S. Chandra, "Oxygenated Chalcones and Bischalcones as Potential Antimalarial Agents", *Bioorg. Med. Chem. Lett.,* **2000,** *10* (19), 2159-2161.

32. R. Li, G. L. Kenyon, F. E. Cohen, X. Chen, B. Gong, J. N. Dominguez, E. Davidson, G. Kurzban, R. E. Miller, E. O. Nuzum, P. J. Rosenthal, and J. H. McKerrow, "In Vitro Antimalarial Activity of Chalcones and Their Derivatives", *J. Med. Chem.,* **1995,** *38* (26), 5031 – 5037.

33. F. Lunardi, M. Guzela, A. T. Rodrigues, R. Correa, I. Eger-Mangrich, M. Steindel, E. C. Grisard, J. Assreuy, J. B. Calixto, and A. R. S. Santos, "Trypanocidal and Leishmanicidal Properties of Substitution-Containing Chalcones", *Antimicrob. Agents Chemother.,* **2003,** *47* (4), 1449 - 1451.

34. L. Zhai, M. Chen, J. Blom, T. G. Theander, S. B. Christensen, and A. Kharazmi, "The Antileishmanial Activity of Novel Oxygenated Chalcones and Their Mechanism of Action", *J. Antimicrob. Chemother.,* **1999,** *43* (6), 793-803.

35. S. F. Nielsen, S. B. Christensen, G. Cruciani, A. Kharazmi, and T. Liljefors, "Antileishmanial Chalcones: Statistical Design, Synthesis, and Three-Dimensional Quantitative Structure-Activity Relationship Analysis", *J. Med. Chem.,* **1998,** *41* (24), 4819-4832.

36. Y. Lin, Y. Zhou, M. T. Flavin, L. Zhou, W. Nie, and F. Chen, "Chalcones and Flavonoids as Anti-Tuberculosis Agents", *Bioorg. Med. Chem.,* **2002,** *10* (8), 2795-2802.

37. S. N. López, M. V. Castelli, S. A. Zacchino, J. N. Domínguez, G. Lobo, J. Charris, J. C. G. Cortés, J. C. Ribas, C. Devia, A. M. Rodríguez, and R. D. Enriz, "In Vitro Antifungal Evaluation and Structure–Activity Relationships of a New Series of Chalcone Derivatives and Synthetic Analogues, with Inhibitory Properties Against Polymers of the Fungal Cell Wall", *Bioorg. Med. Chem.,* **2001,** *9* (8), 1999-2013.

38. J. Wu, X. Wang, Y. Yi and K. Lee, "Anti-AIDS Agents 54. A Potent Anti-HIV Chalcone and Flavonoids from Genus *Desmos*", *Bioorg. Med. Chem. Lett.,* **2003,** *13* (10), 1813-1815.

39. J. D. Bulock "Polyketide Biosynthesis" In *Comprehensive Organic Chemistry: The Synthesis and Reaction of Organic Compounds, Biological Compound;* E. Haslam, Ed.; Pergamon Press Ltd.: Oxford, England, 1979; Vol. 5, pp 950-955.

40. B. A. Bohm "The Minor Flavonoids" In *The Flavonoids: Advances in Research Since 1986;* J. B. Harborne, Ed.; Chapman & Hall: London, UK, 1994; pp 387-440.

41. R. Brouillard and O. Dangles "Flavonoids and Flower Colour" In *The Flavonoids: Advances in Research Since 1986;* J. B. Harborne, Ed.; Chapman & Hall: London, UK, 1994; pp 566-568.

42. G. Litkei "Chalcone Epoxides in Flavonoid Chemistry" In *Recent Developments in the Chemistry of Natural Carbon Compounds;* R. Bognar, V. Bruckner, and C. Sazntay, Eds.; Akademiai Kiado: Budapest, Hungary, 1979; Vol. IX, pp 293-408.

43. H. E. Zimmerman, L. Singer, and B. S. Thyagarajan, "Overlap Control of Carbanionoid Reactions. I. Stereoslectivity in Alkaline Epoxidation", *J. Am. Chem. Soc.,* **1959,** *81* (1), 108-116.

44. M. Jayamani, N. Pant, S. Ananthan, K. Narayanan, and C. N. Pillai, "Synthesis of Indenes From Phenylpropnones Using Alumina Catalyst", *Tetrahedron,* **1986,** *42* (15), 4325-4332.

45. J. J. Eisch and R. Sanchez, "Selective, Oxophilic Imination of Ketones with Bis(dichloroaluminum)phenylimide", *J. Org. Chem.,* **1986,** *51* (10), 1848-1852.

46. M. Brink, "Zur Kenntnis Einiger Kernsubstituierten *trans*-Methylstyrylketone", *Tetrahedron,* **1969,** *25* (5), 995-999.

47. A. C. Hassner and T. C. Mead, "The stereochemistry of 2-benzalcyclohexanones and 2-benzalcyclopentanones", *Tetrahedron,* **1964,** *20* (10), 2201-2210.

48. J. Zabicky, "The Kinetics and Mechanism of Carbonyl-Methylene Condensation Reactions. Part XI. Stereochemistry of the Products", *J. Chem. Soc.,* **1961,** 683-687.

49. H. O. House and R. S. Ro, "The Stereochemistry of Base-catalyzed Epoxidation", *J. Am. Chem. Soc.,* **1958,** *80* (10), 2428 – 2433.

50. H. E. Zimmerman and L. Ahramjian, "Overlap Control of Carbanionoid Reactions. II. The Stereochemistry of the Perkin Reaction and Related Condensation Reations", *J. Am. Chem. Soc.,* **1959,** *81* (9), 2086-2091.

51. H. E. Zimmerman and L. Ahramjian, "Overlap Control of Carbanionoid Reactions. III. The Stereochemistry of the Darzens Reaction", *J. Am. Chem. Soc.,* **1960,** *82* (20), 5459-5466.

52. H. E. Zimmerman, "Base-Catalyzed Rearrangements" In *Molecular Rearrangements,* P. de Mayo, Ed.; John Wiley & Sons, Inc.: New York, 1963; Vol. 1, pp 345-406.

53. D. Y. Curtin, "Stereochemical Control of Organic Reactions Differences in Behavior of Diastereoisomers", *Rec. Chem. Prog.,* **1954,** *15,* 111-128.

54. S. Trippett and D. M. Walker, "The Phosphobetaines: Preparation and Properties", *J. Chem. Soc.,* **1961,** 1266 – 1272.

55. S. Trippett and D. M. Walker, "The Use, in Wittig Reactions, of Phosphonium Salts and Phosphobetaines Containing a Basic Group", *J. Chem. Soc.,* **1961,** 2130 – 2133.

56. W. S. Wadsworth and W. D. Emmons, "The Utility of Phosphonate Carbanions in Olefin Synthesis", *J. Am. Chem. Soc.,* **1961,** *83* (7), 1733-1738.

57. V. T. Ramakrishnan and J. Kagan, "Photochemical Synthesis of 2'-Hydroxychalcones from Phenyl Cinnamates", *J. Org. Chem.,* **1970,** *35* (9), 2901-2904.

58. S. Eddarir, N. Cotelle, Y. Bakkour, and C. Rolando, "An Efficient Synthesis of Chlacones Based on the Suzuki Reaction", *Tetrahedron Lett.,* **2003,** *44* (28), 5359-5363.

59. P. Yates and T. J. Clark, "The thermal decomposition of α-diazoacetophenone", *Tetrahedron Lett.,* **1961,** *2* (13), 435-439.

60. D. N. Dhar and J. B. Lal, "Chalcones. Condensation of Aromatic Aldehydes with Resacetophenone. II", *J. Org. Chem.,* **1958,** *23* (8), 1159 – 1161.

61. W. Davey and J. R. Gwilt, "Chalcones and Related Compounds. Part I. Preparation of Nitro-, Amino-, and Halogen-Chalcones", *J. Chem. Soc.,* **1957,** 1008-1014.

62. J. L. Guthrie and N. Rabjohn, "Some Reactions Effected by Means of Bromomagnesium *t*-Alkoxides", *J. Org. Chem.,* **1957,** *22* (2), 176-179.

63. N. O. Calloway and L. D. Green, "Reactions in the Presence of Metallic Halides. I. β-Unsaturated Ketone Formation as a Side Reaction in Friedel-Crafts Acylations", *J. Am. Chem. Soc.,* **1937,** *59* (5), 809-811.

64. D. S. Breslow and C. R. Hauser, "Condensations. XI. Condensations of Certain Active Hydrogen Compounds Effected by Boron Trifluoride and Aluminum Chloride", *J. Am. Chem. Soc.,* **1940,** *62* (9), 2385 – 2388.

65. C. R. Harrison, "Transient Titanium Enolate Aldol Condensations", *Tetrahedron Lett.,* **1987,** *28* (36), 4135-4138.

66. R. D. Offenhauer and S. F. Nelsen, "Aldehyde and Ketone Condensation Reactions Catalyzed by Boric Acid", *J. Org. Chem.,* **1968,** *33* (2), 775-777.

67. D. S. Tarbell and M. C. Paulson, "Attempted Asymmetric Syntheses Involving the Grignard Reagent in Optically Active Solvents", *J. Am Chem. Soc.,* **1942,** *64* (12), 2842-2844.

68. J. C. Bond and G. F. Wright, "Action of Organometallic Compounds on Geoisomeric Styrenes", *J. Am. Chem. Soc.,* **1950,** *72* (2), 1023-1024.

69. L. Engman and M. P. Cava, "Bis(p-methoxyphenyl)telluroxide, A Novel Organotellurium Aldol Catalyst", *Tetrahedron Lett.,* **1981,** *22* (52), 5251-5252.

70. S. Shimizu, S. Shirakawa, T. Suzuki, and Y. Sasaki, "Water-Soluble Calixarenes as New Inverse Phase-Transfer Catlysts. Their Application to Aldol-Type Condensation and Micheal Addition Reactions in Water", *Tetrahedron,* **2001,** *57* (29), 6169-6173.

71. J. B. Daskiewicz, G. Comte, D. Barron, A. Pietro, and F. Thomasson, "Organolithium Mediated Synthesis of Prenylchalcones as Potential Inhibitors of Chemoresistance", *Tetrahedron Lett.,* **1999,** *40* (39), 7095-7098.

72. R. S. Varma, G. W. Kabalka, L. T. Evans, and R. M. Pagni, "Aldol Condensations on Basic Alumina: The Facile Synthesis of Chalcones and Enones in a Slovent-Free Medium", *Synth. Commun.,* **1985,** *15* (4), 279-284.

73. M. S. Climent, J. M. Marinas, Z. Mouloungui, Y. L. Bigot, M. Delmas, A. Gaset, and J. V. Sinisterra, "$Ba(OH)_2$ as Catalyst in Organic Reactions. 20. Structure-Catalytic Activity Relationship in the Witting Reaction", *J. Org. Chem.,* **1989,** *54* (15), 3695-3701.

74. S. Sathyanarayana and H. G. Krishnamurty, "Corroborative Studies on the Highly Efficient Preparation of 2′-Hydroxychalcones Using Partially Dehydrated Barium Hydroxide Catalyst", *Curr. Sci.,* **1988,** *57* (20), 1114-1116.

75. A. R. Alcantara, J. M. Marinas, and J. V. Sinisterra, "Synthesis of 2′-Hydrocchalcones and Related Compounds in Interfacial Solid-Liquid Conditions", *Tetrahedron Lett.,* **1987,** *28* (14), 1515-1518.

76. A. Aguilera, A. R. Alcantara, J. M. Marinas, and J. V. Sinisterra, "Ba(OH)2 as the Catalyst in Organic Reactions. Part XIV. Mechanism of Claisen-Schmidt Condensation in Solid-Liquid Conditions", *Can. J. Chem.,* **1987,** *65*, 1165-1171.

77. J. V. Sinisterra and A.Raso, "An Improved Procedure for the Claisen-Schmidt Reaction", *Synthesis,* **1984,** *6*, 502-504.

78. M. J. Climent, A. Corma, S. Iborra, and A. Velty, "Activated Hydrotalcites as Catalysts for the Synthesis of Chalcones of Pharmaceutical Interest", *J. Catal.,* **2004,** *221* (2), 474-482.

79. A. Guida, M. H. Lhouty, D. Tichit, F. Figueras, and P. Geneste, "Hydrotalcites as Base Catalysts. Kinetics of Claisen-Schmidt Condensation, Intramolecular Condensation of Acetonylacetone and Synthesis of Chalcone", *Appl. Catal. A,* **1997,** *164* (1-2), 251-264.

80. D. Tichit, M. H. Lhouty, A. Guida, B. H. Chiche, F. Figueras, A. Auroux, D. Bartalini, and E. Garrone, "Textural Properties and Catalytic Activity of Hydrotalcites", *J. Catal.,* **1995,** *151* (1), 50-59.

81. M. J. Climent, A. Corma, S. Iborra, and J. Primo, "Base Catalysis for Fine Chemicals Production: Claisen-Schmidt Condensation on Zeolites and Hydrotalcites for the Production of Chalcones and Flavanones of Pharmaceutical Interest", *J. Catal.,* **1995,** *151* (1), 60-66.

82. M. J. Climent, H. Garcia, and J. Primo, "Zeolites as Catalysts in Organic Reactions. Claisen-Schmidt Condensation of Acetophenone with Benzaldehyde", *Catal. Lett.,* **1990,** *4*, 85-92.

83. A. Azzouz, D. Messad, D. Nistor, C. Catrinescu, A. Zvolinschi, and S. Asaftei, "Vapor Phase Aldol Condensation over Fully Ion-Exchanged Montmorillonite-Rich Catalysts", *Appl. Catal. A*, **2003,** *241* (1-2), 1-13.

84. R. S. Natekar and S. D. Samant, "Gel Entrapped Base Catalyzed (GEBC) Aldol Reaction of Acetophenones with Benzaldehydes", *Indian J. Chem.,* **1996,** *35* B, 1347-1348.

85. F. Fringuelli, G. Pani, O. Piermatti, and F. Pizzo, "Condensation Reactions in Water of Active Methylene Compounds with Arylaldehydes. One-pot Synthesis of Flavonols", *Tetrahedron,* **1994,** *50* (39), 11499-11508.

86. S. Sebti, A. Saber, A. Rhihil, R. Nazih, and R. Tahir, "Claisen-Schmidt Condensation Catalysis by Natural Phosphate", *Appl. Catal. A,* **2001,** *206* (2), 217-220.

87. S. Sebti, A. Solhy, R. Tahir, S. Abdelatif, S. Boulaajaj, J. A. Mayoral, J. I. Garcia, J. M. Fraile, A. Kossir, and H. Oumimoun, "Application of Natural Phosphate Modified with Sodium Nitrate in the Synthesis of Chalcones: A Soft and Clean Method", *J. Catal.,* **2003,** *213* (1), 1-6.

88. S. Sebti, A. Solhy, R. Tahir, S. Boulaajaj, J. A. Mayoral, J. M. Farile, A. Kossir, and H. Oumimoun, "Calcined Sodium Nitrate/Natural Phosphate: An Extremely Active Catalyst for the Easy Synthesis of Chalcones in Heterogeneous Media", *Tetrahedron Lett.,* **2001,** *42* (45), 7953-7955.

89. S. Sebti, A. Solhy, A. Smahi, A. Kossir, and H. Oumimoun, "Dramatic Activity Enhancement of Natural Phosphate Catalyst by Lithium Nitrate. An Efficient Synthesis of Chalcones", *Catal. Commun.,* **2002,** *3* (8), 335-339.

90. J. Matsui, I. A. Nicholls, I. Karube, and K. Mosbach, "Carbon-Carbon Bond Formation Using Substrates Selective Catalytic Polymers Prepared by Molecular Imprinting: An Artificial Class II Aldolase", *J. Org. Chem.,* **1996,** 61 (16), 5414-5417.

91. J. Li, W. Yang, S. Wang, S. Li, and T. Li, "Improved Synthesis of Chalcones under Ultrasound Irradiation", *Ultrason. Sonochem.,* **2002,** *9* (5), 237-239.

92. J. J. V. Eynde, K. Mutonkole, Y. V. Haverbeke, "Surfactant-Assisted Organic Reactions in Water. Effect of Ultrasound on Condensation Reactions Between Active Methylene Compounds and Arylaldehydes", *Ultrason. Sonochem.,* **2001,** *8* (1), 35-39.

93. A. Fuentes, J. M. Mainas, and J. V. Sinisterra, "Catalyzed Synthesis of Chalcones Under Interfacial Solid-Liquid Conditions with Ultrasound", *Tetrahedron Lett.,* **1987,** *28* (39), 4541-4544.

94. Brühne and E. Wright "Benzaldehyde" In *Ullmann's Encyclopedia of Industrial Chemistry;* 6th ed.; M. Bohnet, C. J. Brinker, B. Cornils, T. J. Evans, H. Greim, L. L. Hegedus, J. Heitbaum, W. A. Herrmann, W. Keim, A. Kleemann, G. Kreysa, T. Laird, J. Loliger, R. O. McClellan, J. L. McGuire, J. W. Mitchell, A. Mitsutani, T. Onoda, L. Plass, G. Stephanopoulos, D. Werner, P. Woditsch, and N. Yoda, Eds.; Wiley-VCH Verlag GmbH & Co. KGaA.: Weinheim, 2003; Vol. 4, pp 701-713.

95. D. S. Noyce and W. A. Pryor, "Carbonyl Reaction. I. Kinetics and Mechanism of the Acid-Catalyzed Aldol Condensation of Benzaldehyde and Acetophenone", *J. Am. Chem. Soc.,* **1955,** *77* (6), 1387-1401.

CHAPTER 5

5. SELECTIVE N-METHYLATION OF ANILINE USING DIMETHYL CARBONATE AND NANOPARTICULATE PAO$^-$-DERIVED FERRITE

5.1. INTRODUCTION

Selective methylation of the nitrogen atom of aniline to yield *N*-methylaniline (NMA) and *N,N*-dimethylaniline (NNDMA), is an important step in the industrial production of numerous agrochemicals, pharmaceuticals, drugs, dyes, fine chemicals, synthetic rubbers, herbicides, and explosives.[1-26] Due to the many applications of NMA and NNDMA, there is a continuous search for active and selective catalysts, non-toxic methylating reagents, and optimum reaction conditions (e.g. temperature, pressure, solvent, etc.) for inexpensive, environmentally benign production of NMA and NNDMA.[1-46] There is a significant emphasis on solid acids and bases such as metal oxides, mixed oxides, clays, and zeolites as catalysts instead of the toxic, hazardous, homogeneous Lewis acid catalysts due to the elevated concerns about the environment.[1-55] Dimethyl sulphate [$(H_3C)_2SO_4$], monohalomethane, and primary alkyl halides were used for the methylation of aniline and other chemicals but these compounds are highly toxic and corrosive and lead to the formation of a stoichiometric amount of the corresponding salt of the base employed as a catalyst.[2,6,19,27,29-31,34,35,37,38,47-50,52,.53] Methanol and dimethyl carbonate (DMC) are much less toxic and non-corrosive and thus, they have been extensively used as methylating agents using several solid acid-base catalysts.[1-57] Methanol is cheaper and

requires higher temperature for the methylation process but is a less effective methylating reagent compared to DMC.[1,2,4,5,9-11,24,31,38,49-51] It has been demonstrated that a total conversion of aniline, selectivity for NMA and NNDMA, and production of side products such as toluidines (*C*-alkylated anilines) and carbamate methyl esters depend strongly on the nature of the catalyst utilized and the reaction conditions employed.[1-33,35-39,41-46,55,57] The formation of toluidines requires the presence of strong acid sites, while the *N*-alkylated anilines (NMA and NNDMA) can be produced by weak to moderate acid sites.[2,4,7,12-14,16-18,21-23,26,28,36,37,39,41,44,55] However, very strong acid catalysts should be avoided because they may have their activity inhibited by the strong adsorption of the moderately basic aniline or may lead to deamination of aniline to benzene.[7,8,16-18,26,28,45] Several catalysts have been employed for the methylation of aniline with methanol. Zeolites, for instance, resulted in both *N*- and *C*-methylated products, while cocrystallized zeolites selectively resulted only in NNDMA.[3,7,8,18,23,26,31,36,37,44,55,57] On the other hand, metal oxides give preferably the *N*-alkylated products.[2,3,8-11,13,15,16,18,22,28] However, a large molar ratio of methanol:aniline and high temperature conditions were needed.[2,3,7-17,20-23,26,28,36,39,44,46,55,57] Recent work of Sreekumar *et al.*[8,9,15,28] showed that NMA was obtained in very high selectivity and good yield even at a low molar ratio of methanol:aniline at 350 ^{o}C over $M_xZn_{1-x}Fe_2O_4$, where M is Co^{2+} or Ni^{2+} and $0.0 \leq x \leq 1.0$. The best results regarding the activity of the catalyst and selectivity toward NMA were obtained with $x = 0.2$. These authors also used DMC and $Co_xZn_{1-x}Fe_2O_4$ at 250 ^{o}C.[9,10] Catalyst systems with x of 0.2 and 0.5 showed the highest selectivity for NMA, but selectivity is lower than that when using methanol as the alkylating agent.[8-10] However, very high selectivity for NMA was reported using DMC over Mg-Al hydrotalcites

(Mg/Al = 3),[11] faujasite X- and Y-type zeolites,[19] Y-zeolites,[24] NaY faufasite,[27] and alumina coated with K_2CO_3 and polyethylene glycol.[32,33] It is noteworthy to mention that under refluxing conditions for 4 hours over amorphous Co-$AlPO_4$ catalyst and a mole ratio of 1aniline:1DMC, *N,N`*-biphenylurea was obtained as the major product along with byproducts of NMA and methyl *N*-phenylcarbamate.[5] Increasing the reaction time led to disappearance of the carbamate and to an increase of the yield of the urea product. There was no carbamate observed and only NMA (minor product) and urea (major product) were detected when the mole ratio was changed to 2 aniline:1 DMC. Performing this reaction in the vapor phase in the same mole ratio, in the presence of amorphous V-$AlPO_4$ or Co-$AlPO_4$ resulted in the formation of NMA in 100% selectivity whether the alkylating agent was methanol or DMC.[4]

5.2. EXPERIMENTAL

Dimethyl carbonate [$(H_3CO)_2CO$, 99% (Aldrich)], aniline [$C_6H_5NH_2$, 99% (Lancaster)], methanol [H_3COH], *N*-methylaniline [$C_6H_5NHCH_3$, (Aldrich)], *N,N*-dimethylaniline [$C_6H_5N(CH_3)_2$, (Aldrich)], N-phenylcarbamic acid methyl ester [$C_6H_5NHCOOCH_3$, TCI], hexamethylbenzene [$C_6(CH_3)$, TCI], tetrachloro-1,4-benzoquinone [(*p*-chloranil) (Aldrich)], acetonitrile [H_3CCN, HPLC grade (Spectrum)], methylene chloride [H_2CCl_2, Optima (Fisher Scientific)] were commercial and used-as-received. The $Ni_{0.2}Zn_{0.8}Fe_2(PAO)_6{\cdot}6H_2O$-derived ferrite (NZFPAO) and $Ni_{0.2}Zn_{0.8}Fe_2(OH)_8$-derived ferrite (NZFOH) catalysts were prepared according to the procedures described below. The crystalline phase identification and crystallite size of the synthesized catalysts were performed using powder X-ray diffraction (XRD) technique. The XRD patterns were recorded on a Bruker AXS D-8Advance X-ray

diffractometer using copper K_α radiation. The crystalline phase identification was achieved using a search/match program and the PDF-2 database of the International Center for Diffraction Data.[58] The catalysts were also characterized by infrared (IR) spectroscopy. The diffuse reflectance infrared fourier transform (DRIFT) spectra of a ground powder of the catalysts diluted with KBr were recorded on a Nicolet Magna 750 FTIR. The chemical composition of the surface of the prepared ferrites was established by X-ray photoelectron spectroscopy (XPS) using magnesium K_α radiation for excitation ($h\nu$ = 1253.6 eV). The XPS analyses were performed by Dr. Nicholas F. Materer. The surface areas of the catalysts were determined using BET six-point surface area measurements, performed on a Quantachrome Nova 1200 instrument by nitrogen adsorption at the temperature of liquid nitrogen. A Hewlett Packard G1800A Gas Chromatograph-Mass Spectrometer GC-MS, equipped with 30 m x 0.25 mm HP5 column (crosslinked 5% PhMe silicone), was used to analyze the products of the alkylation reactions. The temperature program used was an initial hold of 2 min at 35^{o}C, a ramp of 5^{o}C/min to 170^{o}C, and a final hold of 5 min. The helium flow rate was 1 ml/min and the injection port was set at 250^{o}C.

NMA and NNDMA were obtained as the major products with methyl *N*-phenylcarbamate as a minor byproduct of alkylation of aniline employing DMC as a methylating agent and NZFPAO as a catalyst. The catalyst was prepared by pyrolysis of $Ni_{0.2}Zn_{0.8}Fe_2(PAO)_6{\cdot}6H_2O$ at 512^{o}C and then activated at 500^{o}C for one hour in a muffle furnace. Samples of aniline (0.9367g, ~ 10 mmol) and DMC (9.9393 g, ~ 100 mmol) were placed in a Teflon-lined stainless steel bomb. A drop (0.1280 g) of this solution was taken, diluted with 20.4460 g of an internal standard solution of

hexamethylbenzene/CH_2Cl_2 ($\approx$1:600) in a 20-ml vial and labeled as t = 0 hr. Then NZFPAO (0.4986 g, ~ 5 wt% of reactants) was added to the reactant mixture in a bomb reactor. The sealed reaction system was then placed in a digitally-controlled oven at 150^{o}C to start the reaction. Several samples were taken at different intervals, diluted with the internal standard solution of hexamethylbenzene/CH_2Cl_2 ($\approx$1:600), and then injected (1-μl samples) into a GC/MS. The stainless steel bomb was cooled to room temperature before taking every sample. Response factors of the reactants and the products were determined using the internal standard solution of hexamethylbenzene/CH_2Cl_2 ($\approx$1:600) and were subsequently used to determine the concentrations in the samples from the catalysis experiments. Comparing the mass spectra of the reactants and the products to those available in the NIST database helped identify them. Verification of the products identities was established by determination of the retention times of standard samples of the reactants and products by GC/mass spectroscopy. Similar reaction conditions, mole ratio of reactants, and products analyses were used when NZFOH, obtained by calcination of $Ni_{0.2}Zn_{0.8}Fe_2(OH)_8$ at 300^{o}C and then activated at 500^{o}C for an hour, was used as a catalyst along with DMC or methanol as a methylating reagent. However, the only products detected by GC/MS with this catalyst were NMA and NNDMA, irrespective of the utilized methylating agent. The reaction was also run under the same aforementioned conditions without catalyst using DMC as a methylating agent. The detected products were *N*-methyleneaniline (*N*-phenylformaldimine) ($C_6H_5N{=}CH_2$), NMA, and NNDMA. *N*-Methyleneaniline has been reported as an intermediate in the conversion of its cyclic trimer (hexahydro-1,3,5-triphenyl-1,3,5-triazine) to other organic

molecules.[59-61] However, *N*-methyleneaniline monomer has been recently prepared and polymerized and its polymer has been characterized.[62]

Preparation of NZFPAO Catalyst

Samples of $NiSO_4 \cdot 6H_2O$ (0.78807 g, 3 mmol), $ZnSO_4 \cdot 7H_2O$ (3.4500 g, 12 mmol), and $FeSO_4 \cdot 7H_2O$ (8.3403 g, 30 mmol) were mixed together and dissolved in 100 ml of H_2O. A sample of $Na(PAO) \cdot H_2O$ (12.870 g, 90 mmol) was dissolved in 100 ml of distilled water. A yellow green precipitate formed upon combining both solutions. This solid was isolated and dried under vacuum to provide a yield of 13.43 g (99.95 %) of product. IR (cm^{-1}) (KBr): 3226(s, br), 3104(s, br), 2947(s), 2873(s), 2835 (s), 2388(m), 2285(m), 2029(vw), 1965(vw), 1837(w), 1769(w), 1671(vs), 1651(vs), 1534(w), 1481(s), 1432(m), 1390(s), 1367(vs),1218(vs), 1046(vs), 891(m), 858(s), 778(s), 768(s, sh), 695(m), 559(w), 498(s) .

A yield of 0.4436 g (26.86 %) of a dark brown product of NZFPAO catalyst was obtained when 1.6517 g of $Ni_{0.2}Zn_{0.8}Fe_2(PAO)_6 \cdot 6H_2O$ was heated overnight at 512°C in a muffle furnace. IR (cm^{-1}) (KBr): 3449(vw, br), 3071(vw), 2952(vw), 2886(vw), 2831(vw), 2344(vw), 1778(vw), 1728(vw), 1513(vw), 1452(w), 1365(vw), 1146(vw), 1097(vw), 1049(vw), 969(vw), 894(vw), 828(vw), 598(m).

Preparation of NZFOH Catalyst

This catalyst was fabricated according to the previously reported procedure by Date *et al.*[63] The solid obtained was then calcined at 300°C for 36 hours.[15]

This catalyst was activated for one hour at 500°C before running the reaction. IR (cm^{-1}) (KBr):3443(w, br), 2425(vw), 1769(vw), 1589(m), 1415(m), 1381(m), 1055(w), 854(w), 831(w), 712(w), 496(w), 464(vw), 411(vw).

Catalyst Characterization

Table 5.1 displays the specific surface area, phase identification, and crystallite size of the catalysts fabricated in this study. The surface area of NZFOH catalyst is ~ 2.4 times that of NZFPAO. The XRD patterns of both catalysts, on the other hand, matched well with those of nickel zinc ferrite. Both catalysts have similar crystallite size.

Table 5.1. Characters of the Prepared Catalysts Characters of the Prepared Catalysts

Catalyst	Surface Area (m^2/g)	Crystalline Phase	Crystallite Size (nm)
NZFPAO	18.82	Ferrite	6.7
NZFOH	44.42	Ferrite	7.1

The two IR bands at 828 and 598 cm^{-1} in the IR spectrum of NZFPAO can be ascribed to the stretching vibration of the tetrahedral and the octahedral M—O groups, respectively. Similarly, the two bands at 711 and 496 cm^{-1} in the IR spectrum of NZFOH are assigned, respectively, to the vibrational stretching of the tetrahedral and the octahedral M—O groups. The tetrahedral group has its band located at higher frequency because the tetrahedral cations provide an auxiliary restoring force in a preferential direction along the tetrahedral M—O bond.[64,65]

Acidity and Basicity Measurements

It has been shown that acidity and basicity properties of the surface of the ferrite catalyst systems strongly affect both the activity and selectivity of the catalyst during the *N*-methylation reaction course of aniline using either methanol or DMC as the methylating agent.[2,8-10,15,28] The oxide anions on the surface represent the basic sites, while the acidic sites are created by the metal ions found on the surface of the oxide system. For spinels, metal ions exist in both tetrahedral (tet) and octahedral (oct) sites. This distribution of metal cations results in two types of ferrites; normal having the formula of $M^{(II)}_{tet}[Fe^{(III)}_{oct}]_2O_4$ in which the divalent cation occupy the tet-sites, and inverse with the general formula of $Fe^{(III)}_{tet}[M^{(II)}Fe^{(III)}]_{oct}O_4$, where the ferric cation is distributed equally in both the tet- and the oct-sites. Such distribution of cations in the spinel lattice is controlled by three major factors; ligand field stabilization energy (LFSE), cation size and charge, and Madelung constant (*M*).[66-68] This distinctive structural characteristic endows spinels with special resistance to high reducing conditions because if some ferric ions were reduced to ferrous ions, the lattice configuration would be kept intact upon reoxidation.[69] It was claimed that the octahedral-cations were responsible of the activity of such systems owing to their large exposure on the surface as supported by low energy ion scattering (LEIS) measurements.[70] From the above brief elucidation of the cation distribution in the spinel structure, one can perceive that surface acidity and basicity properties are strongly influenced by the structure and cation distribution. Therefore, these properties of the surface have been investigated in the work reported herein. Basicity was determined by the adsorption of chloranil, which is an electron acceptor. The basicity of NZFOH (9.286

μmol/g) was found to be almost 3 times that of NZFPAO (3.103 μmol/g) as determined graphically from the Langmuir adsorption isotherms (Figure 5.1.).

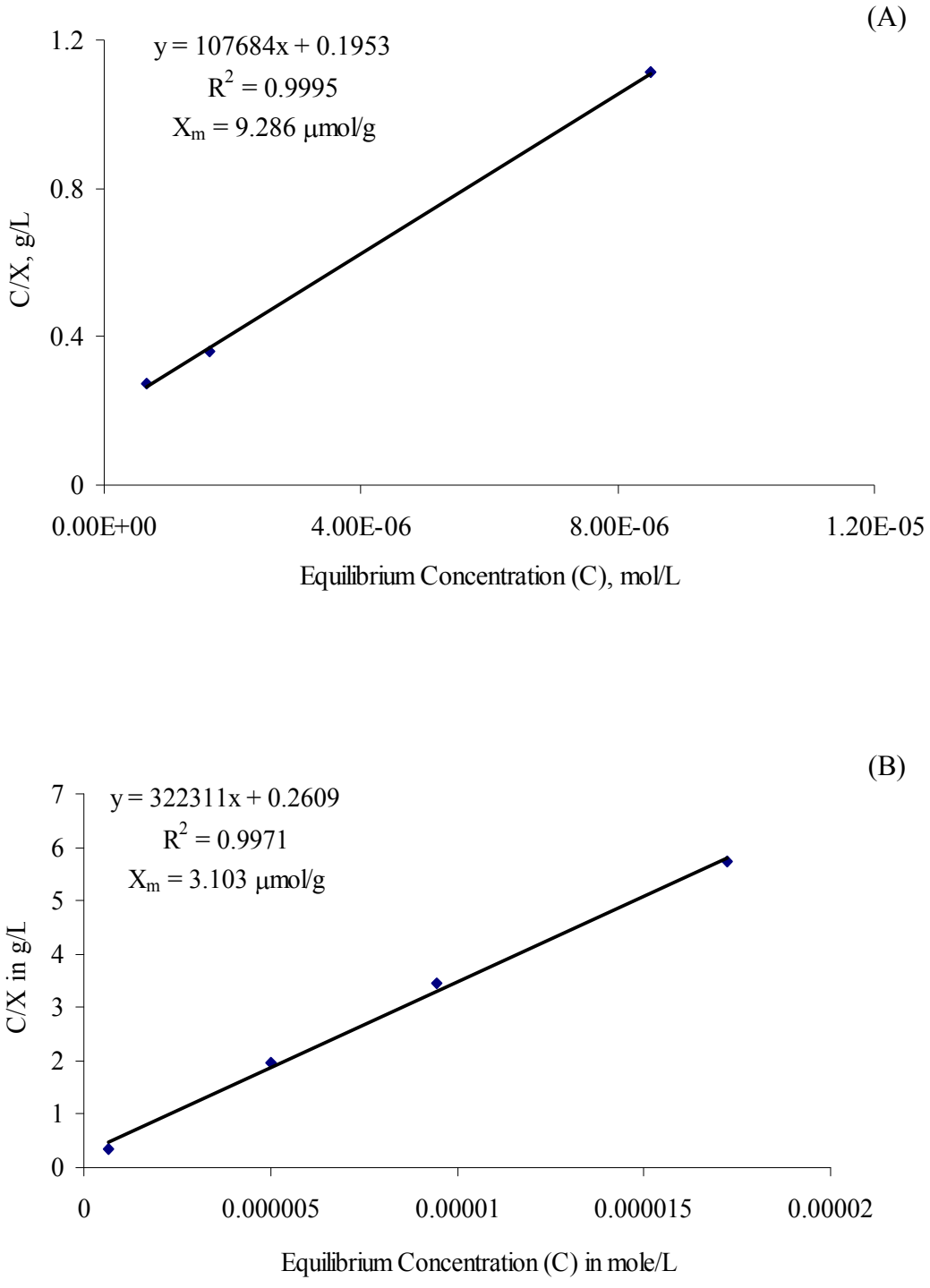

Figure 5.1. Langmuir adsorption basicity isotherms for (A) NZFOH and (B) NZFPAO

XPS Measurements

Table 5.2 displays the surface metal compositions of the synthesized catalysts. The amount of each metal ion on the surface is expressed as a ratio of the amount of the metal ions to the amount of nickel(II) ions.

Table 5.2. Surface Metal Composition Ratios of the Catalysts as Determined by XPS

Catalyst	Zn/Ni	Fe/Ni
NZFPAO	14.36	4.32
NZFOH	15.40	7.05

It is obvious from Table 5.2 that the two catalysts have different surface metal constituents. The NZFPAO catalyst has more nickel on its surface than NZFOH does. However, the latter catalyst possesses more zinc and iron on its surface in comparison to the former one. This variation of the surface metal compositions between the two catalysts is partially responsible for the different catalytic behavior observed for the two catalysts, as discussed below.

5.3. RESULTS AND DISCUSSION

The alkylation of aniline with DMC can be schematically represented as follows (Figure 5.2):

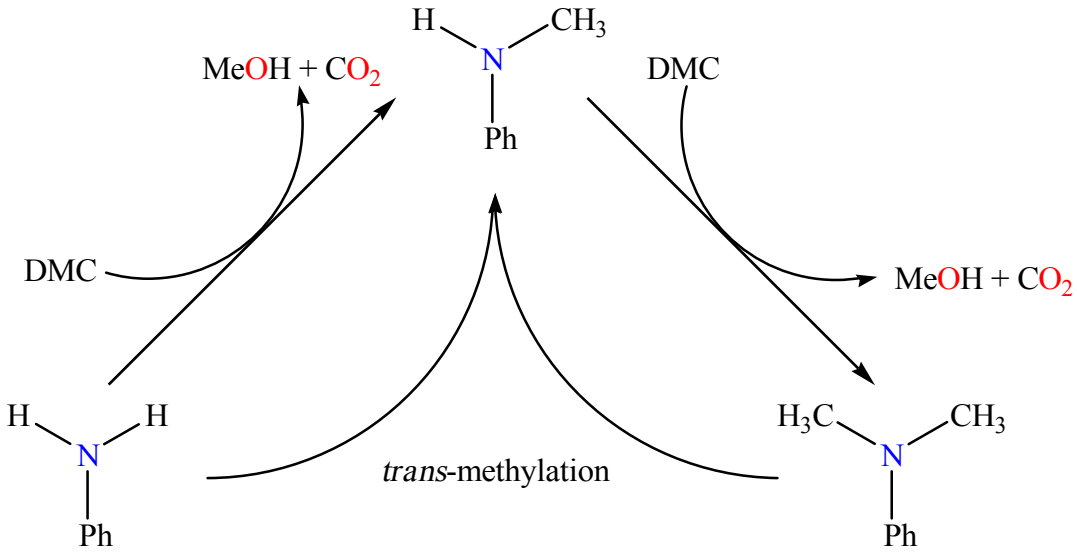

Figure 5.2. The multistep, sequential reaction between aniline and DMC

As can be seen, the reaction between aniline and DMC is a stepwise, consecutive electrophilic substitution of the methyl group on the nitrogen atom leading to the formation of NMA, NNDMA, methanol, and carbon dioxide. This sequential nature of *N*-methylation of aniline to NNDMA has been noted and confirmed experimentally.[1,2,4,7,8,10,14-17,21-23,28,46] Furthermore, NMA may be produced via the *trans*-methylation between the adsorbed NNDMA and aniline. The latter path for the formation of NMA was proven to occur, as reported by Rao *et al.*[18]

Figure 5.3 shows that the change of the natural logarithm of the mole fraction of aniline versus time is a linear relationship when the reaction catalyzed by NZFPAO catalyst. Such observation implies that the reaction is first-order in aniline and the reaction was following pseudo-first order kinetics due to the excess DMC used. This result is consistent with the previous reported kinetic studies showing that the *N*-methylation reaction was pseudo-first order in aniline when using methanol as a methylating agent.[16,17,22] The rate constant (k) in our study was determined to be 0.0097

hr^{-1}. This small value of k reflects the slowness of the reaction at 150°C and the necessity for a long period of time to reach a high degree of aniline conversion to products. Monitoring the change in mole fraction of aniline, NMA, and NNDMA with time resulted in the observation of a decrease in the mole fraction of aniline and an increase in the mole fraction of NMA until it reached a maximum after 112 hours. The maximum concentration was maintained up to 180 hours, after which it dropped to 0.17 when the reaction was almost complete. On the other hand, no NNDMA was detected until 25 hours, while after this point its mole fraction increased with time and reached its maximum at the end of the reaction. The production of NNDMA was accompanied by a reduction in the concentration of NMA, implying that the latter species was being methylated (Figure 5.4).

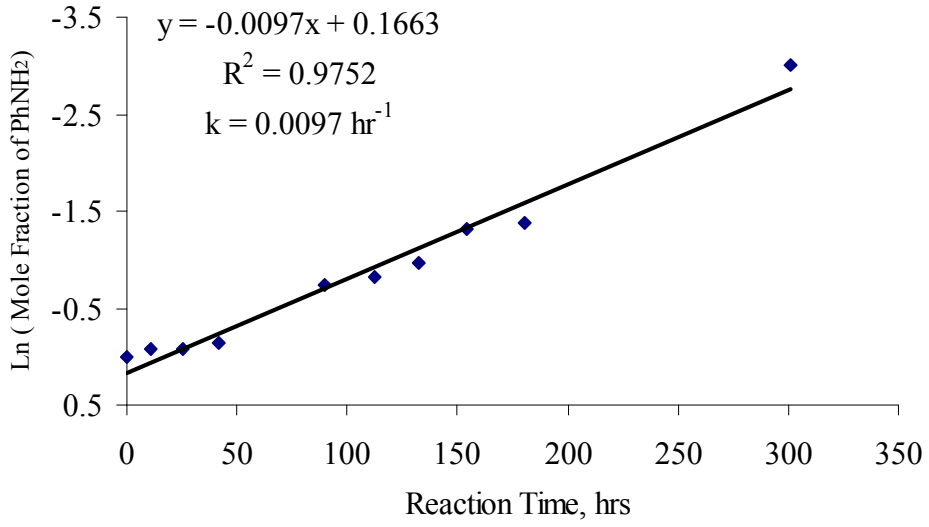

Figure 5.3. First-order plot for the methylation of aniline with DMC at 150 °C over NZFPAO catalyst

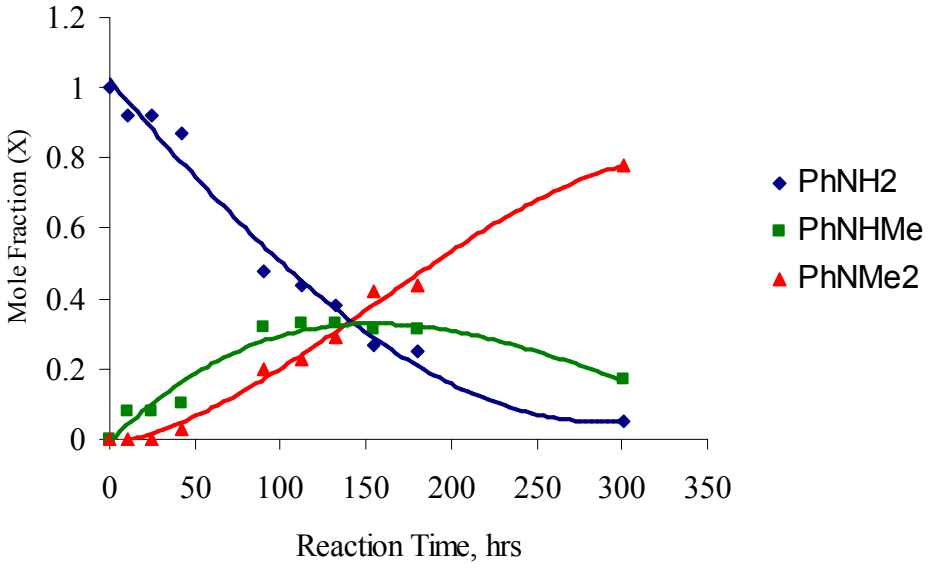

Figure 5.4. Change of mole fraction of aniline, NMA, and NNDMA with reaction time in methylation process with DMC over NZFPAO catalyst at 150°C

In terms of small catalytic activity, the percentage conversion of aniline reached 95% after 301 hours. The selectivity for NMA was at its maximum (100%) during the first 25 hours after which it dropped with the formation of NNDMA. The selectivity of NMA declined to 18% with the end of the reaction. Unfortunately, the high selectivity towards NMA at the beginning corresponded to a very low yield of 8%. The selectivity towards NNDMA, on the other hand, increased from 0% at 25 hr to 23% at 42 hr and kept increasing with reaction progress to 82% at the end of the reaction (Figure 5.5). The selectivity of NNDMA did not reach 100% because of the probability of a *trans*-methylation reaction to occurr between the adsorbed NNDMA and aniline to give NMA, as illustrated schematically in Figure 5.5.

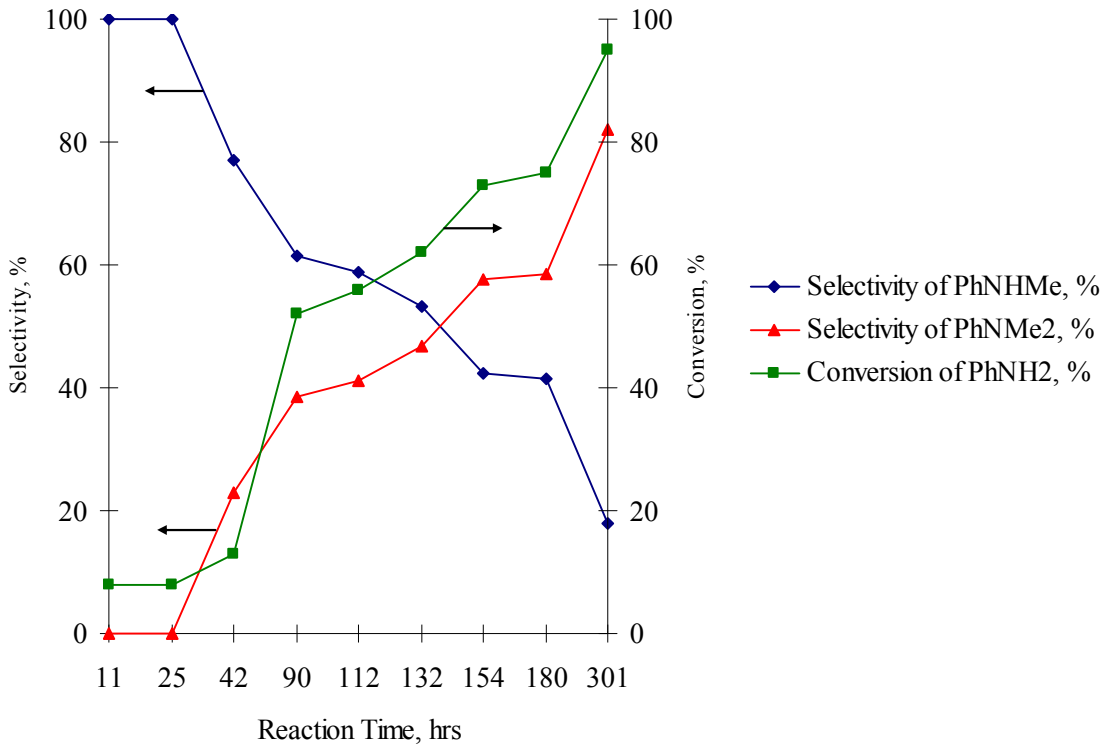

Figure 5.5. Conversion % of aniline and selectivity % towards NMA and NNDMA in the methylation reaction of aniline with DMC over NZFPAO catalyst at 150^{o}C

Similarly, investigation of methylation of aniline with DMC over NZFOH catalyst resulted in first-order reaction with respect to aniline (Figure 5.6). The reaction with this catalyst proceeded faster than with NZFPAO catalyst at 150^{o}C, as reflected by the higher rate constant (k) of 0.0157 hrs^{-1}, which is 1.62 times larger than the k obtained with NZFPAO catalyst. The proceeding of the reaction at higher rate over NZFOH catalyst is probably due to the higher surface area of this catalyst, as compared to that of NZFPAO catalyst (see Table 5.1).

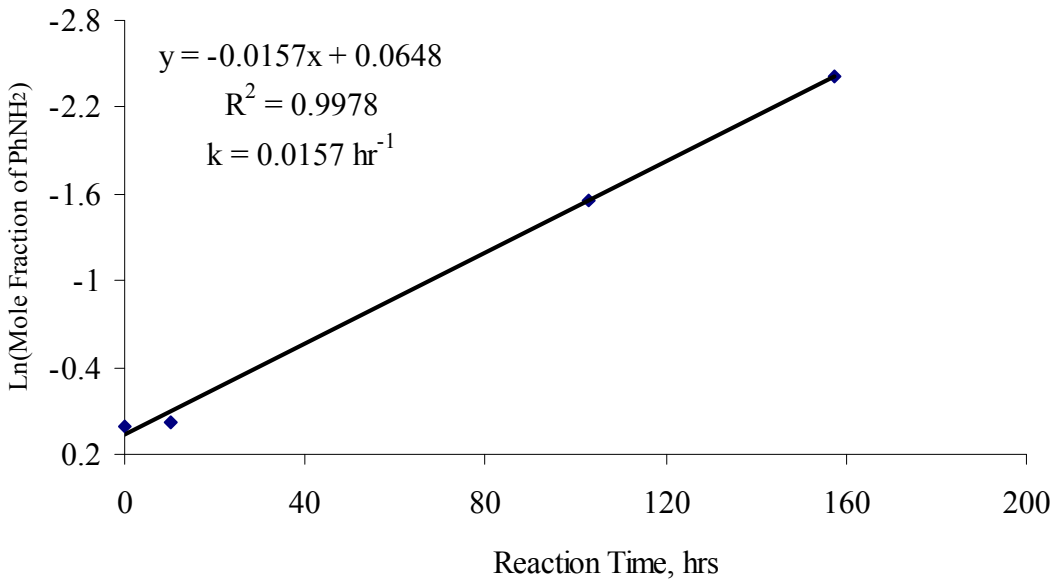

Figure 5.6. First-order plot for the methylation of aniline with DMC at 150 ^{o}C over NZFOH catalyst

The decline in the mole fraction of aniline with reaction time in the presence of NZFOH catalyst is more rapid than that observed over NZFPAO catalyst. The mole fraction of aniline, for example, after a 103-hour run with the former catalyst, was only 0.21, while with the latter catalyst at a similar period of time (112 hours), the mole fraction of aniline was 0.44 (Figure 5.7). The mole fractions of NMA varied also with time (Figure 5.7), where its mole fraction increased until it reached a maximum and then decreased to reach its minimum (0.16) at the end of reaction (t = 126 hrs). This was similar to that observed over NZFPAO catalyst (0.17) after a 301-hour run. NNDMA began to appear along with NMA after 10 hours, but its mole fraction was very small (Figure 5.7). The concentration of NNDMA increased gradually up to 38 hours reaction time after which it increased dramatically to reach its maximum (0.76) at 126 hours. This final yield was similar to that (0.78) observed over NZFPAO catalyst after 301 hours.

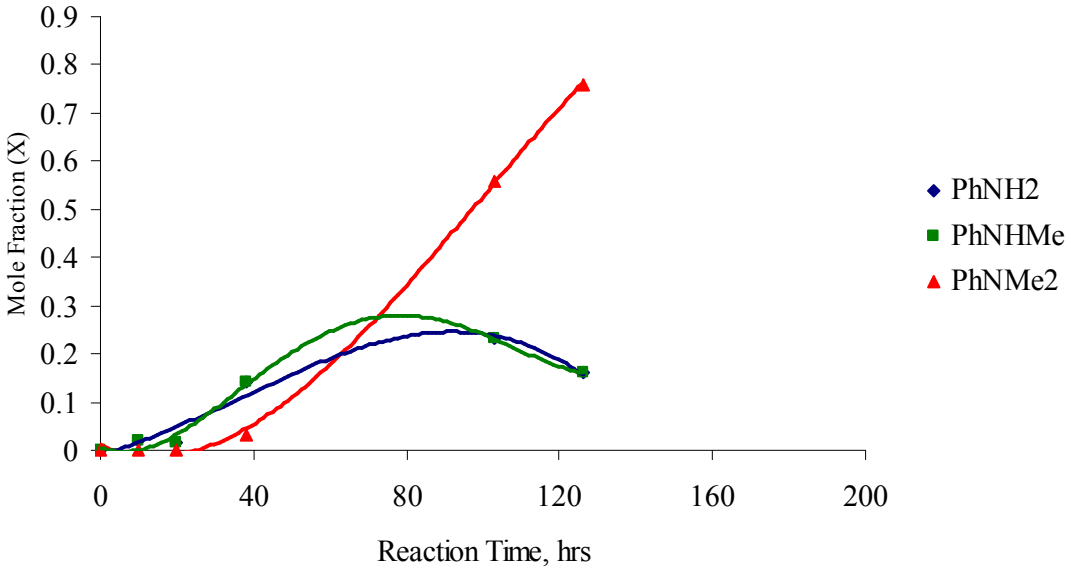

Figure 5.7. Change of mole fraction of aniline, NMA, and NNDMA with reaction time in methylation process with DMC over NZFOH catalyst at 150°C

The catalytic activity of NZFOH catalyst expressed in terms of percent aniline conversion, and NMA and NNDMA selectivities is shown in Figure 5.8. The percent conversion of aniline increased with time until it reached 92% at 126 hours. The selectivity for NMA was at its maximum (95.5%) at the beginning of the reaction and NMA was produced in a yield of 1.91% at 10 hours. After this point, the selectivity decreased and was only 17.4% when the reaction was terminated at 126 hours. The selectivity % for NNDMA increased with time from its minimum (4.5%) at the beginning of the reaction to its maximum (82.6%) after a 126-hour run. The yield NNDMA obtained in this case is similar to that observed over NZFPAO catalyst but was achieved in a shorter time because the reaction was faster.

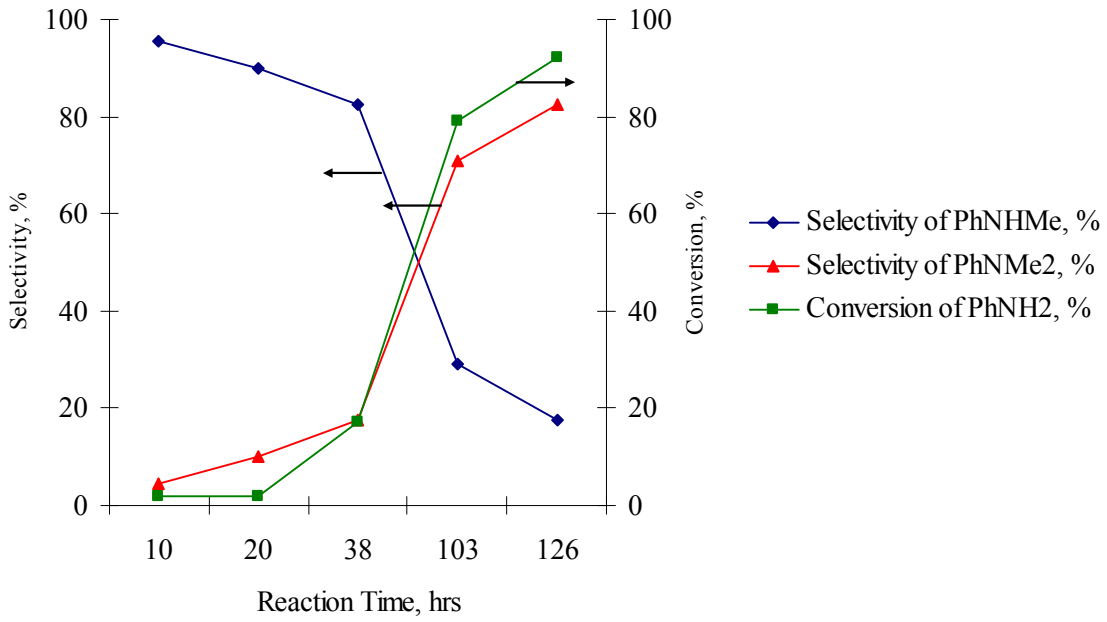

Figure 5.8. Conversion % of aniline and selectivity % towards NMA and NNDMA in the methylation reaction of aniline with DMC over NZFOH catalyst at 150°C

The methylation of aniline was also performed using methanol as a methylating agent over NZFOH catalyst at 150°C and a mole ratio of 1 aniline:10 methanol. The reaction was also found to be first-order in disappearance of aniline with a rate constant (k) of 0.0016 hr^{-1} (Figure 5.9). The small value of k reflects the slowness of methylation of aniline at this temperature and emphasizes that methanol is less effective methylating agent than DMC. The slowness of the reaction at 150°C is consistent with previous reports that the optimum temperature for methylation of aniline with methanol was 350 °C.[8,9,15,28] In addition, methanol yields as a byproduct upon the reaction of DMC with aniline. This coexistence of two methylating agents can be also responsible for making the reaction more rapid when employing DMC as the methylating agent. The rate constants for methylation of aniline over NZFPAO and NZFOH catalysts using DMC as

an alkylating agent are, respectively, 6 and 10 times the value of k for disappearance of aniline over NZFOH with methanol.

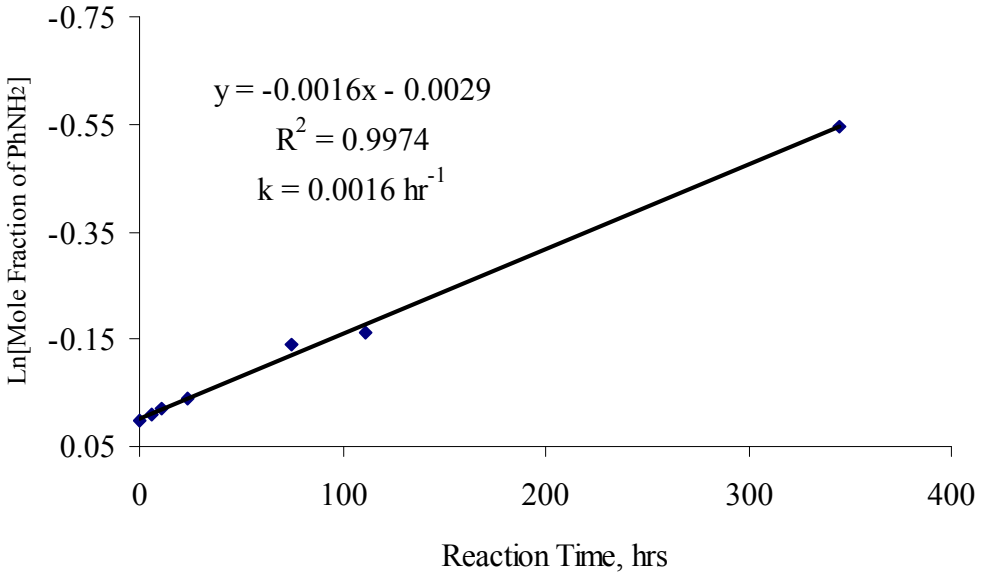

Figure 5.9. First-order plot for the methylation of aniline with methanol at 150°C over NZFOH catalyst

The mole fraction changes of aniline and products with time confirmed the slowness of the reaction. The aniline mole fraction gradually varied with time and reached 0.58 after 345-hour run (Figure 5.10). The mole fraction of NMA increased very slowly, reached its maximum (0.13) at 111 hours, and then it disappeared completely by 345 hours. The NNDMA did not appear before 75 hours, after which time its mole fraction increased gradually to reach 0.42 at 345 hours. The catalytic activity is also in consistent with the above discussion. The percent conversion of aniline is very small with time, and it only reached 42% after 345 hours (Figure 5.11). The selectivity for NMA was 100%, but at a very low yield between (1-4%) in the reaction period of 6-24 hours. The selectivity for NAM subsequently decreased with time and then became 0 at

345 hours. The selectivity for NNDMA increased from 0 after 24-hour run to 100 at 345 hours, indicating the formation of NNDMA at the expense of NMA.

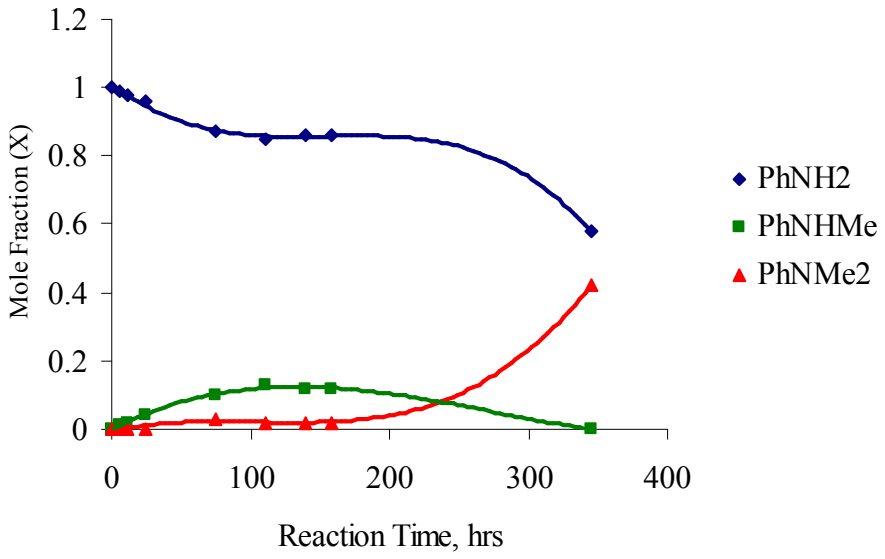

Figure 5.10. Change of mole fraction of aniline, NMA, and NNDMA with reaction time in methylation process with methanol over NZFOH catalyst at 150°C

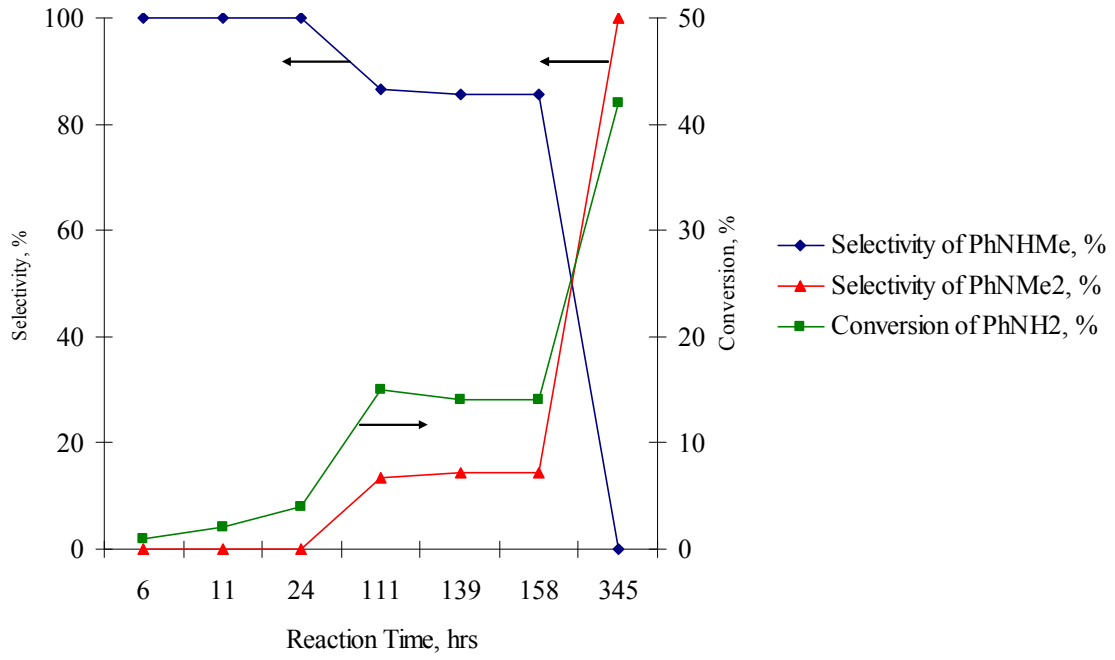

Figure 5.11. Conversion % of aniline and selectivity % towards NMA and NNDMA in the methylation reaction of aniline with methanol over NZFOH catalyst at 150°C

The methylation of aniline was conducted without catalyst using DMC as a methylating agent at 150°C and a mole ratio of 1aniline:10 methanol. The reaction was also found to be first-order in disappearance of aniline with a rate constant (k) of 0.0339 hr^{-1} (Figure 5.12). Again, the small value of k reflects the slowness of methylation of aniline at such low temperature. However, the rate constant for the uncatalyzed methylation of aniline is, respectively, 3.49 and 2.15 times the value of k over NZFPAO and NZFOH catalysts using DMC as a methylating agent and 21 times the rate constant over NZFOH employing methanol as a methylating reagent. The slowness of the catalyzed reaction in comparison to the uncatalyzed one under the same reaction circumstances can be ascribed to the inhibition caused by the strong adsorption of aniline on the acidic sites on the surface of the catalyst. In addition, in the case of using DMC as a methylating agent, the CO_2 released during the reaction of DMC with aniline can

deactivate the catalyst via its adsorption on the basic sites of the surface of the catalyst,[50,53,56,71] contributing to the inhibition of the catalyst activity. This because the basic sites, besides the acidic ones, have their own role in catalyzing the *N*-methylation reaction, as have been reported by several authors.[2,3,8-11,14,15,18,20-22,24,26,28,44,55]

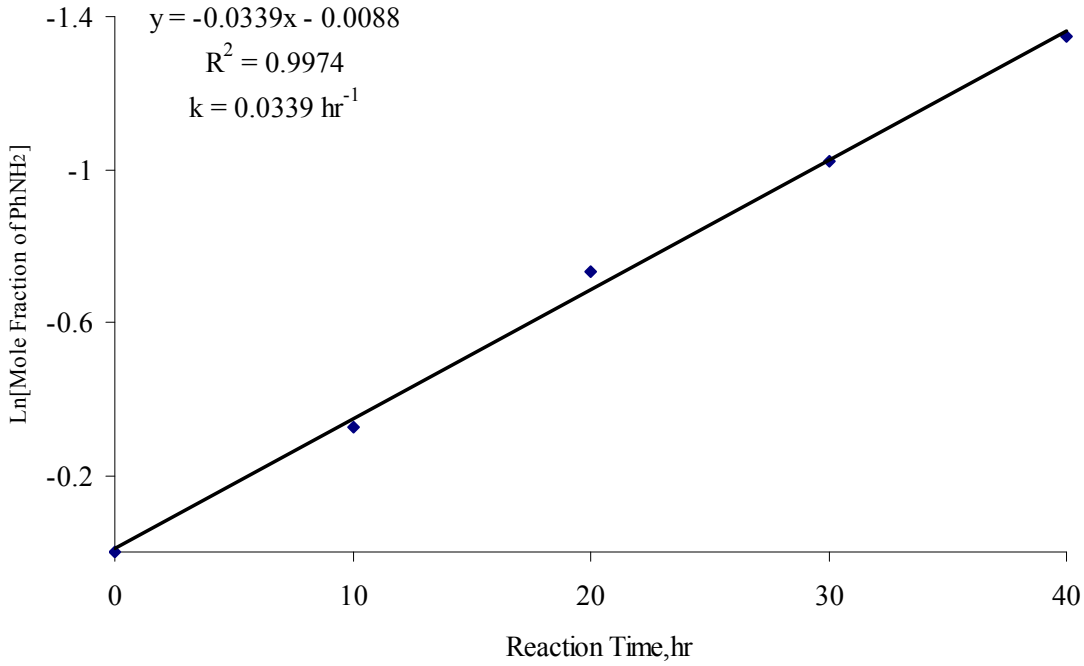

Figure 5.12. First-order plot for the methylation of aniline with DMC at 150 ^{o}C without catalyst

The mole fraction changes of aniline and products with time confirmed the relative slowness of the reaction. The aniline mole fraction was gradually varied with time and reached 0.26 after 40-hour run, and 0.0 after 80 hours (Figure 5.13). The mole fraction of NMA increased very slowly, reached its maximum (0.29) at 30 hours, and then it decreased slightly by 40 hours. The NNDMA started to appear with NMA and had its mole fraction increased gradually with reaction time to reach 1.0 at 80 hours. The catalytic activity is also consistent with the above discussion. The percent conversion of

aniline is relatively high with time and it reached 100% after 80 hours (Figure 5.14). The maximum selectivity for NMA was ~ 61% with a low yield of 17% after 10 hours. The selectivity for NAM subsequently decreased with time and then became 0 at 80 hours. The selectivity for NNDMA increased from ~ 39% after a 10-hour run to 100 at 80 hours, indicating the formation of NNDMA at the expenses of NMA.

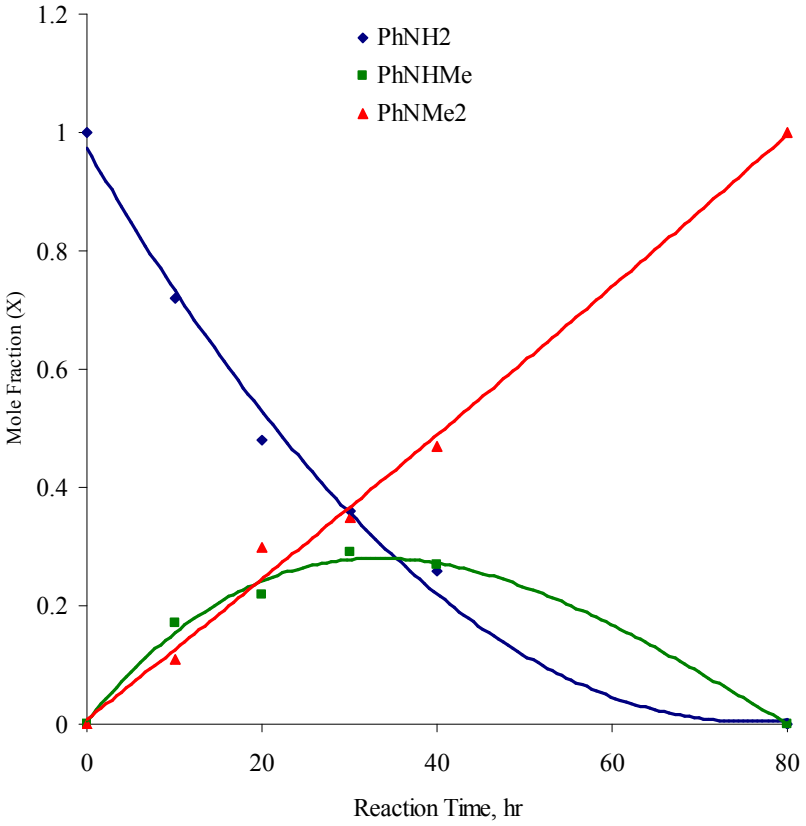

Figure 5.13. Change of mole fraction of aniline, NMA, and NNDMA with reaction time in methylation process with DMC without catalyst at 150°C

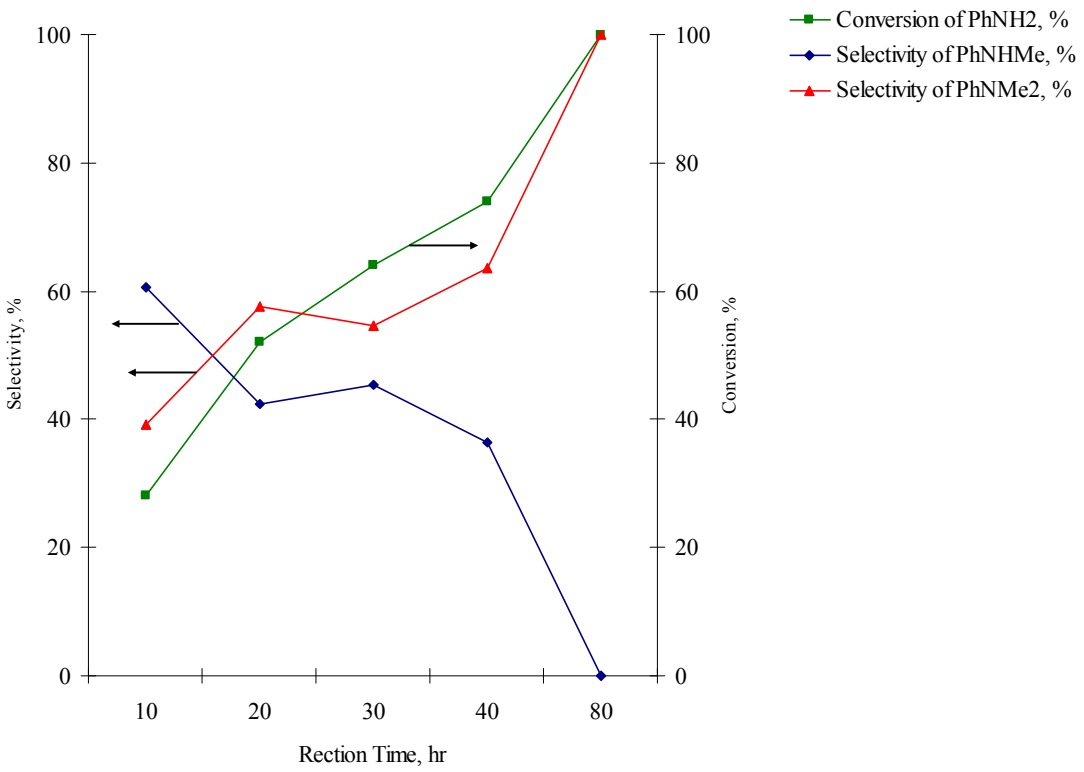

Figure 5.14. Conversion % of aniline and selectivity % towards NMA and NNDMA in the methylation reaction of aniline with DMC without catalyst at 150°C

N-Methyleneaniline (*N*-phenylformaldimine) was detected by GC/MS as a minor product during the uncatalyzed reaction from 10 hours to 40 hours, but it disappeared at the end of the reaction at 80 hours. Such a molecule was reported as an intermediate in the methylation of aniline with methanol to NMA.[72,73] A proposed mechanism for the formation of this molecule and its transformation to NMA is provided below.

Mechanism of the Reaction

The suggested mechanism of *N*-methylation of aniline with DMC is shown in Figure 5.15. First, the hydroxyl group on the surface of the catalyst attacks the carbonyl carbon of DMC to form an intermediate that loses a methanol molecule and produces methyl carbonate ester that is attached to the surface of the catalyst. This latter ester can

be attacked by the aniline molecule in an addition reaction either at its carbonyl carbon, a mechanism categorized as $\mathbf{B_{Ac}2}$ (**b**ase promoted, **bimolecular**, with attack on the **ac**yl group), or at its alkyl carbon, a mechanism termed $\mathbf{B_{Al}2}$ (**b**ase promoted, **bimolecular**, with attack on the **al**kyl group).[32,38,74] The former mechanism, upon the attack of aniline on the carbonyl carbon, includes the formation of a tetrahedral intermediate that decomposes to give NMA and metal bicarbonate that dissociates to regenerate the catalyst after the loss of a molecule of carbon dioxide. The latter mechanism shows the attachment of aniline on the methyl carbon to produce NMA and metal bicarbonate which decomposes to carbon dioxide and the active catalyst. Consecutive methylation of the produced NMA in a similar mode leads to the formation of NNDMA. Noticeably, NMA can undergo faster methylation and be more strongly adsorbed on the surface of the catalyst than aniline because the electron releasing (ER) methyl group makes the amine nitrogen atom of NMA more basic.[2,16,17,22]

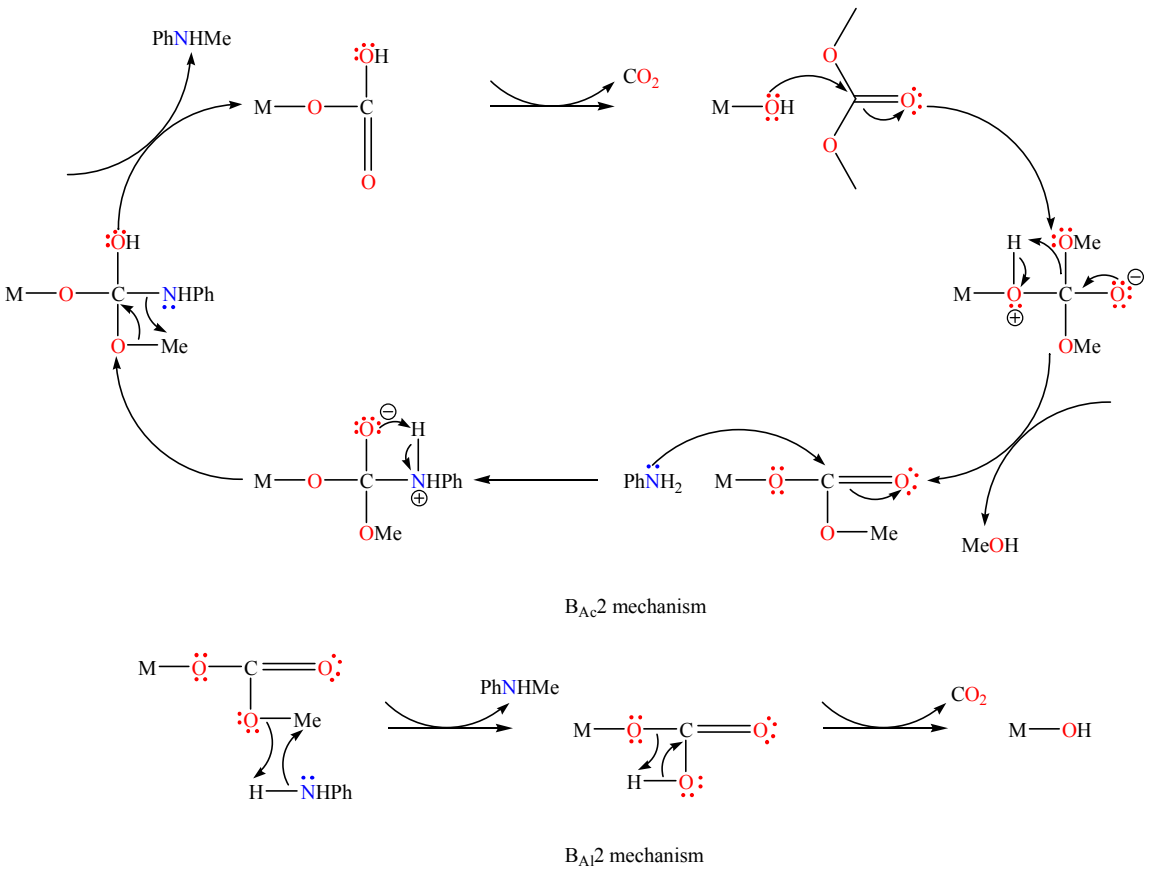

Figure 5.15. Proposed mechanism of N-methylation of aniline with DMC over ferrite catalyst

Figure 5.16 displays a plausible mechanism for the *N*-methylation of aniline with methanol. Lewis acid and base sites on the surface of the metal oxide catalyst are responsible for catalyzing the methylation process, as established by Ko *et al.*[22] and adopted by Sugunan *et al.*,[2,8] Rao *et al.*,[15] and Sreekumar and Sugunan.[28] Adsorption of aniline takes place via the interaction of the aniline nitrogen atom with a Lewis acid site and the interaction of one of the undissociated protons of the aniline amine bonds with a neighboring Lewis base site. Similarly, methanol is adsorbed where the methanol oxygen is bonded to a Lewis acid site and its undissociated proton is bonded to an adjacent Lewis base site. Subsequent electrophilic attack of the methyl group of the adsorbed methanol on the adsorbed aniline nitrogen atom leads to the formation of NMA. The formation of

NNDMA from NMA follows the same pattern where NMA is similarly adsorbed like aniline. It is anticipated, however, that NMA is more favorably adsorbed on the catalyst's surface and more rapidly subjected to methylation than aniline due to the basicity enhancement of the secondary amine nitrogen atom of NMA resulting from the ER effect of the methyl group.[2,16,17,22]

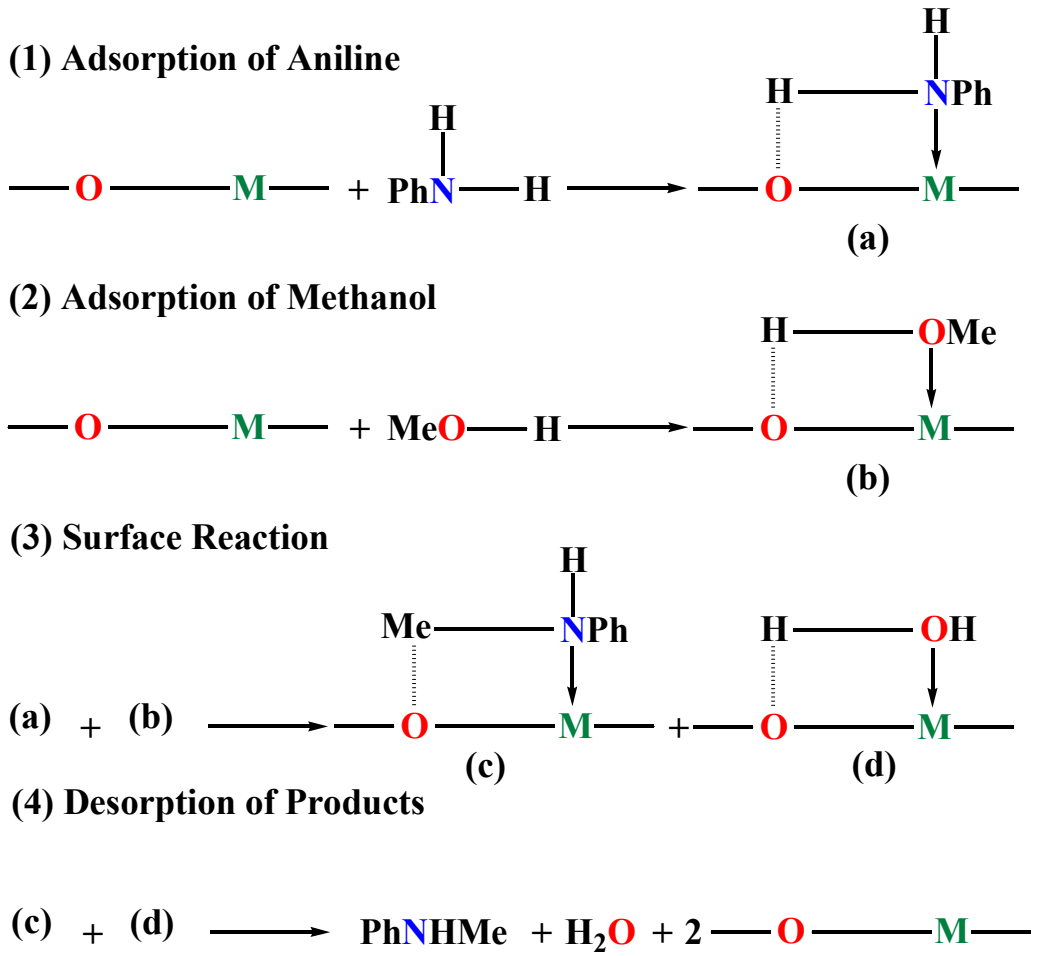

Figure 5.16. Proposed mechanism of N-methylation of aniline with methanol over ferrite catalyst

The formation of *N*-methyleneaniline and NMA in the uncatalyzed methylation of aniline with DMC can possibly take place according to the mechanism depicted in Figure 5.17. The former product has been shown to be an intermediate species in the

methylation of aniline to NMA using methanol as a methylating agent over basic zeolite CsOH/Cs,Na-Y.[72,73] Methanol is essential in the production of *N*-methyleneaniline because the latter is formed upon the condensation of aniline with the formaldehyde that is produced via the oxidation of methanol. Therefore, the first step in our proposed mechanism is the fabrication of methanol either via the attack of aniline on the carbonyl carbon of DMC (**$B_{Ac}2$** mechanism) to give methanol and methyl *N*-phenylcarbamate ester or the attack of aniline on a methyl carbon of DMC (**$B_{Al}2$** mechanism) to produce carbon dioxide, methanol, and NMA. The methanol thus produced undergoes dehydrogenation (oxidation) to formaldehyde which condensates with aniline to give *N*-methyleneaniline. Reaction of the latter with the hydrogen, resulting from the dehydrogenation of methanol, yields NMA. NNDMA is produced upon repeating the previous steps with NMA instead of aniline. The production of NMA via two different steps according to this suggested mechanism is responsible for the fast formation of NNDMA with the early stages of the reaction and may be also responsible for the speed of the reaction. It is noteworthy to mention that this suggested mechanism of the un-catalyzed reaction can also be supported by the previous observations and findings from investigating *N*-alkylation of aniline with alcohols.[7,42,75] These studies confirmed the dehydration of the alcohol to its corresponding carbonyl compound. Furthermore, the data provided evidences of a condensation of formaldehyde with aniline to give an intermediate of *N*-alkylideneamine (Schiff base), which upon hydrogenation, was converted to the desired *N*-alkylaniline.

(1) Formation of Methanol

a) $B_{AC}2$ mechanism

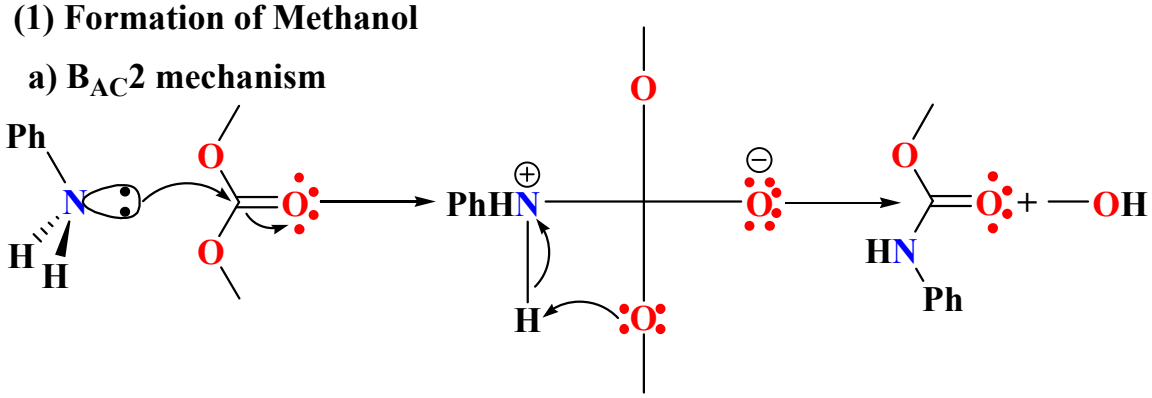

b) $B_{Al}2$ mechanism

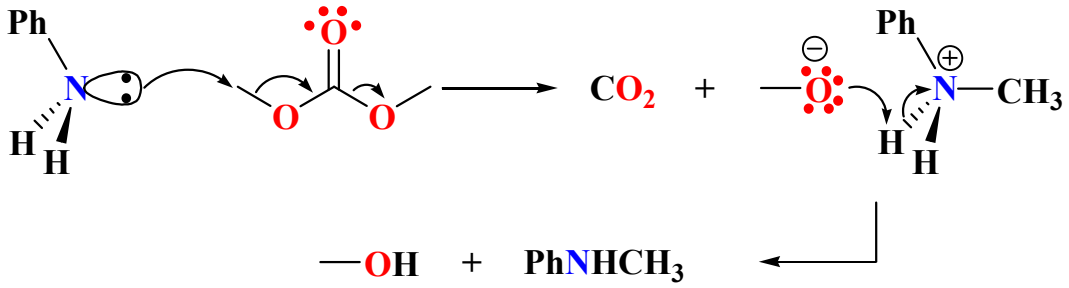

(2) Dehydrogenation of Methanol

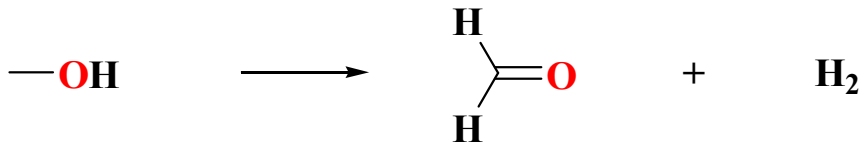

(3) Formation of *N*-methyleneaniline

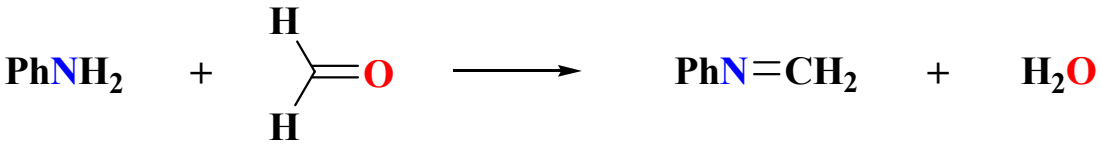

(4) Hydrogenation of *N*-methyleneaniline

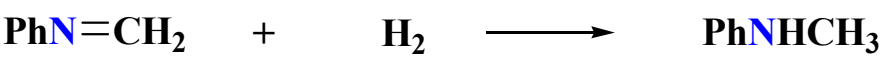

Figure 5.17. Proposed mechanism of N-methylation of aniline with DMC without catalyst

5.4. CONCLUSION

The NZFPAO and NZFOH catalysts were found to be excellent for highly selective production of NNDMA without forming any *C*-methylated products (toluidines) at 150 ^{o}C and using a mole ratio of 1aniline:10 DMC. The reaction, however, is very slow at this temperature, indicating that higher temperature is required to perform the *N*-methylation of aniline at faster rate. Changing the temperature will help to find the optimum conditions for the production of NMA and/or NNDMA at high selectivity and yield. Moreover, the activation energy (Ea), and the other activation parameters ($\Delta G^{\ddagger}$, $\Delta H^{\ddagger}$, $\Delta S^{\ddagger}$) can be assessed upon the variation of the temperature. The variation of the mole ratio of aniline:DMC will be very useful to determine the optimum mole ratio for the highest yield and selectivity toward NMA or NNDMA. The last two points regarding the temperature and mole ratio impacts on the behavior of the reaction and will be the subject of our future investigation.

The NZFOH and NZFPAO catalysts were found to have the ability to promote the *N*-methylation of aniline with DMC at 150^{o}C and a mole ratio of 1aniline:10DMC. However, the reaction rate differed depending upon the catalyst employed. This observation is most likely ascribed to the differences in the surface properties of the two catalysts (area, acidity, basicity, and ionic distribution between the surface and the bulk).

When using NZFOH catalyst, the reaction was faster upon using DMC as a methylating agent instead of methanol. This observation can be partially attributed to the fact that the two methylating agents exist when employing DMC as a methylating agent. The DMC itself and the methanol resulted from the reaction of DMC with aniline.

The uncatalyzed reaction is relatively much faster than the catalyzed one, irrespective of the catalyst used. This behavior accounts for absence of the inhibition caused by the strong adsorption of aniline and CO_2 released during the reaction of DMC with aniline, on the acidic and basic sites, respectively, on the surface of the catalyst.

The absence of *C*-alkylated products among the detected reaction products implies that the catalysts employed in our investigation do not possess strong acid sites on their surfaces and weak to medium acid sites do exist. This inference is based on the finding results of Woo *et al.*[57] Another evidence which supports this conclusion regarding the type of acidic sites on the surface of our catalysts is the absence of benzene as a product of deamination of aniline, which requires strong acidic sites to take place, as reported previously.[8,28] The reaction favorably gives NNDMA because of the high ratio of DMC or methanol to aniline (10:1).

The detection of methyl *N*-phenylcarbamate is evidence for the possible reaction via a $B_{Ac}2$ mechanism, i.e. the nucleophilic attack by aniline on the carbonyl carbon of DMC. However, the S_N2 attack of aniline on the methyl carbon of DMC (the $B_{Al}2$ mechanism) is not ruled out as a pathway for the formation of the final products. The formation of *N*-methyleneaniline is an indication of the importance of methanol as an intermediate for the production of NMA during the reaction run without catalyst.

REFERENCES

1. A. B. Shivarkar, S. P. Gupte, R. V. Chaudhari, "Selective Synthesis of *N,N*-Dimethyl Aniline Derivatives Using Dimethyl Carbonate as a Methylating Agent and Onium Salt as a Catalyst", *J. Mol. Catal.,* **2004,** *A 226* (1), 49-56.

2. K. Nishamol, K. S. Rahna, S. Sugunan, "Selective Alkylation of Aniline to *N*-Methyl Aniline Using Chromium Manganese Ferrospinels", *J. Mol. Catal.,* **2004,** *A 209* (1-2), 89-96.

3. L. J. Garces, V. D. Makwana, B. Hincapie, A. Sacco, S. L. Suib, "Selective *N,N*-Methylation of Aniline Over Cocrystallized Zeolites RHO and Zeolite X (FAU) and Over Lind Type L (Sr, K-LTL)", *J. Catal.,* **2003,** *217* (1), 107-116.

4. N. Nagaraju, G. Kuriakose, "Activity of Amorphous V-$AlPO_4$ and Co-$AlPO_4$ in the Selective Synthesis of *N*-Monoalkylated Aniline via Alkylation of Aniline with Methanol or Dimethyl carbonate", *New J. Chem.,* **2003,** *27* (4), 765-768.

5. N. Nagaraju, G. Kuriakose, "A New Catalyst for the Synthesis of *N,N*-Biphenylurea from Aniline and Dimethyl carbonate", *Green Chemistry,* **2002,** *4* (3), 269-271.

6. R. N. Salvatore, C. H. Yoon, K. W. Jung, "Synthesis of Secondary Amines", *Tetrahedron,* **2001,** *57* (37), 7785-781.

7. S. Narayanan, K. Deshpande, "Aniline Alkylation over Solid Acid Catalysts", *Appl. Catal.,* **2000,** *A 199* (1), 1-31.

8. K. Sreekumar, T. M. Jyothi, M. B. Talawar, B. P. Kiran, B. S. Rao, S. Sugunan, "Selective *N*-Monomethylation of Aniline using $Zn_{1-x}Co_xFe_2O_4$ (x = 0, 0.2, 0.5, 0.8 and 1.0) Type Systems", *J. Mol. Catal.,* **2000,** *A 152* (1-2), 225-236.

9. K. Sreekumar, T. Mathew, S. P. Mirajkar, S. Sugunan, B. S. Rao, "A Comparative Study on Aniline Alkylation Activity Using Methanol and Dimethyl Carbonate as the Alkylating Agents over Zn-Co-Fe Ternary Spinel Systems", *Appl. Catal.,* **2000,** *A 201* (1), L1-L8.

10. K. Sreekumar, T. M. Jyothi, T. Mathew, M. B. Talawar, S. Sugunan, B. S. Rao, "Selective *N*-Methylation of Aniline with Dimethyl Carbonate over $Zn_{1-x}Co_xFe_2O_4$ (x = 0, 0.2, 0.5, 0.8 and 1.0) Type Systems", *J. Mol. Catal.,* **2000,** *A 159* (2), 327-334.

11. T. M. Jyothi, T. Raja, M. B. Talawar, K. Sreekumar, S. Sugunan, B. S. Rao, "Selective Methylation of Phenol, Aniline and Catechol with Dimethyl Carbonate over Calcined Mg-Al Hydrotalcites", *Synth. Commun.,* **2000,** *30* (21), 3929-3934.

12. M. A. Aramendia, V. Borau, C. Jimenez, J. M. Marinas, F. J. Romero, "Effects of Na_2CO_3 Impregnation on the Catalytic Activity of $Mg_3(PO_4)_2$ in the Gas-Phase Conversion of 2-Hexanol and the Alkylation of Aniline with Methanol", *Colloids Surf.,* **2000,** *A 170* (1), 51-58.

13. M. A. Aramendia, V. Borau, C. Jimenez, J. M. Marinas, F. J. Romero, "Synthesis, Characterization, and Catalytic Uses of $Mg_3(PO_4)_2$/MgO Systems", *J. Colloid Interface Sci.,* **1999,** *219* (1), 201-209.

14. M. A. Aramendia, V. Borau, C. Jimenez, J. M. Marinas, F. J. Romero, "*N*-Alkylation of Aniline with Methanol over Magnesium Pholsphates", *Appl. Catal.,* **1999,** *A 183* (1), 73-80.

15. K. Sreekumar, T. Raja, B. P. Kiran, S. Sugunan, B. S. Rao, "Selective *N*-Monomethylation of Aniline over $Zn_{1-x}Ni_xFe_2O_4$ (x = 0, 0.2, 0.5, 0.8 and 1.0) Type Systems", *Appl. Catal.,* **1999,** *A 182* (2), 327-336.

16. F. M. Bautista, J. M.Campelo, A. Garcia, D. Luna, J. M. Marinas, A. A. Romero, "*N*-Alkylation of Aniline with Methanol over $AlPO_4$-Al_2O_3 Catalysts", *Appl. Catal.,* **1998,** *A 166* (1), 39-45.

17. F. M. Bautista, J. M.Campelo, A. Garcia, D. Luna, J. M. Marinas, A. A. Romero, M. R. Urbano, "*N*-Alkylation of Aniline with Methanol over $CrPO_4$ and $CrPO_4$-$AlPO_4$ (5-50 wt% $AlPO_4$) Catalysts", *J.Catal.,* **1997,** *172* (1), 103-109.

18. R. Bandyopadhyay, P. S. Singh, B. S. Rao, "Formation of *N*-Methylaniline by Transalkylation of Aniline with *N,N*-Dimethylaniline over Zeolite Beta", *Appl. Catal.,* **1997,** *A 155* (1), 27-39.

19. M. Selva, A. Bomben, P. Tundo, "Selective Mono-*N*-Methylation of Primary Aromatic Amines by Dimethyl Carbonate over Faujasite X- and Y-type Zeolites", *J. Chem. Soc., Perkin Trans. 1,* **1997,** *7,* 1041-1046.

20. J. Santhanalakshmi, T. Raja, "Selective *N*-methylation of Aniline by Calcined Mg^{II}-Al^{III} Layered Double Hydroxides", *Appl. Catal.,* **1996,** *A 147* (1), 69-80.

21. P. S. Singh, R. Bandyopadhyay, B. S. Rao, "Aniline Methylation over AEL type Molecular Sieves", *Appl. Catal.,* **1996,** *A 136* (2), 177-189.

22. A. Ko, C. Yang, W. Zhu, H. Lin, "Selective *N*-alkylation of Aniline with Methanol over γ-Alumina", *Appl. Catal.,* **1996,** *A 134* (1), 53-66.

23. Y. K. Park, K. Y. Park, S. I. Woo, "Selective Alkylation of Aniline with Methanol over Metallosilicates", *Catal. Lett.,* **1994,** *26* (2), 169-180.

24. Z. Fu, Y. Ono, "Selective *N*-Monomethylation of Aniline with Dimethyl Carbonate over Y-Zeolites", *Catal. Lett.,* **1993,** *22* (3), 277-281.

25. G. Janner, A. B. Taleb, "Reductive *N*-Alkylation of Nitroarenes Using Methyl Formate as a Simultaneous Hydrogenating and Methylating Agent", *J. Mol. Catal.,* **1992,** *77* (3), 247-255.

26. P. Y. Chen, M. C. Chen, H. Y. Chu, N. S. Chang, and T. K. Chuang "The Selective Alkylation of Aniline with Methanol over ZSM-5 Zeolite" In *New Development in Zeolite Science and Technology, Stud. Surf. Sci. Catal.,* Elsevier Science B. V.: Amsterdam, 1986; Vol. 28, pp 739-746.

27. M. Selva, P. Tundo, A. Perosa, "Reaction of Primary Aromatic Amines with Alkyl Carbonates over NaY Faujasite: A Convenient and Selective Access to Mono-*N*-Alkyl Anilines", *J. Org. Chem.,* **2001,** *66* (3), 677-680.

28. K Sreekumar, S. Sugunan, "A Comparison on the Catalytic Activity of $Zn_{1-x}Co_xFe_2O_4$ (x = 0, 0.2, 0.5, 0.8, 1.0)-type Ferrospinels Prepared via a Low Temperature Route for the Alkylation of Aniline and Phenol Using Methanol as the Alkylating Agent", *Appl. Catal.,* **2002,** *A 230* (1-2), 245-251.

29. S. Hayat, Atta-ur-Rahman, M. I. Choudhary, K. M. Khan, W. Schumann, E. Bayer, "*N*-Alkylation of Aniline, Carboxamides and Several Nitrogen Heterocycles Using CsF-Celite/Alkyl Halides/CH_3CN Combination", *Tetrahedron,* **2001,** *57* (50), 9951-9957.

30. Y. Ono, "Dimethyl Carbonate for Environmentally Benign Reactions", *Catal. Today,* **1997,** *35* (1-2), 15-25.

31. Y. Ono, "Solid Acids and Bases Catalyze Selective Alkylations", *Cattech,* **1997,** *1* (1), 31-38.

32. P. Tundo, G. Moraglio, F. Trotta, "Gas-Liquid Phase-Transfer Catalysis: A New Continuous-Flow Method in Organic Synthesis", *Ind. Eng. Chem. Res.,* **1989,** *28* (7), 881-890.

33. F. Trotta, P. Tundo, G. Moraglio, "Selective Mono-*N*-Alkylation of Aromatic Amines by Dialkyl Carbonate under Gas-Liquid Phase-Transfer Catalysis (GL-PTC) Conditions", *J. Org. Chem.* **1987,** *52* (7), 1300-1304.

34. Y. Ono, "Solid Base Catalysts for the Synthesis of Fine Chemicals", *J. Catal.,* **2003,** *216* (1-2), 406-415.

35. Y. Ono, T. Baba, "Selective Reactions over Solid Base Catalysts", *Catal. Today,* **1997,** *38* (3), 321-337.

36. P. R. H. P. Rao, P. Massiani, and D. Barthomeuf "Alkylation of Aniline with Methanol on Beta and EMT Zeolites Exchanged with Alkaline Cations" In *Zeolite Science 1994: Recent Progress and Discussions, Stud. Surf. Sci. Catal.,* H. G. Karge and J. Weitkamp, Eds.; Elsevier Science B. V.: Amsterdam, 1995; Vol. 98, pp 287-294.

37. P. R. H. P. Rao, P. Massiani, D. Barthomeuf, "Selectivity to *N*-Mono or Dialkylation in the Reaction of Aniline with Dimethyl Carbonate on Faujasite, EMT and Beta Alkaline Zeolites", *Catal. Lett.,* **1995,** *31* (1), 115-120.

38. Y. Ono, "Catalysis in the Production and Reactions of Dimethyl Carbonate, An Environmentally Benign Building Block", *Appl. Catal.,* **1997,** *A 155* (2), 133-166.

39. S. P. Elangovan, C. Kannan, B. Arabindoo, V. Murugesan, "Aniline Methylation over AFI and AEL Type Molecular Sieves", *Appl. Catal.,* **1998,** *A 174* (1-2), 213-219.

40. C. Siswanto, J. F. Rathman, " Selective *N*-Alkylation of Aniline by Micellar Catalysis", *J. Colloid Interface Sci.,* **1997,** *196* (1), 99-102.

41. S. Narayanan, K. Deshpande, "A Comparative Aniline Alkylation Activity of Montmorillonite and Vanadia-Montmorillonite with Silica and Vanadia-Silica", *Appl. Catal.,* **1996,** *A 135* (1), 125-135.

42. S. Narayanan, K. Deshpande, "Mechanism of Aniline Alkylation over Vanadia and Supported Vanadia", *J. Mol. Catal.,* **1995,** *A 104* (2), L109-L113.

43. S. Narayanan, B. P. Prasad, "Characterization and Aniline Alkylation Activity of Vanadia and Silica-Supported Vanadia Catalysts", *J. Mol. Catal.,* **1995,** *A 96* (1), 57-64.

44. B. L. Su, D. Barthomeuf, "Alkylation of Aniline with Methanol: Change in Selectivity with Acido-Basicity of Faujasite Catalysts", *Appl. Catal.,* **1995,** *A 124* (1), 73-80.

45. S. Narayanan, D. Kumari, A. S. Rao, "Vapour Phase Aniline Alkylation Activity and Selectivity over H-ZSM-5", *Appl. Catal.,* **1994,** *A 111* (2), 133-142.

46. S. Prasad, B. S. Rao, "Mechanism of Aniline Alkylation with Methanol over AlPO4-5", *J. Mol. Catal.,* **1990,** *62* (2), L17-L22.

47. Y. Ono, Y. Izawa, Z. Fu, "Regioselective *N*-Alkylation of Imidazole with Alcohols over Zeolites", *J. Chem. Soc., Chem. Commun.,* **1995,** *1*, 9.

48. Y. Ono and Z. Fu, Y. Izawa "Vapor-Phase *N*-Alkylation of Imidazole with Alcohols over Zeolites" In *Catalysis by Microporous Materials, Stud. Surf. Sci.*

Catal., H. K. Beyer, H. G. Karge, I. Kiricsi, and J. B. Nagy, Eds.; Elsevier Science B. V.: Amsterdam, 1995; Vol. 94, pp 697-704.

49. M. Okamoto, M. Tanaka, Y. Ono, "Methylation of Pyridin-2-one with Methanol over γ-Alumina in Vapor Phase", *Catal. Lett.,* **1997,** *46* (1-2), 123-126.

50. Y. Fu, T. Baba, Y. Ono, "Vapor-Phase Reactions of Catechol with Dimethyl Carbonate. Part I. *O*-Methylation of Catechol over Alumina", *Appl. Catal.,* **1998,** *A 166* (2), 419-424.

51. Y. Fu, T. Baba, Y. Ono, "Vapor-Phase Reactions of Catechol with Dimethyl Carbonate. Part II. Selective Synthesis of Guaiacol over Alumina Loaded with Alkali Hydroxide", *Appl. Catal.,* **1998,** *A 166* (2), 425-430.

52. Y. Fu, T. Baba, Y. Ono, "Vapor-Phase Reactions of Catechol with Dimethyl Carbonate. Part III: Selective Synthesis of Veratrole over Alumina Loaded with Potassium Nitrate", *Appl. Catal.,* **1999,** *A 176* (2), 201-204.

53. Y. Fu, T. Baba, Y. Ono, "Vapor-Phase Reactions of Catechol with Dimethyl Carbonate. Part IV: Synthesis of Catechol Carbonate over Alumina Loaded with Cesium Hydroxide", *Appl. Catal.,* **1999,** *178* (2), 219-223.

54. Y. Ono and T. Baba "Strong Solid Bases for Organic Reactions" In *Catalysis,* J. J. Spivey, Ed.; Royal Society of Chemistry: Cambridge, England, 2000; Vol. 15, pp 1-39.

55. B. L. Su, D. Barthomeuf, "Comparison of Acid-Base Properties of FAU, EMT, LTL and MOR (Na Forms) in Benzene Adsorption and Alkylation of Aniline with Methanol", *Appl. Catal.,* **1995,** *124* (1), 81-90.

56. Z. Fu, Y. Ono, "Selective *O*-methylation of Phenol with Dimethyl Carbonate over X-zeolites", *Catal. Lett.,* **1993,** *21* (1), 43-47.

57. S. I. Woo, J. K. Lee, S. B. Hong, Y. K. Park, Y. S. Uh, "Selective Alkylation of Aniline with Methanol Over Boronsilicate Molecular Sieve" In *Zeolite: Facts, Figures, Future, Stud. Surf. Sci. Catal.,* P. A. Jacobs and R. A. Van Santen, Eds.; Elsevier Science B. V.: Amsterdam, 1989; Vol. 49 B, pp 1095-1103.

58. "Powder Diffraction File (PDF-2)" (International Center for Diffraction Data, Newtown Square, PA).

59. K. G. Rasmussen, K. A. Jørgensen, "Metal-Catalyzed Reactions of Imines with Ethyl Diazoacetate Leading to Aziridines", *J. Chem. Soc., Perkin Trans. 1,* **1997,** *9,* 1287-1291.

60. H. Ha, K. Kang, J. Suh, Y. Ahu, "A New Synthesis of Aziridine-2-carboxylates by Reaction of Hexahydro-1,3,5-triazines with Alkyldiazoacetates in the Presence of Tin(IV) Chloride", *Tetrahedron Lett.,* **1996,** *37* (39), 7069-7070.

61. K. Ikeda, K. Achiwa, M. Sekiya, "Trifluoromethanesulfonic Acid-Promoted Reaction of Hexahydro-1,3,5-triazines with Ketene Silyl Acetates. Convenient Synthesis of Alkyl β-Aminocarboxylates", *Tetrahedron Lett.,* **1983,** *24* (9), 913-916.

62. A. Hashidzume, A. Kajiwara, A. Harada, M. Kamachi, "Polymerization of Azastyrene Derivatives. 3. Preparation and Polymerization of *N*-Methyleneaniline", *Macromolecules,* **1998,** *31* (2), 535-537.

63. P. S. Kumar, J. J. Shrotri, S. D. Kulkarni, C. E. Deshpande, S. K. Date, "Low Temperature Synthesis of $Ni_{0.8}Zn_{0.2}Fe_2O_4$ powder and its Characterization", *Mat. Lett.,* **1996,** *27* (6), 293-296.

64. R. D. Waldron, "Infrared Spectra of Ferrites", *Phys. Rev.,* **1955,** *99* (6), 1727-1735.

65. W. B. White, B. A. Deangelis, "Interpretation of the Vibrational Spectra of Spinels", *Spectrochim. Acta,* **1967,** *A 23* (4), 985-995.

66. M. T. Weller "Inorganic Material Chemistry" In *Oxford Chemistry Primers,* J. Evans, Ed.; Oxford University Press: Oxford, 1994; Vol. 23, pp 44-48.

67. A. F. Wells "Structural Inorganic Chemistry" 5th ed.; Oxford University Press: Oxford, 1984; pp 592-596.

68. F. C. Romeijn, "Physical and Crystallographical Properties of Some Spinels", *Philips Res. Rep.,* **1953,** *8,* 304-342.

69. C. S. Narasimhan, C. S. Swamy, "Studies on the Decomposition of Isopropyl Alcohol on $MgAl_{2-x}Fe_xO_4$", *Appl. Catal.,* **1982,** *2* (4-5), 315-328.

70. J. P. Jacobs, A. Maltha, J. G. Reintjes, J. Drimal, V. Ponec, H. H. Brongersma, "The Surface of Catalytically Active Spinels", *J. Catal.,* **1994,** *147* (1), 294-300.

71. M. A. Aramendia, V. Borau, C. Jimenez, J. M. Marinas, F. J. Romero, "Vapor-Phase Reaction of Acetophenone with Methanol or Dimethyl Carbonate on Magnesium Oxide and Magnesium Phosphates", *J. Catal.,* **1999,** *183* (1), 119-127.

72. I. I. Ivanova, E. B. Pomakhina, A. I. Rebrov, W. Wang, M. Hunger, J. Weitkamp, " Mchanism of Aniline Methylation on Zeolite Catalysts Investigated by *In Situ* ^{13}C NMR Spectroscopy", *Kinet. Catal.,* **2003,** *44* (5), 701-709.

73. W. Wang, M. Seiler, I. I. Ivanova, J. Weitkamp, M. Hunger, "*In Situ* Stopped-Flow (SF) MAS NMR Spectroscopy: A Novel NMR Technique Applied for the Study of Aniline Methylation on a Solid Base Catalyst", *J. Chem. Soc., Chem. Commun.,* **2001,** *15,* 1362-1363.

74. F. A. Carroll "Perspectives on Structure and Mechanism in Organic Chemistry" 1st ed.; Brooks/Cole Publishing Company: Pacific Grove, California, 1998; pp 438-448.

75. R. G. Rice, E. J. Kohn, "Raney Nickel Catalyzed *N*-Alkylation of Aniline and Benzidine with Alcohols", *J. Am. Chem. Soc.,* **1955,** *77* (15), 4052-4054.

CHAPTER 6

6. FRIEDEL-CRAFTS ALLYLATION OF BENZENE PROMOTED BY NANOPARTICULATE $Co(PAO)_2 \cdot 2H_2O$-DERIVED TRICOBALT TETRAOXIDE

6.1. INTRODUCTION

Friedel-Crafts alkylation and acylation reactions are among the most powerful, synthetic routes for organic compounds.[1-5] Friedel-Crafts reactions are generally defined as those reactions catalyzed either by a Lewis acid type halide (e.g. $AlCl_3$, $SbCl_5$, $FeCl_3$, BF_3, etc.) or by a Brønsted-Lowry type proton acid (e.g. HF, H_2SO_4, H_3PO_4, etc.).[1a,2] These promoted reactions can be substitution, isomerization, elimination, cracking, polymerization, or addition.[1a,2] Therefore, a Friedel-Crafts reaction mixture can have six components including a material to be substituted, a material providing the substituents (e.g. olefin, alkyl halide, alcohol, etc.), a catalyst (as identified above), a solvent (generally one of the reactants, non-ionizing, or having very high dielectric constants), the substituted product resulting from the reaction, and the side product HX.[1a,2] One type of Friedel-Crafts reaction is the monoallylation of aromatic compounds to obtain aromatics with alkyl substituents terminated with double bonds, i.e. the products are monoallylarenes.[6-11] Allylation of benzene and arenes represent an indirect method to prepare 1-arylalkanes, which are important lubricants, due to their high viscosity, and are also used to produce biodegradable detergents. Furthermore, Friedel-Crafts allylation

provides a cheaper and more environmentally-friendly route for the synthesis of 1-arylalkanes than Friedel-Crafts acylation of aromatics, followed by reduction of the ketones thus produced.[8] Friedel-Crafts allylation can be catalyzed homogeneously or heterogeneously using an allyl halide or an allyl alcohol as the allylating reagent.[1b-3,5-14] In both cases, the desired allylic product is obtained in a low to good yield owing to the lack of functional selectivity, resulting in the formation of byproducts and incompleteness of the reaction.[1b-3,5-11,13,14] The absence of functional selectivity is mainly ascribed to the high activity of the acid catalyst used.[9] Expectedly, when the allylation was carried out using an allyl halide as an allylation reagent and homogeneously catalyzed by sulfuric acid, a side product consisting of an aromatic bearing a halo-substituted alkyl group was obtained. The allyl double bond was first electropholically attacked by the catalyst proton on the basis of Markovnikov's rule to generate the alkyl carbocation. An electrophilic attack on the aromatic ring was then caused by the latter to form the final product, as can be shown in the following example:[3,5,13,14]

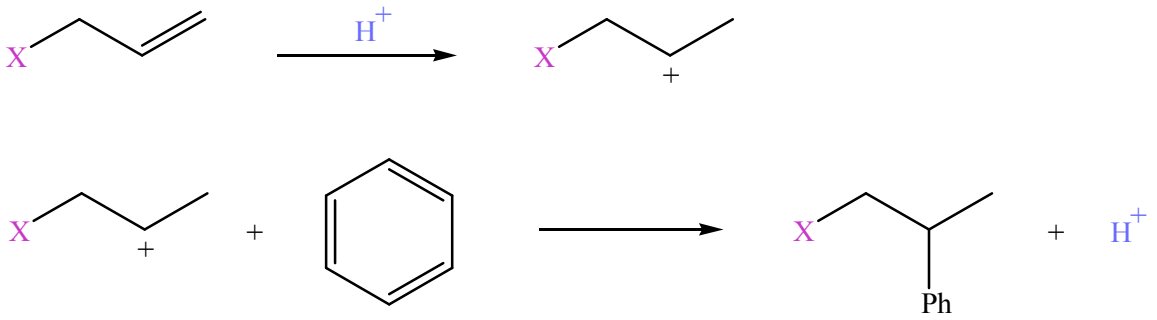

Polyaryl-substituted alkanes are produced under the influence of a Lewis acid type halide catalyst due to the occurrence of the reaction at the allylic carbon and the

double bond. The latter is subjected to an electrophilic addition by the hydrogen halide, the byproduct of the Friedel-Crafts reaction. Subsequent reaction with the catalyst leads to further condensation with aromatics via Friedel-Crafts alkylation. Allylation of benzene with ally chloride, for example, in the presence of anhydrous ferric chloride, led to the formation of allylbenzene, 2-chloro-propylbenzene, and 1,2-diphenylpropane:[5,13]

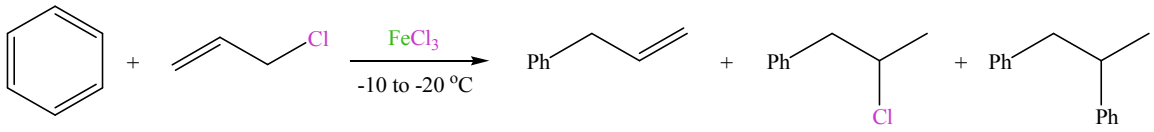

On the other hand, with the aluminum chloride acting in the capacity of a catalyst, the products of the reaction were strongly dependent upon the reaction conditions employed.[5,13]

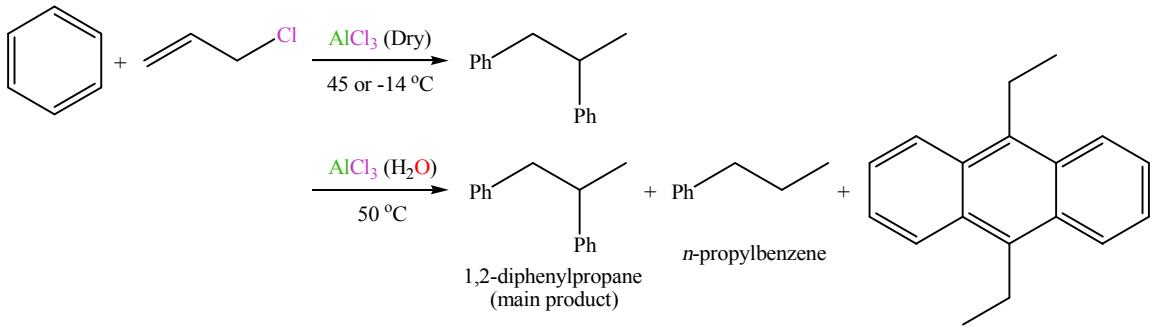

A plausible rationalization for the production of the products obtained, in case of poisoning $AlCl_3$ with water, was given through the following mechanism:[1b-3,5,13]

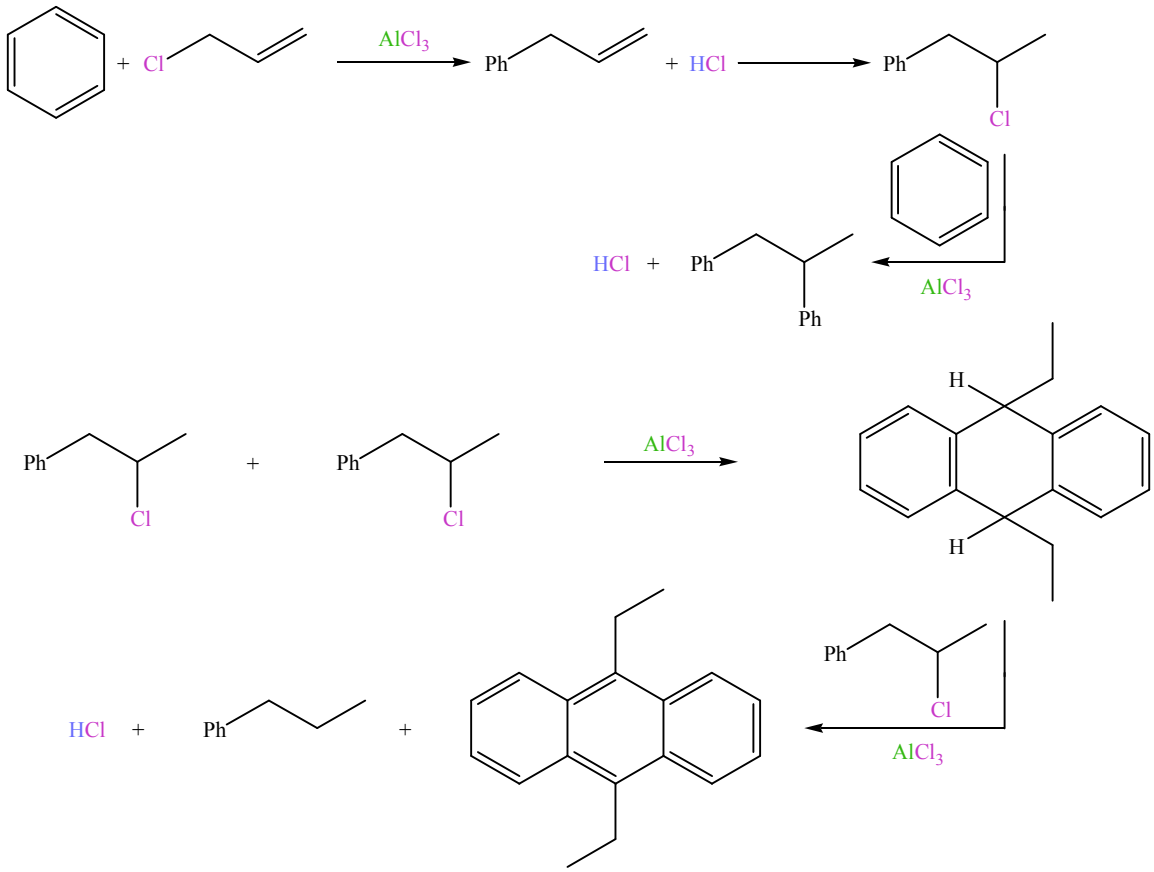

Allyl metal compounds (e.g. allylsilane, allylgermane, and allylstannane), along with suitable homogeneous catalyst systems such as thalium trifluoroacetate or iodosyl/boron trifluoride-ethyl ether, were found to be useful for the synthesis of allyl benzene or its derivatives, as illustrated in the following two examples:[10,11]

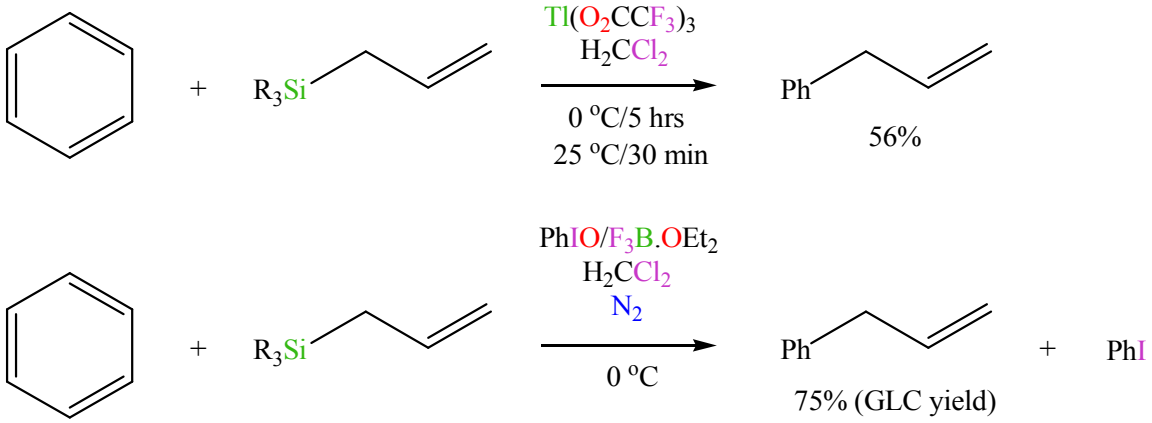

A phenyl-copper-magnesium reagent is also among the catalysts that have been used for homogeneous production of allyl benzenes, as shown in the following examples:[12]

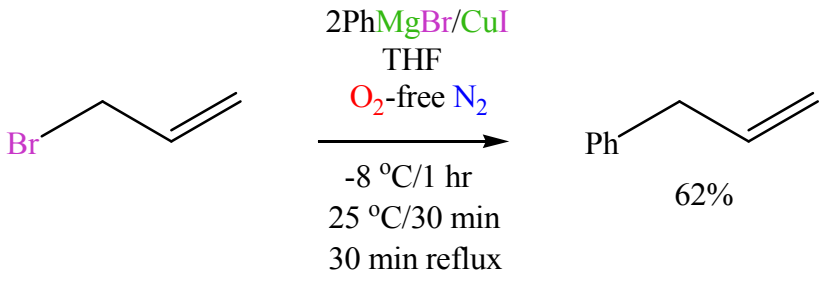

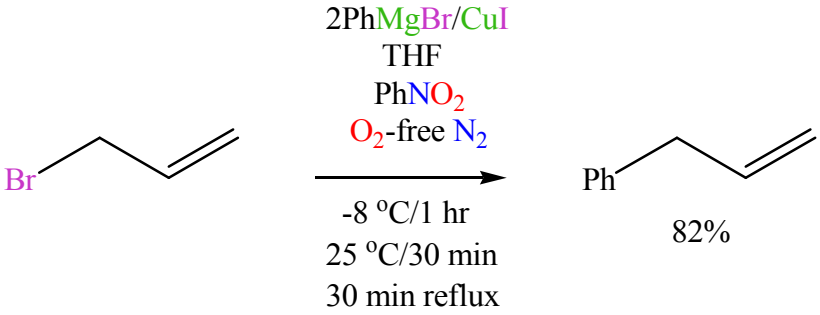

From the above examples, it can be concluded that homogeneous catalysts have several drawbacks that need to be overcome for production of allyl benzenes in better selectivity and higher yield. Homogeneous Brønsted-Lowry type proton acids (e.g. H_2SO_4) lead to the condensation at the double bond of the allyl halide to form aromatics with a halo-substituted alkyl group substituent.[1b,2,5,9,13] Homogeneous Lewis acid type halides (e.g. $AlCl_3$, $FeCl_3$), on the other hand, lack the functional selectivity towards the allylic halide and the allyl double bond as is reflected by the production of alkane chains multiply-substituted with the aryl ring.[1b,2,5-7,9,13,14] Organometallic reagents, in addition, give good yield of the monoallylated aromatics. However, such reagents are expensive and air- and moisture-sensitive.[10-12]

Acidic zeolites have been used as heterogeneous catalysts for the synthesis of allyl benzenes. It was found that when allyl chloride was utilized as an allylating agent, the yield of allyl benzene was less than 10% due to the formation of hydrogen chloride, which promoted the isomerization of allyl benzene to 1-phenylpropene. The latter was able to react further with benzene because of the activation of its double bond by the conjugation with the aromatic ring, as schematically shown in the following scheme:[9]

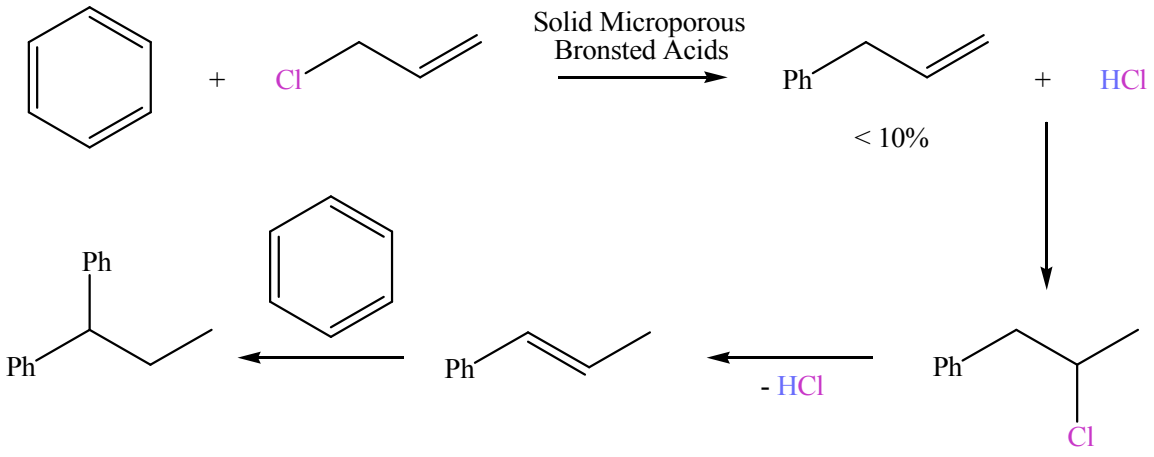

However, using allyl alcohol for the allylation of toluene with the same catalyst gave good selectivity for allyl toluenes.[9]

As an attempt to overcome the problems encountered with both homogeneous Brønsted-Lowry type proton acids and Lewis acid type halides, Kodomari *et al.*[7] employed a heterogeneous catalyst system composed of both acid and base constituents, in which the basic component react with the hydrogen halide to suppress the electrophilic addition of the double bond, as illustrated in the following equation:

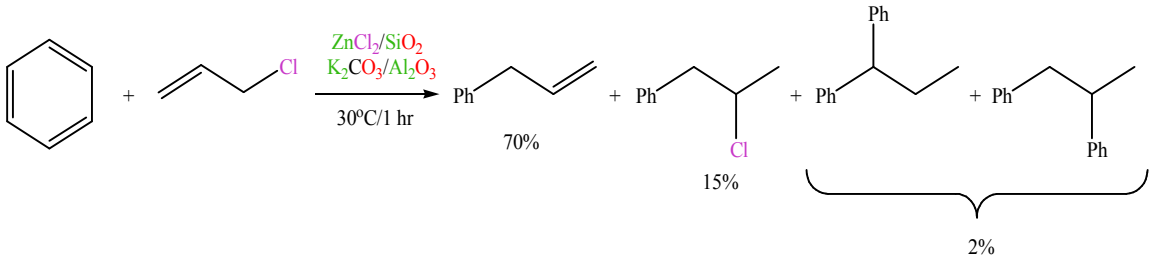

Recently, excellent yields of allylbenzenes have been obtained when a lead bromide fluoride reagent was employed as a heterogeneous catalyst, as shown in the following example:[6]

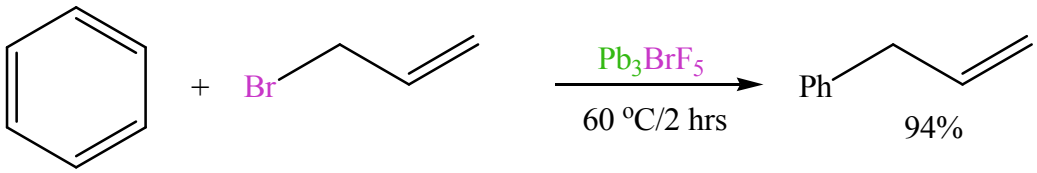

It can be inferred from the previous examples of heterogeneous catalyst systems that they also suffer from some drawbacks that have to be reduced or eliminated to achieve excellent selectivity and high yield for allylbenzenes. Heterogeneous Brønsted-Lowry solid acids (e.g. Zeolites, clays), for instance, give a very low to moderate yield of the desired product when an allyl halide is used as an allylating agent due to the

formation of the undesirable hydrogen halide.[8,9] The latter product is highly corrosive, has the ability to destroy the structure of the solid catalyst, and can serve as a competitive catalyst, resulting in the formation of unfavorable side products.[8] Supported metal halides combined with supported alkali carbonates, on the other hand, give good yield of the allylaromatics.[7] The lead bromide fluoride reagent gives high yields and induces high selectivity towards monoallylation of aromatics. However, the reaction is stoichiometric instead of catalytic.[6] Moreover, lead is not benign to the environment. Therefore, further investigations are required for the development of a catalyst system that improves the yield and the selectivity for the allyl benzenes that is environmentally-sustainable. Searching the literature, moreover, reveals that metal oxides have not been utilized as catalysts for the allylation of aromatics. This motivated an investigation of the use of nanoparticulate tricobalt tetraoxide, Co_3O_4, as a heterogeneous catalyst for Friedel-Crafts allylation that is reported herein.

6.2. EXPERIMENTAL

Anhydrous cobalt bromide [$CoBr_2$, Co 26.6% min, (Alfa Aesar)], hexaquadibromocobalt(II) [$CoBr_2 \cdot 6H_2O$, 99% (Alfa Aesar)], silica gel [SiO_2, Davisil, grade 644, 100-200 mesh, 150 Å, 99+% (Aldrich)] allyl bromide [$H_2C{=}CHCH_2Br$, 98% (Lancaster)], benzene [C_6H_6, thiophene free (Fisher Scientific)], cyclohexylamine [$C_6H_{11}NH_2$ (Aldrich)], phenol [C_6H_5OH (EM Science)], cyclohexane [C_6H_{12}, reagent grade (Fisher Scientific)], methylene chloride [H_2CCl_2, Optima (Fisher Scientific)] were commercial reagents and used without further purification. Benzene was dried over molecular sieves. The $Co_2(PAO)_2 \cdot 2H_2O$-derived tricobalt tetraoxide was prepared as described previously in Chapter 2. The $CoBr_2$-derived tricobalt tetraoxide was obtained

by heating anhydrous $CoBr_2$ in a muffle furnace at 500 ^oC, according to its thermal gravimetric analysis (TGA), for 12 hours. The Co_3O_4 (20% wt) supported on SiO_2 Davisil was prepared by mixing $CoBr_2 \cdot 6H_2O$ (8.141 g, 24.9 mmol) with SiO_2 Davisil (8.00 g, 133.13 mmol). An amount of distilled water (30 ml) was added to this mixture to dissolve the cobalt bromide to help distribute it homogeneously within the silica gel. This resulting mixture was then dried by a passing air stream. The dried solid was then deposited in a digitally controlled muffle furnace at 500 ^oC for 12 hours to give 10.0 g of the desired catalyst. The surface morphology and the qualitative elemental analyses of the $Co_2(PAO)_2 \cdot 2H_2O$-derived tricobalt tetraoxide, the $CoBr_2$-derived tricobalt tetraoxide, and the $CoBr_2$-derived tricobalt tetraoxide supported on silica gel Davisil were investigated by scanning electron microscopy (SEM) coupled with energy dispersive X-ray spectroscopy (EDXS). Images were also obtained using electron back scattering, where higher atomic numbered elements appear brighter than lower atomic numbered elements. A Hewlett Packard G1800A Gas Chromatograph-Mass Spectrometer GC-MS, equipped with 30 m x 0.25 mm HP5 column (crosslinked 5% PhMe silicone), was used to analyze the products of the Friedel-Crafts allylation. The temperature program used had an initial hold of 2 min at 35^oC, a ramp of 5^oC/min to 170^oC, and a final hold of 5 min. The helium flow rate was 1 ml/min and the injection port was set at 250^oC.

A sample of benzene (1.5756 g, ~ 20 mmol) was allylated by allyl bromide (1.2113 g, ~ 10 mmol) at 150^oC in a digitally-controlled oven in a Teflon-lined stainless steel bomb reactor. This reaction was catalyzed by the Co_3O_4 (2.4095 g, ~ 10 mmol) obtained from either the pyrolysis of $Co(PAO)_2 \cdot 2H_2O$ at 276^oC or the decomposition of anhydrous $CoBr_2$ at 500^oC. An excess of benzene was intentionally used to serve as a

solvent for the reaction. Several samples were taken at different intervals, and 2-μl samples were injected into a GC/MS. The stainless steel bomb was cooled to room temperature before taking every sample. Response factors and retention times of the reactants and the products were determined by the injection of a standard H_2CCl_2-solution containing specific amounts of authentic samples of reactants and products into the GC/MS. Comparing the mass spectra of the reactants and the products to those available in the NIST database helped identify them. Similar reaction conditions, mole ratio of reactants, and product analyses were used when the supported catalyst was employed. Irrespective of the catalyst employed, the reaction always gave allyl benzene as the major product, allyl ether as the minor product, and no other by products were detected due to the electrophilic attack of HBr, the other product of the Friedel-Crafts allylation, on the olefinic double bond of the allyl benzene.

Acidity and Basicity Measurements

The acidity and basicity of the $Co_2(PAO)_2 \cdot 2H_2O$-derived tricobalt tetraoxide were measured by adsorption of cyclohexylamine and phenol from cyclohexane, respectively, according to the procedure outlined in Chapter 2.

6.3. RESULTS AND DISCUSSION

The Langmuir adsorption isotherms of acidity and basicity of $Co_2(PAO)_2 \cdot 2H_2O$-derived tricobalt tetraoxide are displayed in Figure 6.1.

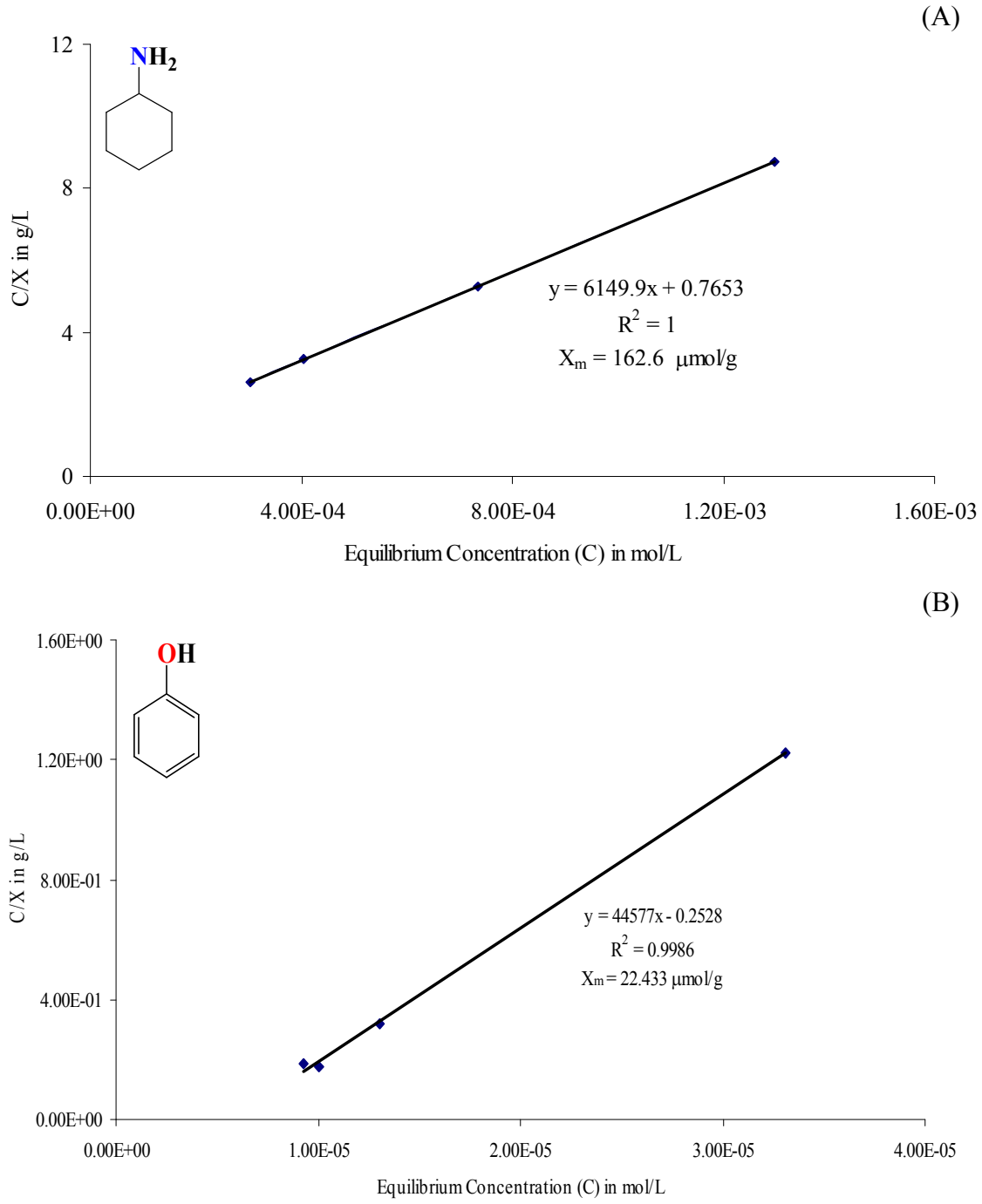

Figure 6.1. Langmuir adsorption isotherm of (A) acidity and (B) basicity of $Co_2(PAO)_2 \cdot 2H_2O$-derived Co_3O_4

The acidic site population is almost 7 times that of the basic sites. This predominance of acidity on the surface of the Co_3O_4, prepared from the PAO^- complex of Co^{2+}, meets the acidity requirement for the catalyst employed in Friedel-Crafts reactions and thus, makes it a suitable catalyst for the allylation of aromatics. The basic sites on the oxide surface, on the other hand, play an important role in preventing the side reactions by providing the capacity to neutralize the HBr produced during the reaction course and hence in converting Co_3O_4 to $CoBr_2 \cdot XH_2O$ (X = 2 or 4). The XRD pattern recorded for the catalyst after the end of the reaction confirms the conversion of Co_3O_4, the active catalyst, to cobalt bromide. However, Co_3O_4 is readily regenerated by heating the $CoBr_2$ under air at 500°C as follows:

$$3CoBr_2 + 2O_2 \xrightarrow[500\ ^oC]{} Co_3O_4 + 3Br_2$$

The Friedel-Crafts allylation of benzene using allyl bromide as the allylating agent at 150°C in a bomb reactor gives allyl benzene as the major product and allyl ether as the minor product (equation below). The formation of those products is likely assisted by both the acidic and basic sites on the surface on the catalyst.

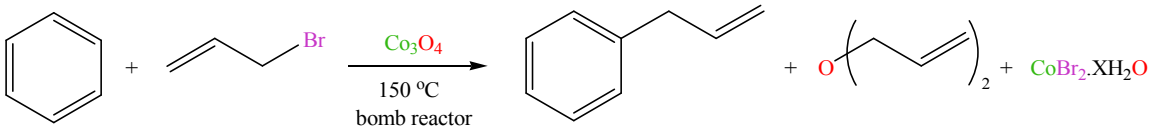

"major" "minor" X = 2 or 4

Investigation of the reaction kinetics revealed that the reaction is first-order in the disappearance of allyl bromide, irrespective of the catalyst used, as can be seen from

plotting the natural logarithm of the molar concentration of allyl bromide versus the reaction time in Figure 6.2. However, the rate constant (k) in case of using $Co_2(PAO)_2{\cdot}2H_2O$-derived Co_3O_4 was almost 3 times the k observed when using $CoBr_2$-derived Co_3O_4. Similarly, 20% Co_3O_4/Davisil silica resulted in accelerating the reaction about 3 times compared to the reaction rate of unsupported Co_3O_4 derived from $CoBr_2$. Both $Co_2(PAO)_2{\cdot}2H_2O$-derived Co_3O_4 and the $CoBr_2$-derived Co_3O_4 on Davisil silica gel catalyzed the reaction with a similar rate. These observations concerning the reaction rate in case of each catalyst could be rationalized on the basis of the differences in surface properties (acidity, basicity, and surface area) among the three catalysts. However, the surface area would be the most important factor that makes the three catalysts promote the reaction with different rates because increasing the surface area of the catalyst led to an increase in the reaction rate. The specific surface area of each catalyst is given in Table 6.1. The surface area of the $Co_2(PAO)_2{\cdot}2H_2O$-derived Co_3O_4 is 92 times higher than that of $CoBr_2$-derived Co_3O_4. The surface area of the supported catalyst, on the other hand, is 188 times that of the $CoBr_2$-derived Co_3O_4 and twice that of the $Co_2(PAO)_2{\cdot}2H_2O$-derived Co_3O_4. In the latter case, the fact that the rate of reaction is similar despite the disparity on surface area suggests that coverage of the silica with Co_3O_4 is not even in the supported catalyst.

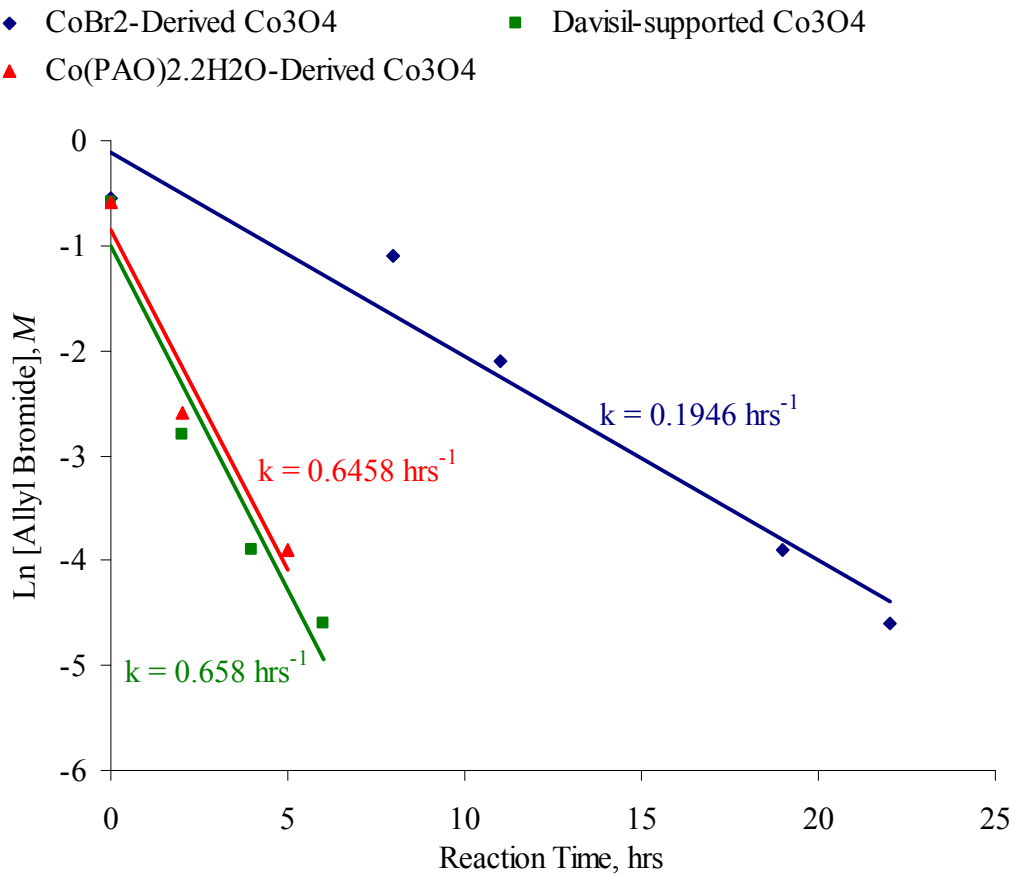

Figure 6.2. First-order plot of changing the concentration of allyl bromide with time

Table 6.1. Specific Surface Area of each Catalyst Used to Promote the Allylation of Benzene

Co_3O_4 Catalyst	Specific Surface Area (m^2/g)
$Co_2(PAO)_2 \cdot 2H_2O$-derived	58.76
$CoBr_2$-derived	0.6357
Davisil-supported	119.6

The percent conversion of allyl bromide with time (Figure 6.3) is roughly correlated with the variation of the surface area of the catalyst. The catalytic activity of both $Co_2(PAO)_2{\cdot}2H_2O$-derived Co_3O_4 and the 20% wt $CoBr_2$-derived Co_3O_4 supported on silica gel Davisil was similar because allyl bromide was converted to products during the reaction course with the same percentage, as also confirmed by their superimposing curves. For instance, after 2 hours, the conversion of allyl bromide was 87.7% with the former catalyst, while it was 88.7% with the latter catalyst system. In contrast, the conversion of allyl bromide became almost 80% after 11 hours of running the reaction using the $CoBr_2$-derived as a catalyst.

The relatively high surface area of the $Co_2(PAO)_2{\cdot}2H_2O$-derived Co_3O_4 may be attributed to the porosity of its particles. The existence of pores was confirmed by the SEM technique (Figure 6.4). It can be inferred from the electromicrographs that the particles of this Co_3O_4 catalyst have a rod-like "French Fries" shape. The $CoBr_2$-derived Co_3O_4, on the other hand, has a completely different surface morphology than that observed for the $Co_2(PAO)_2{\cdot}2H_2O$-derived Co_3O_4. The particles of the $CoBr_2$-derived Co_3O_4 are surprisingly almost perfect octahedrons with different sizes (Figure 6.5). The EDXS showed only the presence of cobalt and there was no bromine (Figure 6.6). Moreover, the electron back-scattered images showed the whole particles in the same degree of brightness (Figure 6.6). Both of these analyses demonstrate the conversion of cobalt(II) bromide to Co_3O_4.

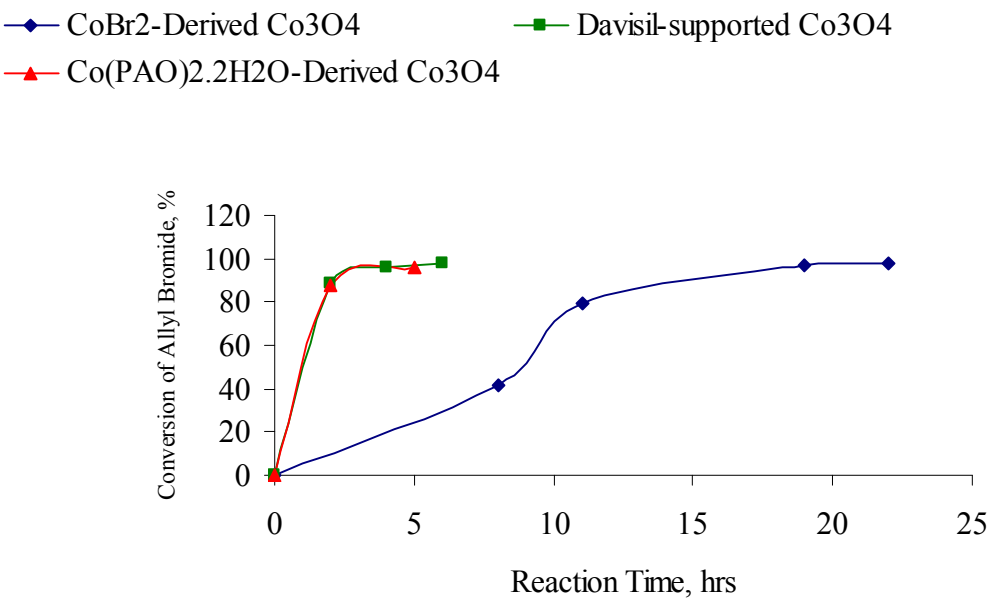

Figure 6.3. Conversion % of allyl bromide in the Friedel-Crafts allylation of benzene at 150°C

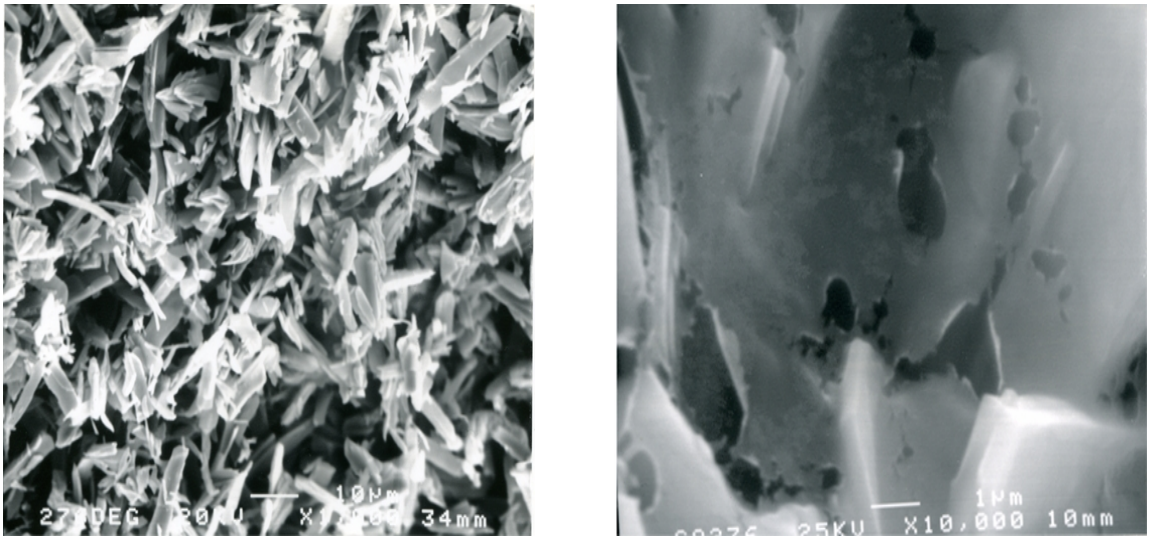

Figure 6.4. SEM micrographs of the $Co_2(PAO)_2 \cdot 2H_2O$-derived Co_3O_4 (A) x 1,000 and (B) x 10,000

The formation of such Co_3O_4 octahedrons may be due to partial volatilization of $CoBr_2$ followed by deposition on the growing crystal surface. Halogens are often used in transport-assisted crystallization of metal oxides, and such a process is likely to occur in

the site during the oxidation of $CoBr_2$ to Co_3O_4 that was also demonstrated by XRD. Investigation of the morphology of the anhydrous $CoBr_2$, on the other hand, revealed that its particles were not octahedrons, but rather they were overlapping sticks (Figure 6.7).

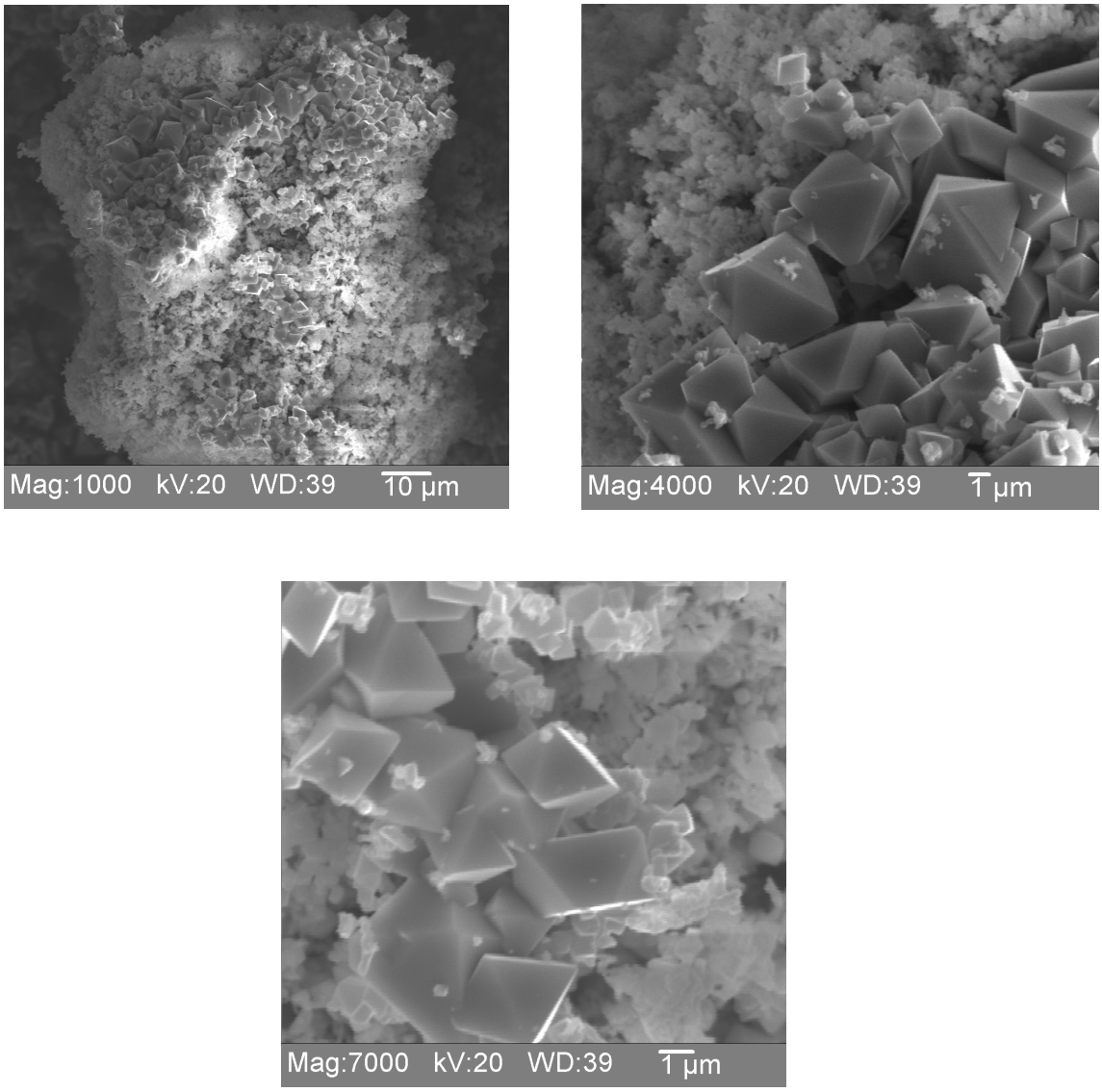

Figure 6.5. SEM micrographs of the $CoBr_2$-derived Co_3O_4 taken at voltage of 20 kV and magnifications of (A) 1000, (B) 4000, and (C) 7000

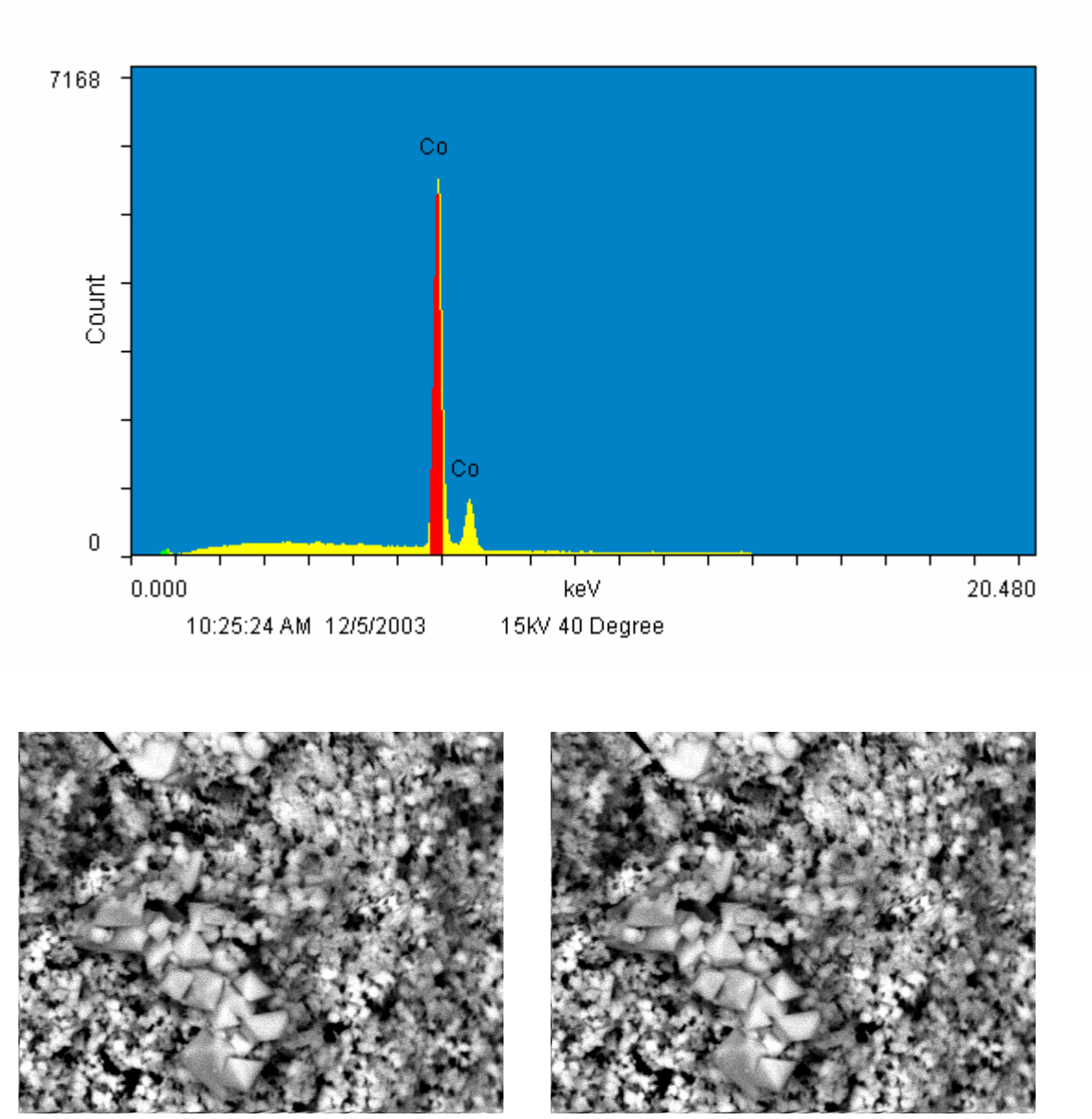

Figure 6.6. EDXS (A), primary electron back-scattered image (B), and secondary electron back-scattered image (C) of the $CoBr_2$-derived Co_3O_4 taken at a voltage of 20 kV and magnification of 2700

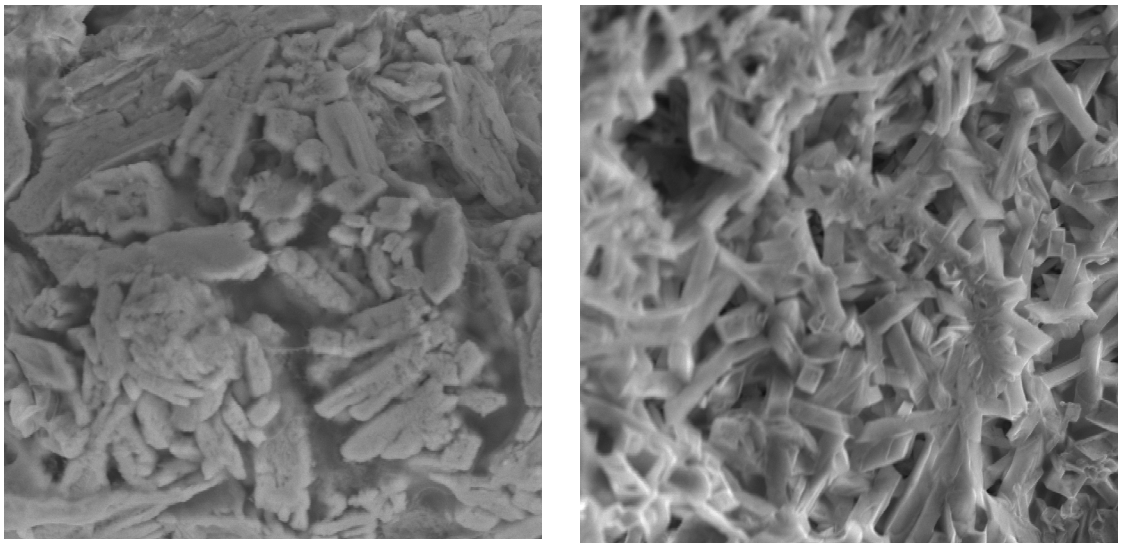

Figure 6.7. SEM micrographs of anhydrous $CoBr_2$ taken at a voltage of 25 kV and magnification of (A) 1000 and (B) 1400

The morphology of the supported catalyst had also been studied, and again the Co_3O_4 octahedra were observed on the bed of Davisil silica gel (Figures 6.8 and 6.9). However, elemental mapping demonstrates that there is also finer Co_3O_4 particles distributed over the surface of the silica. In order to isolate the Co_3O_4, silica on the supported catalyst was leached out of the catalyst using 10% wt/wt NaOH to leave behind the octahedral crystals of Co_3O_4 (Figure 6.10). In keeping with the SEM images of the supported catalyst, the Co_3O_4 was obtained both as fine particles and large octahedral crystals. The EDXS analysis showed a very small amount of silica remained, indicating the effectiveness of removing the silica support by sodium hydroxide.

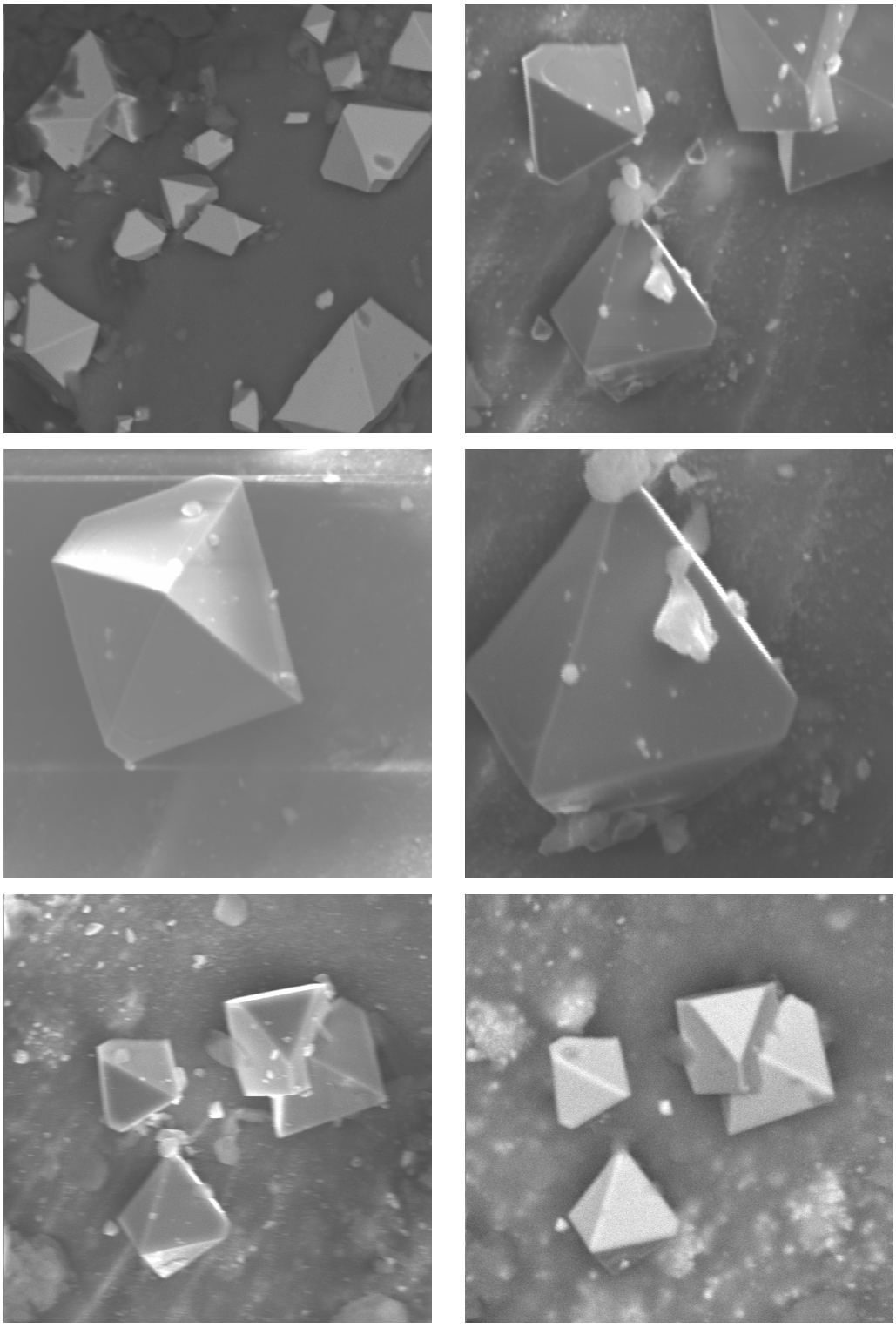

Figure 6.8. SEM micrographs of the supported catalyst at magnification of (A) 1400, (B) 3500, (C) 4500, and (D) 7000. Primary electron back-scattered image (E) and secondary electron back-scattered image (F) at magnification of 2300

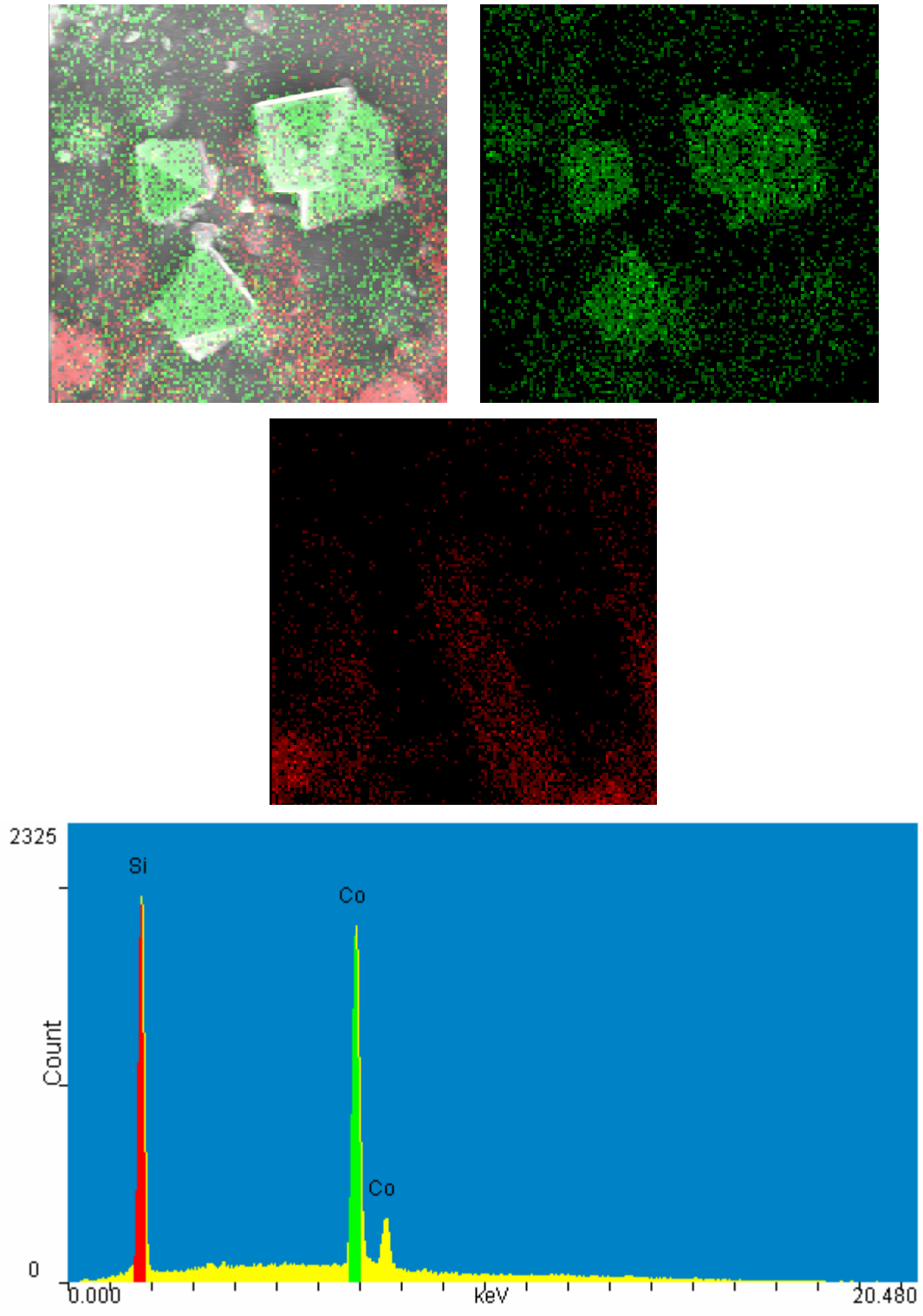

Figure 6.9. EDXS images and spectrum of the supported catalyst at magnification of 2300

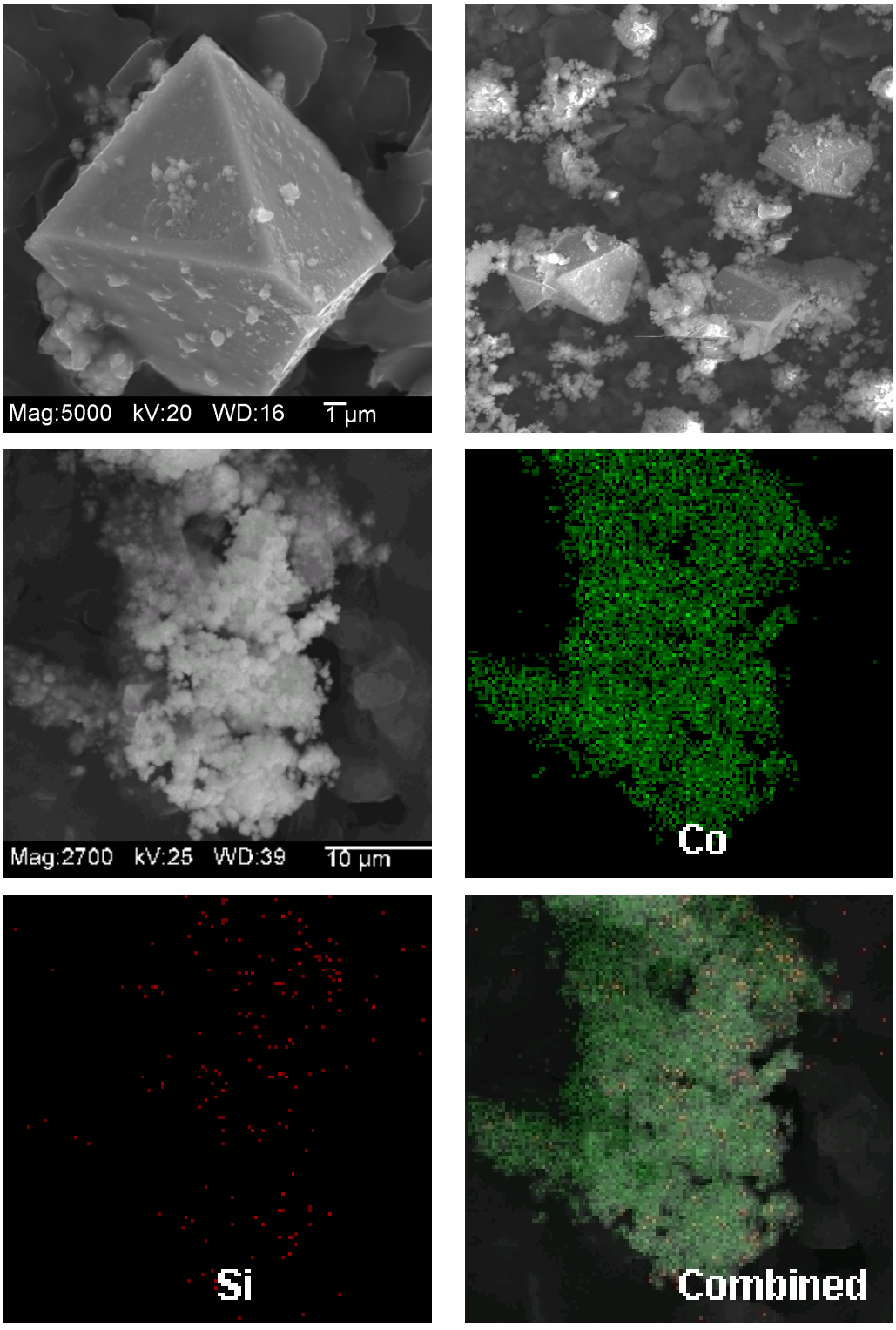

Figure 6.10. SEM micrographs of the supported catalyst after removing the silica support at magnification of (A) 1500, (B) 5000, and (C) 2700. (D), (E), and (F) are the mapping images obtained from EDXS at magnification of 2700

6.4. CONCLUSION

Nanoparticulate tricobalt tetraoxide derived from $Co(PAO)_2 \cdot 2H_2O$ has been used for the first time for the catalysis of Friedel-Crafts allylation and a high yield of allyl benzene was obtained. The catalyst is converted to $CoBr_2$ during the reaction course. However, the latter can be pyrolyzed to regenerate the active oxide catalyst providing a unique cyclic method for use and recycling of a Friedel-Crafts catalyst. Upon decomposition, $CoBr_2$ gives octahedral crystals of Co_3O_4. This oxide is used for the first time and is the first oxide reported as a catalyst in such application.

REFERENCES

1. (a) G. A. Olah "Definition and Scope" In *Friedel-Crafts and Related Reactions,* G. A. Olah, Ed.; John Wiley & Sons: New York, 1963; Vol. I, pp 25-168. (b) G. A. Olah "Reactivity and Selectivity" In *Friedel-Crafts and Related Reactions,* G. A. Olah, Ed.; John Wiley & Sons: New York, 1963; Vol. I, pp 853-935.

2. G. A. Olah "Friedel-Crafts Chemistry" In *Interscience Monographs on Organic Chemistry,* G. A. Olah, Ed.; John Wiley & Sons: New York, 1973; pp 25-168 and pp 303-475.

3. C. A. Thomas "Anhydrous Aluminum Chloride in Organic Chemistry"; ACS Monograph 87; Reinhold Publishing Corporation: New York, 1941; pp 4-11, 96, 121, 430-431, 441, 620, 664-665, and 876.

4. C. C. Price "The Alkylation of Aromatic Compounds by the Friedel-Crafts Method" In *Organic Reactions;* R. Adams, W. E. Bachmann, L. F. Fieser, J. R. Johnson, and H. R. Snyder, Eds.; John Wiley & Sons, Inc.: New York, 1946; Vol. III, pp 1-82.

5. R. M. Roberts and A. A. Khalaf "Friedel-Crafts Alkylation Chemistry: A Century of Discovery"; Marcel Dekker, Inc.: New York, 1984; pp 1-6 and pp 404-520.

6. J. Ichihara, "Functional Selectivity in Friedel-Crafts Alkylations with Allylic Halides Promoted by solid Composite Lead Fluoride Reagent", *Chem. Commun.,* **1997,** *19,* 1921-1922.

7. M. Kodomari, S. Nawa, T. Miyoshi, "Direct Allylation of Aromatic Compounds with Allylic Chloride Using the Supported Reagents System $ZnCl_2/SiO_2$-K_2CO_3/Al_2O_3", *J. Chem. Soc., Chem. Commun.,* **1995,** *18,* 1895-1896.

8. K. Smith, G. M. Pollaud, "Synthesis of 1-Arylalk-2-enes and 1-Arylalkanes via Friedel-Crafts Alkylation with Allylic Alcohols Catalysed by an Acidic Clay", *J. Chem. Soc., Perkin. Trans. 1,* **1994,** *24,* 3519-3520.

9. P. H. Espeel, B. Janssens, P. A. Jacobs, "Functional Selectivity in Friedel-Crafts Alkylations with Polyfunctional Reactants over Acid Zeolites", *J. Org. Chem.,* **1993,** *58* (27), 7688-7693.

10. K. Lee, D. Y. Kim, D. Y. Oh, "Reaction of Allyltrimethylsilane with an Aromatic Compound using Hypervalent Organoiodine Compound: A new Allylation of Aromatic Compounds", *Tetrahedron Lett.,* **1988,** *29* (6), 667-668.

11. M. Ochiai, M. Arimoto, E. Fujita, "Umpolung of Reactivity of Allylsilane, Allylgermane, and Allylstannane via their Reaction with Thallium (III) Salt: A New Allylation Reaction for Aromatic Compound", *Tetrahedron Lett.,* **1981,** *22* (45), 4491-4494.

12. M. T. Rahman, S. K. Nahar, "The Reaction of the Phenyl-Copper-Magnesium Reagent, Prepared from 2 PhMgBr and CuI, with Some Organic Halides", *J. Organomet. Chem.,* **1987,** *329* (1), 133-138.

13. R. Koncos and B. S. Friedman "Alkylation of Aromatics with Dienes and Substituted Alkenes" In *Friedel-Crafts and Related Reactions,* G. A. Olah, Ed.; John Wiley & Sons: New York, 1964; Vol. II, Part 1, pp 289-412.

14. T. M. Patrick, E. T. McBee, H. B. Hass, "Synthesis of Arylpropylamines. I. From Allyl Chloride", *J. Am. Chem. Soc.,* **1946,** *68* (6), 1009-1011.

CHAPTER 7

7. ARSENIC REMIDIATION IN AQUEOUS MEDIUM USING NANOPARTICULATE TRANSITION METAL OXIDES

7.1. INTRODUCTION

Arsenic is rated the twentieth most abundant element in the crust of the earth.[1,2] It is more abundant than mercury, cadmium, gold, silver, antimony, and selenium, but less than copper and tin.[1] Moreover, it is counted to be the twelfth most plentiful element available in the biosphere.[2] Normally, arsenic is found along with sulfide ores[1,3,4] such as orpiment (As_2S_3), realgar (AsS), mispickel (FeAsS), cobaltite (CoAsS), tennantite ($Cu_{12}As_4S_{13}$), and enargite (Cu_3AsS_4).[1,3,5] Arsenic compounds also accompany most gold and silver ores.[1,2,5,6] An average of 6 ppm is estimated for arsenic in the upper earth crust on the basis of 4.01×10^6 kg of abundance.[1] Soil content of arsenic is reported in several countries. For example it ranges from 1 to 20 ppm in the USA, and from 0.01 to 626 ppm in China.[1] This geochemical occurrence of arsenic is one of the most common natural causes of groundwater and soil pollution with arsenic in many places globally such as Bangladesh, India, Nepal, Germany, Italy, and USA.[1-4,6-12] The arsenic contamination of groundwater and the arsenic disaster encountered nowadays in Bangladesh are ascribed mainly to the naturally occurring arsenic deposits and ores, reflecting the significant role of this factor. Eruption of volcanoes and weathering processes are other natural contributors to the contamination of environment, especially

the atmosphere, with arsenic.[1,2,6] The eruption of volcanoes is responsible for emitting an amount of 17,150 tons of arsenic to the atmosphere.[1]

Man and the industrial revolution lead to dramatic increases in arsenic pollution by numerous pathways. The smelting of zinc, copper, nickel, and lead, for instance, is the most significant process for arsenic contamination, providing 62,000 tons of arsenic yearly.[1,3-6,12] Mining processes of arsenic-containing ores also helps to contaminate soil with arsenic.[1-3,6,9,10] Most of gold and silver, as well as uranium minerals mining processes, are well-known for their arsenic pollution because arsenic compounds are concomitants of these ores.[1,2,6] Burning of arsenic-containing fossil fuels and coal in households and power plants, a second aspect of human pollution, emits arsenic in the volatile form of As_4O_6.[1,4,6,11,12] Another anthropogenic route for arsenic pollution is the use of arsenic compounds in many production processes and products such as coloring process in tannery, dye pigments, refining of petroleum, manufacturing of glass and ceramic, and the synthesis of H_2SO_4.[1,3,4,6,10] The extensive use of inorganic arsenic compounds (e.g. zinc arsenite, zinc arsenate, sodium arsenate, and lead arsenate) for agricultural purposes and wood preservation industry as fungicides, herbicides, and insecticides is another important route for contaminating the environment with arsenic.[1,3,4,6,10-12] Uncontrolled discharging of arsenic-bearing industrial waste, in addition, substantially contribute to the pollution of the environment with arsenic and is responsible for a large part of arsenic calamity in the industrial countries.[1,6,9-11]

Arsenic is harmful and causes multiple and serious hygienic problems,[1-3,6,8] which cause it to be rated among the twenty most toxic materials by the US Agency for Toxic Substances and Disease Registry (ATSDR).[10,13] It prevents repairing DNA, for example.[1]

It is also biologically accumulated[13] and carcinogenic and may cause lung, bladder, and liver cancer.[1,3] Many of arsenic compounds are toxic.[1] The inorganic ones, however, are more hazardous than the organic ones.[1,11,17] Moreover, arsenite $[As^{III}O_3]^{3-}$ compounds are more toxic than those of arsenate $[As^{V}O_4]^{3-}$ compounds.[3,8,12, 16] The latter anion of arsenate is molecularly analogous to phosphate anion $[P^{V}O_4]^{3-}$ and thus has the ability to replace it in a variety of biochemical cell reactions. For instance, it uncouples oxidative phosphorylation, preventing the conservation of the high energy bonds of adenosine triphosphate (ATP) and consequently reducing the life term of the most important energy-producing system. Inorganic and organic As^{III} compounds, on the other hand, are capable of inhibiting the activity of proteins, containing thiol (sulfhydryl) functional groups.[1,5,14] Arsenic compounds may cause chronic and acute poisoning, depending on the compound, the arsenic uptake, the duration of exposure, and the individual's sensitivity.[1,10,11,13] Due to this highly dangerous nature of arsenic and its compounds, arsenic remediation has become an internationally important research field in order to properly manage water resources and reduce or eliminate the costs of the treatment of water used for human consumption and irrigation. Therefore, numerous technologies of microbiological and chemical bases have been employed for arsenic removal from aqueous media. Bacteria, co-precipitation, adsorption to various solids, fixed-bed filters, anion exchange, electrocoagulation, membrane filtration by ultrafiltration, nanofiltration or reverse osmosis, and electrodialysis are among the most important techniques applied for the attainment of this target.[4,6,9-11,13,15] Development of potent, safe, inexpensive, readily operated, and easy-to-handle methods that can be adopted either at large industrial scale or household level applications is required.[2,11,13-15] Moreover, the search for the

optimum conditions of purifying water and the environment from arsenic and its compounds is the subject matter of great interest to environmentalists in the different fields of chemistry, physics, biology, geology, ecology, and soil science.

Arsenic exists in the natural waters as inorganic species in the trivalent (3-) oxidation state (arsine), the zero valent oxidation state (elemental arsenic), the trivalent (3+) oxidation state (arsenite), or the pentavalent (5+) oxidation state (arsenate), depending on the pH value, the reduction-oxidation conditions, and the presence of complexing ions.[1,2,5,6,9,14,16] The latter oxidation state is predominant under aerobic (oxic or oxidizing) conditions and thus, is more likely to occur in surface waters.[2,5,6,11,14,16] The (3+) oxidation state, on the other hand, is found in groundwaters where anaerobic (anoxic or reducing) conditions prevail.[2,5,6,10,11,14,16] It has been demonstrated that arsenate is much easily removed than the arsenite.[5-7,9,14,15] Thus, a pre-oxidation of As^{3+} to As^{5+} is an essential treatment towards the complete removal of arsenic or at least the reduction of its concentration to 10 ppb, the allowed maximum contaminant level (MCL) in drinking water recommended by the world health organization (WHO) and the united states environmental protection agency (US EPA).[1-4,6,8-11,13-16,18-21] Oxidation of As^{3+} to As^{5+}, furthermore, will assist the reduction of arsenic toxicity and mobility.[1,5,6,8,12,16,18] The oxidation of As^{3+} has been reported to be accomplished by several oxidants such as ozone,[2,8,13-15,21] chlorine,[2,6,13,14,21] bleaching powder,[2] chlorine dioxide,[21] sodium chlorite,[7,21] manganese dioxide,[2,8,14,15,18,21] potassium permanganate,[2,6,7,14,15,21] potassium ferrate,[8,22] hydrogen peroxide,[8,13-15] Fenton's reagent (H_2O_2 + Fe^{2+} salt as a catalyst),[11,15] monochloramine,[21] natural clays (e.g. kaolin and illite),[18] anatase phase of titanium oxide,[18] and UV irradiation at 254 nm.[15,21] The effectiveness of these oxidants and the

optimization of the conditions for the oxidation of As^{3+} to As^{5+} have been investigated in detail. Several kinds of bacteria for the oxidation of arsenite to arsenate have been recently reported.[12-15]

Remediation of arsenic by a co-precipitation technique is cheap and highly effective for removing arsenate.[2-4,6,8,11,15,22] However, the success of this process in purifying groundwater depends on the pH and the absence of other species such as silicate, orthophosphate, sulfate, and natural organic matter.[7,15,23] Arsenic in this method is usually co-precipitated with ferric hydroxide, where the source of ferric cations is ferric chloride, which is inexpensive, readily available, easily handled, and not hazardous.[2,13,15] Alum (hydrated aluminum sulfate) has been applied for the coagulation of arsenic because of its cheapness, availability, and safe usage. However, alum is less efficient than ferric chloride in removing arsenic and is more pH dependent.[2] Aluminum phosphate, in addition, has been used instead of $FeCl_3$. However, aluminum phosphate is generally less effective in removing arsenic, and the co-precipitation process in this case depends strongly upon the pH parameter.[15] Vogels and Johnson have reported the co-use of ferrous (Fe2+) and ferrate (Fe6+) and the use of ferrate by itself to remove As5+ or As3+, which is oxidized to As5+ by the quick action of ferrate, as ferric arsenate (FeAsO4) precipitate. This method has been shown to be cheap and effective for arsenic remediation from drinking waters.[22] Recently, Yoon *et al.* have investigated the oxidation of As^{3+} by ferrate, explored its kinetics and mechanism over a pH range of 8.4-12.9, studied the effect of carbonate anion on the oxidation process, investigated the removal of arsenic from river water by using only ferrate anion which worked as an oxidizing agent, and examined the subsequent coagulation of As^{5+} by the action of ferric

cations resulted from the reduction of the ferrate anions. They also combined small amounts of ferrate anions with ferric cations as the major coagulant for the removal of arsenic from the river water in order to compare the efficiency in both situations. Excellent results were obtained by this procedure in the sense of reducing the concentration of arsenic from 517 ppb to 50 ppb.[8] Arsenic (As^{3+} or As^{5+}) removal has also been improved using ferrous ions instead of ferric ions, where the former ions are subjected to oxidation by dissolved oxygen leading to partial oxidation of As^{3+}. The hydrous ferric oxide (HFO) formed by the oxidation of ferrous ions has displayed a higher adsorption capacity of arsenic than that one formed directly from ferric ions. Phosphate and silicate compete with arsenate on the sorption sites on the surface of HFO causing a decrease on the amount of arsenic removed. However, phosphate competes strongly with arsenate and is mainly responsible for reducing the arsenic adsorbed.[7] Fenton's reagent in the natural pH range of water (6.8-7.1) has also been found to be effective for both oxidizing As^{3+} and removing As^{5+} formed from the oxidation process as a precipitate along with the ferric cations which resulted from the oxidation of ferrous cations by hydrogen peroxide (the Fenton's reaction). Replacing hydrogen peroxide in the Fenton's reagent with chlorine water (as NaOCl solution, 4% available chlorine) was also shown to be effective for arsenic remediation. However, a disadvantage of this method is that the residual chlorine concentration is higher than the allowed level for potable water.[11] Co-precipitation for arsenic removal has also been performed using MnO_2, $Mg(OH)_2$, and $CaCO_3$.[15] The first reagent has been shown to be effective under neutral condition. The second substance has the ability to remove arsenic up to 100% in the pH range of 11.0-11.5 because at higher [OH^-] the hydroxide anions compete with

arsenic anions for adsorption sites. Moreover, carbonate anions have been shown also to reduce the ability of $Mg(OH)_2$ to remove arsenic. The third reagent removed arsenic much better upon the addition of a small amount of ferric cations to the aqueous medium.[15]

Adsorption is another inexpensive method that has been widely applied for arsenic remediation in groundwater. One successful form of this technique is the fixed-bed filters, which have proved their potential for the arsenic removal. Moreover, they have many attractive features including simplicity of operation, feasibility for small scale requirements, cost-effectiveness, and lowness of maintenance tasks. Furthermore, using adsorbents having high capacities of adsorption reduces the amount of residuals and eliminates dosing of chemicals.[15] For example, ferric hydroxide containing β-FeOOH, known as GEH®, has been extensively used for arsenic removal in the drinking water industry in Germany because a small period of time ranged from 3-10 minutes is required for water treatment with treatment capacities up to 250,000 bed volumes. However, the presence of phosphate anion and dissolved organic matter reduces the amount of the arsenic adsorbed by GEH®.[19] Sand coated with iron oxide, as another example, has also been found to remove arsenic effectively.[15] Iron metal has also been tested in packed columns or batch reactor designs for arsenic remediation.[4,10,11,15,23] It has been shown that this method is twice as effective for As^{5+} removal in comparison of As^{3+} removal.[15] This method has the advantage of cheapness and efficiency for the purification of contaminated water with arsenic.[15] *In situ* formation of iron hydroxide and by corrosion of fine wool of iron in oxygenated water has also been shown to be effective for arsenic removal.[15] The arsenic remediation takes place by the adsorption of arsenic on the

surface of iron hydroxide formed by the corrosion process.[15] Peerless iron has recently been shown to be effective for arsenic remediation in a permeable reactive barrier (PRB) whether in batches or packed in columns. The effectiveness of this method has been investigated in the absence and presence of competitive ions of phosphate and silicate. Again, corrosion of iron metal to form iron oxides and hydroxides is responsible for the sorption of arsenic.23 Arunachalam *et al.*[11] have recently improved a simple, practical procedure for arsenic remediation in the natural pH of water based on the treatment of arsenic-containing water with Fenton's reagent, followed by passing water through a column filled with iron metal scrap and then through a sand bed. This treatment procedure has the advantage over just using only Fenton's reagent for arsenic removal in that it reduces the arsenic concentration below 10 ppb, the MCL. Activated alumina has also been utilized for remediation of arsenic.[15,16] The process in this case is pH dependent and negatively influenced by the presence of Cl^-, F^-, SO_4^{2-}, and PO_4^{3-}. A drawback of using activated alumina is that it has an ill-defined pore structure, has low adsorption capacity, adsorbs arsenic slowly from a kinetic standpoint, needs to be regenerated, and the regenerate needs to be treated and disposed. Mesoporous alumina has recently been proved to have much higher capacity for arsenic adsorption and remediate arsenic in much less time comparing to activated alumina. This superiority of mesoporous alumina in arsenic remediation is mainly attributed to its pore size uniformity and its interlinked pore system.[16]

As a contributing attempt towards the improvement of cost-effective arsenic remediation based on the adsorption technique and the search for an excellent sorbent for arsenic, nanocrystalline Fe_2O_3, Co3O4, and ZnO obtained from the low temperature

thermal decomposition of their corresponding pyruvic acid oxime (PAO) complexes [$M(PAO)_2 \cdot 2H_2O$ ($M = Fe^{2+}$, Co^{2+},or Zn^{2+})] have been investigated in this research work. Excellent, promising results for As^{5+} removal from aqueous medium, at room temperature at the natural pH of water, were obtained. The Fe_2O_3 obtained at 285°C, which consists of two ferric oxide [maghemite (γ-Fe_2O_3) and hematite (α-Fe_2O_3)] as indicated by the XRD investigation (see Chapter 2), was found to have a higher arsenic sorption capacity than that of the Fe_2O_3 obtained at 463°C, composed only of hematite as revealed by XRD (see Chapter 2), although the former has a smaller specific surface area ($65 m^2/g$) than the latter one ($140 m^2/g$). It seemed that surface properties (surface area, acidity, and basicity) and the iron oxide phase present in the sorbent were the critical factors in determining the capability of arsenic uptake.

7.2. EXPERIMENTAL

Sodium arsenate heptahydrate [$Na_2HAsO_4 \cdot 7H_2O$, ACS reagent (GFS Chemicals, Inc.)], phenol [C6H5OH (EM Science)], cyclohexylamine [C6H11NH2 (Aldrich)], and cyclohexane [C6H12, reagent grade (Fisher Scientific)] were commercial and used-as-received without further purification. Fe_2O_3 was obtained at two different decomposition steps (285°C and 463°C), according to the thermogram resulted from the TGA study, after the pyrolysis of $Fe(PAO)_2 \cdot 2H_2O$, as described previously in Chapter 2. The equilibrium concentration of arsenic was determined using a water analysis test kit (EM Science, Gibbstown, NJ, USA).

A series of 50-ml, standard, aqueous solutions of As^{5+}, varying in their concentrations by increment of 3 ppm, was prepared by consecutive dilution from a 1-L stock solution of 30 ppm As^{5+}. The latter was obtained by dilution from a stock solution of 300 ppm As^{5+}.

This solution was prepared by dissolving 1.249 g of $Na_2HAsO_4 \cdot 7H2O$ in 1-L of water. A 10-ml (~ 10 g) sample of the arsenate solution was rotated using rotator machine at a rate of 55 rpm with 0.1 g of the synthesized transition metal oxide for 7 hours. After this time, the mixture was filtered off through a 0.20 μm, disposable membrane filter for the determination of the arsenic concentration in the filtrate using the EM science test kit. To gain an insight on the arsenic sorption, a Langmuir sorption isotherm, $C/X = C/M + 1/KM$, was developed. C is the equilibrium concentration of arsenic expressed in mg/L (ppm), X is the amount of arsenic sorbed in mg per kg of sorbent, M is the maximum amount of arsenic in mg sorbed by one kg of the sorbent, and K is a constant related to the affinity of the sorbent for the sorbate (arsenic in this situation). M and K are determined from the slope and the intercept, respectively, of plotting C/X against C. The value of K is physically and/or chemically meaningless regarding the forces that are responsible of sorption process. On the other hand, the magnitude of M is beneficial in this regard, as it is reflected by the above definition of M.

Acidity and Basicity Measurements

The acidity and basicity of Fe_2O_3 obtained at 463^{o}C were measured by adsorption of cyclohexylamine and phenol from cyclohexane, respectively, according to the procedure outlined in Chapter 2.

7.3. RESULTS AND DISCUSSION

The Langmuir acidity and basicity adsorption isotherms of iron oxide resulting from the thermal decomposition of $Fe(PAO)_2 \cdot 2H_2O$ at 463°C are displayed in Figure 7.1.

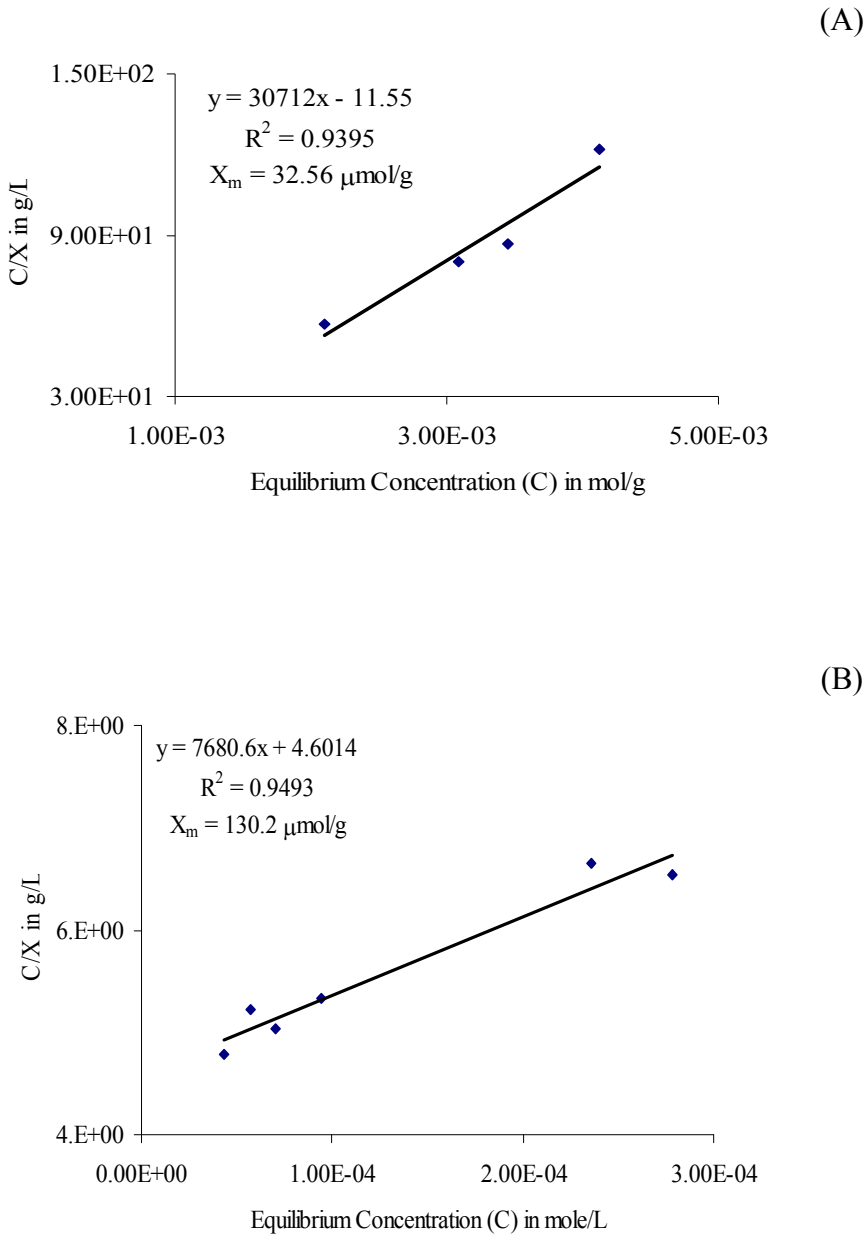

Figure 7.1. Langmuir adsorption isotherm of (A) acidity and (B) basicity of Fe_2O_3 obtained upon pyrolysis of $Fe(PAO)_2 \cdot 2H_2O$ at 463°C

These two surface properties of iron oxide were discussed in detail in Chapter 2. While the population of the basic sites is predominant on the surface, acidic sites (Lewis and/or Brønsted) are present on the surface and provide the necessary sites for the adsorption process of the negatively-charged, basic arsenate species from the aqueous medium to take place. These acidic sites should be mainly responsible for the affinity of the iron oxide for arsenate and play a significant role in creating attracting forces that facilitate the sorption process.

Separate treatment of each solution of the standard, aqueous arsenate solutions having the concentrations of 3, 6, 9, 12, …, 30 ppm with 0.1 g of nanoparticulate $Fe(PAO)_2{\cdot}2H_2O$-derived iron oxide (resulted from firing $Fe(PAO)_2{\cdot}2H_2O$ at 285 ^oC) at room temperature at the natural pH of water for a period of time lasting for 7 hours led to arsenic-free water depending on the initial concentration of arsenate $[AsO_4^{3-}]_0$ used. Examination of the Langmuir sorption isotherm was found to adequately correlate with the equilibrium curve of the sorption of this iron oxide for arsenate removal (the correlation coefficient, $R^2 = 0.99122$) from the aqueous medium (Figure 7.2).

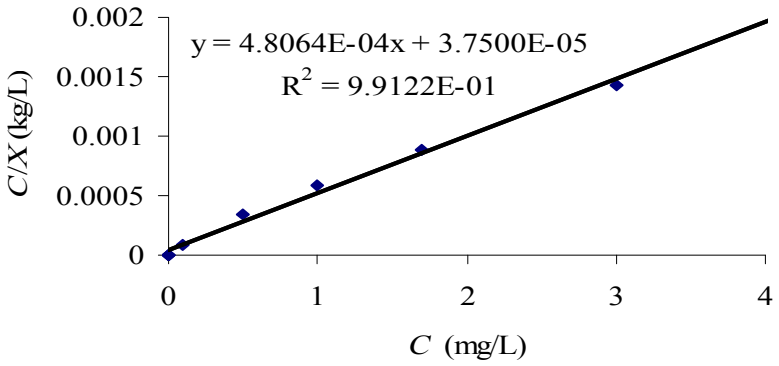

Figure 7.2. Langmuir sorption isotherm for arsenate by iron oxide obtained at 285^{o}C

The maximum arsenate sorption capacity (*M*) had a value of 2080.56 mg/kg. This *M* value is much higher than those reported for arsenate uptake by sand/Peerless iron system,[23] ferric-loaded Dowex 650C resin-derived hematite,[24] ferrihydrite,[25] and iron oxide-coated sand[25] (380,[23] 303,[24] 285,[25] and 18.3[25] mg/kg, respectively). However, it is beneath the capacity of those ferric-treated activated carbon,[15] copper-treated activated carbon,[15] granular activated alumina,[16] and mesoporous alumina[16] (4530,[15] 5790,[15] 16000, [16] and 121000[16] mg/kg, respectively). This relative high arsenate capacity for the iron oxide obtained at 285°C may be attributed to the existence of the γ-Fe_2O_3, its ferromagnetism, and the acidity and basicity properties of the surface.

Iron oxide prepared from the pyrolysis of $Fe(PAO)_2 \cdot 2H2O$ at 436°C was found to have a smaller arsenic adsorption capacity (846.17 mg/kg) than that of the iron oxide obtained at 285°C under the same experimental conditions mentioned above. Plotting ***C/X*** versus the equilibrium concentration of arsenate gave a linear relationship, implying the compliance of the sorption process with Langmuir isotherm, as shown in Figure 7.3.

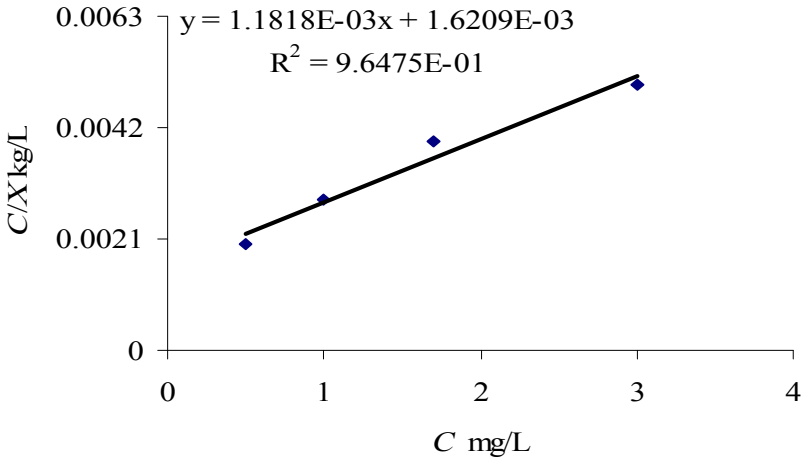

Figure 7.3. Langmuir sorption isotherm for arsenate by iron oxide obtained at 463°C

The lower capacity of this iron oxide for arsenate can be ascribed to the presence of the paramagnetic α-Fe_2O_3, which is less magnetic than the γ-Fe_2O_3, and the predominance of the basic sites on the surface, which may have repulsive interaction with the basic arsenate species bearing negative charges.

Zinc oxide prepared from the thermal decomposition of the zinc PAO complex at 389^{o}C showed similar arsenate affinity and sorption capacity to that of the iron oxide obtained at 285^{o}C, as inferred from the following Langmuir sorption isotherm:

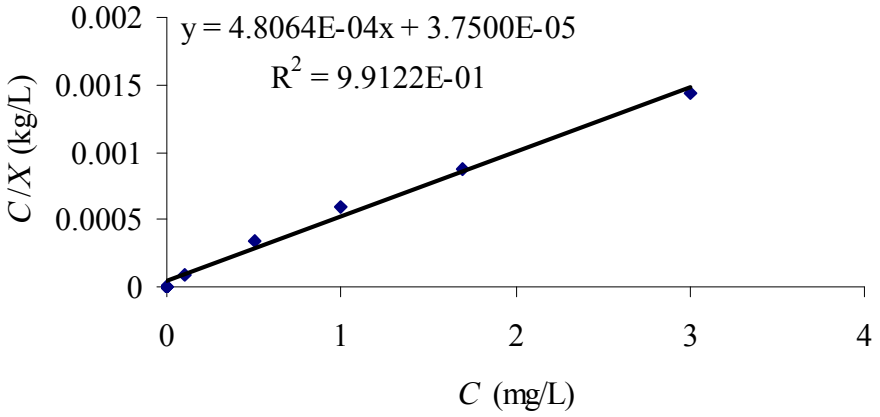

Figure 7.4. Langmuir sorption isotherm for arsenate by zinc oxide obtained at 389^{o}C

This high sorption capability of zinc oxide towards arsenate exceeds the one reported for zinc oxide derived from zinc-loaded cation-exchange resin (985 mg/kg),[26] and can be accounted for the high surface acidity property of this oxide as discussed in detail previously in Chapter 2.

Cobaltocobaltic oxide (Co_3O_4), resulted from the thermal decomposition of cobaltous PAO derivative at 276^{o}C, was also tested for arsenate soption. A capacity of 1423.93 mg/kg was observed for this oxide according to Langmuir sorption isotherm displayed in Figure 7.5. Once again, the relative high affinity of this oxide for arsenate

sorption may be ascribed to dominant acidic sites on the surface as explained in the discussion of the surface acidic and basic properties of this oxide in Chapter 2. It is the first time this oxide is used for such an application because no previous literature has reported this particular use to the best of our knowledge.

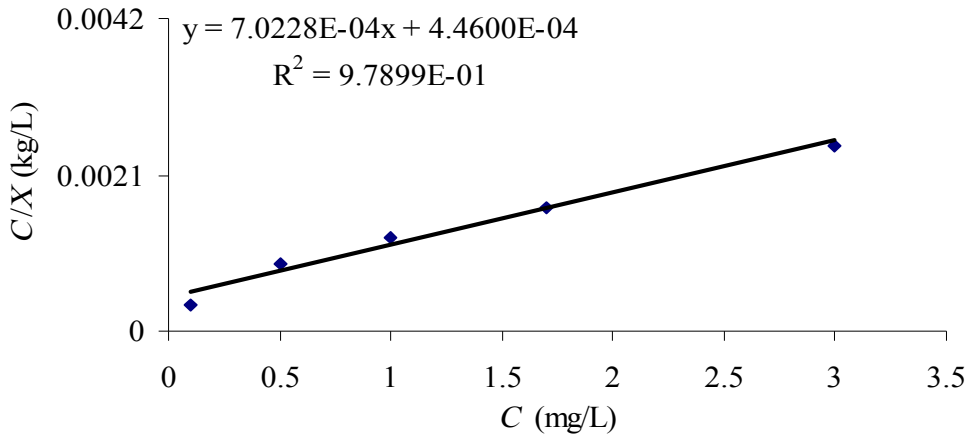

Figure 7.5. Langmuir sorption isotherm for arsenate by Co3O4 obtained at 276°C

The arsenate anion is chemisorbed on the surface of these oxides (Figure 7.6), but it does not react to form crystalline arsenate phases since analysis of these oxides after the adsorption process by XRD does not show any peaks due to the metal arsenate. The only observed peaks are those of the metal oxide itself.

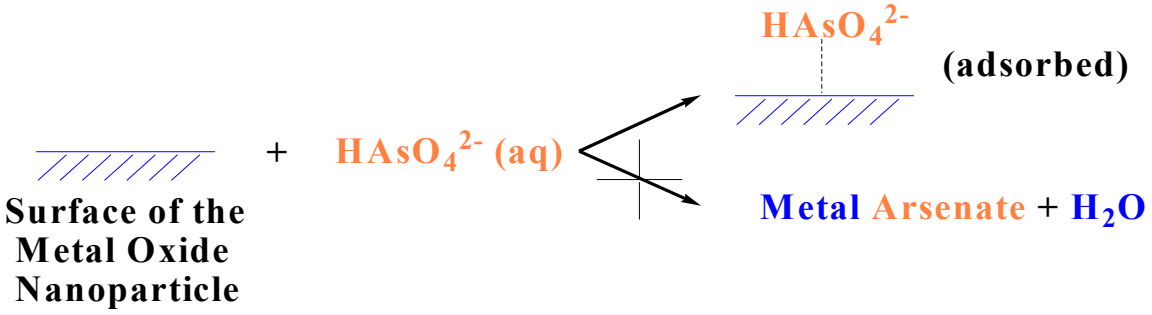

Figure 7.6. The chemisorption of arsenate on the surface of transition metal oxide nanoparticulate

7.4. CONCLUSION

Iron oxide prepared at 285^{o}C, zinc oxide, and Co_3O_4 were thermally derived from their corresponding PAO complexes. All of these oxides had moderate capacities for arsenate sorption that satisfactorily followed the Langmuir sorption isotherm relationship. The relatively high sorption affinities displayed by these oxides were attributed to the high surface acidity of them. The positive charge of the Lewis acid site and/or the proton of the Lowry-Brønsted acid site served as attractive factors and pulled the negatively charged arsenate anion towards the surface of these oxides. On the other hand, the iron oxide obtained at 463^{o}C had more basic sites population on its surface, and thus had a lower affinity for the sorption of arsenate from the aqueous medium due to the predominance of the repulsion interaction between the negative charges or the electron pairs residing on these basic sites and the negative charge of the arsenate anion.

Treatment of the transition metal oxide nanoparticulate with the aqueous solution of arsenate led only to the chemical adsorption of arsenate on the surface of the oxide with no transformation of the metal oxide bulk to the corresponding arsenate, as revealed by an XRD study.

REFERENCES

1. M. Bissen and F. H. Frimmel, "Arsenic- A Review. Part I: Occurrence, Toxicity, Speciation, Mobility", Acta Hydrochim. Hydrobiol., **2003**, 31(1), 9-18.
2. M. M. T. Khan, K. Yamamoto, and M. F. Ahmed, "A Low Cost Technique of Arsenic Removal from Drinking Water by Coagulation Using Ferric Chloride Salt and Alum", Water Sci. Technol.: Water Supply, **2002**, 2(2), 281-288.
3. M. C. F. Magalhães, "Arsenic. An Environmental Problem Limited by Solubility", Pure Appl. Chem., **2002**, 74(10), 1843-1850.

4. J. A. Lackovic, N. P. Nikolaidis, and G. M. Dobbs, "Innovative Arsenic Remidiation Technology (AsRT) for Ground Water, Drinking Water, and Waste Streams", Hazardous and Industrial Waste, **1998**, 30, 604-613.

5. R. S. Oremland and J. F. Stolz, "The Ecology of Arsenic", Science, **2003**, 300, 939-944.

6. M. Misra and P. Lenz, "Removal of Arsenic from Drinking and Process Water" US Patent WO 03/086564 A2, October 23, 2003.

7. L. C. Roberts, S. J. Hug, T. Ruettimann, A. W. Khan, and M. T. Rahman, "Arsenic Removal with Iron(II) and Iron(III) in Waters with High Silicate and Phosphate Concentrations", Environ. Sci. Technol., **2004**, 38, 307-315.

8. Y. Lee, I. Um, and J. Yoon, "Arsenic(III) Oxidation by Iron(VI) (Ferrate) and Subsequent Removal of Arsenic(V) by Iron(III) Coagulation", Environ. Sci. Technol., **2003**, 37 (24), 5750-5756.

9. S. Chakravarty, V. Dureja, G. Bhattacharyya, S. Maity, and S. Bhattacharjee, "Removal of Arsenic from Groundwater Using Low Cost Ferruginous Manganese Ore", Water Res., **2002**, 36, 625-632.

10. B. A. Manning, M. L. Hunt, C. Amrhein, and J. A. Yarmoff, "Arsenic(III) and Arsenic(V) Reactions with Zerovalent Iron Corrosion Products", Environ. Sci. Technol., **2002**, 36 (24), 5455-5461.

11. M. V. B. Krishna, K. Chandrasekaran, D. Karunasagar, and J. Arunachalam, "A Combined Treatment Approach Using Fenton's Reagent and Zero Valent Iron for the Removal of Arsenic from Drinking Water", J. Haz. Mat., **2001**, B84, 229-240.

12. W. Weeger, D. Lievremont, M. Perret, F. Lagarde, J. Hubert, M. Leroy, and M. Lett, "Oxidation of Arsenite to Arsenate by a Bacterium Isolated from an Aquatic Environment", BioMetals, **1999**, 12, 141-149.

13. S. A. Mokashi and K. M. Paknikar, "Arsenic (III) Oxidizing Microbacterium Lacticum and Its Use in the Treatment of Arsenic Contaminated Groundwater", Lett. Appl. Microbio., **2002**, 34 (4), 258-262.

14. I. A. Katsoyiannis and A. I. Zouboulis, "Application of Biological Processes for the Removal of Arsenic from Groundwaters", Water Res., **2004**, 38 (1), 17-26.

15. M. Bissen and F. H. Frimmel, "Arsenic- A Review. Part II: Oxidation of Arsenic and its Removal in Water Treatement", Acta Hydrochim. Hydrobiol., **2003**, 31(2), 97-107.

16. Y. Kim, C. Kim, I. Choi, S. Rengaraj, and J. Yi, "Arsenic Removal Using Mesoporous Alumina Prepared via a Templating Method", Environ. Sci. Technol., **2004**, 38, 924-931.

17. R. Pongratz, “Arsenic Speciation in Environmental Samples of Contaminated Soil”, Sci Total Environ., **1998**, 224, 133-141.

18. A. L. Foster, G. E. Brown, and G. A. Parks, “X-ray Absorption Fine-Structure Spectroscopy Study of Photocatalyzed, Heterogeneous As(III) Oxidation on Kaolin and Anatase”, Environ. Sci. Technol., **1998**, 32, 1444-1452.

19. W. Driehaus, “Arsenic Removal-Experience with the GEH® Process in Germany”, Water Sci. Technol.: Water Supply, **2002**, 2(2), 275-280.

20. A. H. Smith, P. A. Lopipero, M. N. Bates, and C. M. Steinmaus, “Arsenic Epidemiology and Drinking Water Standards”, Science, **2002**, 296, 2145-2146.

21. G. Ghurye and D. Clifford, “Laboratory Study on the Oxidation of Arsenic III to Arsenic V”, US Environmental Protection Agency: Cincinnati, OH, **2001.**

22. C. M. Vogels and M. D. Johnson, “Arsenic Remediation in Drinking Waters Using Ferrate and Ferrous Ions”; WRRI Technical Completion Report No. 307; New Mexico Water Resources Research Institute: Las Cruces, NM, **1998**.

23. C. Su and R. W. Puls, “In Situ Remediation of Arsenic in Simulated Groundwater Using Zerovalent Iron: Laboratory Column Tests on Combined Effects of Phosphate and Silicate”, Environ. Sci. Technol., **2003**, 37, 2582-2587.

24. A. W. Apblett, S. I. Kuriyavar, and B. P. Kiran, “Preparation of Micron-sized Spherical Porous Iron Oxide Particles”, J. Mater. Chem., **2003**, 13, 983-985.

25. O.S. Thirunavukkarasu, T. Viraraghavan, and K. S. Subramanian, “Removal of Arsenic in Drinking Water by Iron Oxide-Coated Sand and Ferrihydrite - Batch Studies”, Water Qual. Res. J. Can., **2001**, 36(1), 55-70.

26. S. Kuriyavar and A. Apblett, “Arsenic Remediation with Aggregates of Nanoparticulate Zinc Oxide”, Abstracts of Papers, 59th Southwest Regional Meeting of the American Chemical Society, Oklahoma City, OK, Oct 25-28, American Chemical Society: Washington, DC, **2003**; 182.

APPENDICES

APPENDIX A

CRYSTALLOGRAPHIC DATA

Table A 1. Atomic coordinatates (x 10^4) and equivalent isotopic displacement coefficients ($Å^2$ x 10^3) for $Mg(PAO)_2(H_2O)_3 \cdot 2H_2O$

	x	y	z	U(eq)
Mg(1)	2909(1)	4881(1)	2708(1)	26(1)
O(1)	5094(2)	6623(1)	4113(1)	33(1)
O(2)	7145(2)	8766(2)	4527(1)	40(1)
C(1)	5906(2)	7627(2)	3742(2)	28(1)
C(2)	5337(2)	7410(2)	2238(2)	27(1)
C(3)	6247(2)	8497(2)	1696(2)	38(1)
N(4)	4022(2)	6227(2)	1542(1)	27(1)
O(4)	3426(2)	6011(2)	177(1)	35(1)
O(91)	879(2)	3277(2)	1154(1)	38(1)
O(92)	800(2)	3586(2)	-839(1)	38(1)
C(91)	263(2)	2881(2)	-121(2)	29(1)
C(92)	-1219(2)	1411(2)	-819(2)	28(1)
C(93)	-2088(3)	705(3)	52(2)	42(1)
N(94)	-1549(2)	872(2)	-2135(1)	31(1)
O(94)	-2915(2)	-498(2)	-2742(1)	40(1)
O(21)	4452(2)	3271(2)	2309(2)	44(1)
O(22)	2376(2)	4176(2)	4273(1)	35(1)
O(23)	999(2)	6149(2)	3101(1)	35(1)
O(31)	1853(2)	6283(2)	6636(2)	48(1)
O(32)	934(2)	8451(2)	5511(2)	46(1)

U(eq) is defined as one third of the trace of the orthogonalized U_{ij} tensor.

Table A 2. Anisotropic displacement coefficients ($Å^2$ x 10^3) for $Mg(PAO)_2(H_2O)_3 \cdot 2H_2O$

	U_{11}	U_{22}	U_{33}	U_{12}	U_{13}	U_{23}
Mg(1)	27(1)	27(1)	22(1)	2(1)	-2(1)	12(1)
O(1)	35(1)	34(1)	26(1)	-1(1)	-4(1)	16(1)
O(2)	45(1)	35(1)	28(1)	-8(1)	-4(1)	11(1)
C(1)	28(1)	30(1)	26(1)	4(1)	-1(1)	11(1)
C(2)	27(1)	29(1)	25(1)	5(1)	2(1)	12(1)
C(3)	37(1)	41(1)	34(1)	-4(1)	3(1)	18(1)
N(4)	30(1)	30(1)	21(1)	4(1)	0(1)	11(1)
O(4)	40(1)	38(1)	22(1)	-2(1)	-2(1)	13(1)
O(91)	41(1)	36(1)	27(1)	0(1)	-9(1)	11(1)
O(92)	40(1)	33(1)	32(1)	-3(1)	-6(1)	14(1)
C(91)	30(1)	24(1)	28(1)	7(1)	-3(1)	9(1)
C(92)	29(1)	25(1)	26(1)	4(1)	-1(1)	9(1)
C(93)	49(1)	40(1)	31(1)	-2(1)	3(1)	15(1)
N(94)	33(1)	25(1)	27(1)	-1(1)	-2(1)	8(1)
O(94)	48(1)	31(1)	26(1)	-9(1)	-1(1)	4(1)
O(21)	35(1)	38(1)	54(1)	9(1)	4(1)	14(1)
O(22)	38(1)	42(1)	31(1)	10(1)	2(1)	22(1)
O(23)	43(1)	39(1)	28(1)	16(1)	4(1)	17(1)
O(31)	37(1)	62(1)	49(1)	14(1)	11(1)	24(1)
O(32)	43(1)	35(1)	55(1)	5(1)	8(1)	15(1)

The anistropic displacement exponent takes the form: $-2\pi^2(h^2a^{*2}U_{11} + \ldots + 2hka^*b^*U_{12})$

Table A 3. H-Atoms coordination (x 10^4) and isotropic displacement coefficients ($Å^2$ x 10^3) for $Mg(PAO)_2(H_2O)_3 \cdot 2H_2O$

	x	y	z	U
H(3A)	5723	8196	739	80
H(3B)	6102	9497	2172	80
H(3C)	7513	8506	1827	80
H(3D)	7283	9058	2036	50
H(3E)	6398	7874	773	50
H(3F)	5587	9376	1723	50
H(4A)	2557	5224	-195	80
H(93A)	-2986	-204	-518	80
H(93B)	-1191	453	624	80
H(93C)	-2654	1412	612	80
H(93D)	-3566	696	-45	50
H(93E)	-1820	-373	-272	50
H(93F)	-1389	1059	1043	50
H(94B)	-3010	-830	-3601	80
H(21B)	3692	2440	2260	50
H(21A)	5546	3561	2449	50
H(22A)	3136	3869	4625	50
H(22B)	2063	4807	4968	50
H(23A)	1146	6841	3775	50
H(23B)	744	6380	2565	50
H(31A)	1698	7050	6509	50
H(31B)	915	5840	6765	50
H(32A)	1513	9278	5590	50
H(32B)	-238	8494	5390	50

Table A 4. Atomic coordinates (x 10^4) and equivalent isotropic displacement parameters ($Å^2$ x 10^3) for $Zn(PAO)_2 \cdot 2H_2O$

	x	y	z	U(eq)
Zn(1)	5000	5000	5000	9(1)
O(1)	8774(2)	5372(2)	1961(1)	12(1)
O(2)	3269(2)	408(2)	2555(1)	13(1)
O(3)	3355(2)	2546(2)	4392(1)	11(1)
O(4)	8733(2)	2654(2)	6082(1)	10(1)
N(1)	6939(3)	4377(2)	2819(1)	9(1)
C(1)	6918(3)	2244(2)	642(2)	14(1)
C(2)	6099(3)	2938(2)	2163(2)	10(1)
C(3)	4070(3)	1863(2)	3106(2)	10(1)

U(eq) is defined as one third of the trace of the orthogonalized U_{ij} tensor.

Table A 5. Anisotropic displacement parameters ($Å^2$ x 10^3) for $Zn(PAO)_2 \cdot 2H_2O$

	U_{11}	U_{22}	U_{33}	U_{23}	U_{13}	U_{12}
Zn(1)	9(1)	11(1)	7(1)	-2(1)	-1(1)	-5(1)
O(1)	12(1)	16(1)	11(1)	-1(1)	1(1)	-10(1)
O(2)	17(1)	14(1)	12(1)	-2(1)	-1(1)	-9(1)
O(3)	12(1)	14(1)	9(1)	-3(1)	0(1)	-6(1)
O(4)	10(1)	12(1)	11(1)	1(1)	0(1)	4(1)
N(1)	8(1)	12(1)	7(1)	1(1)	0(1)	-4(1)
C(1)	17(1)	17(1)	11(1)	4(1)	1(1)	9(1)
C(2)	8(1)	11(1)	10(1)	0(1)	1(1)	2(1)
C(3)	9(1)	10(1)	11(1)	0(1)	3(1)	2(1)

The anisotropic displacement factor exponent takes the form: $-2\pi^2[h^2 a^{*2} U_{11} + ... + 2 h k a^* b^* U_{12}]$

Table A 6. Hydrogen coordinates (x 10^4) and isotropic displacement parameters ($Å^2$ x 10^3) for $Zn(PAO)_2 \cdot 2H_2O$

	x	y	z	U(eq)
H(1)	9592	6066	2562	18
H(4D)	10093	2218	5411	16
H(4E)	8190	1571	6556	16
H(1A)	8392	2958	227	21
H(1B)	5159	2642	-1	21
H(1C)	7744	671	694	21

Table A 7. Torsion angles [°] for $Zn(PAO)_2 \cdot 2H_2O$

O(3)#1-Zn(1)-O(3)-C(3)	52(100)
N(1)#1-Zn(1)-O(3)-C(3)	178.10(10)
N(1)-Zn(1)-O(3)-C(3)	-1.90(10)
O(4)#1-Zn(1)-O(3)-C(3)	87.00(10)
O(4)-Zn(1)-O(3)-C(3)	-93.00(10)
O(3)-Zn(1)-N(1)-C(2)	3.29(10)
O(3)#1-Zn(1)-N(1)-C(2)	-176.71(10)
N(1)#1-Zn(1)-N(1)-C(2)	-77(100)
O(4)#1-Zn(1)-N(1)-C(2)	-86.90(10)
O(4)-Zn(1)-N(1)-C(2)	93.10(10)
O(3)-Zn(1)-N(1)-O(1)	178.11(11)
O(3)#1-Zn(1)-N(1)-O(1)	-1.89(11)
N(1)#1-Zn(1)-N(1)-O(1)	98(100)
O(4)#1-Zn(1)-N(1)-O(1)	87.92(11)
O(4)-Zn(1)-N(1)-O(1)	-92.08(11)
O(1)-N(1)-C(2)-C(1)	1.0(2)
Zn(1)-N(1)-C(2)-C(1)	176.76(11)
O(1)-N(1)-C(2)-C(3)	-179.63(10)
Zn(1)-N(1)-C(2)-C(3)	-3.88(14)
Zn(1)-O(3)-C(3)-O(2)	-179.54(11)
Zn(1)-O(3)-C(3)-C(2)	0.50(15)
N(1)-C(2)-C(3)-O(2)	-177.54(13)
C(1)-C(2)-C(3)-O(2)	1.88(19)
N(1)-C(2)-C(3)-O(3)	2.42(18)
C(1)-C(2)-C(3)-O(3)	-178.16(12)

Symmetry transformations used to generate equivalent atoms: #1 -x+1,-y+1,-z+1

Table A 8. Atomic coordinates (x 10^4) and equivalent isotropic displacement parameters (Å^2 x 10^3) for $Pr(PAO)_3(H_2O)_2$

	x	y	z	U(eq)
Pr(1)	2624(1)	3970(1)	3795(1)	12(1)
O(1)	2452(2)	3381(1)	6830(1)	26(1)
O(2)	259(2)	1695(1)	4280(1)	21(1)
O(3)	1512(2)	2692(1)	3561(1)	19(1)
O(4)	752(2)	5718(1)	3010(1)	27(1)
O(5)	2520(1)	5595(1)	6857(1)	22(1)
O(6)	2824(2)	4631(1)	5674(1)	22(1)
O(7)	5072(2)	2863(1)	1576(1)	24(1)
O(8)	2448(2)	4903(1)	137(1)	25(1)
O(9)	1684(2)	4508(1)	1919(1)	21(1)
O(10)	5082(2)	4813(1)	3420(1)	20(1)
O(11)	-664(2)	3996(1)	3945(1)	21(1)
N(1)	2018(2)	3158(1)	5703(1)	19(1)
N(2)	1465(2)	5346(1)	3942(1)	18(1)
N(3)	4009(2)	3459(1)	1738(1)	18(1)
C(1)	1742(3)	1936(1)	6594(2)	34(1)
C(2)	1672(2)	2477(1)	5623(2)	19(1)
C(3)	1117(2)	2267(1)	4394(2)	17(1)

U(eq) is defined as one third of the trace of the orthogonalized U_{ij} tensor.

Table A 9. Anisotropic displacement parameters ($Å^2$ x 10^3) for $Pr(PAO)_3(H_2O)_2$

	U_{11}	U_{22}	U_{33}	U_{23}	U_{13}	U_{12}
Pr(1)	14(1)	10(1)	11(1)	0(1)	-1(1)	1(1)
O(1)	43(1)	23(1)	12(1)	-3(1)	-5(1)	-4(1)
O(2)	20(1)	17(1)	26(1)	0(1)	-2(1)	-6(1)
O(3)	25(1)	15(1)	17(1)	-1(1)	-1(1)	-4(1)
O(4)	39(1)	20(1)	23(1)	5(1)	-5(1)	8(1)
O(5)	23(1)	23(1)	20(1)	-7(1)	-2(1)	2(1)
O(6)	36(1)	14(1)	17(1)	0(1)	-5(1)	4(1)
O(7)	36(1)	18(1)	19(1)	-2(1)	-3(1)	9(1)
O(8)	22(1)	30(1)	21(1)	9(1)	1(1)	3(1)
O(9)	19(1)	25(1)	17(1)	1(1)	0(1)	2(1)
O(10)	17(1)	22(1)	22(1)	-2(1)	0(1)	-2(1)
O(11)	16(1)	23(1)	23(1)	-2(1)	0(1)	4(1)
N(1)	23(1)	20(1)	13(1)	-1(1)	-3(1)	-1(1)
N(2)	19(1)	17(1)	20(1)	4(1)	-1(1)	1(1)
N(3)	19(1)	15(1)	18(1)	-2(1)	-1(1)	0(1)
C(1)	47(1)	28(1)	27(1)	11(1)	-10(1)	-11(1)
C(2)	19(1)	20(1)	19(1)	4(1)	-1(1)	-4(1)
C(3)	15(1)	17(1)	21(1)	-1(1)	-2(1)	1(1)
C(4)	31(1)	16(1)	34(1)	-3(1)	1(1)	4(1)
C(5)	19(1)	14(1)	25(1)	1(1)	3(1)	0(1)
C(6)	15(1)	16(1)	19(1)	-3(1)	2(1)	-1(1)
C(7)	36(1)	24(1)	16(1)	-1(1)	1(1)	1(1)
C(8)	19(1)	19(1)	15(1)	-1(1)	-1(1)	-3(1)
C(9)	15(1)	18(1)	17(1)	0(1)	-4(1)	-2(1)

The anisotropic displacement factor exponent takes the form: $-2\pi^2[h^2 a^{*2} U_{11} + ... + 2 h k a^* b^* U_{12}]$

Table A 10. Hydrogen coordinates (x 10^4) and isotropic displacement parameters ($Å^2$ x 10^3) for $Pr(PAO)_3(H_2O)_2$

	x	y	z	U(eq)
H(1D)	2682	3829	6826	38
H(4D)	889	5474	2391	41
H(7D)	5449	2720	2230	36
H(10D)	5698(14)	4888(10)	4015(7)	30
H(10E)	5808(13)	4695(11)	2905(9)	30
H(11D)	-1200(18)	4031(10)	3305(7)	31
H(11E)	-1173(18)	4300(7)	4375(12)	31
H(1A)	2953	1873	6850	50
H(1B)	1281	1467	6318	50
H(1C)	1037	2111	7255	50
H(4A)	748	6705	4284	40
H(4B)	2072	6771	5366	40
H(4C)	94	6529	5589	40
H(7A)	4399	3006	-418	38
H(7B)	5039	3815	-724	38
H(7C)	3059	3583	-964	38

Table A 11. Torsion angles [°] for $Pr(PAO)_3(H_2O)_2$

O(2)#1-Pr(1)-O(3)-C(3)	76.60(13)
O(9)-Pr(1)-O(3)-C(3)	-154.16(13)
O(6)-Pr(1)-O(3)-C(3)	-6.67(15)
O(10)-Pr(1)-O(3)-C(3)	118.54(13)
O(11)-Pr(1)-O(3)-C(3)	-82.82(13)
N(1)-Pr(1)-O(3)-C(3)	2.82(12)
N(2)-Pr(1)-O(3)-C(3)	-90.77(14)
N(3)-Pr(1)-O(3)-C(3)	150.93(13)
O(2)#1-Pr(1)-O(6)-C(6)	146.75(14)
O(9)-Pr(1)-O(6)-C(6)	5.06(17)
O(10)-Pr(1)-O(6)-C(6)	73.52(14)
O(3)-Pr(1)-O(6)-C(6)	-134.72(13)
O(11)-Pr(1)-O(6)-C(6)	-67.57(14)
N(1)-Pr(1)-O(6)-C(6)	-143.81(16)
N(2)-Pr(1)-O(6)-C(6)	-1.34(13)
N(3)-Pr(1)-O(6)-C(6)	97.78(16)
O(2)#1-Pr(1)-O(9)-C(9)	4.88(16)
O(6)-Pr(1)-O(9)-C(9)	130.82(14)
O(10)-Pr(1)-O(9)-C(9)	63.15(14)
O(3)-Pr(1)-O(9)-C(9)	-81.74(14)
O(11)-Pr(1)-O(9)-C(9)	-149.64(15)
N(1)-Pr(1)-O(9)-C(9)	-126.85(15)
N(2)-Pr(1)-O(9)-C(9)	136.94(15)
N(3)-Pr(1)-O(9)-C(9)	-17.23(13)
O(2)#1-Pr(1)-N(1)-C(2)	-80.42(14)
O(9)-Pr(1)-N(1)-C(2)	62.49(18)
O(6)-Pr(1)-N(1)-C(2)	-179.27(16)
O(10)-Pr(1)-N(1)-C(2)	-130.10(13)
O(3)-Pr(1)-N(1)-C(2)	9.29(13)
O(11)-Pr(1)-N(1)-C(2)	85.15(14)
N(2)-Pr(1)-N(1)-C(2)	145.18(14)
N(3)-Pr(1)-N(1)-C(2)	-28.92(16)
O(2)#1-Pr(1)-N(1)-O(1)	83.62(13)
O(9)-Pr(1)-N(1)-O(1)	-133.46(12)
O(6)-Pr(1)-N(1)-O(1)	-15.23(11)
O(10)-Pr(1)-N(1)-O(1)	33.94(15)
O(3)-Pr(1)-N(1)-O(1)	173.33(14)
O(11)-Pr(1)-N(1)-O(1)	-110.81(13)
N(2)-Pr(1)-N(1)-O(1)	-50.78(14)
N(3)-Pr(1)-N(1)-O(1)	135.13(12)
O(2)#1-Pr(1)-N(2)-C(5)	-49.18(16)
O(9)-Pr(1)-N(2)-C(5)	-172.11(14)
O(6)-Pr(1)-N(2)-C(5)	2.12(13)
O(10)-Pr(1)-N(2)-C(5)	-84.82(13)

Table A 11 (continued)

O(3)-Pr(1)-N(2)-C(5)	112.24(13)
O(11)-Pr(1)-N(2)-C(5)	104.17(14)
N(1)-Pr(1)-N(2)-C(5)	39.54(14)
N(3)-Pr(1)-N(2)-C(5)	-146.06(13)
O(2)#1-Pr(1)-N(2)-O(4)	128.46(12)
O(9)-Pr(1)-N(2)-O(4)	5.53(11)
O(6)-Pr(1)-N(2)-O(4)	179.75(14)
O(10)-Pr(1)-N(2)-O(4)	92.82(12)
O(3)-Pr(1)-N(2)-O(4)	-70.13(15)
O(11)-Pr(1)-N(2)-O(4)	-78.19(12)
N(1)-Pr(1)-N(2)-O(4)	-142.82(12)
N(3)-Pr(1)-N(2)-O(4)	31.58(13)
O(2)#1-Pr(1)-N(3)-C(8)	-159.18(13)
O(9)-Pr(1)-N(3)-C(8)	3.24(12)
O(6)-Pr(1)-N(3)-C(8)	-106.90(14)
O(10)-Pr(1)-N(3)-C(8)	-82.48(12)
O(3)-Pr(1)-N(3)-C(8)	115.70(13)
O(2)#1-Pr(1)-O(3)-C(3)	76.60(13)

Symmetry transformations used to generate equivalent atoms:
#1 x+1/2,-y+1/2,z #2 x-1/2,-y+1/2,z

Table A 12. Atomic coordinates (x 10^4) and equivalent isotropic displacement parameters ($Å^2$ x 10^3) for $[(H_3C)_4N][Cu(PAO^-)(PAO^{2-})(H_2O)]\cdot H_2O$

	x	y	z	U(eq)
Cu(1)	6258(1)	3176(1)	6850(1)	16(1)
O(1)	5077(1)	2546(2)	7689(1)	20(1)
O(2)	2952(1)	2767(1)	7331(1)	22(1)
O(3)	4553(1)	4249(1)	4265(1)	15(1)
O(4)	7936(1)	2331(2)	8160(1)	23(1)
O(6)	6907(1)	3976(2)	4647(1)	15(1)
O(7)	6584(1)	6451(2)	7624(1)	20(1)
O(8)	10055(1)	2219(2)	8526(1)	40(1)
N(1)	4623(1)	3740(2)	5428(1)	14(1)
N(2)	7360(1)	3481(2)	5885(1)	14(1)
C(1)	3865(1)	2880(2)	6982(1)	16(1)
C(2)	3578(1)	3471(2)	5635(1)	14(1)
C(3)	2211(1)	3639(2)	4692(1)	19(1)
C(4)	8592(1)	3244(3)	6506(1)	15(1)
C(5)	8899(1)	2565(2)	7839(1)	20(1)
C(6)	9629(1)	3470(2)	5992(1)	20(1)
N(3)	12839(1)	7841(2)	8850(1)	16(1)
C(7)	14192(1)	7822(2)	8862(2)	26(1)
C(8)	12598(2)	5939(2)	9415(1)	22(1)
C(9)	11860(1)	8005(3)	7525(1)	26(1)
C(10)	12703(1)	9608(2)	9585(1)	21(1)
O(9)	10826(1)	2813(2)	11101(1)	36(1)

U(eq) is defined as one third of the trace of the orthogonalized U_{ij} tensor.

Table A 13. Anisotropic displacement parameters ($Å^2$ x 10^3) for $[(H_3C)_4N][Cu(PAO^-)(PAO^{2-})(H_2O)]\cdot H_2O$

	U11	U22	U33	U23	U13	U12
Cu(1)	14(1)	25(1)	11(1)	3(1)	6(1)	-1(1)
O(1)	19(1)	28(1)	13(1)	2(1)	8(1)	-3(1)
O(2)	24(1)	22(1)	27(1)	-2(1)	18(1)	-3(1)
O(3)	15(1)	18(1)	11(1)	2(1)	5(1)	-2(1)
O(4)	21(1)	29(1)	16(1)	6(1)	5(1)	1(1)
O(6)	14(1)	21(1)	12(1)	4(1)	6(1)	1(1)
O(7)	21(1)	20(1)	16(1)	3(1)	4(1)	0(1)
O(8)	24(1)	72(1)	21(1)	5(1)	6(1)	24(1)
N(1)	18(1)	12(1)	13(1)	-1(1)	8(1)	-1(1)
N(2)	17(1)	14(1)	12(1)	1(1)	7(1)	-1(1)
C(1)	22(1)	12(1)	18(1)	-4(1)	12(1)	-3(1)
C(2)	16(1)	8(1)	19(1)	-2(1)	8(1)	-1(1)
C(3)	14(1)	18(1)	27(1)	3(1)	9(1)	1(1)
C(4)	15(1)	12(1)	17(1)	-2(1)	6(1)	0(1)
C(5)	21(1)	22(1)	16(1)	-2(1)	5(1)	5(1)
C(6)	14(1)	23(1)	23(1)	-3(1)	9(1)	0(1)
N(3)	17(1)	19(1)	13(1)	-1(1)	5(1)	-2(1)
C(7)	20(1)	29(1)	32(1)	-3(1)	14(1)	-2(1)
C(8)	33(1)	15(1)	22(1)	0(1)	14(1)	-2(1)
C(9)	27(1)	33(1)	12(1)	0(1)	3(1)	-6(1)
C(10)	27(1)	17(1)	20(1)	-2(1)	11(1)	1(1)
O(9)	42(1)	40(1)	20(1)	-1(1)	5(1)	16(1)

The anisotropic displacement factor exponent takes the form: $-2\pi^2[h^2 a^{*2}U_{11} + ... + 2 h k a^* b^* U_{12}]$

Table A 14 Hydrogen coordinates (x 10^4) and isotropic displacement parameters ($Å^2$ x 10^3) for $[(H_3C)_4N][Cu(PAO^-)(PAO^{2-})(H_2O)]\cdot H_2O$

	x	y	z	U(eq)
H(6D)	6062(5)	4170(30)	4497(14)	23
H(7D)	6274(9)	7402(9)	7043(7)	30
H(7E)	7420(4)	6733(19)	8078(11)	30
H(3A)	2216	4104	3888	29
H(3B)	1728	4598	4991	29
H(3C)	1784	2324	4573	29
H(6A)	9502	4738	5530	29
H(6B)	9572	2354	5420	29
H(6C)	10495	3466	6687	29
H(7A)	14356	9090	8518	39
H(7B)	14274	6707	8345	39
H(7C)	14833	7659	9729	39
H(8A)	11698	5935	9374	33
H(8B)	13215	5848	10297	33
H(8C)	12723	4790	8945	33
H(9A)	10974	8031	7520	38
H(9B)	11947	6850	7039	38
H(9C)	12015	9243	7147	38
H(10A)	11827	9608	9602	31
H(10B)	12828	10844	9186	31
H(10C)	13366	9532	10448	31
H(9E)	10502(19)	2650(20)	10272(3)	54
H(9D)	10949(19)	4116(6)	11257(14)	54

Table A 15. Torsion angles [°] for $[(H_3C)_4N][Cu(PAO^-)(PAO^{2-})(H_2O)]\cdot H_2O$

N(1)-Cu(1)-O(1)-C(1)	-3.35(9)
N(2)-Cu(1)-O(1)-C(1)	-75.5(3)
O(4)-Cu(1)-O(1)-C(1)	-176.77(9)
O(7)-Cu(1)-O(1)-C(1)	91.81(9)
N(1)-Cu(1)-O(4)-C(5)	66.1(4)
O(1)-Cu(1)-O(4)-C(5)	179.17(10)
N(2)-Cu(1)-O(4)-C(5)	6.63(10)
O(7)-Cu(1)-O(4)-C(5)	-88.02(10)
O(1)-Cu(1)-N(1)-C(2)	-0.28(9)
N(2)-Cu(1)-N(1)-C(2)	172.54(9)
O(4)-Cu(1)-N(1)-C(2)	113.8(4)
O(7)-Cu(1)-N(1)-C(2)	-92.23(9)
O(1)-Cu(1)-N(1)-O(3)	-175.87(9)
N(2)-Cu(1)-N(1)-O(3)	-3.06(10)
O(4)-Cu(1)-N(1)-O(3)	-61.8(4)
O(7)-Cu(1)-N(1)-O(3)	92.18(9)
N(1)-Cu(1)-N(2)-C(4)	179.11(11)
O(1)-Cu(1)-N(2)-C(4)	-109.5(3)
O(4)-Cu(1)-N(2)-C(4)	-7.03(12)
O(7)-Cu(1)-N(2)-C(4)	83.23(12)
N(1)-Cu(1)-N(2)-O(6)	1.27(11)
O(1)-Cu(1)-N(2)-O(6)	72.6(4)
O(4)-Cu(1)-N(2)-O(6)	175.14(11)
O(7)-Cu(1)-N(2)-O(6)	-94.60(10)
Cu(1)-O(1)-C(1)-O(2)	-173.38(10)
Cu(1)-O(1)-C(1)-C(2)	6.00(14)
O(3)-N(1)-C(2)-C(3)	0.74(19)
Cu(1)-N(1)-C(2)-C(3)	-175.00(10)
O(3)-N(1)-C(2)-C(1)	179.05(10)
Cu(1)-N(1)-C(2)-C(1)	3.32(14)
O(2)-C(1)-C(2)-N(1)	173.09(12)
O(1)-C(1)-C(2)-N(1)	-6.33(16)
O(2)-C(1)-C(2)-C(3)	-8.50(18)
O(1)-C(1)-C(2)-C(3)	172.08(12)
O(6)-N(2)-C(4)-C(6)	0.2(2)
Cu(1)-N(2)-C(4)-C(6)	-177.76(13)
O(6)-N(2)-C(4)-C(5)	-176.18(12)
Cu(1)-N(2)-C(4)-C(5)	5.88(17)
Cu(1)-O(4)-C(5)-O(8)	176.80(13)
Cu(1)-O(4)-C(5)-C(4)	-5.47(16)
N(2)-C(4)-C(5)-O(8)	177.70(15)
C(6)-C(4)-C(5)-O(8)	1.2(2)
N(2)-C(4)-C(5)-O(4)	-0.2(2)
C(6)-C(4)-C(5)-O(4)	-176.69(14)
N(1)-Cu(1)-O(1)-C(1)	-3.35(9)

VITA

Abdulaziz Ahmed Bagabas

Candidate for the Degree of

Doctor of Philosophy

Thesis: LOW TEMPERATURE PRECURSORS FOR METAL OXIDE CATALYSTS

Major Field: Chemistry

Biographical:

Personal Data: Born in Jeddah, Kingdom of Saudi Arabia, on October 30th, 1975, the son of Ahmed M. Bagabas and Sua'ad M. Bagabas.

Education: Graduated from Model Capital Institute, Riyadh, Kingdom of Saudi Arabia in June, 1993; received Bachelor of Science degree in Chemistry from King Saud University (KSU), Riyadh, Kingdom of Saudi Arabia in July, 1997; completed the requirements for the Doctor of Philosophy degree with a major in Chemistry at Oklahoma State University in July 2005.

Experience: Summer Trainee, Saudi Basic Industrial Corporation (SABIC), Riyadh, Kingdom of Saudi Arabia, June, 1996 to September, 1996; Researcher, Catalysis Group, Petroleum and Petrochemicals Research Institute (PAPRI), King Abdulaziz City for Science and Technology (KACST), Riyadh, Kingdom of Saudi Arabia, October, 1997 to July, 1998; Graduate Research Assistant, Department of Chemistry, Oklahoma State University, Stillwater, Oklahoma, USA, June, 2002 to July, 2005.

Professional Affiliation: American Chemical Society (ACS), American Association for the Advancement of Science (AAAS), Materials Research Society (MRS), American Diabetes Association (ADA), American Ceramic Society (ACS), Phi Lambda Upsilon (PLU) Honorary Chemical Society.

Name: Abdulaziz Ahmed Bagabas
Institution: Oklahoma State University
Advisor: Dr. Allen W. Apblett

Date of Degree: July, 2005
Location: Stillwater, Oklahoma

Title of Study: LOW TEMPERATURE PRECURSORS FOR METAL OXIDE CATALYSTS

Pages in Study: 298 Candidate for the Degree of Doctor of Philosophy

Major Field: Chemistry

Scope and Method of Study: The purpose of the investigation conducted in this project was to establish a simple, cost-effective, environmentally benign method, utilizing the distinctive thermal instability of the metal complexes of pyruvic acid oxime (PAO) ligand, for the synthesis of high surface area, porous, nanocrystalline metal oxide ceramics and testing them as heterogeneous catalyst systems and adsorbents for the remediation of arsenate in aqueous medium. The metal complexes of PAO were readily prepared in aqueous medium via ligand exchange strategy. Structural characterization of these complexes was to verify their formation on the basis of their infrared (IR) and solid-state ^{13}C nuclear magnetic resonance (NMR) spectra, X-ray powder diffraction (XRD), single crystal X-ray diffraction, and thermal gravimetric and differential thermal analyses (TGA and DTA). IR and XRD analyses were used to confirm the formation of metal oxides as the final products of the pyrolysis of the metal complexes of PAO. The crystallite size, the surface properties (acidity, basicity and BET surface area), and the morphology of the metal oxides were to be determined by XRD, the adsorption of base and acid probe molecules, and by scanning and transmission electron microscopes (SEM and TEM), respectively. Some of the metal oxides were to have their catalytic activity examined with either Friedel-Crafts alkylation or Claisen-Schmidt condensation in Teflon bomb reactors at 150 ^{o}C. The analyses of the products were to be executed by gas chromatography/mass spectrometry technique. The adsorption ability of some of the metal oxides for arsenate in aqueous solution was to be performed in the natural pH range of water (6.8-7.1) at room temperature. The equilibrium concentration of arsenic was to be determined using a water analysis test kit (EM Science, Gibbstown, NJ, USA).

Findings and Conclusions: Zinc oxide was very good catalyst for the coupling reaction between benzaldehyde and acetophenone. It was the first time that zinc oxide was used for this kind of reactions. Nickel zinc ferrite was an excellent catalyst for the selective *N*-methylation of aniline using either methanol or dimethyl carbonate as a methylating agent. Tricobalt tetraoxide was the first oxide used for the allylation of benzene. Allybenzene was obtained in very high yield along with a small amount of diallyl ether. Iron, cobalt, and zinc oxides were excellent adsorbent for arsenate in aqueous medium. The cobalt oxide was also used for the first time in such an application. The adsorption capacity of the oxide was found to depend on its surface properties. It appeared that surface acidity played a key role in determining the capacity of the oxide.

ADVISOR'S APPROVAL Dr. Allen Apblett